Magnetic Field Sensing Based on the Infrared Absorption of Nitrogen-Vacancy Centers in Diamond

Dissertation

zur Erlandung des Grades
des Doktors der Naturwissenschaften
der Naturwissenschaftlich-Technischen Fakultät
der Universität des Saarlandes

von

Himadri Chatterjee

Saarbrücken
2021

Tag des Kolloquiums: 02. Dezember 2021

Dekan:	Prof. Dr. Jörn Erik Walter
Berichterstatter:	Prof. Dr. Christoph Becher
	Prof. Dr. Rainer Birringer
Vorsitz:	Prof. Dr. Rolf Pelster
Akad. Mitarbeiter:	Dr. Mina Mohammadi-Kambs

Abstract

In recent years negatively charged nitrogen-vacancy (NV) color centers in diamond have garnered much interest as solid-state quantum sensors for magnetic fields, electric fields, and temperature. These centers are described as two-electron system, whose spin state can be optically initialized, read out, and coherently manipulated, rendering it as an outstanding quantum sensor, even at room temperature. In this work we explore the use of NV ensembles as magnetometer platforms, which promises sensitivities exceeding those of single centers. Our work covers both common optical readout techniques, i.e. recording of the emitted fluorescence or measuring the absorption of infrared light, with a focus on the latter. Furthermore, we investigate the enhancement in sensitivity by multiple internal reflections of the optical fields within a two-dimensional diamond waveguide which increases the interaction path length. These monolithic waveguide structures have the advantage of simpler experimental realization over cavity based setups. Additionally, the experimental findings are corroborated by a semi-empirical rate equation model that takes into account all available setup and sample parameters. In course of this work, we demonstrate sensitivities ranging into the sub-nT/$\sqrt{\text{Hz}}$ regime, being competitive with state-of-the-art demonstrations.

Zusammenfassung

In den letzten Jahren haben negativ geladene Stickstoff-Fehlstellen (NV) Farbzentren in Diamant viel Interesse als Festkörper-Quantensensoren für Magnetfelder, elektrische Felder und Temperatur geweckt. Diese Zentren werden als Zwei-Elektronen-System beschrieben, deren Spinzustand optisch initialisiert, ausgelesen und kohärent manipuliert werden kann, was sie zu einem hervorragenden Quantensensor macht, insbesondere auch bei Raumtemperatur. In dieser Arbeit untersuchen wir die Verwendung von NV-Ensembles als Magnetometerplattformen, deren Empfindlichkeiten potentiell die von einzelnen NV-Zentren übertreffen können. In der vorliegenden Arbeit werden die beiden gängigsten optischen Detektionstechniken verwendet, d.h. Messung der emittierten Fluoreszenz oder der Absorption infraroten Lichtes, wobei der Schwerpunkt dieser Arbeit auf der zweiten Technik liegt. Darüber hinaus untersuchen wir die Verbesserung der Empfindlichkeit, durch mehrfache interne Reflexionen der optischen Felder im zweidimensionalen Diamant-Wellenleiter-Strukturen, was die Wechselwirkungslänge deutlich erhöht. Diese monolithischen Wellenleiterstrukturen können im Vergleich zu Resonator-basierten Aufbauten wesentlich leichter experimentell implementiert werden. Zusätzlich werden die experimentellen Ergebnisse durch ein semi-empirisches Ratengleichungsmodell untermauert, welches alle verfügbaren Parameter der Proben und des Aufbaus berücksichtigt. In dieser Arbeit zeigen wir Empfindlichkeiten für Magnetfeldmessungen, welche die bis in den sub-nT/$\sqrt{\text{Hz}}$-Bereich reichen und damit konkurrenzfähig mit weiteren Experimenten auf dem aktuellen Stand der Wissenschaft sind.

Contents

List of Figures

List of Tables

Acronym	Description
AC/ ac	Alternative Current
BB	Beam Block
BP	Band pass
CW	Continuous Wave
CVD	Chemical vapour deposition
DAQ	Data acquisition
DC/ dc	Direct current
DP	Double Pass
ESR	Electron spin resonance
FID	Free induction decay
FM	Frequency modulation
FWHM	Full width half maxima
HPHT	High pressure high temperature
HWP	Half wave plate
IR	Infrared
ISC	Intersystem Crossing
LIA	Lock-in-apmlifier
LP	Long pass
LTDW	Light trapping diamond waveguide
MFD	Mode field diameter
MM	Multimode
MPCVD	Microwave plasma-activated chemical vapour deposition
MRFM	Magnetic resonance force microscopes
MW	Microwave
NMR	Nuclear magnetic resonance
NV	Nitrogen vacancy
ODMR	Optically detected magnetic resonance
PBS	Polarizing beam splitter
SM	Singlemode
SNR	Signal to noise ratio
SP	Single pass
SQUID	Superconducting quantum interference devices
ZCF	Zero crossing frequency
ZFS	Zero field splitting
ZPL	Zero phonon Line

Table 1: **Frequently used acronyms and abbreviations.**

1 Introduction

Since the advent of quantum mechanics in the early twentieth century, it has always been a pressing question whether this knowledge of atomic and sub-atomic world can be put into concrete applications. On the one hand quantum mechanics helped to enhance the understanding of atomic world, on the other hand its primary applications were seen in the development of lasers, transistors etc. These advances paved the way for the development of modern computers as well as the information technology [1]. In fact, modern human society is completely dependent on these technologies. In the recent years researchers are pushing the boundaries of application of quantum mechanics. The most popular and sought after direction in which academic research and several industries are going right now is the development of quantum computer, quantum communication, and quantum information processing [1, 2, 3]. In this context, in recent years researchers have realized that another most prominent and immediate application of quantum mechanics is to use quantum mechanical systems as sensors. The basic principle for using such systems as sensors lie in the fact that these systems are highly sensitive to external fields. Any tiny disturbance in the "environment" due to external fields affects the quantum mechanical system.

These systems are named "quantum sensors" as they exploit the basic principle of quantum mechanics to sense wide range of physical quantities such as magnetic fields, electric fields, temperature, strain, pressure etc [4, 5, 6, 7]. This nomenclature is used exclusively to distinguish these class of sensors from classical sensors [1, 4], where the quantum mechanical principles are not used. Research in the field of atomic physics, nuclear magnetic resonance, and high resolution spectroscopy over few decades in the twentieth century aiding the present rapid development in this field [4]. The present state of the art research is mainly focusing on the possibility to enhance the sensitivity and resolution as well as miniaturization of these sensors such that it can be used in various fields. For everyday use of quantum sensors in the field of medical sciences,

aviation industry, automobile industry or in space technology all these aspects have to be taken care of [8, 9].

Quantum Sensing

By definition quantum sensing can be of three types. A system can be called "quantum sensor" if the working principle of that sensor falls under any of the following categories [4] : i) a quantum mechanical system is used as a sensor or ii) fundamental quantum mechanical principle such as quantum entanglement is used for sensing purpose or iii) inherent quantum coherence time of a quantum system is used to measure a physical quantity. The quantum mechanical system which is used as a sensor is characterized by quantized energy levels. When the quantum coherence time is used to measure a physical quantity in the type iii) quantum sensors, superposition states of the quantum mechanical system are exploited. The physical quantity which is sensed by this class of sensors can be classical or quantum in nature.

Degen *et al.* [4] have listed four necessary criteria for a quantum mechanical system which can be used for quantum sensing. These set of criteria is analogous to the DiVincenzo criteria for quantum computation [10]. Out of four, three are original DiVincenzo criteria while the fourth one is specific to quantum sensing. The criteria are as follows:

1. "The quantum system has discrete, resolvable energy levels. Specifically, we assume it to be a two-level system (or an ensemble of two-level systems) with a lower energy state $|0\rangle$ and an upper energy state $|1\rangle$ that are separated by a transition energy $E = \hbar\omega_0$."

2. "It must be possible to initialize the quantum system into a well-known state and to read out its state."

3. "The quantum system can be coherently manipulated, typically by time-dependent fields. This condition is not strictly required for all protocols; examples that fall outside of this criterion are continuous-wave spectroscopy or relaxation rate measurements."

4. "The quantum system interacts with a relevant physical quantity $V(t)$, such as an electric or magnetic field. The interaction is quantified by a coupling or transduction parameter of the form $\gamma = \partial^q E = \partial V^q$ which relates changes in the transition energy E to changes in the external

parameter V. In most situations the coupling is either linear ($q = 1$) or quadratic ($q = 2$). The interaction with V leads to a shift of the quantum system's energy levels or to transitions between energy levels."

Several quantum mechanical systems are being investigated as quantum sensors which exploit the above mentioned properties such as, Atomic vapors [5, 11], MRFM (magnetic resonance force microscopy) [12], Trapped ions [13], Rydberg atoms [14], Atomic clocks [15], NMR (nuclear magnetic resonance) ensemble sensors [16], NV (nitrogen vacancy) ensemble sensors [8, 9], Superconducting circuits such as SQUID [17] and Superconducting qubits [18] etc. Among these quantum sensors, in recent years nitrogen vacancy (NV) color centers in diamond [9] have attracted lots of research interest as quantum sensors [19]. These atomic size color centers can exist in three charge states; NV^-, NV^+, and NV^0. Out of these three charge states only the negatively charged NV centers (NV^-) are used as quantum sensors or in quantum information processing [20, 21, 22]. For convenience in this work we refer the NV^- center as NV center unless stated otherwise. NV centers in diamond qualify for all of the above mentioned criteria for a quantum sensor. Interest in NV based sensors increased due to several reasons such as its excellent spin properties at room temperature along with its photostability [23, 24]. Due to the fact that single NV centers are of atomic size (angstrom-scale), with these sensors ultra-high-resolution sensing is possible [25]. Apart from these reasons, research in the field of NV centers rapidly over the last years increased as working with these systems does not require much technical complexity. NV spin states can be optically initialized by a single free-running solid-state green laser mostly at 532 nm wavelength. To readout the NV spin state either the spin state dependent fluorescence signal is collected or spin state dependent absorption of an infrared laser is measured. Apart from these optical detection methods photoelectric detection of NV spin state is possible [26]. Other than the optical and the electrical spin readout protocols, nuclear-assisted readout and spin-to-charge conversion readout techniques are also used to readout the NV spin state [27]. The spin state is coherently manipulated by microwave signal. NV based sensors can operate under ambient conditions therefore no cryogenics or vacuum system is required.

NV center as magnetometer

This work is focused on NV magnetometry therefore we discuss the historical background of NV centers as magnetometer first before explaining the basics

of NV physics. From the historical point of view, the NV color center in diamond was first observed by du Preez in 1965 [28, 29]. In 1997 Gruber *et al.* performed magnetic resonance experiments with individual NV centers at room temperature by using scanning confocal microscope [30] and in 2000, Kurtsiefer *et al.* proved that NV centers are single photon sources by measuring second order autocorrelation function ($g^{(2)}(\tau)$) for a single NV center [31]. In 2004, Jelezko *et al.* performed coherent manipulation and optical readout of NV spin state [32, 33]. These experiments led the way for single electron spin resonance (ESR) experiments with NV centers.

Around year 2008, the NV center was first proposed and demonstrated to be used as magnetometer by Taylor *et al.* [34], Degen *et al.* [35], and Maze *et al.* [36]. Following these experiments, NV magnetometer based on single NV center or ensemble of NV centers became a prime research area [8, 9, 24, 36, 37, 38]. NV sensors can be employed to sense DC and AC signals. For DC signal sensing it measure signals that are slowly varying with a bandwidth from DC up to 100 kHz [39, 40, 41]. Thus, due to broadband operation these sensors are called broadband NV sensors. In the AC sensing protocol, it is possible to measure a time-varying signal with frequencies up to GHz regime, in principle these signal are narrowband in nature [42, 43, 44, 45, 46, 47, 48, 49, 50, 51, 52, 53, 54, 55, 56].

As stated before, the use of single NV centers as sensor may yield high spatial resolution [25, 57, 58]. In contrast to that, using ensembles of NV centers can enhance the signal-to-noise ratio thus increases the sensitivity by the virtue of statistical average over multiple NV spins. In some applications where the requirement does not demand high spatial resolution but high sensitivity, the use of NV center ensembles is advantageous [59]. NV magnetometers with high NV concentration can be used for high-sensitivity measurements as wide-field magnetic imaging sensors or vector magnetometer [19]. In a diamond sample the single NV center's symmetry axis lies along one of the four <111> crystallographic orientations. Therefore in an ensemble of NV centers there is an equal probability to have NV centers whose symmetry axes distributed along all four crystallographic orientations. Each of these classes of NV in each orientation is sensitive to different magnetic field components. Due to this fact magnetometers based on ensemble of NV centers can provide full vector magnetic field sensing [34, 36, 41, 47, 60, 61, 62, 63].

Apart from the most common scheme for NV magnetometry which is based on spin state detection by collection of NV fluorescence there is another optical

detection protocol for NV based magnetometry. This scheme is based on the spin state dependent infrared absorption measurement in a NV ensemble. This technique was first demonstrated by Acosta *et al.* [64]. A high NV concentration is required to perform this protocol for NV magnetometry as the infrared transition absorption cross section is very small. An improved version of this protocol uses cavity based path length enhancement to increase the interaction path length [65, 66, 67]. Other than employing an optical cavity an alternative way for infrared absorption magnetometry is to use diamond waveguide structures. In these structures the optical path length is increased by means of multiple total internal reflections of the optical beams inside the diamond waveguide as shown by Bougas *et al.* [68]. This approach was adapted from the work of Clevenson *et al.* [69], where they used a similar approach for enhancing the sensitivity by means of increasing the sensing volume for fluorescence magnetometry.

NV center based quantum sensors have been used in many examples of applied or fundamental research, such as sensing temperature [70, 71], pressure [7], strain [72], and electric fields [6]. They have been used to probe geological samples [73], meteorite composition [74], and paleomagnetism [75]. Scanning NV center magnetometry is used to explore fundamental problems of condensed matter physics [76]. In biological applications NV based sensors stand out as diamond is bio compatible [77, 78]. Magnetic imaging of single living cells or biological tissue with sub-cellular resolution has been performed with NV sensors [46, 60, 63] as well as detecting single protein [79]. Barry *et al.* [40] performed experiment to sense single-neuron action potentials by the use of ensemble NV magnetometer.

There are several advantages of NV center based magnetometer compared to other magnetometers. First, the NV center in diamond is an atom like defect center embedded in the diamond lattice therefore localized on a sub-nanometer length scale [8]. For this reason, magnetometers based on single-NV center can achieve a spatial resolution of sub nanometer scale and a sensitivity in the $\mathrm{nT}/\sqrt{\mathrm{Hz}}$ regime [25, 58], in room temperature. Compared to NV based magnetometers, superconducting quantum interference devices (SQUID) [17] can reach a sensitivity in the $\mathrm{fT}/\sqrt{\mathrm{Hz}}$ regime in cryogenic temperature but not the spatial resolution achieved in NV magnetometers. Quantum sensors such as magnetic resonance force microscopes (MRFM) [12] can offer a spatial resolution and a sensitivity ($\mathrm{nT}/\sqrt{\mathrm{Hz}}$) in nanoscale regime. However it needs large

magnetic field gradient as well as cryogenic temperature [12]. An atomic vapour magnetometer [11] can reach a sensitivity of 1 fT/$\sqrt{\text{Hz}}$ in room temperature but the spatial resolution is few mm.

Another advantage of NV magnetometers is, its high magnetic field sensitivity with a small sensing volume. In the work of Le Sage *et al.* [37] a sensitivity of 100 pT/$\sqrt{\text{Hz}}$ was achieved with a sensing volume of 10^{-4} mm^3. Single-neuron action potential has been detected by Barry *et al.* [40] with a sensing volume of (13 × 200 × 2,000) mm^3, where the achieved sensitivity was 15 pT/$\sqrt{\text{Hz}}$. These characteristics of NV magnetometers to reach high sensitivity with small sensing volume in room temperature paving the way for practical applications [80]. Recently Stüner *et al.* [81, 82], demonstrated an integrated and portable NV magnetometer.

This dissertation focuses mainly on infrared absorption based magnetometry with NV centers. As stated in the previous paragraph, for infrared absorption magnetometry it is necessary to use ensemble of NV centers. In our work therefore we use bulk diamond samples enriched with NV centers. It is also crucial to enhance the optical interaction path length which effectively increases the sensing volume of the magnetometer. For our experiments we use diamond waveguide structures where the optical beams undergo multiple total internal reflections from the diamond sidewalls. With different interaction path lengths and different NV concentrations we investigate the magnetic field sensitivity of our magnetometers. We further investigate fluorescence magnetometry with the same samples for bench marking of the absorption magnetometry.

Thesis Outline

In chapter 2 the discussion is mainly focused on diamond as a host material for the nitrogen vacancy (NV) center and on the physical properties of NV centers in sections 2.1 and 2.2 respectively. In section 2.3, a description of the spin dynamics of NV centers is given. As quantum sensors NV center possess characteristic quantum coherence times which are intrinsic to the NV spin system. These characteristic coherence times play crucial roles to determine the sensitivity of NV based sensors and we give a broad overview in the section 2.4. In chapter 3, different magnetometry methods based on ensemble and single NV center magnetometry are discussed to give an overview of NV magnetometry and compare the advantages and disadvantages of the individual schemes. A discussion regarding the sensitivity and the limiting factors for sensitivity is

also provided in this chapter.

Chapter 4 is dedicated to the discussion of the semi-empirical NV center rate equation model. This is used as a theoretical framework for the experimental results presented in this thesis. It takes into account all the sample and setup parameters used in our experiments.

The experimental method and the experimental set up are described in chapter 5. In this chapter the discussion is focused on the experimental method we use to measure magnetic fields which is continuous wave optically detected magnetic resonance (CW-ODMR) for infrared absorption based magnetometry and fluorescence magnetometry. Along with the experimental method here we also discuss the experimental setup and the choices of specific electronic instruments and optical elements. In chapter 6 the discussion is on the experimental results obtained with fluorescence magnetometry on different samples with varying NV concentrations. Along with the magnetometry results obtained with fluorescence magnetometry, in section 6.1 provides the magnetometer characterization results. These set of experiments were performed to characterize our magnetometers in different phases of our experiments to optimize the magnetometry performances. Chapter 7 analogously provides the results obtained from infrared absorption magnetometry. Future possible experiments to enhance the magnetic field sensitivity are discussed in the chapter 8. Chapter Appendices provides the appendices where we discuss on the attempt to build a monolithic ring cavity for infrared absorption magnetometry. Other appendices are providing determination of beam waist with sharp knife edge method and details regarding sample orientation for hyperfine coupling experiments, and path length calculation.

2 Nitrogen-Vacancy Centers in Diamond

The experimental results, which are presented in this work have been performed with nitrogen-vacancy (NV) color centers in diamond. The above mentioned amazing properties of the NV center make this color center in diamond a very good candidate for sensing of magnetic field, electrical field, temperature shift and crystal strains [6, 24, 71, 83, 84]. In this chapter the discussion is about the host material for NV center, which is diamond (section 2.1), how synthetic diamond is grown for experimental purpose, creation of NV centers in synthetic diamond and its properties (section 2.2), and finally the spin dynamics along with characteristics times of NV center itself (section 2.3 and 2.4).

2.1 Diamond

Since long diamond has amazed humans due to its lustre as a beautiful gemstone. But, it is not just the lustre, which makes diamond a fascinating gemstone. The other physical properties such as extraordinary hardness or high thermal conductivity makes it interesting for scientists and engineers. Because of these physical properties, diamond has application in polishing, grinding, as heat sink or in high power electronic devices [85, 86, 87].

To understand these physical properties of diamond we have to look into the crystal structure of diamond. The sp^3- hybridized carbon atom has four valence electrons each, which form a covalent bond with the valence electrons of neighboring atoms. This covalent bond has an angle of 109.5° and the distance between adjacent atoms of 1.54 Å. These conditions result in a face centered cubic (fcc) unit cell, which has a lattice constant of 3.57 Å and basis of {(0, 0, 0), (1/4, 1/4, 1/4)} (Refer to figure 2.1) [88].

This strong covalent bond, which forms the unit cell of diamond makes the

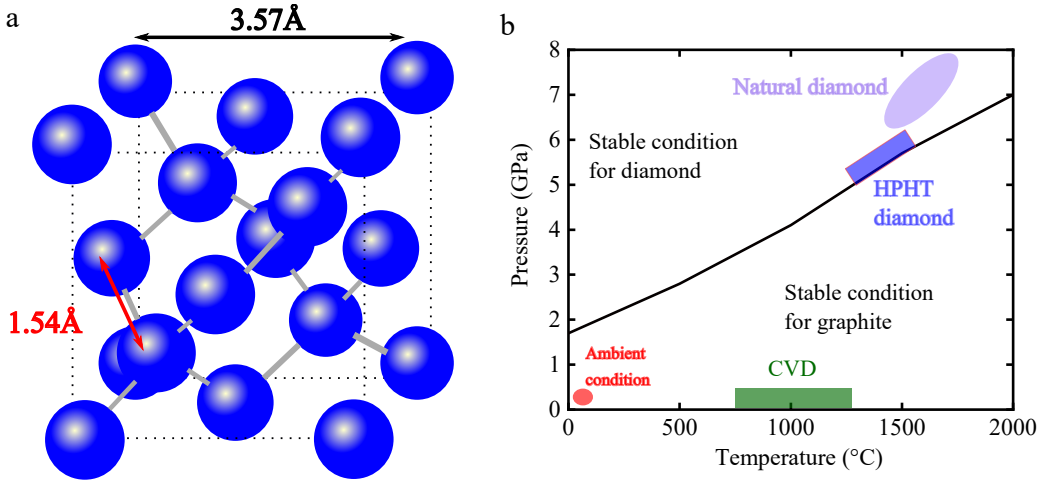

Figure 2.1: **Diamond Lattice and carbon phase diagram**. In figure a) the schematic diagram of diamond lattice is shown. The diamond lattice constant 3.57 Å is shown with black arrow and text and the distance of the two adjacent carbon atoms is shown in red arrow and text. In figure b) the carbon phase diagram is plotted to show the natural conditions for diamond growth as well as the stable and unstable conditions to grow synthetic diamonds (both HPHT and CVD grown diamonds). The graph in figure b) is recreated with values adapted from [85]

material very rigid and hard. Diamond is the naturally occurring hardest material available on earth. In Mohs scale of hardness diamond has the highest rating of 10. Due to this strong covalent bond and the high energy phonons, diamond also has high specific heat of 2240 K and very high thermal conductivity of 2200 $Wm^{-1}K^{-1}$. Diamond has a bandgap of 5.48 eV (wavelength of 226.25 nm), which makes the material a wide band gap semiconductor as well as optically transparent for the entire visible range of light (wavelength in between 400 nm to 800 nm) [88]. The lustre of polished diamond comes from the fact that it is transparent for the visible range of light as well as it has a very high refractive index of 2.42 [88].

Natural diamond is formed near the earth's mantle; which is around 200 km deep inside earth; in extreme temperature and pressure conditions. In this condition, the pressure and temperature is typically in the range of 7 - 8 GPa and 1400° C - 1600° C respectively [85], which is stable condition for diamond in the carbon phase diagram (Refer to figure 2.1 b)). At ambient conditions graphite is the stable allotrope of carbon and diamond is metastable allotrope of carbon, as it can be seen in the carbon phase diagram 2.1. Still diamond is

considered stable at ambient conditions due to the fact that, the diamond to graphite conversion is extremely slow under these conditions due to high energy barrier of 728 kJ/mol [85].

Due to the fact that the diamond lattice is very rigid, it is unlikely for other atom impurities to enter the lattice. However, depending on different growth conditions, natural diamonds can have impurities of nitrogen or boron atoms, which are of about the same size of carbon atoms. These impurities inside diamond lattice lead to different color of the diamond, due to specific absorption lines or bands [89]. While abundance of nitrogen impurities make the diamond appear as yellow, boron impurities turn diamond more into blue colored stone. The natural occurrence of nitrogen and boron and their difference in concentration in a diamond has led to classification of diamond into sub-classes. This modern classification of diamond was first done by Dyer *et al.* in 1965 [90]. Main four sub-classes of diamonds are following

1. **Type Ia**: This type of diamond has a high nitrogen concentration of around 500 – 3000 ppm (non-paramagnetic aggregates of nitrogen).

2. **Type Ib**: This type of diamond has a nitrogen concentration of around 40 – 100 ppm (single substitutional nitrogen atoms).

3. **Type IIa**: This type of diamond has a low nitrogen concentration of $\sim$ 1 ppm and lower.

4. **Type IIb**: This type of diamond has a low nitrogen concentration of $\sim$ 1 ppm and lower, but boron is main impurity here (10^{17}cm^{-3}, in natural diamond)

Synthetic Diamonds

Due to above mentioned special optical and physical properties of diamond, there have been a special industrial effort to manufacture synthetic diamonds. These efforts started since 1880 onward. Scientists, such as J. B. Hannay, Sir Charles Parson tried to make synthetic diamonds by various means. The first successful method to produce artificial diamond was demonstrated by F. P. Bundy *et al.* of General Electric Company in 1955 [91]. These synthetic diamonds are used not only in scientific and technical research and applications but also as gemstones. The techniques to produce artificial diamonds got perfected

by the middle of twentieth century, from thereon more and more such artificial diamonds are being produced for several purposes. There are mainly two way to produce synthetic diamonds, namely High Pressure High Temperature (HPHT) synthesis and Chemical Vapour Deposition (CVD).

High Pressure High Temperature synthesis

Historically the first production of artificial diamonds was done by High Pressure high temperature (HPHT) synthesis by Bundy *et al.* in 1955. In this process, as the name suggests, high pressure and high temperature conditions are used as it is present during natural growth of diamond. To reach the high pressure high temperature conditions they used pressure vessels, which they operated at pressures up to 10 GPa with temperatures more than 2000°C [91]. From the phase diagram of carbon (figure 2.1 b)), it is evident that at such conditions, diamond is thermodynamically stable. The diamonds which are grown under HPHT conditions are found to be enriched with nitrogen impurities thus leading to the growth of Ib diamonds. This happens due to less control over the parameters during growth process and is one of the disadvantages of HPHT growth of synthetic diamond [85]. In applications where the the purity of diamond is not that critical, HPHT diamonds are typically still preferred [92].

Chemical Vapour Deposition

Another popular method to grow diamond is the Chemical Vapour Deposition (CVD) synthesis. Compared to stable regime of phase transition in HPHT synthesis of diamond, in CVD synthesis the growth regime is metastable [85, 93]. Therefore, in the CVD synthesis, growth of diamond is governed by kinetics rather than thermodynamics . In CVD process, first a diamond seed crystal is placed on a heater inside a growth chamber. The surface of that seed diamond serves as a growth substrate. The heater inside the growth chamber is heated typically to the range of 700 – 1300°C, while the pressure is kept around 30 mbar [92]. For this process of diamond growth, chemical activation of the gaseous reactants (mainly hydrogen and a few percentage of methane) is required. This activation process of the gaseous mixture is achieved by plasma activation. On that account the reactants are irradiated with microwave radiation of several hundred Watts, generating a plasma of the gas mixture. Therefore this synthesis

process is often named microwave plasma-activated chemical vapour deposition (MPCVD) [85, 86, 93].

The gas mixture which consists of mostly hydrogen (H_2) and 0.5 % - 5 % of methane (CH_4) is heated up by the microwave radiation, eventually reaching temperatures at which the gas mixture turns into a plasma. The hydrogen in the plasma converts into highly reactive atomic hydrogen (H) which etches graphite from the diamond surface. This step is crucial as the synthesis happens in a regime where graphite is the stable allotrope of carbon instead of the desired diamond. Etching of the diamond surface by the atomic hydrogen leads to formation of dangling carbon bonds. These dangling bonds can be either terminated by hydrogen atoms or the carbon atom of a CH_3 radical, where the latter is created from the CH_4 in the plasma. By this process then the diamond slowly grows in layers. It has been shown by Mizuochi *et al.* [94] that using deuterium instead of hydrogen in the gas mixture can indeed improve the sample quality even more.

As the quality of gas mixture can be highly controlled, the CVD process leads to production of high quality pure diamond (mostly of Type IIa) compared to HPHT process. CVD method can also provides the opportunity to perform isotopically controlled growth. Samples consisting of up to 99.997% ^{12}C atoms, with nitrogen content as low as 4 ppb [95] were produced by using isotopically enriched methane. Recently diamond samples with 99.999% ,^{12}C enriched atoms have became available and were used in sensing experiments with nitrogen-vacancy center [96].

2.2 Nitrogen-Vacancy center

The nitrogen-vacancy (NV) center in diamond crystal is a stable defect center consisting of a substitutional nitrogen atom and a vacancy on an adjacent lattice site [8, 9]. The defect has a symmetry of C_{3v} with the symmetry axis of the defect oriented along one of the four possible body diagonals $\langle 111 \rangle$. Both the substitutional nitrogen and the vacancy lie on the symmetry axis of the nitrogen-vacancy center. Thus, depending on the crystallographic orientation of the NV center it could be classified in four classes of NV for convenience of description while working with ensemble of NVs in a diamond (e.g. Class A, Class B, Class C, Class D of NV). These four classes of NV have the same

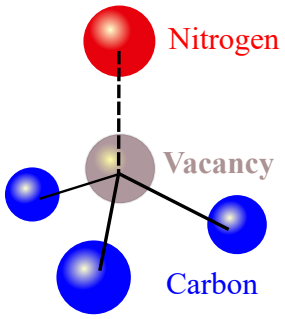

Figure 2.2: **NV center schematic diagram**.This figure shows the simple schematic diagram for NV center. Blue spheres represent carbon atoms, red and brown spheres represents nitrogen atom and vacancy respectively.

spin and optical properties. In an ensemble there is equal probability to find these four classes of NVs. The NV centers in diamond can exist in three charge states namely NV^-, NV^0, and NV^+[97]. Before we are going to further discuss the properties of NV^- center in more details, here the process of creating NV centers in diamond is discussed briefly.

Nitrogen-Vacancy center generation

The nitrogen-vacancy (NV) centers in diamond can be found in natural diamonds, where the concentration of nitrogen impurity is high. In synthetic diamond, during the growth of diamond in HPHT or in CVD process NV centers can form inside diamonds. For industrial applications or in research these CVD or HPHT grown diamonds with NV centers in it are used. There are mainly two ways to form NV centers in synthetic diamond. One way is implantation of nitrogen ions in CVD or HPHT diamonds, followed by an annealing process and the other way is incorporating NV centers inside the diamond during the growth process. The later process is mainly used in CVD grown synthetic diamond. Both of these processes are discussed briefly in the following text.

Ion implantation and annealing process

NV centers can be created in diamond by implanting ions and successive annealing of the implanted diamond. For ion implantation either N^+ or $N_2{}^+$ ions

are used. In this process different parameters can be varied to create desired diamond samples with desired NV vacancy concentration or to create NV implanted layer at different depths of the diamond samples depending on the application. For example, depending on the implantation energy, implanted layer is created at different depths of the diamond. NV layers can be created very near (few nm) to the surface of the diamond, e.g. for applications in quantum sensing [38, 42, 76]. In some application though it is more important to have a specified concentration of NV centers in the diamond, which can be achieved by varying the implantation time and ion fluence accordingly. Naturally abundant isotope of nitrogen is ^{14}N (99.6%), therefore to distinguish the implanted ion species of nitrogen from the substitutional nitrogen which was present during the diamond synthesis process often ions of ^{15}N isotope is implanted [98, 99, 100]. The optically detected magnetic resonance spectrum gets influenced by the nuclear spin of the substitutional nitrogen; from these experiments (see section 2.3.1) it is possible tell the nitrogen isotope which is mostly present in the diamond sample. Therefore in many cases, isotopes of nitrogen (^{14}N and ^{15}N) which is implanted is varied, to distinguish the naturally abundant nitrogen isotopes from the implanted nitrogen in the diamond samples.

The implantation process plays two major roles in forming NV centers in diamond. First, it introduces the substitutional nitrogen in the diamond and second, it creates vacancies by damaging the diamond crystal. After the implantation process the diamond is annealed above 600°C. This annealing process mobilizes the vacancies in diamond crystal, which were created during the ion bombardment process. The mobile vacancies then get trapped adjacent to substitutional nitrogen atoms, which yields the desired NV centers. Implantation of nitrogen impurities create crystal strain in the diamond due to the slight difference in the atomic size. Trapping of the vacancies adjacent to the substitutional nitrogen atoms thus releases the crystal strain.

Creation of NV centers by ion implantation and subsequent annealing process has some advantages as well as disadvantages. As stated before ion implantation allows much control over implantation dosage, ion fluence, ion energy which are varied to get desired NV concentration and the depth of resultant doped layer. By masking the diamond surface, it is furthermore possible to laterally position NV centers in desired position during the implantation process. NV centers can be positioned laterally with high precision ($\tilde{}$ 10 nm), which can

be used as qubit in quantum computation or quantum information, where NV centers are positioned in desired array [98, 101].

The disadvantages of ion implantation process to create NV centers in diamond can be summarized as follows. NV centers formed by ion implantation often exhibit less photo-stability [23, 24], experience more charge instability for NV^-charge state or photochromism (conversion from NV^- to NV^0 charge state) [102, 103, 104]. These NV centers tend to have even shorter spin coherence times (T_2 time, typical values are around 10µs) [105]. These inferior properties might result from crystal damages, surface defects or formation of other defects during the implantation process [99, 106].

CVD growth process

NV center can also be created by incorporating nitrogen impurities during CVD growth process of diamond sample. It is done via controlled in-flow of nitrogen gas into the growth chamber. In this process of creating NV centers, the distribution of NV centers could be homogeneous throughout the grown crystal or can be restrained to a narrow spatial distributions [107, 108]. In the work of Ohno *et al.* [109] it has been demonstrated that approximately 2 nm thick nitrogen doped layer was grown in CVD synthesis.

In this process they introduced a thin nitrogen doped layer (1–2 nm) by reducing the growth rate to 0.1 nm/min. Nitrogen (N_2) gas was introduced in a controlled manner during plasma enhanced chemical vapor deposition (PECVD) of high quality, single-crystal diamond. To create this thin nitrogen doped layer the timing and the duration of nitrogen inflow is controlled by a mass flow controller. In previous discussion on ion implantation, it has been stated that the ion implantation plays a dual role of creating vacancy as well as implanting nitrogen ions. In contrast to the ion implantation process in CVD synthesis of NV center, vacancies are created separately. Although during the growth process some vacancies are created but the number of such vacancies are much less than required to transform each nitrogen atoms to NV center. Therefore the vacancies are created by electron irradiation and by subsequent annealing the NV centers are created [107, 109, 110]. In this process of creating vacancies the damage in the nitrogen-doped layer is very much less compared to the ion implantation method. Therefore in CVD synthesis the crystal quality is high as the in-situ grown NV centers experience less strain compared to

the implanted NV centers. CVD growth process provide depth localization of NV center enriched layer. The depth localization can also be achieved by low energy implantation but has some drawbacks. After low energy implantation the NV centers are close to the surface. Due to the close vicinity to the surface these NVs suffer from charge state instability also comparatively inferior spin coherence to their counterparts which are deep into the diamond samples. These can be improved by CVD diamond overgrowth on top of NV enriched layer. In the same work the spin coherence time (T_2 time varies from 70µs to 250µs) has been measured to be very high compared to the ion implantation method [109]. The NV centers grown in nitrogen delta doping during CVD growth shows more charge stability. The spin coherence time is limited only by the presence of ^{13}C nuclear spin, which could be also increased in ^{12}C enriched diamonds [109].

Charge states of NV centers

The NV center in diamond can exist in one of the three possible charge states namely NV^0, NV^- and NV^+[97]. These charge states can be understood by the electronic structure of NV centers in diamond crystal. In diamond crystal each carbon atom has four neighbors. During the formation of NV center one of this carbon atom is replaced by a substitutional nitrogen atom and the adjacent carbon atom is replaced by a vacancy. Both the nitrogen atom and the vacancy therefore have three neighboring carbon atoms. For the nitrogen-vacancy system, the three carbon atoms adjacent to the vacancy donate one electron each while the nitrogen atom donates two electrons making a total of five electrons for NV center. This configuration is called the neutral state of the NV center, with the electron spin S = 1/2 and denoted by NV^0. If there is a donor nearby which donates one more electron to the NV system the total number of electron becomes six and electron spin system S = 1. This charge state is negatively charged NV state and denoted by NV^-[111]. In case there are acceptors present in the diamond crystal, then the neutral NV^0donate one electron and becomes NV^+(with four electron) . To distinguish between the NV^0 and NV^-charge states, one has to collect emission spectrum, where zero phonon line for the two charge states (575 nm and 637 nm respectively) can be identified (see Figure (2.3)).

Out of all these charge states, NV^- charge state can be optically initialized and

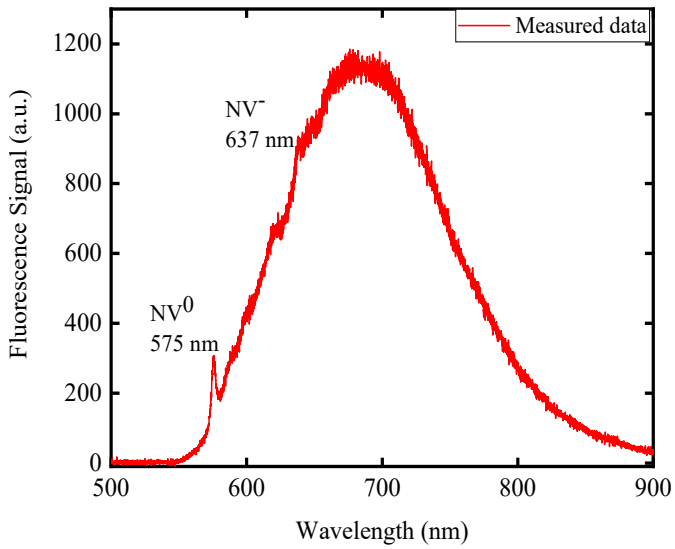

Figure 2.3: **Nitrogen-Vacancy spectrum.** In this spectrum the zero phonon lines of NV^0 and NV^- charge states, respectively at 575 nm and 637 nm, can be seen. Note that the ZPL for NV^- at 637 nm is not very prominent in the obtained spectrum. The phonon sideband for $NV^-$is spread over 640 nm to 800 nm. The spectrum was measured in our experiment.

read out along with microwave manipulation. It is sensitive to magnetic field, electric field as well as crystal strain [8, 9]. Therefore the negatively charged nitrogen-vacancy (NV^-) color centers are employed as quantum sensors. As this work solely focuses on the application of the NV^- centers as a magnetic field sensors, it is simply referred to as NV center in the following sections and chapters, if not stated otherwise.

Energy level of NV center

From the above description we know that NV center has six electrons. Out of these six electrons two electrons are unpaired electrons. The NV centers can be described by triplet ground and excited states with two singlet intermediate states. From group theoretical analysis the symmetry of these triplet and singlet states have been described [111]. The ground and excited states have $^3A_2$ and ^3E symmetry respectively, whereas the intermediate states have $^1A_1$ and ^1E symmetry (Please refer to figure 2.4).

In the triplet ground state, the $m_s = 0$ and the $m_s = \pm 1$ states experiences a zero-field-splitting (ZFS) due to spin-spin interactions between the two unpaired

electrons [111]. This ZFS has a value of 2.87 GHz [112]. A zero-field-splitting is also observed in the excited state with a value of 1.42 GHz [113, 114].Accordingly, transitions between the split ground and exited states can be conveniently addressed using microwave frequencies. When an additional bias magnetic field is aligned parallel to the NV axis (B_{NV}), the degeneracy of the $m_s = \pm 1$ states is lifted due to Zeeman shift. This Zeeman shift is given by $\Delta = m_s \gamma B_{NV}$. Here $\gamma = g_e \mu_B / \hbar = 1.76 \times 10^{11} \mathrm{s}^{-1}\mathrm{T}^{-1}$, is the NV gyromagnetic ratio [69].

Optical properties

At room temperature the main optical transitions are characterized by a 637 nm Zero-Phonon-Line (ZPL) transition from the ^{3}E excited state to ^{3}A$_2$ ground state followed by a broad phonon sideband (640 - 800 nm) [115, 116]. This transition is spin conserving and only a few percentage (4%) of the fluorescent photons are emitted in the ZPL while the majority of fluorescence is emitted in the phonon sideband. Another transition is present via the intermediate singlet states (^{1}A$_1$ and ^{1}E) with ZPL value of 1042.5 nm [39]. The non radiative decay from the triplet excited states to the singlet intermediate states is known as intersystem crossing (ISC) [117, 118]. For optical excitation of the NV center, an off resonant green laser can be used (mostly 532 nm wavelength).

The energy levels along with the main transitions can be seen in figure (2.4), and the detailed physics is described in the following section. In principle, when the NV center is off resonantly excited by a green laser, the excited state gets populated. From the excited state, it can decay to the ground sate in two different way. The first one is the above mentioned spin conserving transition with the 637 nm ZPL. The alternative decay path involves a intersystem crossing from the triplet excited states to singlet intermediate states and back to ground states. The $m_s = \pm 1$ states have much higher probability to undergo the intersystem crossing (ISC) than the the $m_s = 0$ state. In the intermediate singlet states there is another transition from the ^{1}A$_1$state to the ^{1}E state, which is in the infrared region (1042.5 nm). From the ^{1}E singlet state, there is higher probability that the NV state will decay back to $m_s = 0$ state rather than $m_s = \pm 1$. Due to this preferential decay to the $m_s = 0$ state, with continuous optical excitation the NV spin is polarized to the $m_s = 0$ state. The fluorescence lifetimes in the triplet system are 12 ns for $m_s = 0$ and 7.8 ns for $m_s = \pm 1$, while it is below 1 ns in the singlet system. the singlet system

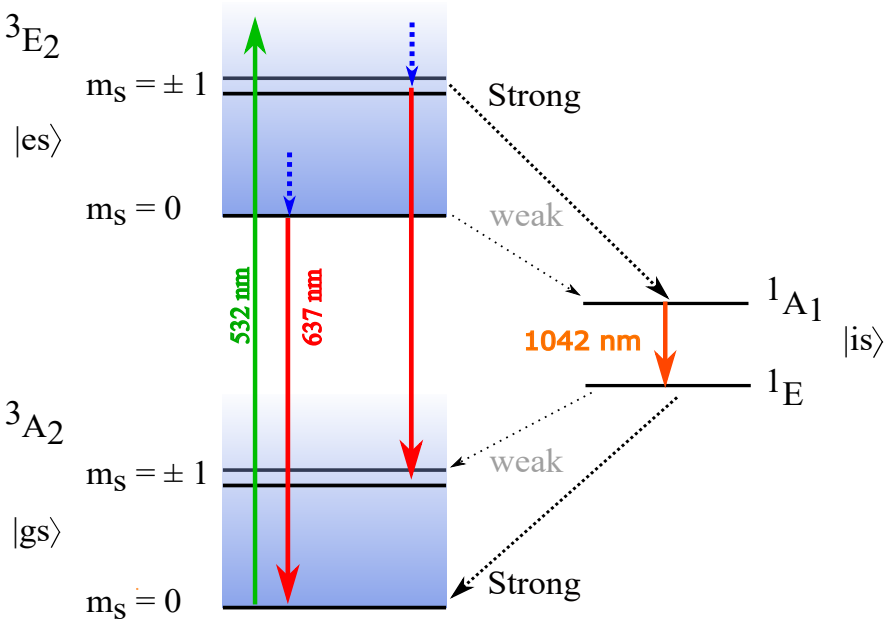

Figure 2.4: **Nitrogen-Vacancy optical transitions.** In this diagram the energy level scheme and the optical transitions for NV^- charge state is shown. The green arrow refer to the off-resonant green pump laser (532 nm). The red arrows shows the zero phonon line optical transitions (637 nm) from the excited state to the ground state. In between the excited state and the ground state NV center has an intermediate metastable state. The orange arrow here depicts the infrared transition in the metastable state. There is a strong probability of ISC from the $m_s = \pm 1$ state than the $m_s = 0$ state in the excited state. From the lower metastable state the probability for ISC is strong to $m_s = 0$ state rather than $m_s = \pm 1$.

ground state is metastable and relaxes with a time constant of 220 ns at room temperature back to the triplet system [39, 119].

Given the facts, that the continuous optical excitation results in spin polarization into $m_s = 0$ and the ISC mechanism is mostly non-radiative [39, 117, 118], when NV centers are in $m_s = 0$ state they have higher fluorescence compared to when they are in $m_s = \pm 1$ states. The difference between the fluorescence of $m_s = 0$ state and $m_s = \pm 1$ state is quantified as the fluorescence contrast. The fluorescence contrast between both states can be up to 30% for single NV centers, but is reduced for ensembles [37, 83, 120, 121].

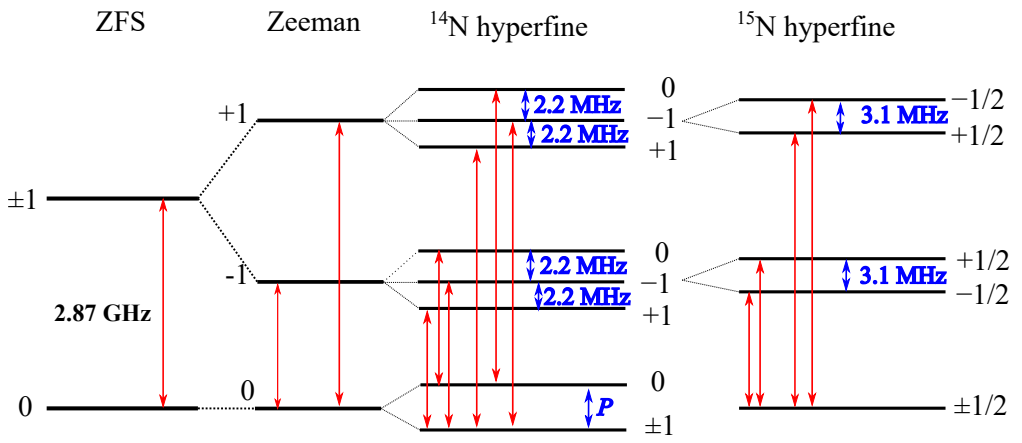

Figure 2.5: **Microwave transitions for NV center.** In this figure the microwave transitions are shown for zero-field-splitting (far left), Zeeman splitting of the $m_s = \pm 1$ spin sublevel and the hyperfine coupling with ^{14}N and ^{15}N nuclear spin. These transitions are experimentally verified in optically detected magnetic resonance (see section 2.3). Image adapted and modified from [120] and values for ^{15}N hyperfine coupling are taken from [123, 124]. P is the quadrupole interaction for ^{14}N nuclear spin. Values for ^{14}N is taken from our experimental results (see section 6.1). See text for more details.

Hamiltonian for NV center ground state

The Hamiltonian for the ground state of the NV center consists of three different parts as described in the following equations (equations 2.1 to 2.4) [9, 122, 123]. In the Hamiltonian, H_{ZFS} describes the electronic part which consists of axial zero-field-splitting and non-axial zero-field-splitting due to local strains and electric field. The electron Zeeman splitting in the presence of a bias magnetic field is described by the H_{ZS} part of the Hamiltonian. Finally, H_{HF} describes the hyperfine interaction in between and the nitrogen's nuclear spin.

$$H_{gs} = H_{ZFS} + H_{ZS} + H_{HF}. \tag{2.1}$$

$$H_{ZFS}/h = D_{gs} S_z^2 + E(S_x^2 - S_y^2). \tag{2.2}$$

$$H_{ZS} = \gamma_{NV} B_z S_z. \tag{2.3}$$

$$H_{HF}/h = A_{\parallel} S_z I_z + A_{\perp}(S_x I_x + S_y I_y) + P I_z^2. \tag{2.4}$$

The terms in the above equations 2.2 and 2.3 are as follows; D_{gs} is the ground state zero-field-splitting as mentioned before with a value of 2.87 GHz,

E is the off-axis parameter arises from electric fields and local strain. The value of E is much smaller than D_{gs}. With variation of temperature and pressure the value of D_{gs} varies. For variation of temperature the rate of change is $dD_{gs}/dT = -74.2$ kHz/K, reported in the work of Acosta *et al.* [125]. The rate of change with pressure (p), is $dD_{gs}/dp = 1.46$ kHz/bar shown in the work of Doherty *et al.* [7]. S_x, S_y, S_z are the spin-1 projection operators for the NV spin system. $\gamma_{NV} = g_e \mu_B/\hbar$, is the NV gyromagnetic ratio where g_e is the Lande´ g-factor, μ_B is the Bohr magneton. B_z is the z-component of the magnetic field along the NV axis. $A_\parallel$ and $A_\perp$ are the parameters of the hyperfine tensor describing interactions with local nuclear spin. $I_x I_y, I_z$ are dimensionless spin operators for the nitrogen nuclear spins. For ^{14}N isotope, the values for $A_\parallel$ and $A_\perp$ are around -2.14 MHz and -2.70 MHz respectively and for ^{15}N isotope these values are +3.03 MHz and +3.65 MHz respectively [123]. For ^{15}N nuclear spin ($I = 1/2$) there are no quadrupole interaction with the NV spin [124], whereas for ^{14}N ($I = 1$) this additional interaction is present which is given as parameter P in the above equation, with a value of - 5.01 MHz 2.4 [123]. In the figure 2.5, all the possible transitions which can be verified in experiment is shown with a schematic diagram.

2.3 Spin dynamics of nitrogen-vacancy center

In this section we will go through the theory of continuous wave optically detected magnetic resonance (ODMR) with fluorescence signal as well as infrared laser signal used to probe the singlet spin states of NV centers. These methods are extensively used in this presented work therefore we need to understand the physics behind these methods. Before we delve into the magnetometry results we also need to understand how NV centers can be be employed as a sensor for magnetic field. For optical magnetometry a two level system [5] is needed. In section 2.3.2, the discussion is centered around the fact that NV center can be approximated as two level system hence can be employed as an optical magnetometer.

2.3.1 Continuous Wave Optically detected magnetic resonance

The fact that fluorescence of NV center is spin state dependent and the transitions ($m_s = 0$ to $m_s = \pm 1$) can be driven by applying microwave (MW) radiation, gives the opportunity to perform continuous wave optically detected magnetic resonance (CW - ODMR) [30]. By performing CW - ODMR, NV spin resonances are determined experimentally. To perform CW - ODMR, simultaneous green laser (mostly at 532 nm) excitation and microwave (MW) radiation are applied on the NV spin. The continuous green laser illumination polarizes the NV spin into $m_s = 0$ state which results in high fluorescence. One way to display the spin transitions is to simply sweep the frequency of the MW field across the respective resonances. When the MW is off-resonant with the possible transitions, which are $m_s = 0$ to $m_s = +1$ and $m_s = 0$ to $m_s = -1$, the NV spin state stays at the high fluorescence $m_s = 0$ state. On the other hand, as soon as the MW is resonant with either of the above mentioned transitions, spin state is transferred into one of those states ($m_s = \pm 1$). This spin transfer into one of the low fluorescent states ($m_s = \pm 1$) results in reduced fluorescence intensity due to the above mentioned reason of intersystem crossing [117, 118].

With no applied bias magnetic field along the NV axis, the only possible transition is from $m_s = 0$ to $m_s = \pm 1$ and in the recorded fluorescence has only one dip, which is observed at the frequency of 2.87 GHz (figure 2.6 b)). This transition is at the ZFS as described in equation 2.2. In the presence of a magnetic field, degeneracy of the $m_s = \pm 1$ state is lifted and the two possible transitions are observed in the ODMR spectrum. From the Zeeman splitting part of the NV ground state Hamiltonian (equation 2.3), the transition frequencies can be determined. One transition frequency is $\nu_- = 2.87\text{GHz} - g_e \mu_B B_z$, for the $m_s = 0$ to $m_s = -1$ transition and the other transition frequency is $\nu_+ = 2.87\text{GHz} + g_e \mu_B B_z$. The overall splitting of the states $m_s = +1$ and $m_s = -1$ thus becomes $\Delta\nu = 2 g_e \mu_B B_z$. However, this simple case is typically only observed for single NV centers. In ensembles of many NV centers all four possible crystallographic orientations occur and each one of them is generally exposed to a different projection of the magnetic field. Therefore, the ODMR spectrum of ensembles will display up to 8 distinct resonances, as can be seen in figure 2.6 d).

With low laser and MW power the hyperfine interactions can also be resolved

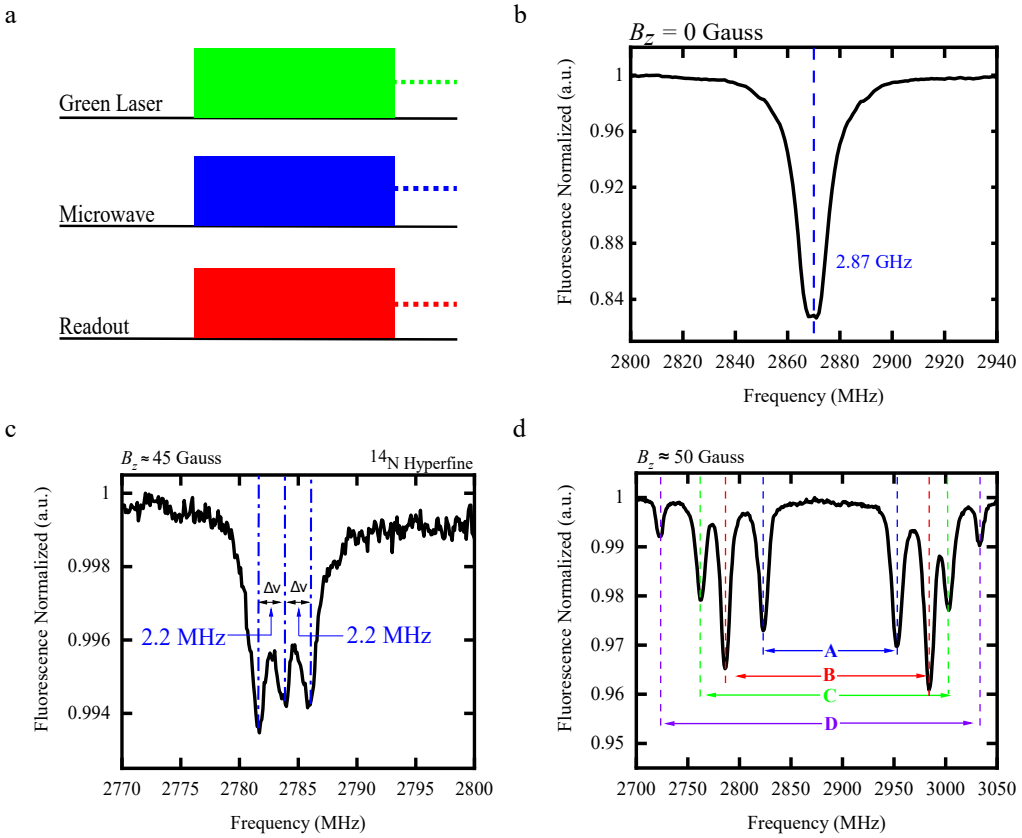

Figure 2.6: **ODMR scheme and ODMR spectrum.** In figure a), a schematic for ODMR experiment is shown. In this scheme continuous green laser excitation along with microwave manipulation is done and simultaneously the fluorescence signal is recorded. Figure b) shows an example ODMR spectrum without any bias magnetic field. Contrast of the ODMR spectrum is approximately 17.5 %. In figure c) Hyperfine coupling for ^{14}N nuclear spin is shown. Figure d) depicts ODMR spectrum with a bias magnetic field. The field strength is approximately 50 Gauss and the magnetic field is arbitrarily aligned for ensemble measurement and here 8 dips are visible from 4 classes of NV centers in the ensemble. All the ODMR spectrum are obtained from our experiments.

in the ODMR spectrum. The hyperfine interaction splits the transitions of $m_s = 0$ to $m_s = \pm 1$ even further. For the ^{14}N isotope, these transitions get splitted into two triplets with $\Delta\nu = 2.2$ MHz (see figure 2.6 c)) and for ^{15}N isotope this transition get splitted into two doublets with $\Delta\nu = 3.1$ MHz [123, 124]. With all these transitions observed in an ODMR spectrum, therefore confirms the above mentioned Hamiltonian (equations 2.1 to 2.4) for NV center and the NV center's energy level scheme in general.

Apart from ODMR measurements done with the NV fluorescence, it is also possible to determine the NV spin polarization by applying an infrared (1042.5 nm) probe laser along with the green pump laser while scanning the microwave frequency over a frequency range [64]. In fluorescence ODMR the NV spin polarization is determined by reading the spin state dependent fluorescence. In contrast to that, infrared absorption ODMR determines the NV spin polarization by reading the spin state dependent infrared absorption of NV system. The infrared laser probes the absorption on the on resonance transition of the NV's singlet states (refer to figure 2.4). With continuous green laser exciting a NV center while there are no on-resonant microwave radiation applied to the NV ground state, the NV spin state is polarized to $m_s = 0$ state. In this condition the applied infrared laser is not absorbed hence the transmission is maximal. With an on-resonant microwave radiation the probability of the NV spin state to be in the metastable state increases, therefore, in that situation less transmission (more absorption) of infrared laser is observed. More details regarding infrared absorption ODMR will be discussed in chapter 3. An example of infrared absorption ODMR along with the schematic diagram for the scheme is given in the figure 2.7 a) and b). The contrast of infrared absorption ODMR shown in figure 2.7 b) is approximately 0.16 %. More details regarding these values are discussed in chapter 7.

In general the linewidth of the observed transitions in ODMR spectrum for single NV centers are limited by power broadening caused by the excitation green laser power and microwave power [126]. However, the fundamental limit for these linewidths is given by the dephasing time (T_2^*) of the NV center for single NV. For an ensemble of NV centers additional inhomogeneous broadening is observed. This broadening occurs due to distribution of resonance linewidth and distribution of resonance frequency of the individual NV spins of the ensemble [127]. The inhomogeneous broadening of linewidth for ensemble of NV spins and dephasing time (T_2^*) is further discussed in section 2.4.3.

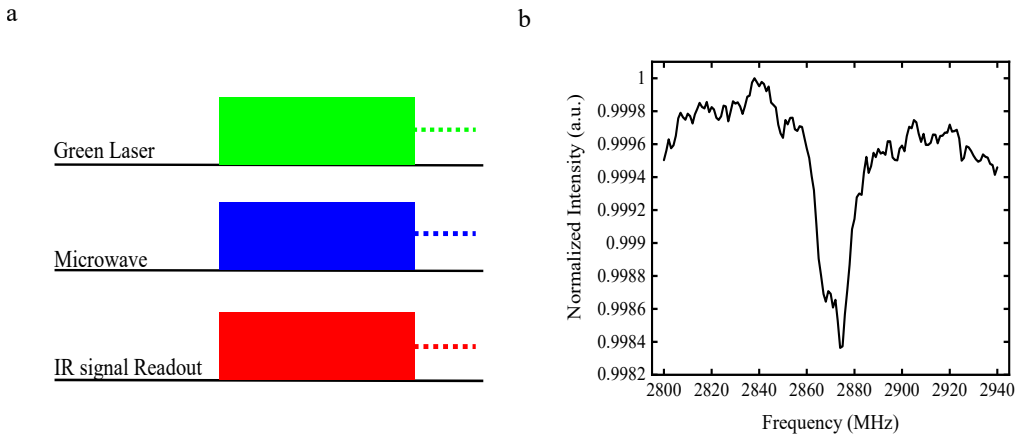

Figure 2.7: **Infrared absorption ODMR scheme and example graph.** Figure a), shows CW- ODMR scheme for infrared laser absorption ODMR. Green laser and IR laser simultaneously addresses NV center and the MW is swept over a frequency range. Figures b), shows an experimental data of obtained infrared absorption ODMR spectrum.

2.3.2 Rabi oscillations

A two level system can be driven in resonance with to the transition frequency, which leads to the coherent exchange in population of the two states. This effect is known as Rabi oscillation [32]. In the figure 2.8 a) a simple schematic diagram is shown for the Rabi oscillation measurement with laser and MW pulses. As discussed in the previous section, when a bias magnetic field is applied, the $m_s = \pm 1$ state undergoes Zeeman splitting. In the ODMR experiment the transitions from $m_s = 0$ to $m_s = -1$ or $m_s = +1$ can be detected. Therefore, with applied bias magnetic field the ground state of NV center can be considered as a set of two level system. Each of these transitions in the ground state of NV center can be driven as a two level system. When on-resonant MW driving is applied to one of these transitions, it induces population oscillation in between the two spin states (e.g. $m_s = 0$ to $m_s = -1$) [32].

To perform Rabi oscillation with NV center, first an excitation green laser pulse is applied. This green laser pulse polarizes the NV spin state to $m_s = 0$. Then, a resonant MW pulse is applied, which coherently transfers the NV spin population between $m_s = 0$ and $m_s = +1$ states. To detect the resultant NV spin state another green laser pulse is applied and the fluorescence signal from NV center is collected. From the collected fluorescence intensity the NV spin

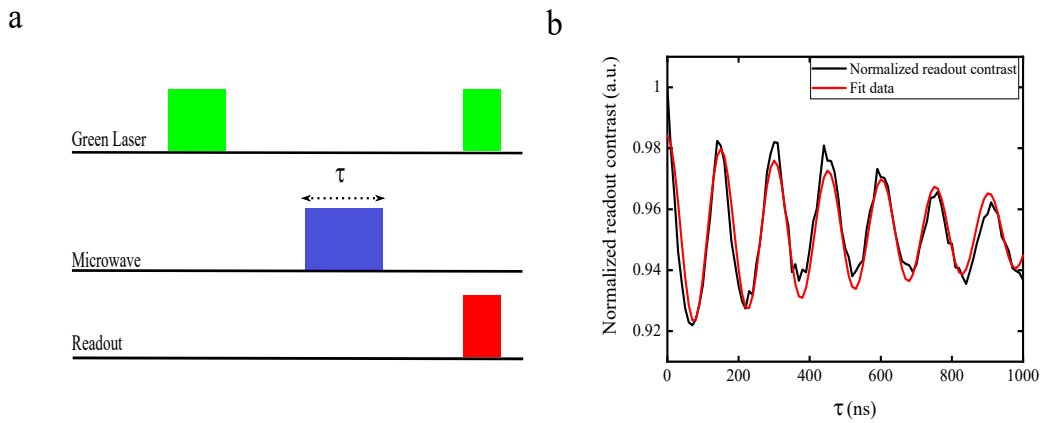

Figure 2.8: **Rabi oscillation.** In figure a), a schematic diagram for pulse sequence to measure Rabi oscillation (see text for detail explanation of the pulse sequence) is shown. Figure b) depicts an example graph for Rabi measurement performed with a single NV center. Data for figure b) is adapted and modified from N. Oshnik, under the terms of a CC BY-NC-SA license.

state is detected. Typically the pulse length of the green laser is 300 ns and the MW pulse length τ is varied [128]. The pulsed scheme for Rabi oscillation along with an example graph for Rabi oscillation measurement is given in the figure 2.8.

By Plotting the collected fluorescence signal for different MW pulse lengths τ one can see the Rabi oscillations as shown in figure 2.8. For a certain time τ, population can be completely transferred from $m_s = 0$ into the $m_s = +1$ state, which is known as π- pulse. The population goes into the superposition state of $m_s = 0$ and $m_s = +1$, which is $|\psi_{sp}\rangle = \frac{1}{\sqrt{2}}(|0\rangle + |1\rangle)$ after half of the time τ, is known as $\pi/2$- pulse. The Rabi oscillation frequency is given by the following equation [129]:

$$\Omega_0 = \gamma_{NV} B_1. \tag{2.5}$$

In the above equation γ_{NV} is the NV center gyromagnetic ratio,which is $\gamma = g_e \mu_B/\hbar = 1.76 \times 10^{11} \mathrm{s}^{-1}\mathrm{T}^{-1}$, and B_1 is the magnetic flux density of the MW excitation perpendicular to the NV axis.

2.4 Characteristic coherence times for NV centers

In the following section, a short introduction to the characteristics coherence times for NV center is presented. The main purpose of this section is to discuss briefly about the different characteristic coherence times such as spin-phonon relaxation time (T_1 time), coherence time (T_2 time) and dephasing time (T_2^* time) and how those characteristic times are measured generally to characterize either single NV center or NV ensemble to know the limitations of NV magnetometers.

2.4.1 T_1 Relaxation time

As described in section 2.3.1, the NV spin state can be polarized into $m_s = 0$ ground state by green laser. By applying MW π- pulse the NV spin can also be transferred to $m_s = +1$ or $m_s = -1$ state (refer section 2.3.2). Such a prepared spin state decays to a thermal equilibrium state due to the interactions with phonons in the diamond lattice. This characteristic time of NV spin relaxation is known as T_1 relaxation time or sometime spin-lattice relaxation time. As the spin-lattice relaxation happens mainly due to the phonons present in the diamond lattice, T_1 is sensitive to temperature [130, 131].

To measure the T_1 relaxation time, first a green laser pulse is applied, which polarizes the NV spin state into the $m_s = 0$ state. After a certain waiting time τ another laser pulse is applied to read out the fluorescence which is dependent on the NV center spin state. After the spin state is initialized to $m_s = 0$, an optional MW π- pulse can transfer the state to $m_s = +1$ or $m_s = -1$. By applying this optional MW pulse one can measure the decay from the $m_s = +1$ or $m_s = -1$ states as well as mentioned before. The waiting time τ in between the excitation pulse and the read out pulse is varied. When the measured fluorescence intensity is plotted for different values of τ , and a typical exponential decay is observed. The pulsed scheme for T_1 relaxation measurement is shown in the figure 2.9 along with an example plot for T_1 time measurement.

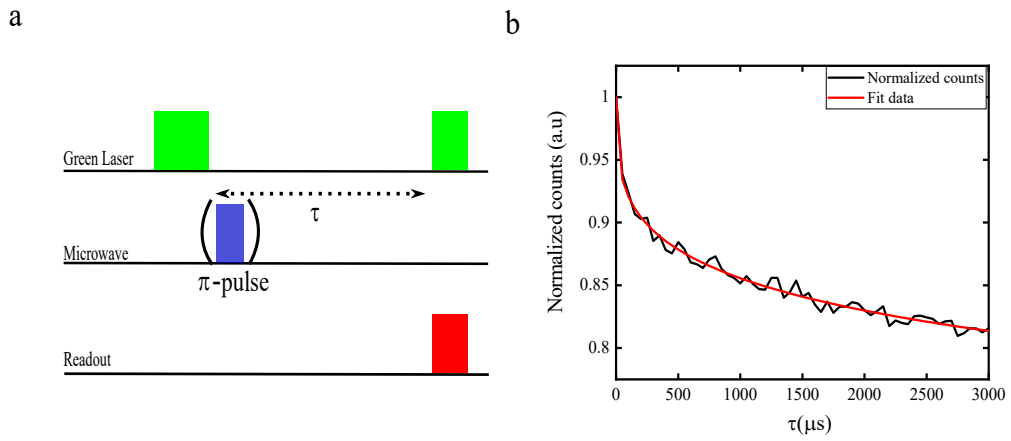

Figure 2.9: **Spin-phonon relaxation time.** Figure a) shows schematic diagram of the pulse sequence to measure T_1 time measurement. In figure b) an example graph for T_1 time measurement with single NV center is shown. Data for figure b) is adapted and modified from N. Oshnik, under the terms of a CC BY-NC-SA license.

By fitting this plot with the following equation 2.6 one can extract the T_1 relaxation time for NV centers [128]:

$$P(t) = P_0 e^{-\tau/T_1}. \tag{2.6}$$

In the above equation $P(t)$ is the time dependent polarization, whereas P_0 is the maximum polarization after initialization of the spin state into $m_s = 0$ state. As described before τ is the variable time in between the initialization and readout pulses and T_1 is the spin-lattice relaxation time. Therefore, T_1 is the time taken for the population to decrease to the 1/e th value $\approx 37\%$ of the initial population [128].

2.4.2 T_2 coherence time

Interactions with the spin impurities present in the diamond can cause decoherence of the NV spin. Most commonly the coherence time for NV spin is referred as T_2 time. The spin impurities which commonly interacts with the NV spin are, nuclear spins of ^{13}C isotope, electronic spins of donor nitrogen present in the diamond and in some special cases other NV spins. Compared to T_1 time, which is a spin-lattice process T_2 is spin-spin process and is often referred as spin-spin relaxation time. As T_2 is intrinsic to the NV center and

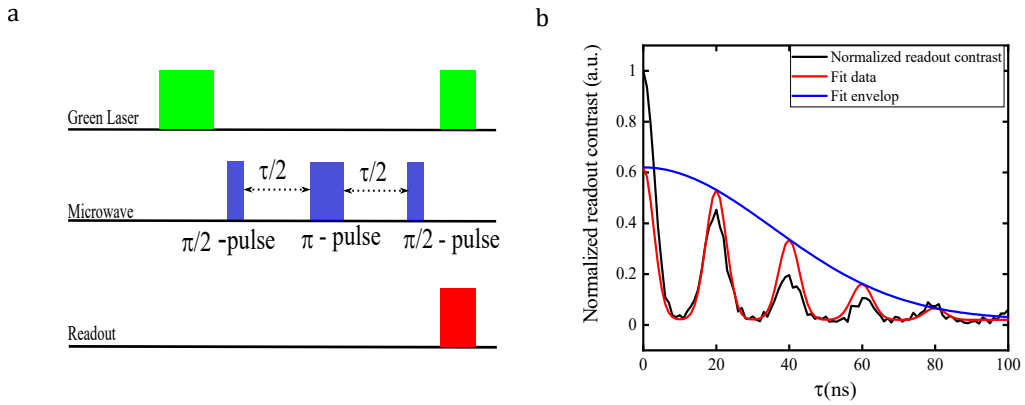

Figure 2.10: **Hahn echo pulse scheme and graph.** Figure a) depicts Schematic diagram for Hahn echo pulse sequence. In figure b), an example graph for T_2 time measurement with single NV center is shown. Data for figure b) is adapted and modified from N. Oshnik, under the terms of a CC BY-NC-SA license.

its local spin environment, therefore in a diamond sample depending on the spin environment the T_2 time for different NV centers can vary significantly [132, 133, 134].

Typically the NV spin coherence time or the T_2 is measured by using a Hahn echo pulse sequence. The pulse sequence for Hahn echo is shown in figure 2.10. First the NV spin is initialized in the $m_s = 0$ state by applying a green laser pulse. After the initialization, the NV spin is prepared in a superposition state of $m_s = 0$ and $m_s = +1$, which is $|\psi_{sp}\rangle = \frac{1}{\sqrt{2}}(|0\rangle + |1\rangle)$, by applying a MW $\pi/2$- pulse. In this state the system then evolves freely for a time span of $\tau/2$ [134]. Within this time period, the NV spin accumulates a phase, which is caused by the local fluctuating magnetic field. This fluctuating magnetic field is arising from the local spin bath. After the free evolution time $\tau/2$, a MW π-pulse is applied. If the magnetic field fluctuations due to the local spins are slow on the time scale of $\tau/2$,this MW π-pulse refocuses the phase after another free evolution time period of $\tau/2$. Another MW $\pi/2$- pulse is used to put the NV spin state in a measurable state. Therefore, after these two free evolution time of $\tau/2$, which leads to a total free evolution time of τ, the NV spin gets decoupled from the noise with a frequency corresponding to $\tau/2$. There is a second laser pulse in this scheme. From this second laser pulse, spin-dependent fluorescence of the NV spin is read out. The pulse scheme for Hahn echo and an example graph is shown in the figure 2.10.

In experiment, this free evolution time is increased gradually and the spin dependent fluorescence signal is collected. The collected fluorescence intensity, when plotted, shows an exponential decay. This figure from Hahn echo is fitted by the following equation [128]:

$$I(\tau) = I(0).e^{-(\tau/T_2)^p}. \tag{2.7}$$

where $I(\tau)$ is the collected fluorescence after time period τ, $I(0)$ is the initial maximum fluorescence, p is a free parameter which depends on the type of noise and T_2 is the coherence time. In the Hahn echo scheme the NV spin is more efficiently decoupled from the local spin bath than the Ramsey sequence (see section 2.4.3) due to the fact that in Hahn echo there is an addition of refocusing MW π-pulse. Though the MW π- pulse can efficiently refocus the NV spin, it is possible only when the field fluctuations are much slower than the free evolution time. If the field fluctuations are much faster than the free evolution time, then the refocusing does not work efficiently.

As mentioned before, the Larmor precession of ^{13}C nuclei present in the vicinity of the NV spin is the dominant source of local field fluctuations in most samples. When the free precession time period τ is equal to a multiple number of ^{13}C Larmor precision periods, the phase contributions from each individual ^{13}C cancels out. This leads to collapses and revivals of the observed decoherence curve. Therefore, from this plot the true NV spin decoherence is extracted by the decay of the envelope of Larmor-resonant peaks in the ^{13}C-induced revivals, which in a ^{13}C-dominated sample arises from dipole-dipole coupling [135, 136].

2.4.3 T_2^* dephasing time

T_2^* time is the time scale referred in nuclear magnetic resonance techniques, over which dephasing occurs for one spin or an ensemble of spins. In general, this dephasing occurs due to inhomogeneities present in the environment; for the particular case of the NV spins, the dominant inhomogeneities are variations in the local spin bath experienced by each NV center and temporal fluctuations in each NV center's local magnetic field due to dynamics in the surrounding spin bath [23, 123, 135, 137].

To measure the T_2^* dephasing time, the a Ramsey pulse sequence is used. In comparison to Hahn echo sequence, Ramsey pulse sequence does not have the

refocusing MW π-pulse in between the MW $\pi/2$-pulses. In Ramsey sequence, after the first laser pulse initialize the NV spin in its $m_s = 0$ state, a MW $\pi/2$-pulse puts the NV center spin into its superposition state.The superposition state is as described before $|\psi_{sp}\rangle = \frac{1}{\sqrt{2}}(|0\rangle + |1\rangle)$. In the superposition state, then the NV spin evolve for time period of τ. Another MW $\pi/2$-pulse put the NV spin state in a measurable state, which is then read out by second laser pulse as shown in figure 2.11 a). The free evolution time is gradually increased and the collected fluorescence is plotted to extract the dephasing time.

Generally this plotted curve has a exponential decay characteristics and known as free induction decay (FID) curve. The FID curve contains the beating from the nitrogen hyperfine transitions (three in the case of ^{14}N, two in the case of ^{15}N) [138]. In figure (2.11) b) these beatings are seen, which arose from the ^{14}N hyperfine transitions. The T_2^* time is extracted from characteristic time of the decay envelope. In case of ensemble of NV centers the same method does not yield efficient extraction of the dephasing time. As depicted in figure (2.11) c), the three hyperfine transitions arising from ^{14}N is not well resolved. This leads to inefficient fitting of the Ramsey fringe.

For an ensemble of NV centers, inhomogeneities arising from the different local spin environments experienced by each NV center often broaden the hyperfine transition frequency components of the Ramsey FID. The reasons for this broadening is as follows. In an ensemble different individual NV spins experiences different spin bath throughout a sample, leading to different magnetic environment [127]. Inhomogeneous distribution of strain throughout the sample also affect the resonance frequencies of the constituent NV spins in the ensemble [121]. Along with that variation of temperature and electric field in the local environment affect each NV spins differently. Therefore in an ensemble of NV, each NV spin has different linewidths ($\Delta\nu$) and differentT_2^* time, as the relation between linewidth and dephasing time is $\Delta\nu \propto \frac{1}{T_2^*}$ [126].

This broadening makes it difficult to extract the T_2^* time. Therefore in case of NV ensemble T_2^* time measurement an alternative method is used. In this method ODMR spectra is taken with a bias magnetic field after proper alignment of the magnetic field so that the hyperfine transitions are clearly visible. Then by gradually reducing the MW power a series of ODMR spectra is taken for the hyperfine transitions. It is necessary to align the magnetic field properly in this method. Otherwise broadening due to inhomogeneous external magnetic field again make it difficult to extract the dephasing time. The laser power is

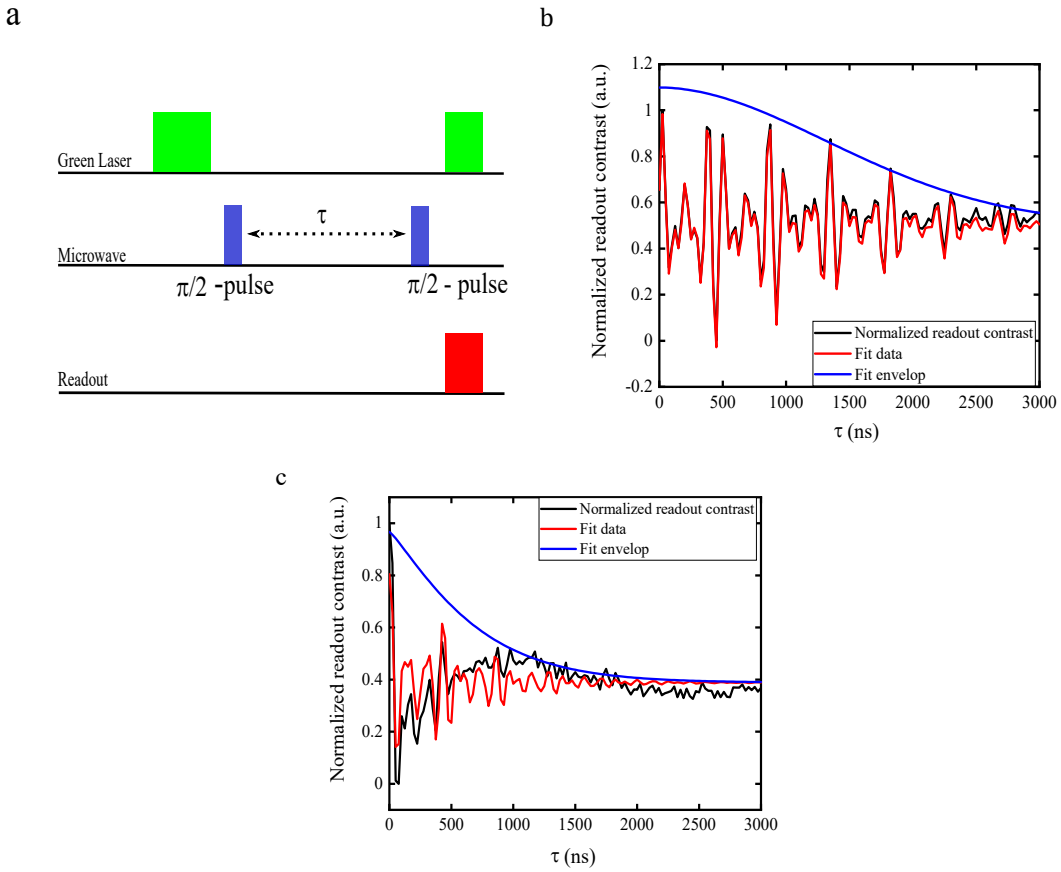

Figure 2.11: **Dephasing time scheme and example graph.** In figure a), a schematic diagram for Ramsey pulse sequence is shown. Figure b), depicts an example graph for the Ramsey measurement performed with a single NV center. Figure c), shows graph of Ramsey measurement with NV ensemble shows that the Ramsey fringe fit is not at all fitting as in the case of single NV center shown in figure (b). For this reason the T_2^* measurement for ensemble of NV centers are done in alternative method (Refer to text for details). Data for figure b) is adapted and modified from N. Oshnik, under the terms of a CC BY-NC-SA license.

maintained as low as possible. The linewidth of these transitions are extracted from the full-width at half maximum (FWHM) of the resonances. These values of linewidths are then used to linearly extrapolate the value of linewidth (FWHM of the resonance) at zero MW power. It is observed that the lineshape at low laser power and MW power is generally Lorentzian. Extrapolating the value of the FWHM ($\Delta\nu$) at zero MW power gives the dephasing time, which is related to the FWHM by the following equation [59, 126]:

$$T_2^* = \frac{1}{\pi\Delta\nu}. \tag{2.8}$$

3 NV Magnetometry

In this chapter the discussion is regarding different magnetometry methods with NV centers in diamond. The results presented in this dissertation are obtained with CW-ODMR method, but there are other dc magnetometry method. Therefore in the first section different dc field magnetometry is discussed to compare CW-ODMR with the other methods. In the second section a brief discussion on ac field magnetometry is presented. After that advantages and challenges for magnetometry with ensemble of NV center is discussed.

As mentioned in the previous chapter, the NV centers in diamond posses excellent spin coherence time under ambient conditions [23]. Along with that, the spin state can be initialized and read out optically and can be manipulated via microwave signal [9]. The optical signals from NV centers are sensitive to magnetic fields [59], electrical fields [6], temperature [71, 84], and strain [7]. All of these together make NV centers a very good candidate for sensing purpose. Particularly, magnetic field sensing with NV centers (single or ensemble) has seen a rapid growth in recent years. The use of color centers in crystal as an active element for an optical microscope was first proposed by Sekatskii *et al.* [139] and Chernobord *et al.* [140]. To use NV centers as magnetic field sensors was first proposed by Degen *et al.* [35] and Taylor *et al.* [34]. Demonstration of single NV based magnetometry was shown by Balasubramanian *et al.* [24] and Maze *et al.* [36]. Ensemble NV based magnetometry was demonstrated by Acosta *et al.* [59]. After these initial demonstrations, NV based magnetometers for different applications found more popularity.

NV based magnetometers have been used as magnetic sensors of external (with respect to the diamond sample) magnetic fields produced by electronic devices [8], biological samples [77] or to detect other elements in nuclear magnetic resonance experiments [96]. Therefore NV magnetometer finds its uses therefore in biological research, research in geomagnetism or in microelectronics industry [9, 78]. As the NV spin get affected by the magnetic field fluctuations from the impurities present in the diamond, it is used for sensing purpose of

internal magnetic field. More specifically to detect the spin species which affects the environment of the NV spin and how it decreases the coherence time or dephasing time, which in a way affects the performance of the NV based magnetometer. This investigation therefore helps to grow diamonds with less impurities so that the NV magnetometer performance is not limited by the impurity spins [121].

3.1 DC field magnetometry

With NV centers (single or ensemble), external dc field and ac field could be measured. The detection of dc field is done with any of the following magnetometry schemes such as continuous-wave optically detected magnetic resonance (CW-ODMR) [30], pulsed ODMR [126] or Ramsey measurements [23]. As the dc sensing protocols are sensitive to static, slow-varying magnetic fields, the choice of technique employed to detect the external dc magnetic field depends on the scope of the experiments. All the experimental results presented in this work were acquired by using CW-ODMR method. Therefore, the discussion in this chapter will be emphasized on the CW-ODMR method and later in this chapter briefly other methods will be discussed.

CW-ODMR magnetometry

The continuous-wave optically detected magnetic resonance (CW-ODMR) is a very simple magnetometry method. The nomenclature of this technique is self-explanatory. In this technique the green excitation laser is continuously illuminating the NV center and continuous microwave radiation is swept over a frequency range while the readout signal is collected simultaneously to take the ODMR spectrum in the presence of a bias magnetic field [59]. For infrared absorption ODMR, along with the continuous green pump laser a continuous infrared laser is applied and the transmitted infrared laser is collected for ODMR spectrum [64]. When the bias magnetic field is known and the shift of the resonance is in accordance to that known field B_0, presence of any unknown static magnetic field δB shifts the resonance in ODMR spectrum. Information of this static magnetic field δB can be extracted from the ODMR spectrum. Detail description of the spin dynamics for fluorescence CW-ODMR and infrared absorption CW-ODMR is given in section 2.3.1 and the experimental method has

been discussed in section 5.1.2.

The sensitivity η_{CW} of an NV magnetometer is related to the minimum detectable magnetic field δB_{min}. This minimum detectable magnetic field is measured by the CW-ODMR spectra, whose intensity profile can be written as [126]:

$$I(\nu_m) = R\left[1 - C_{CW}F_L\left(\frac{\nu_m - \nu_0}{\Delta\nu}\right)\right]. \tag{3.1}$$

Where $I(\nu_m)$ is the frequency dependent intensity of the spectra, R is the photon detection rate, C_{CW} is the contrast of the resonance feature, F_L is the function describing the resonance lineshape, $\nu_0$is the resonance frequency, and $\Delta\nu$ is the linewidth of the resonance feature. Due to Zeeman effect, any magnetic field fluctuation of δB, changes the resonance frequency ν_0. The ODMR intensity is most sensitive to small changes of magnetic field where the resonance feature has the highest slope [34, 126]:

$$max\left|\frac{\partial I(\nu_m)}{\partial\nu_0}\right| = \frac{C_{CW}R}{\Delta\nu p_F}. \tag{3.2}$$

Where the numerical parameter P_F is related to the lineshape of the resonance. For a measurement duration of t_m, and photon detection rate R, the photon-shot-noise can be approximated to $\sqrt{Rt_m}$. and the sensitivity is $\eta_{CW} = \delta B_{min}\sqrt{t_m}$. From these relations the photon shot-noise-limited sensitivity in CW-ODMR magnetometry is given by the following equation [34, 40, 126]:

$$\eta_{CW} = P_F\frac{h}{g_e\mu_B}\frac{\Delta\nu}{C_{CW}\sqrt{R}}. \tag{3.3}$$

In the above equation C_{CW} is the contrast of the resonance, R is the photon detection rate, $\Delta\nu$ is the linewidth of the resonance, h is the Planck's constant, $g_e$is the Lande´ g-factor, $\mu_B$is the Bohr magneton, and P_F is the numerical prefactor, which depends on the resonance lineshape. For Gaussian lineshape $P_F = \sqrt{e/8\ln 2} \approx 0.70$, and for Lorentzian lineshape $P_F = 4/3\sqrt{3} \approx 0.77$ [126]. The above mentioned parameters in the equation 3.3 are dependent on each other. For example, to increase the contrast C_{CW} , for a constant pump power (green laser power) the microwave power has to be increased. In that situation, while with increasing microwave power the contrast is increased at the same time the linewidth of the resonance $\Delta\nu$ is also increased due to power broadening effect. Another example which shows the strong interdependence

of these parameters is the relation between the photon detection rate R and linewidth $\Delta\nu$. To increase the photon detection rate the laser power has to be increased which in turn also increases the linewidth due to power broadening. However the photon detection rate can be increased by increasing photon collection efficiency by several methods [27]. To achieve the T_2^* limited linewidth it is necessary to lower the optical pump power along with the microwave power. This decreasing of optical pump power leads to decrease in the photon detection rate R [27, 69, 126].

CW-ODMR is applied widely for magnetometry purpose for the technical convenience where technical complexity to implement pulsed schemes are needed to circumvent. With ensemble NV magnetometry, where the number of NV sensor is very high to perform magnetometry, CW-ODMR may reach the similar sensitivity level of Ramsey magnetometry [126].

Though CW-ODMR may reach the sensitivity level mostly achieved by Ramsey magnetometry by using ensemble NV as magnetometer it has some drawbacks. As discussed above the most prominent problem for CW-ODMR magnetometry method is the power broadening of the linewidth due to optical power and microwave power. To achieve optimal sensitivity with CW-ODMR magnetometry the optical power and microwave power has to be fixed in a way that the ODMR linewidth is limited only by the T_2^* dephasing time [126]. Limitation of this technique is inherent to the scheme due to the use of continuous laser and microwave radiation. The sensitivity in the other schemes such as Ramsey or pulsed ODMR are enhanced by the pulsed techniques [126]. This method is also slow compared to the pulsed techniques, as one needs to scan the MW frequency and simultaneously record the optical read out signals (fluorescence and transmitted infrared laser) over a longer time period.

By optimizing the parameters of the equation 3.3, optimum magnetic field sensitivity can be achieved but that is only possible with pulsed techniques. Mainly because, in pulsed techniques, use of short laser pulses to initialize and read out the spin state along with MW pulses do not lead to power-broadened resonance feature due to shorter interaction time. Compared to that in CW-ODMR, there is always a trade off between the power-broadening of the linewidth at high optical and microwave power to reach higher contrast and low photon collection rate at low optical power [126].

Pulsed ODMR

Another magnetometry method employed to detect static magnetic field is pulsed ODMR technique first demonstrated by Dréau *et al.* [126] with NV centers. With pulsed ODMR technique the problem of power-broadening of the resonance linewidth observed in CW-ODMR magnetometry is avoided and magnetic field sensing is limited by the T_2^* dephasing time limit.

To perform the pulsed ODMR measurement, first the NV spin state is initialized to the $m_s = 0$ spin state with a strong green laser pulse in the presence of a bias magnetic field. After the spin-state initialization a very low power MW π-pulse on resonance with the transition from $m_s = 0$ to $m_s = +1$ or from $m_s = 0$ to $m_s = -1$ is applied. After a waiting time τ, a second laser pulse is applied to readout the NV spin state based on fluorescence intensity. The sensing time τ for pulsed ODMR scheme magnetometry is MW π-pulse duration (τ_π). The condition for the MW π-pulse duration is $\tau_\pi \approx 1/\Delta\nu$, where $\Delta\nu$ is the resonance linewidth. This condition allows to achieve T_2^* limited linewidths while at the same time the value of contrast does not decreases. Therefore one achieve optimum values for both the linewidth and contrast which in turn leads to optimum sensitivity [126]. With the microwave frequency swept over a range a similar spectrum like CW-ODMR is obtained in pulsed ODMR. One limitation for pulsed ODMR based magnetometry is that it is linearly sensitive to any kind of variation of the microwave Rabi frequency as $\Omega_{Rabi} = \pi/\tau_\pi$ and τ_π is the sensing duration for pulsed ODMR scheme.

Compared to the CW-ODMR scheme for magnetometry, in pulsed ODMR magnetometry the optical excitation and the microwave drive is not applied simultaneously. The MW power which is used in case of pulsed ODMR is less than the MW power used in CW-ODMR. For these reasons therefore the problem of power-broadening of the resonance linewidth does not happen in pulsed ODMR magnetometry. Also the photon collection per measurement can be optimized by using a strong laser pulse in the initialization step and not using the optical excitation continuously. As discussed in the above section regarding the CW-ODMR sensitivity measurement with equation 3.3, the parameters for the shot-noise-limited sensitivity is optimized in the pulsed ODMR magnetometry.

The shot-noise-limited sensitivity for pulsed ODMR magnetometry can be written as [126]:

$$\eta_{pulsed} = P_F \frac{\hbar}{\pi g \mu_B} \frac{1}{C_{pulsed}\sqrt{RT_2^*}}. \tag{3.4}$$

In the above equation C_{pulsed} is the contrast of the resonance, R is the photon detection rate, h is the Planck's constant, $g_e$is the Lande´ g-factor, $\mu_B$is the Bohr magneton, T_2^* is the dephasing time and P_F is the numerical prefactor, which depends on the resonance lineshape. For Gaussian lineshape $P_F = \sqrt{e/8\ln 2} \approx 0.70$, and for Lorentzian lineshape $P_F = 4/3\sqrt{3} \approx 0.77$.

Ramsey measurement

To measure dc magnetic field another well known technique is the Ramsey measurement. With NV centers, the first Ramsey based magnetometry measurements was demonstrated by Balasubramanian *et al.* [23]. The Ramsey measurement is done in the following way. As described in the previous section 2.4, first an initialization laser pulse is applied to initialize the NV spin in its $m_s = 0$ state, a MW $\pi/2$-pulse puts the NV center spin into its superposition state.The superposition state is $|\psi_{sp}\rangle = \frac{1}{\sqrt{2}}(|0\rangle + |1\rangle)$. In the superposition state, then the NV spin evolves for time period of τ. Another microwave $\pi/2$-pulse puts the NV spin state in a measurable state, which is then read out by second laser pulse. During the free precision time when the NV spin evolves for time period τ, the NV spin accumulates a phase $\phi = 2\pi\gamma B\tau$, where the B is the unknown static magnetic field, γ is the gyromagnetic ratio of the NV electron spin.

For optimal sensitivity measurement the free precision time τ is chosen to be very close to the T_2^* dephasing time of the NV spin. The accumulated phase depends on the free precision time τ, which in turn is limited by the T_2^* time. That is why the accumulated phase by the NV spin is limited by the T_2^* time. From the readout pulse this accumulated phase is extracted which gives the measurement of the dc magnetic field. The sensitivity for Ramsey magnetometry is given by the following equation [126]:

$$\eta_{Ramsey} \approx \frac{\hbar}{g_e \mu_B} \frac{1}{C_{Ramsey}\sqrt{RT_2^*}}. \tag{3.5}$$

In the above equation C_{Ramsey} is the contrast of the resonance, R is the

photon detection rate, h is the Planck's constant, $g_e$is the Lande´ g-factor, $\mu_B$is the Bohr magneton, T_2^* is the dephasing time.

Compared to the CW-ODMR magnetometry the Ramsey scheme based magnetometry does not suffer the power-broadening effect due to its completely pulsed based scheme and fundamentally limited by the T_2^* time. The improvement in Ramsey method arises from the fact that, by using pulses instead of continuous laser one basically limits the power broadening by pump laser. Here spin initialization is achieved via low power laser pulse and the spin state is detected with a higher power laser pulse. In comparison with CW-ODMR method here MW is also applied in pulses to manipulate the spin state rather than continuously scanning over a frequency range. By doing this one avoid the power broadening due to MW. Altogether this leads to higher sensitivity measurements compared to CW-ODMR sensitivity measurements [126].

3.2 AC field magnetometry

Instead of dc magnetic field when an external ac magnetic field is to be measured with NV center magnetometers, the above discussed techniques are not useful. To detect such oscillating magnetic field the technique used is the spin echo based measurements for magnetometry. The simplest spin echo technique is the Hahn echo technique (see section 2.4) [132]. In the Hahn echo sequence there is an additional MW π-pulse in between the MW $\pi/2$-pulses of a Ramsey sequence (see section 2.4). This MW π-pulse in spin echo technique flips the NV spin. This cancels out the accumulated phase arising from any static magnetic field during the first free evolution time. Therefore this method is insensitive to static magnetic fields but at the same time sensitive to magnetic fields which behave similarly as the NV spin flipping due to the applied π-pulse. This technique is sensitive to the magnetic field whose frequency is same as the inverse of the total free evolution time of the pulsed sequence; $f_{ac} = 1/\tau_{total}$. With ac field sensing schemes signals upto $\sim$10 MHz can be detected [42, 43, 44, 45, 51, 52, 96].

In Hahn echo based ac field magnetometry the limiting factor is T_2 coherence time rather than T_2^* dephasing time for the techniques used for dc field magnetometry [34]. The T_2 coherence time is typically longer than T_2^* dephasing time [141]. With the use of spin echo based technique, in a isotopically purified diamond, sub-nanometer spatial resolution with a sensitivity of few nT/$\sqrt{Hz}$

at ambient conditions was achieved by Balasubramanian *et al.* [23]. Detection of single electron spin was shown by Grinolds *et al.* [142] and the detection of small nuclear spin ensemble was shown by Mamin *et al.* [143] and Staudacher *et al.* [144]. There are multiple measurement schemes based on this spin echo based technique, for details of this scheme please see the reference [145]. The sensitivity of ac field magnetometry is given by the following equation [34]:

$$\eta_{ac} \approx \frac{\hbar}{g_e \mu_B} \frac{1}{C_{echo}\sqrt{RT_2}}. \tag{3.6}$$

3.3 Ensemble NV based magnetometry

All the presented results in this work is based on ensemble NV based magnetometry, therefore it is necessary to discuss the motivation behind it. The magnetometry experiments were done either by collecting fluorescence signal from the NV ensemble or by collecting the transmitted infrared laser passed through the NV ensemble sample. Therefore here the discussion is divided in to two parts to discuss the motivation for ensemble NV based magnetometry in the above mentioned methods respectively.

Fluorescence based magnetometry

From the equation 3.3, regarding shot-noise-limited sensitivity for CW-ODMR magnetometry, it can be inferred that the sensitivity of the method is limited by the C_{CW} contrast of the resonance, photon detection rate R of the measurements and the resonance linewidth $\Delta\nu$. For a particular lineshape of the resonance the relation can be written as $\eta_{CW} \propto \frac{\Delta\nu}{C_{CW}\sqrt{R}}$. From this relation it is understood that the shot-noise-limited sensitivity can be enhanced by improving these parameters. In the previous section 3.1, we have seen that these parameters are interrelated and often improving one parameter leads to decrease in the value of other parameter. For a single NV center improving the contrast by applying more microwave power leads to broadening of linewidth, improving the photon collection rate by applying high pump power also increase the linewidth. On the other hand decreasing the pump power to minimize the linewidth leads to low photon collection rate. To circumvent these problem one way is to use ensemble NV based sensors [27, 37, 38]. Use of ensemble NV sensors gives the direct improvement of the parameter R, the photon detection

rate, which improves the sensitivity to a great extent. By using NV ensemble, the conversion efficiency of the pump photons to detected fluorescence photon can be enhanced $\sim 5\%$ as demonstrated by Clevenson *et al.* [69]. In magnetometers based on ensembles of NV centers the signal-to-noise ratio (SNR) is improved because of the statistical averaging over a huge number of NV spins [37]. The drawback in this case is the much less spatial resolution compared to single NV based sensor [38].

Infrared laser absorption magnetometry

Though in the fluorescence detection based magnetometry the photon detection rate can be increased by using ensemble of NVs for magnetometry one major problem with this method is the collection efficiency. Due to high refractive index ~ 2.41 [88] of diamond majority of the fluorescence photon undergoes total internal reflection and does not reach the detector. Different approaches have been employed to counter this problem such as, to use solid immersion lenses [146] or side collection technique [27, 37]. Another problem of the fluorescence detection method is high background fluorescence. The source of these fluorescence can either be different defect centers other than NV^-or crystal defects present in the diamond, which effectively do not contribute to signal collected for magnetometry purpose [27]. As discussed with the equation 3.3, one more major problem for the fluorescence detection based magnetometry is to optimize the parameters (C_{CW} and R) to avoid the power broadening effect of the resonance linewidth.

To circumvent these problems another approach towards NV magnetometry has been taken Acosta *et al.* [64], where the singlet metastable states ($^1A_1$ and ^1E states) are probed with an infrared laser. The physics of the infrared absorption based CW-ODMR has been already discussed in section 2.3.1. Collection efficiency can approach unity for the NV sensors based on the infrared absorption method compared to the sensors based on fluorescence collection method [64]. For NV centers, the absorption cross section of the infrared (IR) transition is very small $(6.1 \pm 4.4) \times 10^{-23}$ m^2 [147], therefore to achieve higher or similar sensitivities at room temperature experiments compared to fluorescence detection methods it is necessary to use ensemble of NVs rather than single NV for magnetometry. Also it is necessary to increase the sensing volume in infrared absorption magnetometry for achieving higher sensitivity. To do that

two different approaches are taken. In one approach NV enriched diamond samples are placed inside optical cavity [65]. In the work of Jensen *et al.* [66] and Chatzidrosos *et al.* [67], they have reached a magnetic field sensitivity of 2.5 nT/$\sqrt{Hz}$ and 28 pT/$\sqrt{Hz}$ respectively. The other approach to enhance the sensing volume is to use diamond waveguide structures which is demonstrated by Bougas *et al.* [68], with a magnetic field sensitivity of approximately 100–600 nT/$\sqrt{Hz}$.

Another proposal is made by Dumeige *et al.* [147] to enhance the sensitivity based on infrared absorption with a hybrid laser system. In the proposed scheme an NV enriched diamond sample to be placed inside an external half-VCSEL cavity. Simulations of such a system has yield a photon shot-noise limited sensitivity of approximately 250 to 700 fT/$\sqrt{Hz}$. This has not yet been realized experimentally.

3.4 Limiting factor for sensitivity

From the above discussion it can be concluded that the limiting factors for a given NV based magnetometer would be 1) the dephasing time T_2^* . 2) The total number of sensors (N) in a given sample. For ensemble based magnetometer this number $N = [NV] \times V$; where $[NV]$ is the NV concentration and V is the interrogated diamond volume. 3) Photon shot noise [127].

Dephasing time T_2^*

From equation 3.5 it is evident that for dc field magnetometry with NV based magnetometer the dephasing time T_2^* is the limiting factor. Therefore enhancing the T_2^* time can be a valid approach to enhance the sensitivity of the ensemble NV based magnetometers. For most of the ensemble NV magnetometer for dc field sensing the T_2^* value has been $\lesssim 1\mu s$ [40, 71, 127]. The theoretical limit for $T_2^*$is given by $T_2^* \leq 2T_1$[148]. Although till date this has not been realized, general enhancement of the T_2^*time definitely can enhance the sensitivity. The details of the T_2^*measurement methods have been discussed in the previous section 2.4.

The sources for dephasing of the NV centers are believed to be consists of NV centers (NV^- and NV^0), Nitrogen atoms (N_S^0), ^{13}C atoms, other defect centers X, crystallographic strain present in the diamond sample. The relation

of the T_2^*dephasing time of a particular sample with the constituents of it can be summarized in the following equation [121, 127] :

$$\frac{1}{T_2^*} \approx \frac{1}{T_2^*(X)} + \frac{1}{T_2^*(NV^-)} + \frac{1}{T_2^*(N_S^0)} + \frac{1}{T_2^*(NV^0)} + \frac{1}{T_2^*(^{13}C)} + \frac{1}{T_2^*(strain)}. \tag{3.7}$$

Several measures are taken into account to improve the T_2^* dephasing time of a sensor [127, 148]. From the above equation 3.7, it is evident that to improve the T_2^* dephasing time of a sensor, one has to decrease the influence of ^{13}C atoms in the material. To achieve that diamond sample is grown with isotopically ^{13}C depleted CH_4 (0.005% ^{13}C) rather than natural ^{13}C abundance CH_4 (1.1% ^{13}C). Another factor to improve dephasing time is to mitigate the strain inhomogeneity in the sample. To do so dislocation density in high nitrogen concentration material is controlled. Single crystal CVD grown diamonds which are grown on substrates with low surface damages and low densities of extended defects have relatively lesser dislocations. Along with this inductively coupled plasma (ICP) etching process is used to remove sub-surface damage caused by mechanically processed surfaces. For more details please see reference by Friel *et al.* [149].

Photon-shot-noise

In optical magnetometry scheme another limiting factor for sensitivity is the photon shot noise [4, 5]. In such magnetometers, spin state dependent optical signal is recorded with photodiode detectors. These incident photons excite electrons from valence band to the conduction band in the active area of the photodiode. By this process photocurrent is generated in the external circuit of the photodiode. The photocurrent is proportional to the number of incident photons [150]. The random fluctuations of number of incident photons on the photodiode results in fluctuations of the photocurrent. which is called photon shot noise [150].

These fluctuations are inherently Poisson in nature, therefore the relation between detected photon signal R, and photon shot noise σ_N can be described by the following equation [4, 5, 150]:

$$\sigma_N = \sqrt{R}. \tag{3.8}$$

In fluorescence magnetometry or infrared absorption magnetometry with an ensemble of NV centers, the read out scheme of the NV spin state is in principle optical. The spin state of the NV ensemble is measured by collecting the spin state dependent fluorescence intensity (650 nm - 800 nm) or by measuring the intensity of the transmitted infrared laser (1042.5 nm). Therefore photon shot noise becomes an inevitable part of the measurement uncertainty. The optical readout method does not allow single-shot determination of the NV spin state to the limit of spin projection, thus shot noise of the collected fluorescence photons or infrared laser photons must be taken into account in the sensitivity estimation [4]. This way to measure the spin state deteriorates the sensitivity of the magnetometer and taken into account for shot noise limited sensitivity. Note that in all the above sensitivity equations (equations 3.3 to 3.6) for DC and AC magnetometry photon-shot-noise is incorporated.

Spin-projection-noise

For spin based magnetometers, the ultimate limit for the sensitivity arises from the intrinsic noise associated with spin projection. The quantum mechanical uncertainty in the measurement of spin projection in such magnetometers fundamentally constrains the sensitivity. Therefore it is also called standard quantum limit of sensitivity. For a magnetometer, with N individual spins in the sensing volume, and with a coherence time τ ; under ideal readout condition the spin-projection-noise limited sensitivity is given by following equation [5, 34] :

$$\eta_{SPN} \simeq \frac{1}{\gamma}\frac{1}{\sqrt{N\tau}}. \tag{3.9}$$

Where γ is the gyromagnetic ratio. From equation 3.9, it can be inferred that by increasing the number of sensor spins and the coherence time,the uncertainty in measurements can be reduced by a factor of $\sqrt{N}$ and the fundamental sensitivity, can be improved. This is the reason to look for means to increase the

number of NV spins in a magnetometer. For NV ensemble magnetometers in DC field magnetometry, this limit is given by the following equation [34]:

$$\eta_{SPN} = \frac{\hbar}{g_e \mu_B} \frac{1}{\sqrt{N T_2^*}}. \tag{3.10}$$

Where $\hbar$ is the reduced Planck's constant, $g_e$is the Lande´ g-factor, $\mu_B$is the Bohr magneton. The electron gyromagnetic ratio for NV spin is $\gamma = g_e \mu_B / \hbar = 1.76 \times 10^{11} \mathrm{s}^{-1}\mathrm{T}^{-1}$. For DC magnetometry with NV centers the resonance linewidth is limited by the dephasing time T_2^*. Therefore the coherence time τ in equation 3.9 is replaced with T_2^*. Another way to improve the sensitivity limit is to improve the dephasing time T_2^* as discussed before.

The total number of sensors

While for ensemble NV based magnetometers it is logical to infer that the increasing number of NV sensor will enhance the sensitivity in reality it is not that straight forward. From the equation 3.7, it is evident that the dephasing time of an ensemble NV magnetometer depends on many factors and among them one is dephasing due to other NV centers and strain. Therefore in a given diamond sample if the NV concentration is high it is very likely that the dephasing time of that material will surely be decreased leading to a decreased sensitivity. Taken this into account pragmatic approaches to enhance the sensitivity might be to enhance the path length of the pump and probe laser by which the effective sensor number can be increased for an ensemble NV based magnetometer. This enhancement of the path length can be achieved either by means of cavity [65, 66, 67] or by waveguide configuration of the diamond samples [37, 68, 69].

4 Rate equation model of NV centers

To corroborate the obtained experimental results (see chapters 6 and 7), we used an already established rate equation model for NV photodynamics by Dumeige *et al.* [147]. The model schematics and the model parameters are described in this chapter in the same manner as described by Dumeige *et al.* [147]. The computer simulation work on the NV rate equation model for our experiments is done by Dr. Benjamin Kambs. In this chapter we discuss the model and the theoretical predictions from the simulation.

The photodynamics of the NV center spin system is described by a set of basic rate equations (equation 4.1 to 4.8) [147] . In our simulation, however, we expand the treatment of photodynamics by taking into account the Gaussian beam shape of green and infrared lasers. In the theoretical model, the volume of interest was discretized by setting up a mesh in the diamond along the radial direction r and the the propagation direction z of the Gaussian beam for numerical solution of the rate equations. The rate equations are then solved at each point along the propagation direction which effectively yield the fraction of absorbed infrared laser light at the end of the NV enriched diamond samples. The optical depth of a NV center enriched diamond sample, is then obtained from steady state solution of the below mentioned sets of equations and calculated at each point indexed by z along the path length l for the green and infrared laser in the diamond sample. The absolute infrared absorption inside a diamond sample with a certain NV concentration is calculated from the optical depth for infrared laser. This is dependent on green laser power and the condition of microwave drive being on resonance or off resonance.

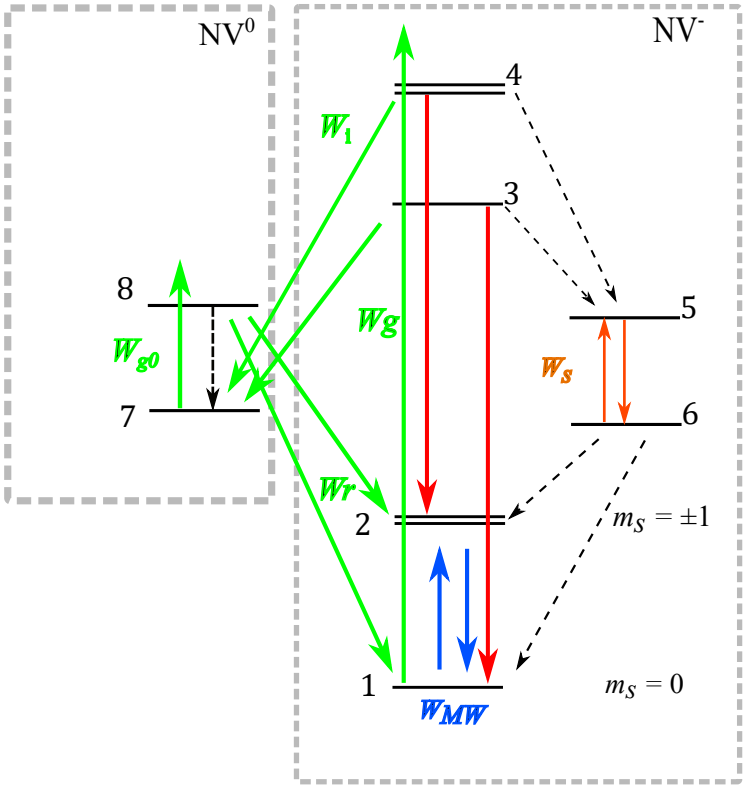

Figure 4.1: **NV energy level scheme for rate model.** In this figure the photodynamics of NV^- and NV^0 charge states is depicted. W_g and W_{g0} (green) is the pumping rate for $NV^-$and NV^0 respectively. W_s (orange) is the transition rate for the infrared resonance for NV^- singlet states. The photoionization and recombination rate between NV^- and NV^0 is labeled as W_i and W_r respectively (green). W_{MW} (blue) is the on resonance microwave transition between the $m_s = \pm 1$ and $m_s = 0$ spin sublevels in NV^- ground state. The figure is adapted with permission from [147] © The Optical Society.

4.1 Rate equations

The fluorescence ODMR or the infrared absorption ODMR works with NV^- centers only and not with NV^0 centers. In an NV ensemble there is a finite probability of photoionization processes between the two charge states of the NV center, which are NV^- and NV^0 (see section 2.2) [97]. It is important to take into account the photoionization processes in the rate equation model as the NV^0 centers reduces the effective ensemble density [97, 151, 152, 153]. Therefore the model comprises the NV^- center triplet ground and excited states and the singlet metastable state, along with ground and excited state of the NV^0 center. This model is relevant for estimating the contrast for the infrared absorption ODMR experiments as well as to describe the experimental results observed with fluorescence ODMR (see section 2.3.1 for more details). Figure 4.1 gives the complete description of the photodynamics. The NV^- triplet ground state spin sublevels $m_s = 0$ and $m_s = \pm 1$ are labeled as 1 and 2 whereas for the excited state, the spin sublevels are labeled as 3 and 4. The upper and lower singlet states for NV^- are labeled as 5 and 6. As we have taken into account the NV^0 ground and excited states, in figure 4.1 those levels are labeled as 7 and 8 respectively.

In section 2.3.1, the NV spin dynamics is discussed in details; therefore here we directly state the relevant parameters and the approximations for the rate equation model. The relaxation rates from different energy levels (as shown in figure 4.1) α to β is labeled as $k_{\alpha\beta}$. At room temperature the spin-relaxation time is longer than 0.2 ms for relaxation from level 2 to 1 [154]. This is much longer compared to all the other decay processes described in this model, therefore this relaxation rate has been neglected. The spin conserving optical transitions are shown with red arrows from level 4 to level 2 and level 3 to level 1 respectively. We assume that there are no spin-flipping optical transitions from level 4 to level 1 and similarly level 3 to level 2 [118]. This leads to the condition $k_{41} = k_{32} = 0$. In figure 4.1 the non-radiative decay from excited triplet states (level 3 and 4) to excited singlet state (level 5) and singlet ground state (level 6) to triplet ground states (level 1 and 2) is shown with dashed black arrows. The NV^-centers in the excited singlet state (level 5) can only decay to the ground singlet state (level 6) via emission of an infrared photon and not directly to the triplet ground states (level 1 and 2), hence the condition is $k_{51} = k_{52} = 0$.

The pumping rates which are necessary to describe the model are shown in

figure 4.1 with label W_α. These pumping rates are dependent on the pump laser intensity I_g, infrared (IR) laser intensity I_s , pump laser wavelength λ_g , infrared laser wavelength λ_s and absorption cross-section σ_β. The optical pumping rates are given by $W_g = \sigma_g I_g \lambda_g / hc$, $W_{g0} = \sigma_{g0} I_g \lambda_g / hc$, $W_i = \sigma_i I_g \lambda_g / hc$, $W_r = \sigma_r I_g \lambda_g / hc$, and $W_s = \sigma_s I_s \lambda_s / hc$. All values for parameters $k_{\alpha\beta}$, and the cross-section σ_β are given in the table 4.1. For our model the microwave pumping rate W_{MW} for level 1 and 2 (blue arrow and text in figure 4.1) was empirically fixed in simulation from the experimental value (see chapter 5.2 for details). With the above mentioned relaxation rates and pumping rates it is possible to write a system of eight linear coupled rate equations for the populations of each state as given equation 4.1 to 4.8. The steady state solution of these rate equations yield the population of each state N_α. The sum of the population over all the states equals to one; $\sum_{\alpha=1}^{8} N_\alpha = 1$. After the rate equations are solved by the matlab script the populations are simply multiplied by the overall concentration to yield the number of NV centers in a certain state (N_α).

$$\frac{dN_1}{dt} = -\left(W_g + W_{MW}\right) N_1 + W_{MW} N_2 + k_{31} N_3 + k_{61} N_6 + \frac{W_r}{2} N_8. \tag{4.1}$$

$$\frac{dN_2}{dt} = W_{MW} N_1 - \left(W_g + W_{MW}\right) N_2 + k_{421} N_4 + k_{62} N_6 + \frac{W_r}{2} N_8. \tag{4.2}$$

$$\frac{dN_3}{dt} = W_g N_1 - \left(k_{31} + k_{35} + W_i\right) N_3. \tag{4.3}$$

$$\frac{dN_4}{dt} = W_g N_2 - \left(k_{41} + k_{45} + W_i\right) N_4. \tag{4.4}$$

$$\frac{dN_5}{dt} = k_{35} N_3 + k_{45} N_4 - \left(k_{56} + W_s\right) N_5 + W_s N_6. \tag{4.5}$$

$$\frac{dN_6}{dt} = \left(k_{56} + W_s\right) N_5 - \left(W_s + k_{61} + k_{62}\right) N_6. \tag{4.6}$$

$$\frac{dN_7}{dt} = W_i N_3 + W_i N_4 - W_{g0} N_7 + k_{87} N_8. \tag{4.7}$$

$$\frac{dN_8}{dt} = W_{g0} N_7 - \left(k_{87} + W_r\right) N_8. \tag{4.8}$$

4.2 Gaussian beam approximation

In this section we discuss the effect of Gaussian beam approximation in our rate equation model. For Gaussian beams the beam intensity varies with beam radius along the propagation direction z as described in equation 4.9 [155],

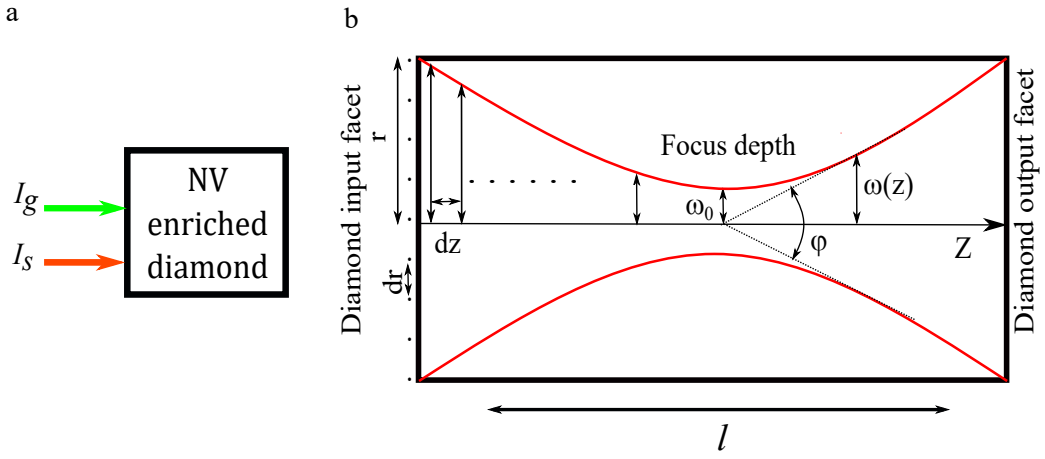

Figure 4.2: **Gaussian beam schematics.** Figure a) shows the schematic of the experimental condition for infrared absorption magnetometry where both the green and infrared laser are applied. In figure b) a simple schematic of the Gaussian beam geometry inside the diamond sample is shown. The discretization consideration of the radial direction r and the the propagation direction z of the Gaussian beam for numerical simulation to solve the rate equation model is also shown here. For more details see text.

where I_0 is the beam intensity at the beam waist with radius ω_0, $\omega(z)$ is the beam radius at point z along the beam path and r is the radial distance from the beam axis.

$$I(r,z) = I_0 \left(\frac{\omega_0}{\omega(z)}\right) \exp\left(\frac{-2r^2}{\omega(z)^2}\right). \tag{4.9}$$

In Gaussian beam optics the laser beams have the smallest beam radius at the focal point, which is the beam waist (see figure 4.2). As the beam radius is smallest at the beam waist, laser intensity is highest at that point. We know from the above stated relations for pumping rates that it is directly proportional to the laser intensities. Therefore the pumping rates are maximal at the beam waists. With a large pumping rate for the green laser the NV spin system will exhibit a large population in the metastable singlet state (level 6) which in turn leads to higher infrared absorption. Thus when the transmission of the infrared laser along the diamond sample is calculated in the simulation, a sudden drop in transmission is observed at the position of the focus (see figure 4.4). With higher infrared absorption at this point the infrared absorption ODMR contrast is also high when on resonance microwave is applied to the NV ensemble.

For IR absorption ODMR first the beam waist inside the diamond sample is

optimized for both green and IR laser with this Gaussian beam approximation. To optimize the beam waists of the laser beams, IR absorption ODMR contrast is simulated by taking different beam waists of green and IR lasers. From this result a range of beam waist is inferred to maximize the contrast. In figure 4.3 the results obtained from the numerical solution of the Gaussian beam waist optimization is shown. The optimization results indicate that the beam waist for green and infrared lasers should be in between 15 to 30 μm for maximum infrared absorption ODMR contrast. The output intensities for the green pump laser I_g and infrared laser I_s are acquired by solving the differential equations 4.10 and 4.11. By integrating these equations along the laser beam path length l inside the diamond at each point we get the transmission of the lasers point wise and finally at the output (see figure 4.2).

$$\frac{dI_g}{dz} = -\left[\sigma_g(N_1 + N_2) + \sigma_{g0}N_7 + \sigma_i(N_3 + N_4) + \sigma_r N_8\right]I_g. \tag{4.10}$$

$$\frac{dI_s}{dz} = -\sigma_s(N_6 - N_5)I_s. \tag{4.11}$$

The motivation to add Gaussian beam optics into the rate equation model is discussed already in section 4.2. In figure 4.4 this is evident where it can be seen that the IR beam is maximally absorbed at the focal depth of the Gaussian beams whether the microwave signal is applied or not. For infrared absorption ODMR with applied microwave the infrared laser is absorbed even more due to the enhanced population in the metastable singlet state. For this result, we considered the Gaussian beam waist of 20 μm, green laser power 440 mW, IR laser power 20 mW, NV concentration of the sample [NV] = 36 ppb and the path length l = 25 mm.

Here we present some important simulation results for our Gaussian beam optimized rate equation model. Figure 4.5 a) and b) shows the result for IR absorption contrast (in percentage) with increasing green laser power at fixed IR laser power for two different samples. In figure a) the results are calculated for a low NV concentration (36 ppb) sample. For this simulation three different path lengths (9 mm, 20 mm, and 40 mm) are used. The simulation results for the high NV concentration sample (1.47 ppm) with with a interaction path length of 2.5 mm, 5 mm, and 10 mm are shown in figure b). For both simulations the IR power was fixed at 20 mW. From these results it can be inferred that the IR

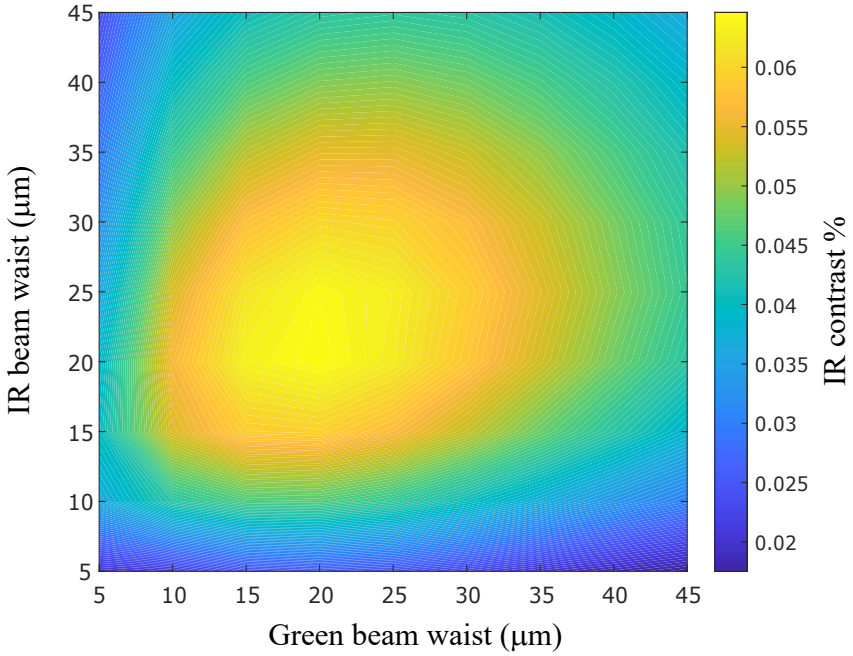

Figure 4.3: **Beam waist optimization.** In this figure the results from laser beam waist optimization for infrared absorption ODMR contrast is shown. The horizontal axis depicts the green beam waist, the left vertical axis shows the infrared beam waist and the color bar shows the infrared absorption contrast. The highest contrast is achieved when both the beam has a beam waist of in the range of 15 to 30 μm.

absorption is directly dependent on the green laser power and with increasing green laser power the IR absorption is increased whereas we did not observe any change in the IR absorption with varied IR laser power. The interpretation for this result is as following: With higher green pump power the probability of the NV system to populate the ground singlet state, which is depicted as level 6 in figure 4.1, is higher and therefore IR laser is mostly absorbed. In both figures we observe that with increasing path length, the contrast becomes larger until at a certain pump power it reaches a saturation level. With high green pump power transition rate to the singlet state (level 6 in figure 4.1) becomes higher. The lifetime of this state is higher as described in section 2.2. Therefore at a certain green power at which the lifetime of the metastable state is higher than the rate of transition to the singlet state, the metastable state (level 6 in figure 4.1) can not be depopulated. Thus leads to saturation of the contrast in IR absorption ODMR. Another important point to be noted here is that the absolute IR absorption is heavily dependent on the NV concentration of the sample and thus it can be seen that the IR absorption contrast is much smaller in low concentration sample compared to the high concentration sample. The contrast value at saturation for the sample with lower NV concentration is ∼0.06 % (L= 40 mm in figure 4.5 a)) compared to the higher NV concentration sample ∼0.6 % (L= 10 mm in figure 4.5 b)). While the NV concentration is almost 40 times higher in the high NV concentration (1.47 ppm) compared to the low NV concentration (36 ppb) sample, the interaction path length is 4 times higher in the low concentration sample. By taking into account the product of NV concentration [NV] and path length L, as a figure of merit β for IR absorption contrast for both the samples, it can be seen the ratio of this figure of merit is approximately 10 (see equation 4.12).

$$\frac{\beta_H}{\beta_L} = \frac{[\mathrm{NV}]_H \times \mathrm{L}_H}{[\mathrm{NV}]_L \times \mathrm{L}_L} = \frac{1470\mathrm{ppb} \times 10\ \mathrm{cm}}{36\mathrm{ppb} \times 40\ \mathrm{cm}} \approx 10. \tag{4.12}$$

The contrast values at the saturation for both the samples are in agreement with this calculation. Therefore it can be concluded that to achieve optimum IR absorption two most important factor is the product of NV concentration and interaction path length, and high green pump power to put the NV system in the metastable singlet state. In figure 4.5 a) and b) it can be seen that the contrast for infrared absorption ODMR, decreases with increasing green laser power at different pump powers after reaching saturation, depending on

Parameters	Values	Reference
$k_{31} = k_{42}$	66 ± 5 μs^{-1}	[153]
k_{35}	7.9 ± 4.1 μs^{-1}	[156]
k_{45}	53 ± 7 μs^{-1}	[156]
k_{61}	1.0 ± 0.8 μs^{-1}	[156]
k_{62}	0.7 ± 0.5 μs^{-1}	[156]
k_{56}	1.0 ns^{-1}	[64]
k_{87}	53 ± 7 μs^{-1}	[153]
σ_g	3.0×10^{-21} m^2	[157]
σ_{g0}	$1.8\sigma_g$	[153]
σ_i	$(9.5 \pm 4.7) \times 10^{-21}$ m^2	[153]
σ_r	$(9.8 \pm 4.9) \times 10^{-21}$ m^2	[153]
σ_s	$(6.1 \pm 4.4) \times 10^{-23}$ m^2	[147]

Table 4.1: **Physical parameters for NV rate equation model.** The physical parameters which were used to model the NV center optical depth and infrared absorption ODMR contrast are given in this table. For details of the parameters refer to text.

the sensing volume. It can be explained by the fact that, after the system reaches saturation point, at even higher pump power, level 6 (figure 4.1) is less populated than level 1, leading to lesser IR absorption, thus reduces the contrast for IR absorption ODMR. Another possibility is, with higher green pump power there is a higher probability of charge state conversion from NV^- to NV^0 [158]. The charge state conversion effectively reduces the number of NV^- centers in the sensing volume, thus the absolute IR absorption and ultimately the IR ODMR contrast is reduced. The same effect is also observed in case of fluorescence ODMR simulation result (figure 4.6) as well as in the experiments (see figure 6.2). The explanation for lesser contrast in IR absorption ODMR also holds here. With higher pumping power, optical pumping rate becomes higher than the MW pumping rate and populate the level 1 more than level 6 (figure 4.1), leading to lesser contrast than saturation point. In table 4.1 we summarize the physical parameters used for calculating the NV rate equation model.

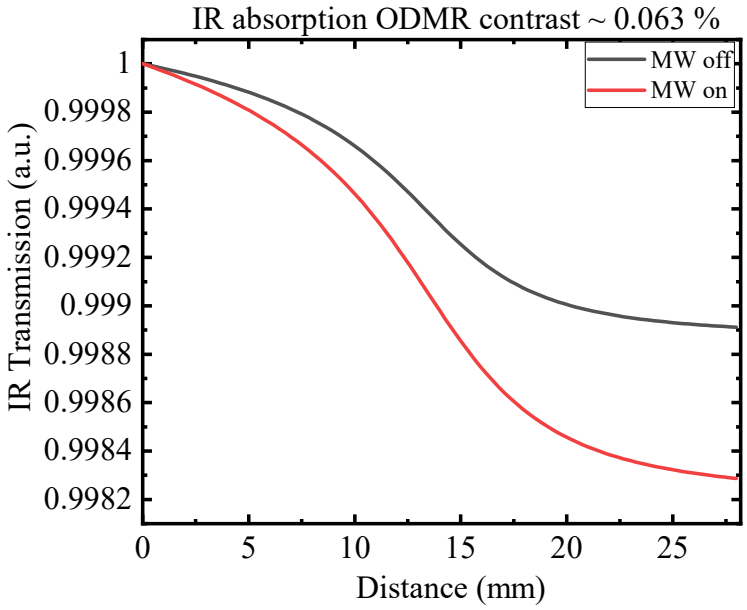

Figure 4.4: **IR absorption contrast with Gaussian beam optimized rate equation model.** This figure shows an example graph for the simulation of infrared (IR) absorption ODMR contrast. Along the x axis the interaction path length inside the diamond sample is given. The y axis gives the transmission of the IR laser at each point for microwave (MW) on and off condition. Finally from the end point IR transmission value for for MW on and off condition at the diamond output facet the contrast is calculated. In this figure the feature coming from Gaussian beam focus is visible around the distance of 10 mm. At this point where the Gaussian beams are focused, the IR absorption is maximum. For further explanation see section 4.2.

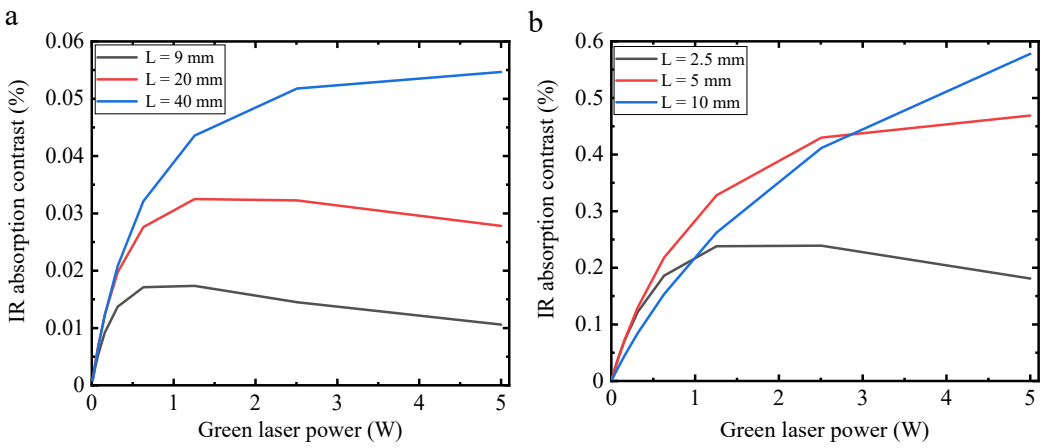

Figure 4.5: **Simulation results for IR absorption ODMR contrast.** Figure a) shows the simulation results of IR absorption contrast values in percentage for low NV concentration sample (sample 1 and 2 in figure 5.8, [NV] = 36 ppb) with different interaction path lengths and gradually increasing green pump power and figure b) shows the same simulation results with higher NV concentration sample (sample 3 in figure 5.8, [NV] = 1.470 ppm) with different interaction path length. For both simulation IR power was fixed at 20 mW.

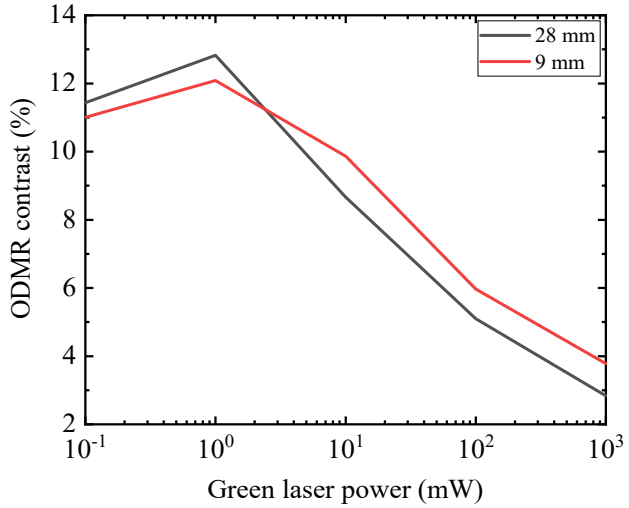

Figure 4.6: **Simulation results for fluorescence ODMR contrast.** In this figure the simulation result for fluorescence ODMR contrast variation with green laser power is shown for the low NV concentration samples (sample 1 and 2 in figure 5.8, [NV] = 36 ppb) with two different interaction path lengths.

5 Experimental Method and Setup

In this chapter the experimental method and the experimental setup is discussed. To understand the experimental results presented in this work, it is necessary to understand the experimental method. For technical convenience to realize the magnetometry with ensemble of NV center in a bulk diamond either for fluorescence magnetometry or for infrared absorption magnetometry, continuous-wave optically detected magnetic resonance (CW-ODMR) magnetometry scheme has been used throughout this work. The simplicity of this scheme arises from the facts that, there is no need to use any extra electronics for producing pulsed laser and pulsed microwave signals and time tagged collection of the fluorescence or transmitted infrared signal. In the previous section 2.3.1 the basics of CW-ODMR magnetometry is described along with the limitations for magnetometry measurements. Here, the discussion is related to the experimental realization of the same.

5.1 Experimental Method

This work consists of magnetometry experiments with infrared absorption and fluorescence. The basic method of magnetometry for both the schemes are in principal same. The only difference is in the collection of readout signals. For fluorescence magnetometry, the spin dependent fluorescence from the NV ensemble is collected while for infrared absorption magnetometry, the collected signal is the transmitted infrared laser. As there is no primary difference in the magnetometry method as such, here the discussion is divided into two sections such as 1) continuous-wave optically detected magnetic resonance (CW-ODMR) and 2) Magnetometry Method. Although the basic principle of CW-ODMR has been already described, here the discussion is necessary to understand the

complete process to perform magnetometry measurements with all the technical aspects. Also in this section more emphasis is given to the technical aspects of performing magnetometry rather than CW-ODMR.

5.1.1 CW-ODMR Method

For the magnetometry scheme with fluorescence signal, CW-ODMR [30] is performed at the first place. As described in the section 2.3.1, a green continuous laser initialize the NV spin state to $m_s = 0$ state. With an applied bias magnetic field B_z, the degeneracy of the $m_s = \pm 1$ state is lifted due to Zeeman splitting. At this point, the microwave is scanned continuously over a broad frequency range and the spin state dependent fluorescence signal is collected by a photodiode simultaneously. In the recorded ODMR spectrum, the transitions from the $m_s = 0$ to $m_s = +1$ and $m_s = 0$ to $m_s = -1$ is detected.

In case of infrared absorption magnetometry scheme [64], along with the green laser, an infrared laser is applied. This infrared laser is on-resonant with the singlet metastable states (^{1}A$_1$ and ^{1}E) transition of the NV center which probes the absorption on this transition. Without any microwave applied to the NV center, the spin state is polarized to the $m_s = 0$ state by the applied continuous green laser (see section 2.3.1). In this condition the transmission of the infrared laser is maximum. When an on-resonant microwave radiation is applied, the probability of the NV spin state being in the metastable states increases and lesser transmission (due to absorption) of the infrared laser is observed. This absorption of the probe infrared laser is observed as an on-resonant ODMR dip in the ODMR spectrum. With an applied bias magnetic field, the transitions from the $m_s = 0$ to $m_s = +1$ and $m_s = 0$ to $m_s = -1$ is observed in the ODMR spectrum, similar to fluorescence ODMR spectrum [64].

For a single NV center, in the ODMR spectrum only two transitions could be observed for the transitions from the $m_s = 0$ to $m_s = +1$ and $m_s = 0$ to $m_s = -1$. As in this work all the measurements have been done with ensemble of NV center in bulk diamond, therefore in the ODMR spectrum all the eight possible transitions for the four classes of NV center present in the diamond could be observed while the applied magnetic field is arbitrarily aligned. To perform magnetometry experiments in this work, the magnetic field was aligned with one class of NV orientation in the diamond and the other three classes of

NV orientation experienced a degenerate projection of the magnetic field.

From these ODMR spectrum it can be inferred different parameters such as contrast and linewidths (FWHM of the resonances) of the transitions and the magnetic field strength of the applied magnetic field. These parameters are crucial to characterize the performance of the magnetometers under investigation as well as to determine the lock-in-amplifier parameters to perform magnetometry experiments. The details regarding lock-in-amplifier based magnetometry scheme is given in the following section.

5.1.2 Magnetometry Method

Before magnetometry measurements were performed, first the characterization of the NV ensemble as magnetometer was performed by collecting fluorescence or transmitted infrared beam on a photodiode. In this work we refer to this scheme of readout as direct readout method. Whereas for magnetometry experiments additional lock-in amplifier after the photodiode was used. For magnetometry experiments with fluorescence and transmitted infrared signal, the lock-in-amplifier gave several advantages over direct readout method. Therefore the most important addition in the detection channel was the addition of lock-in-amplifier after the photodiode. The basic principle of lock-in-amplifier is phasesensitive detection along with filtration of unwanted frequencies and AC-amplification [159]. For phasesensitive detection, the fundamental principle is straightforward, a signal which is buried under noise with low signal-to-noise ratio is recovered by modulating that signal and then mixing that signal with a reference signal with same modulation frequency. The frequency filtration and AC-amplification enhances the signal quality which in turn helps to achieve sensitive measurements. In this work particularly magnetic field sensing was performed with this scheme [159].

The advantages to use lock-in amplifier compared to direct readout of the ODMR spectrum for magnetometry experiments are as follows. First, by the process of modulation and demodulation of the collected signal, the bulk of low frequency noise can be removed from the signal as well as any signal buried under noise could be recovered by amplifying that exact signal. These low frequency noise primarily comes from electronic sources. For example, in case of infrared absorption magnetometry presented in this work, the ODMR signals had low contrast (in between 0.035% to 0.16% for different samples, details are

in chapter 7), with lock-in-amplifier it was possible to recover these signals with high signal-to-noise ratio. Second, the signal produced by the lock-in amplifier is a first order derivative of the CW-ODMR spectrum. This signal can be approximated to be linear over a frequency range as it crosses zero. This spectrum acquired from the lock-in-amplifier simplifies magnetometry measurements as the slope of the zero-crossing demodulated signal can be measured initially and can be tracked over time. As discussed in the previous chapter, this slope is the crucial parameter for magnetometry experiments to measure the sensitivity of the magnetometer. Therefore tracking the slope and the zero-crossing frequency periodically gives advantage in real-time sensing as the need for extensive fitting of the ODMR resonance dip with Lorentzian or Gaussian fit is minimized. In contrast to this situation, when the readout scheme has no lock-in-amplifier it is necessary fit the ODMR spectrum with Lorentzian or Gaussian fit for each acquired spectrum which constrain the real-time sensing protocol to great extent [40, 68, 120, 160].

To utilize the advantages provided by lock-in-amplifier for magnetic field sensing, in the experiments presented in this work following procedure was applied. As already discussed, in phasesensitive detection, modulation and demodulation of the signal of interest should be performed. For performing ODMR in magnetometry experiments, modulation may be applied either to the microwave drive signal or to the pump laser or to the bias magnetic field as in case of microwave free magnetometry [161]. In this work, while the demodulation of the signal was done by the lock-in-amplifier, modulation was performed by modulating the frequency of microwave signal. This modulation technique is known as frequency modulation (FM). The reasons behind the choice for frequency modulation of microwave drive are as follows. To get the advantage of lock-in scheme where the output signal acquired from the lock-in-amplifier has a zero-crossing dispersion line-shape frequency modulation has to be applied to the microwave drive. In contrast to frequency modulation of MW drive, if the modulation is applied to the pump laser (amplitude modulation), the acquired signal results in a Lorentzian or Gaussian line-shape. In this situation the highest sensitivity is on the sides of the line-shape, rather than on the resonant frequency, where the signal is minimum hence more susceptible to fluctuations and noise inherent to the laser [120]. Due to these reasons, we chose FM scheme for our magnetometry experiments and the microwave signal was frequency modulated. As the microwave drive was modulated, continuous

wave lasers were used for technical convenience. In this work the majority of the experiments were done in such a way where it was necessary to maintain uniform intensity of the pump laser over a macroscopic volume of the diamond samples. The use of continuous pump and probe lasers also helped to maintain the uniform intensity over a large volume inside the diamond samples.

As we used frequency modulation technique in our magnetometry scheme, here a brief discussion is presented on this technique [162]. The basic principle of frequency modulation is, here a carrier signal and a modulating signal is chosen where the modulating signal modulates the frequency of the carrier signal. For example, we can think of a carrier signal as $S_c(t) = A_c \cos(2\pi f_c t + \phi)$, where A_c is the amplitude, f_c is the carrier frequency, and ϕ is the phase of the carrier signal. The modulating signal can be similarly $S_{mod}(t) = A_{mod} \cos(2\pi f_{mod} t)$, where A_{mod} is the amplitude, f_{mod} is the modulation frequency, and ϕ is the phase of the modulating signal. A frequency modulated signal can be defined as following [162] :

$$S_{FM}(t) = A_c \cos\left(2\pi f_c t + 2\pi k_f \int_0^t S_{mod}(t)\, dt\right). \tag{5.1}$$

In equation 5.1, the value of constant k_f depends on the modulating system. The instantaneous frequency $f_i(t)$, for such a frequency modulated (FM) signal will be as following [162]

$$f_i(t) = f_c + k_f A_{mod} \cos(2\pi f_{mod} t). \tag{5.2}$$

From the above equation 5.2, it can be inferred that the instantaneous frequency varies or deviates $\pm k_f A_{mod}$ in respect to f_c. This is defined as frequency deviation, $f_{dev} \equiv k_f A_{mod}$, as this is the maximum departure of the instantaneous frequency from the carrier frequency. Equation 5.2 can be rewritten as $f_i(t) = f_c + f_{dev} \cos(2\pi f_m t)$. Combining equation 5.1 and 5.2 the final form of a frequency modulated signal can be written as [162] :

$$S_{FM}(t) = A_c \cos(2\pi f_c t + \beta \sin(2\pi k_{mod} t)). \tag{5.3}$$

Where $\beta = \frac{f_{dev}}{f_{mod}}$, conventionally known as modulation index. In this work for all the presented results with FM, the carrier frequency f_c is the frequency of the microwave signal. For obtaining ODMR spectrum this microwave signal

is swept over a frequency range, whereas for magnetic field sensing experiments this carrier frequency is the center frequency of the resonance feature which is the zero-crossing frequency of the dispersion line-shape acquired from the lock-in-amplifier. The modulating frequency f_{mod} was chosen experimentally where the dispersion line shape was less noisy. The limiting factor for choosing the f_{mod} was the fact that under continuous optical excitation the T_1 relaxation time of NV centers limits the modulation frequency to $\leq$ 20 KHz [42]. The choice of frequency deviation was $f_{dev} \geq \Delta\nu$, where $\Delta\nu$ is the linewidth (FWHM) of the resonance feature on which the magnetometry experiments were performed. The choice of f_{dev} is crucial as wrong choice of f_{dev} can lead to distortion of the dispersion lineshape and effectively reduce the range over which the dispersion curve is approximated as linear. This has been observed in the experiments [67].

For the magnetic field sensing experiment the MW is modulated around the zero-crossing frequency for a particular resonance dip observed in the ODMR spectrum. While modulating the MW the voltage output of the lock-in-amplifier is recorded as a timetrace over some time (600 seconds). From the recorded timetrace the variation in voltage can be converted to the variation of the magnetic field by the following equations [40]:

$$B_{measured}(t) = C_{LIA} V_{LIA}(t). \tag{5.4}$$

In the above equation $B_{measured}(t)$ is the measured magnetic field over time t, $V(t)$ is the recorded voltage in the timetrace from the lock-in-amplifier and C_{LIA} is the voltage-to-magnetic field conversion factor given by [40] :

$$C_{LIA} = \frac{h}{g_e \mu_B b}. \tag{5.5}$$

Where h is Planck constant, g_e is the electron g-factor, and b is the slope of dispersion lineshape at the zero-crossing, $b = \frac{dV_{LIA}}{df} \mid_{V_{LIA}=0}$.

From the above discussion it is clear that to realize the preferred magnetometry scheme experimentally; the requirements are continuous-wave lasers, continuous microwave driving with modulation enabled functionality, lock-in-amplifier and photodiode to collect the readout signals. In the following section, details of the experimental setup, details of the sample is discussed.

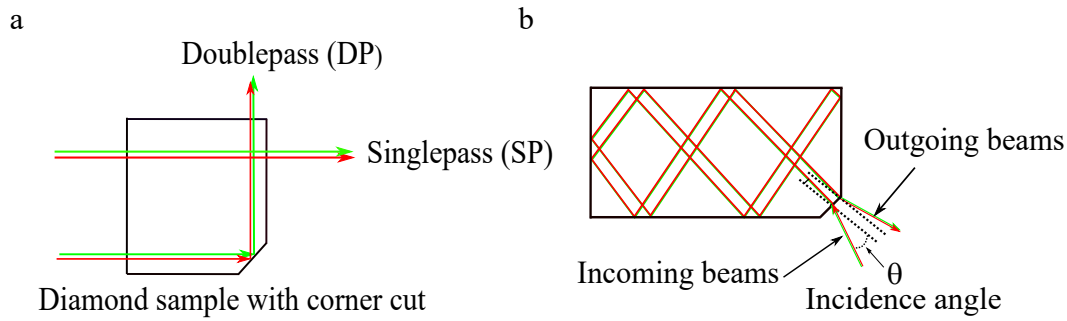

Figure 5.1: **Different configurations for experiments.** In this schematic the green pump laser and infrared laser are depicted as green and red arrows a) This schematic diagram shows the configurations for single pass (SP) and double pass (DP). b) This diagram shows the configuration for LTDW. In the figure the incident angle for the overlapped beams with respect to the cut facet of the diamond is shown as angle θ, the . The overlapped laser beams are getting reflected multiple times inside the diamond due to total internal reflection.

5.2 Experimental Setup

In this work the diamond samples were used in different configurations as shown in figure 5.1 for infrared laser absorption magnetometry as well as for fluorescence magnetometry. The configurations are named as single pass (SP), double pass (DP) and waveguide or light trapping diamond waveguide (LTDW) [68, 69].

For single pass the lasers were entering the samples from one sidewall and exited through the opposite sidewall. In case of double pass configuration the lasers entered the sample from one sidewall then incident on the corner cut of the samples, as the cut facets are 45° in angle respect to the laser path, the lasers went through total internal reflection and exited through another sidewall. Finally for LTDW [68, 69] configuration, the laser entered the diamonds through the cut corner and after several reflections on the sidewalls of the diamond sample due to total internal reflection condition it exited the diamond from the same corner cut.

5.2.1 Optical setup

In the figure 5.2 all the optical component and the schematic diagram of the experimental setup is shown. As described in the previous section 5.1.1 for CW-ODMR with fluorescence or infrared transmission signal continuous lasers were used. A green laser (company: MediaLas, DPSS, max output 1 Watt) of 532 nm wavelength is the pump laser to excite the NV centers in the diamond samples. For Infrared laser absorption magnetometry a probe infrared laser of 1042.5 nm wavelength (company: Toptica, ECDL, max output 100 mW) has been used to probe the metastable singlet states of the NV centers. The infrared laser has been overlapped with the green laser for infrared absorption magnetometry experiments. To see the effect of enhanced path length on sensitivity the lasers made pass through the diamond in different ways such as single pass (SP) , double pass (DP) or light trapping diamond waveguide (LTDW).

The company rated maximum output power for the green laser was 1 Watt but it was only 850 mW of power which was available during stable operation of the laser. To vary the laser power a $\lambda/2$ wave plate and a polarizing beam splitter (PBS) has been used in front of the laser output. The laser was then coupled to a single mode (SM) fiber (P3-460B-FC, Thorlabs). The maximum power available after the fiber coupling section was approximately 540 mW. The main reasons to use a single mode fiber here are twofold; first to get a clean Gaussian beam profile of the laser and secondly decoupling the optical elements before and after the fiber which eased the alignment procedure for the main set up (see also 4.2). For the outcoupler section of the fiber a 11 mm aspheric lens (C220TMD-A, Thorlabs) has been used to collimate the beam. The laser beam is then incident on dichroic mirror (DMLP950, Thorlabs). The dichroic mirror is used to combine or overlap the green laser and the infrared laser. After the dichroic mirror, the green laser was guided by another set of mirrors through a 100 mm plano-convex lens to focus the laser beam inside the diamond samples.

The infrared laser is also fiber coupled and the outcoupler section has a 11 mm aspheric lens (C220TMD-B , Thorlabs). The laser beam then passed through an Optical isolator. The maximum power available after the fiber coupling section and the optical isolator was 80 mW. The optical isolator has been used to protect the infrared laser from any back reflection. After the optical isolator the the infrared laser passed through a $\lambda/2$ wave plate and a polarizing beam

splitter (PBS), which were used to control the optical power. The laser then was guided to the dichroic mirror. At this point, using the mirrors after the PBS, the infrared laser was overlapped with the green laser.

The choice of particular aspheric lenses for both the green and infrared laser arose from the specific requirement of beam waists needed inside the diamond samples for magnetometry experiments. From the theoretical calculations done with the NV rate equation model (chapter 4.1), we came to know that the ideal beam waist for the green pump laser and the IR laser inside the diamond should be within the range of 15 to 30 µm (figure 4.3). For making the optical set up simple we opted beam waist of 20 µm for both the lasers.

Single mode fibers were used to achieve Gaussian beam profile for both lasers. The mode field diameter (MFD) of the single mode fiber used to couple the green laser is; 4.1 µm @ 532 nm (verified experimentally). For collimating the laser beam an aspheric lens was used with focal length of 11.0 mm. By plugging in these values in equation 5.6, the collimated beam diameter D was calculated, which was 1.82 mm. The MFD) of the single mode fiber used to couple the infrared laser is 6.2 µm @ 1042.5 nm. An aspheric lens with focal length of 11.0 mm was used to collimate the laser beam. By using equation 5.6, the beam diameter D of the collimated laser beam was calculated and that was 2.35 mm.

In equations 5.6 and 5.7, MFD is mode field diameter of the single mode fibers, λ is the laser wavelength, and D is the collimated beam diameter, f is the focal length of the lenses, and ϕ_{spot} is the diffraction-limited spot size [155].

$$f = \frac{\pi D\,(MFD)}{4\lambda} \tag{5.6}$$

$$\phi_{spot} = \frac{4\lambda f}{\pi D} \tag{5.7}$$

With these values of collimated beam diameter for green and infrared laser we calculated with equation 5.7 the focal length f of our focusing lens. For green and infrared laser the values of f are approximately 100 mm and 71 mm. We opted for 100 mm focal length spherical plano-convex lens for both the lasers to avoid complexity in our optical setup. Both the lasers were focused inside the diamond samples with same focusing lens with focal length of 100 mm. In appendix (section Appendix C: Beam waist determination), beam waist determination with a sharp edge knife is described.

To probe the the singlet state of the NV ensemble with the infrared laser need

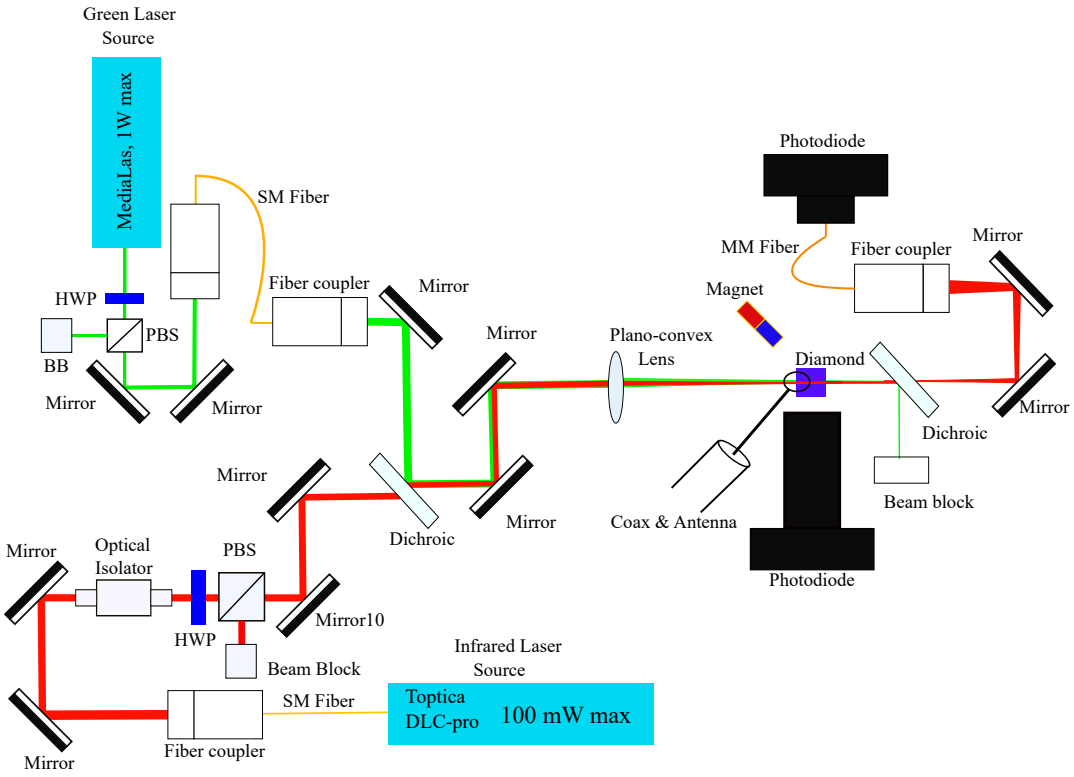

Figure 5.2: **Optical component setup**. In this figure the optical setup is depicted for both the infrared absorption magnetometry and fluorescence magnetometry. The green pump laser and the infrared probe laser are depicted as green and red lines in the figure. Details of the acronyms used in the schematic are as follows. HWP is $\lambda/2$ wave plate, polarizing beam splitter as PBS, beam block as BB and single and multi mode fibers as SM fiber and MM fibers respectively. See the text for detailed description of the setup. Details regarding the antenna position and alignment of the magnet is discussed later in this chapter.

to address the same NVs which were being pumped by the green. In case of offset between these two laser beams in the beam path, optimum magnetic field sensitivity with infrared absorption magnetometry can not be reached. For this reason, in infrared absorption magnetometry experiments precise overlapping of the two lasers is very crucial. To achieve this high precision overlap of the two lasers a SM fiber was used. Both the lasers were simultaneously couple to this SM fiber. Once the overlap of laser beams was achieved, the SM fiber was removed and in place of that the 100 mm focusing lens was placed. In between the focusing lens and the diamond samples there were no optical element (see figure 5.2).

In Fluorescence measurements the fluorescence was collected by an aspheric condenser lens (ACL2520U-A, Thorlabs) and then focused by another aspheric condenser lens on a variable gain photodiode (PDA100A2, Thorlabs). The filters used for fluorescence measurements were, one 700 nm long pass (FEL0700, Thorlabs) and one 532 nm Notch filter (NF533-17, Thorlabs). The 532 nm notch filter was used to block any scattered green laser. It was observed in experiments that the ODMR contrast increased when the 700 longpass (LP) filter was used rather than 620 LP or 650 LP filters. The reason behind this is, by using 700 LP filter the fluorescence from NV^0 was filtered out, which was contributing to the background. The figure 5.3 shows the experimental results for determining the filter choice. Green laser power (50 mW) and microwave power (5 dBm from MW source) were same for all the acquired ODMR spectrum.

In case of infrared absorption magnetometry experiments, the transmitted infrared beam was first separated from the transmitted green beam by a dichroic mirror mirror (DMLP950 Thorlabs). After the dichroic the infrared beam was coupled to a multi mode fiber which was then attached to a variable gain photodiode (PDA100A2 Thorlabs).To couple only the spectrally clean transmitted infrared beam two filters were used. In front of the fiber coupling a 950 Longpass filter (FEL0950, Thorlabs) was used to block any scattered green light or the fluorescence from the diamond samples (600 - 800 nm). Another band pass filter (FB1050-10, Thorlabs) was attached to the photodiode before the fiber coupling component to filter the Raman line of the multi mode fiber.

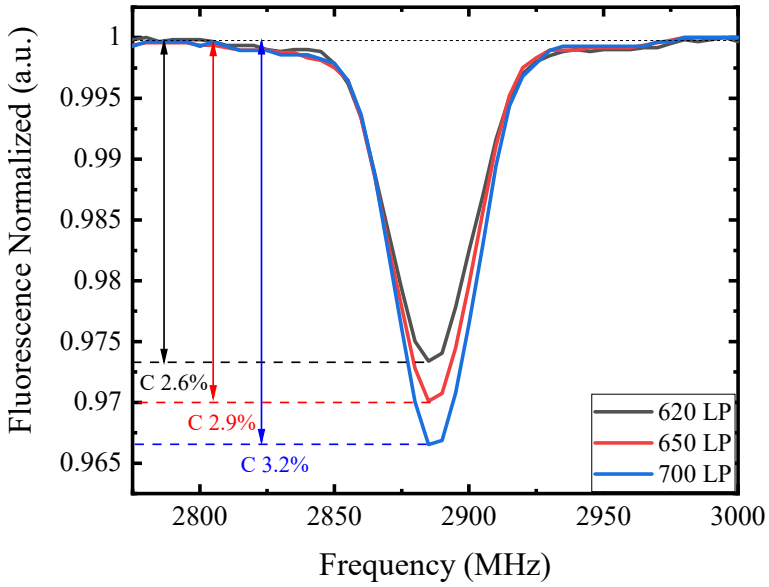

Figure 5.3: **Filter choice for fluorescence ODMR experiment.** In this figure the experimental results with different optical filters are shown. The blue ODMR spectrum shows the highest contrast of 3.2 %, where the filter used was 700 longpass and the black ODMR spectrum shows the lowest contrast of 2.6 % with 620 longpass filter. In between the red ODMR spectrum shows the contrast of 2.9 % with a 650 longpass filter. Laser power and microwave power and the antenna position were same for all the experiments.

5.2.2 Electronic Setup

Apart from the optical components the experimental setup had lots of electronic components which are shown in the figure 5.4. These electronic components which were used in the ODMR and magnetometry experiments were mainly the microwave components for manipulation of the NV ensemble, lock-in -amplifier for magnetometry, combination of passive electric filters for reduction of electric noise, variable gain photodiode for collecting readout signal and National Instruments Data Acquisition system. As discussed before in the section 5.1.1 and section 5.1.2, experiments were done either with direct readout method or with lock-in-amplifier for magnetometry.

In the direct readout method (figure 5.4 b), the fluorescence (depicted as orange trapezoid in figure 5.4 a and b) or infrared transmission signal (depicted as red laser beam in figure 5.4 a and b) were collected by the photodiode (PDA100A2 Thorlabs) which was connected to a 2 kHz lowpass filter (EF112, Thorlabs) to reduce the electrical noise an then to the data acquisition card for data collection. Microwave was delivered via loop antenna.

In case of magnetometry experiments where the lock-in scheme was used the electronic system was different. Here the electrical signal from the photodiode was first made relatively noise free by using of a electrical bandpass filter (combination of electrical highpass filter and a lowpassfilter). The electrical filters used to make the bandpass filters are, 2 kHz highpass filter (EF114, Thorlabs) and a 5 kHz lowpass filter (EF113, Thorlabs) . This filtered electrical signal then attached to the signal input of the lock-in-amplifier. The output of the lock-in-amplifier is again electrically filtered by using of a 2 kHz lowpass filter (EF112, Thorlabs) before it is connected to the data acquisition system,which was connected with a computer for data read out.

To acquire the experimental read out the data; either directly from the photodiode or from the output of Lock-in-amplifier; data acquisition (DAQ card) system from National Instrument was used. The specific DAQ card used for all the experiments is PCIe-6323. Analog voltage from the photodiode or from the lock-in-amplifier was connected to analog voltage input of the DAQ card. The digital output from the DAQ card was used to control the green laser state (ON and OFF). For synchronization of the experiments, the microwave source was also controlled via computer.

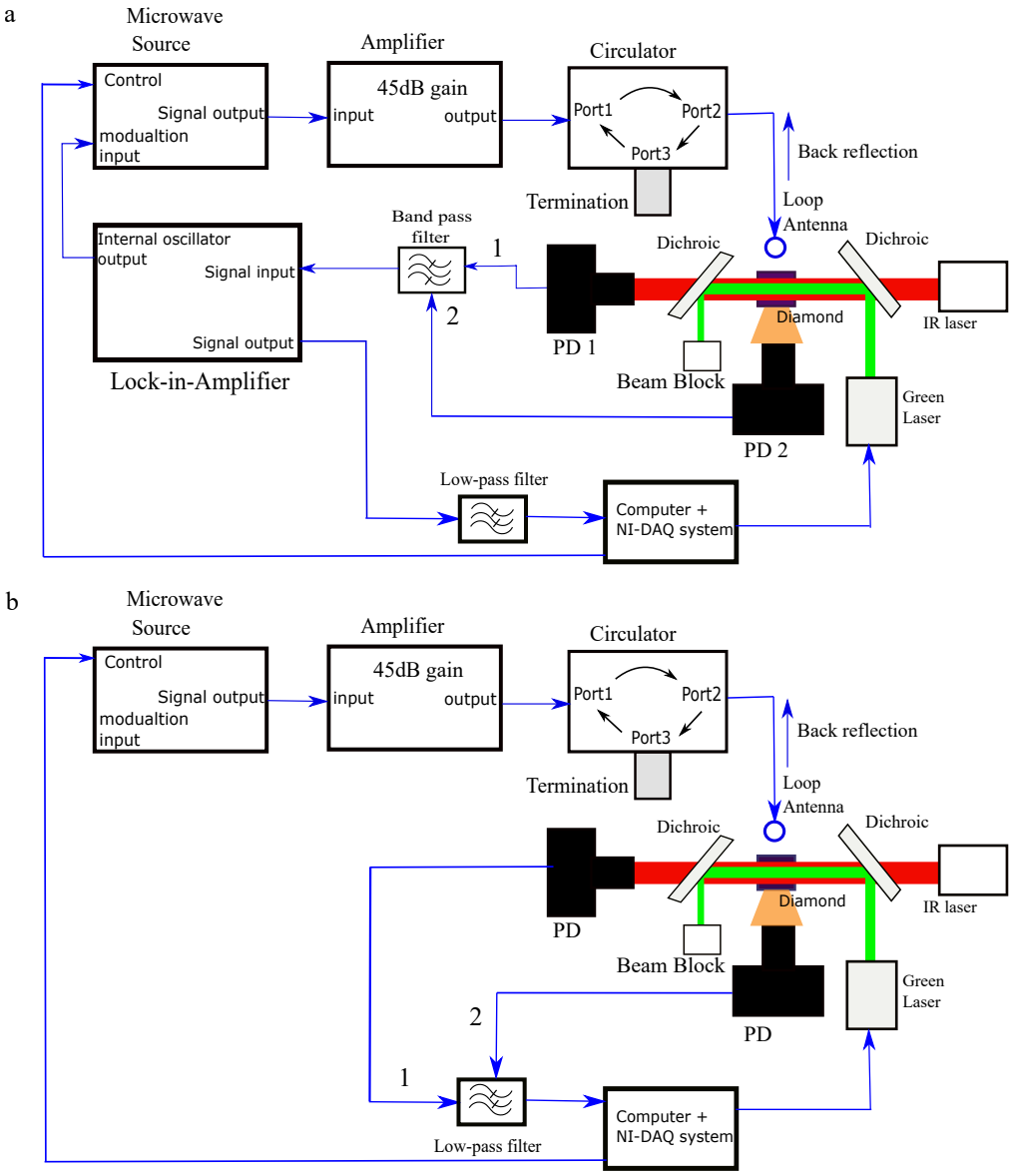

Figure 5.4: **Electronic component setup**. Figure a) depicts the schematic for electronic set-up depicts the microwave delivery to the sample along with lock-in-amplifier scheme and the read out system. Figure b) shows the schematic for electronic set-up depicts the microwave delivery to the sample along without lock-in-amplifier scheme and the read out system. The path 1 and 2 labeled in the schematic diagram are exclusive. At a time either infrared absorption magnetometry or fluorescence magnetometry was performed. In figure a and b, green and IR lasers are depicted as green and red thick lines, the fluorescence is depicted as orange trapezoid. Blue arrows shows the electrical and microwave path in the setup.

5.2.3 Microwave delivery and Lock-in-Amplifier

Here the discussion is about the setup for microwave drive as well as the lock-in-amplifier assisted magnetometry method as discussed in section 5.1.2. For microwave (MW) manipulation of the NV ensemble in the diamond samples a copper wire loop antenna was used (See figure 5.5). For different configurations, the antenna was placed in different manner as shown in figure 5.1. In the figure 5.4, schematic diagram for electronic setup for direct readout (figure5.4 a) method and lock-in-amplifier assisted readout method for the magnetometry (figure 5.4 b) is shown. The path 1 and 2 labeled in the schematic diagram are exclusive in nature, at a time either infrared absorption magnetometry or fluorescence magnetometry was performed. The modulation enabled microwave source (DC to 6.075 GHz signal generator, SG386, Stanford Research Systems Inc) is amplified typically 45 dB by an amplifier (ZHL-16W-43-S+, Mini-Circuits). For magnetometry experiments the MW power used is varied within 5 dBm to 7dBm from the microwave source. For characterizations of the magnetometer the MW source power was varied in between 7dBm to -30 dBm. After the amplifier the MW signal went to a DC block component (BLK-89-S+ , Mini-Circuits) and then to a circulator (SFC2040A, Fairview Microwave). Here the circulator is used to protect the amplifier from any kind of back reflection from the loop antenna as the home-built loop antenna was not impedance matched. The three ports of the circulator was used in the following manner, MW signal enters at the port 1, the loop antenna is connected at port 2 and at port 3 a 30 dB attenuator combined with a 50 Ohm termination is used to terminate the back reflected part of the MW signal. The loop antenna was positioned directly on top of the diamond sample to deliver the maximum possible microwave power. In the magnetometry experiments (see figure 5.4 a) the microwave source was modulated externally and to do that the internal oscillator of the Lock-in-Amplifier (DSP 7265, Stanford Research) was used. The frequency of the modulating signal from the Lock-in-Amplifier (internal oscillator), which was used to modulate the microwave signal, used as the reference signal for the Lock-in scheme and the modulation depth or frequency deviation was set at the microwave source.

The modulation frequency used for the experiment was 3.5 kHz, frequency deviation (e.g. 1.5 MHz, 9.8MHz or 10 MHz) was determined from linewidth measurements of the resonance feature (discussed in section 5.1.2). The time

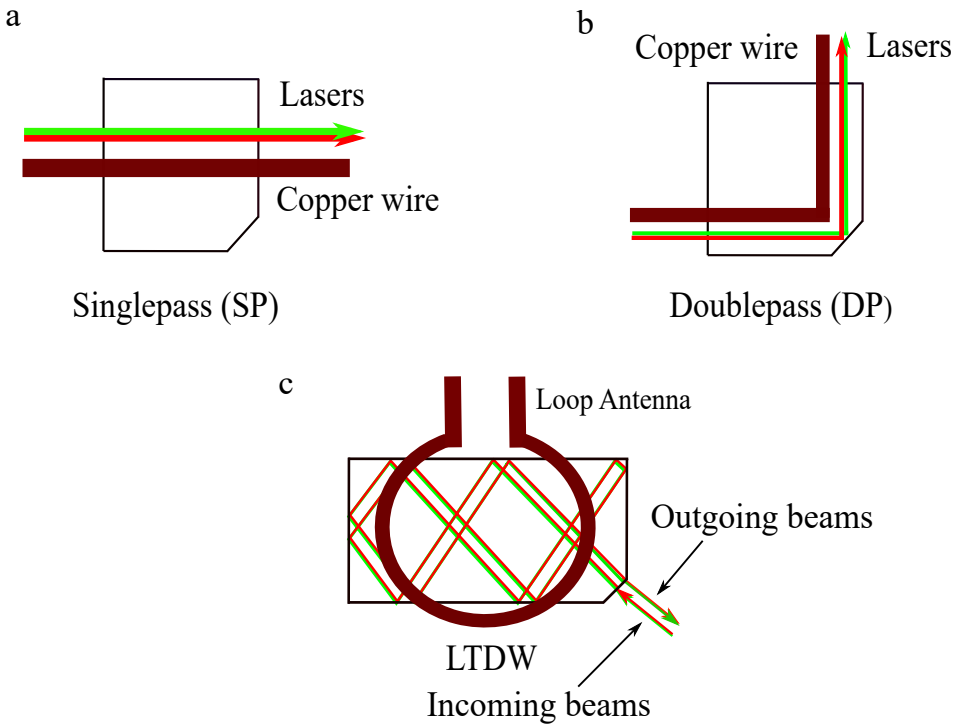

Figure 5.5: **Antenna alignment.** In this schematic the pump and probe lasers are depicted as green and red arrows and the copper wire antennas are depicted as thick brown lines and a loop. In figure a), for single pass configuration the antenna was placed right on top of the beam path for maximum microwave delivery to the NV ensemble. In figure b), for double pass the copper wire antenna was bent same as the beam path shown in figure. In figure c), for LTDW the laser beams were getting reflected many times inside the diamond and covered a bigger area. Here the best solution was to make a loop antenna for delivering maximum microwave power.

constant of 5 ms was used for the lock-in-amplifier settings unless otherwise described in the chapters 6 and 7. The lock-in-amplifier parameters such as sensitivity, AC gain or output channel expansion was set manually for specific experiments and these details are described in the chapters 6 and 7.

5.3 Sample Mounting and beam walkoff

In different experimental configuration as mentioned in the beginning of this chapter (e.g. SP, DP and LTDW) the diamond samples were positioned differently with respect to the laser beams. For LTDW configuration, rotation of the diamond sample was necessary so that the laser beams entered in the diamond sample in a specific angle. Depending on the incident angle at the cut corner facet of the diamond, different path length of the laser beams inside the diamond was achieved. For LTDW configuration in the infrared absorption magnetometry it was very crucial that the laser beams remain overlapped for the entire trip inside the diamond. Therefore in this configuration two conditions had to met, 1) the path length should be increased inside the diamond than double pass configuration significantly (see figure 4.5 a)) and 2) at the same time for entire path inside the diamond both the lasers were overlapped for maximum possible infrared absorption. Now, as the refractive index of the diamond is different for the green laser (2.41 @ 532 nm) and the infrared laser (2.39 @ 1042.5 nm) [88], with increased path length there would be a walkoff of the laser beams (see figure 5.6).

For LTDW to achieve longer path length, the sample needed to be rotated with respect to the laser beams. For different incidence angles the path length will be different inside the diamond as well as the beam walkoff. Therefore, to optimize the above mentioned conditions, angle bound was estimated, taken into account that the beam waist at focal point was $\sim$ 20 µm. As the beam waist of lasers were $\sim$ 20 μm, a walkoff more than 40 μm was not desirable. In figure 5.6, the beam walkoff with increasing incidence angle and path length is shown. It can be noted in figure 5.6, that with an incidence angle in between 5° - 20°, the beams are overlapped for a path length of 12 mm - 30 mm with negligible walkoff. In our experimental realization of LTDW, the incidence angle of the combined laser beams was 20° and a path length of $\sim$ 28 mm was achieved (see Appendix D: Path length calculation for LTDW). From the figure 5.6, it can be

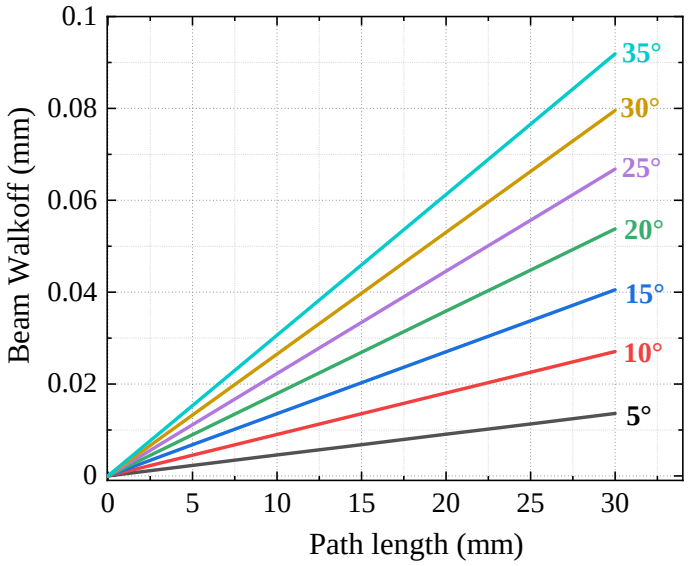

Figure 5.6: **Beam walkoff estimation.** The beam walkoff dependent on the path length and the incidence angle of the laser beams is shown in this figure. The solid lines shows the walkoff distance with increased incidence angles and path lengths.

seen that the beams were significantly overlapped for entire path.. To achieve that, the samples were positioned on a sample holder which was attached to a high precision rotational stage (PR01/M, Thorlabs). In these experiments it was also very crucial to focus the laser beams inside the diamond (in some cases at the cut facet) as predicted by the NV rate equation model combined with Gaussian optics as described in the NV rate equation model in the chapter 4. For that, the rotation stage was attached to a 3-axis translational stage (Newport) to move the sample in x,y and z direction. In order to do that, first the beam waist was measured with sharp knife and optical power meter at 6 different position after the Plano-convex lens (focal length 100 mm). From those set of measurements the exact the focal point was determined in free space (see Appendix C: Beam waist determination). The focal point inside the diamond was calculated taken into account that the focus will be at different position from the lens due to the high refractive index of diamond. Once the focal point was decided from calculation the sample was positioned at the desired position from the focusing lens with the translation stage. This combination of the rotation stage and the 3-axis translation stage made sure precise positioning

and orientation of the diamond sample.

5.4 Magnetic field Alignment

For magnetometry experiments, first a static bias magnetic field was applied. This magnetic field was applied along the $\langle 111 \rangle$ crystallographic direction of the diamond samples [19, 26], which was provided by a Neodymium cube permanent magnet (W-12-N, Supermagnete). The dimension of the magnet was 12 mm$\times$12 mm$\times$12mm. For all the magnetometry experiments, the magnet was positioned from the top respect to the diamond sample with posts. To align the magnetic field along the NV axis of one of the four classes of NV in the ensemble; the magnet was positioned $\sim$54.5° with respect to horizontal plane. The alignment procedure was performed in such a way that in the ODMR spectrum only four resonance dips were visible with outer dips having smaller contrast than the inner dips. Out of these four resonance dips two resonance dips arose from one class of NVs and the other two resonance dips were the resultant dips of the other three classes of NVs present in the ensemble. To perform magnetometry all these resonance dips were well separated from each other. This alignment procedure was performed in a trial and error method at each step of magnet position taken into account the number of visible resonance feature and their contrasts. In the figure 5.7 a schematic diagram shows the orientation of the permanent cube magnet with respect to the diamond sample.

To perform magnetometry test with time varying magnetic field a magnetic coil was used along with the permanent magnet. The coil was positioned in the same plane of the magnetometers. In another word the permanent magnet and the coil magnet were in orthogonal planes. This placement of the coil was preferred only due to space constraint in our setup. With magnetometry experiments the field strength and frequency of these AC magnetic fields were verified, more details about these experiments are discussed in the chapters 6 and 7. The coil used for the AC magnetic field was a multi-turn coil made with copper wire (wire diameter of 0.2 mm). This circular multi-turn coil had number of turns, N = 14, radius of the coil r_{coil} = 1.25 cm, the distance from the magnetometer was approximately 10 cm, the coil current I_{coil} was varied from 100 mA to 200 mA for different measurements and a 50 Ohm resistor was connected in series with the coil for impedance matching. A function generator

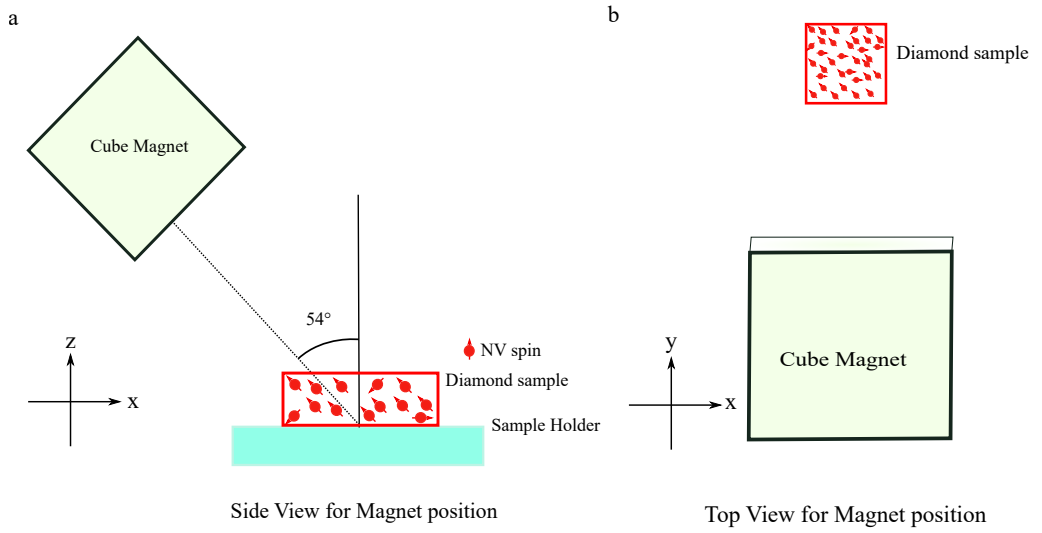

Figure 5.7: **Alignment of magnet with respect to diamond.** Simple schematic diagram depicting the magnet orientation with respect to the diamond sample. a) Shows the side view for the magnet position respect to the diamond sample. b) Shows the top view for the magnet position respect to the diamond sample.

was used to provide the coil current with different frequencies. The test field strength was calculated using the following equation [40] :

$$B_{test} = \frac{\mu_0 N_{turns} I_{coil} r_{coil}^2}{2\left[z_{coil}^2 + r_{coil}^2\right]^{3/2}}. \tag{5.8}$$

The field strength and frequency of the coil magnet was measured with the sensitivity measurement of the magnetometer. These details are provided in the chapter 6 and 7.

5.5 Sample preparation

This section is dedicated to discuss about the samples used in the magnetometry experiments. In the figure 5.8, all the samples are shown together. Here it can be noted that the samples are of different colors. These different colors of the samples are due to different concentration of NV centers in the diamonds. Sample 1 and 2 has low NV concentration and are transparent. Sample 3 and 4 has high NV concentrations. While sample 3 is light purple in color sample 4 has even more high concentration of NV centers thus it is darker purple in

color. The details of the samples are given below.

Sample 1: This sample was provided by Element6. Dimension of this sample were 4.8 mm×2.4 mm×0.5 mm with one corner of the diamond was cut with dimensions of 0.5 mm × 0.5 mm and a angle of 45° with respect to the diamond sidewalls. Material used for this sample is CVD grown standard grade diamond material with initial nitrogen concentration of 0.15 ppm. The sample was electron irradiated for 30 minutes and went through subsequent annealing process above 600° C to create NV centers. The estimated NV concentration ([NV] = [NV^0]+[NV^-]) is approximately 0.036 ppm. The edge of this sample is along ⟨110⟩direction and the surface is of (100) orientation.

Sample 2: This sample was also provided by Element6. The dimensions of this sample were 4.8 mm×4.8 mm×0.5 mm with one corner of the diamond was cut with dimension of 1.0 mm × 0.5 mm and a angle of 45° with respect to the diamond sidewalls. The material used as well as the crystallographic orientations of this sample is same as sample 1 only this sample was electron irradiated for 20 minutes. The estimated NV concentration ([NV] = [NV^0]+[NV^-]) is approximately 0.036 ppm.

Sample 3: Sample provided by Element6. Dimensions of this sample were 2.5 mm×2.5 mm×0.5 mm with one corner of the diamond was cut with dimensions of 0.5 mm × 0.5 mm and a angle of 45° with respect to the diamond sidewalls. Material used for this sample is CVD grown standard grade diamond material with initial nitrogen concentration of 20 ppm. This sample was electron irradiated for 4 hrs and annealed above 800° C. Specific growth process and annealing process for this sample could be found in more detailed manner in the following articles by Edmonds *et al.* [108, 121]. The estimated NV concentration ([NV] = [NV^0]+[NV^-]) is approximately 1.47 ppm. The crystallographic orientations are same as sample 1 and 2.

Sample 4: For this sample the dimensions were 3.2 mm×3.2 mm×0.5 mm with one corner of the diamond was cut with dimension of 1.0 mm × 0.5 mm and a angle of 45° with respect to the diamond sidewalls. HPHT diamond was used for this sample, which was electron irradiated and subsequently annealed for creation of NV centers. The estimated NV concentration ([NV] = [NV^0]+[NV^-]) is approximately 6.8 ppm. This sample was provided by the research group of Applied Quantum Systems under Prof. Dr. Jan Meijer at Universität Leipzig.

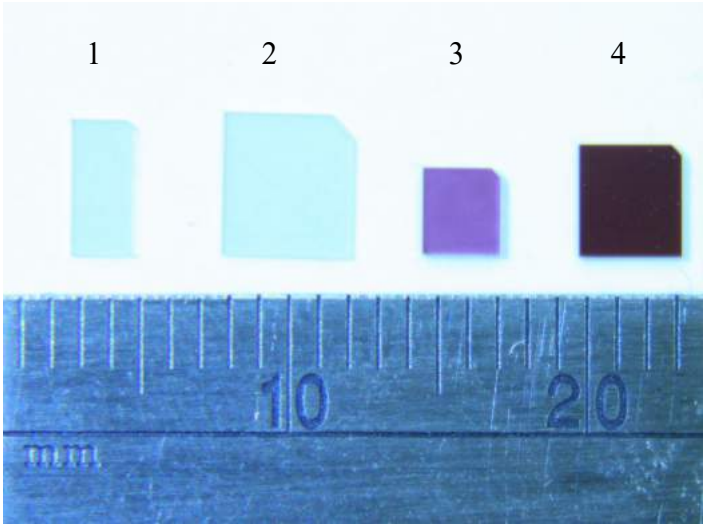

Figure 5.8: **Samples.** In this figure all the samples are shown. With sample 1, 2, and 3 all the magnetometry experiments were performed. Sample color is due to different concentration of NV centers in the diamonds. Sample 1 and 2 has low NV concentration and are transparent. Sample 3 and 4 has high NV concentrations. For detail description of the numbered samples please refer to text.

NV concentration was estimated from transmission experiment with green laser with the following equation of Beer-Lambert law [163], taken in to account the Fresnel reflection from the diamond surfaces:

$$\frac{P_{out}}{P_{in}} = e^{-n.\sigma_{green}.l} \tag{5.9}$$

Where, P_{out} is the out put optical power, P_{in} is the input optical power, σ_{green} is the absorption cross section (value given in table 4.1) of NV center for green laser, n is the NV concentration, and l is the path length of the laser beam inside the diamond sample. To calculate the transmission of the lasers, the Fresnel reflections from the diamond surface was taken into account. Following are the Fresnel equations for s and p polarized light [155].

Sample	P_{out} (mW)	P_{in} (mW)
1	~ 40.1	~ 50
1	~ 16.2	~ 20
1	~ 8.0	~ 10
3	$\sim$61.3	~ 500
3	~ 36.1	~ 300

Table 5.1: **NV concentration measurement.** In this table input (P_{in}) and output (P_{out}) optical powers are given which were measured to calculate NV concentrations of sample 1, 2 and 3. Samples 1 and 2 are from same batch and calculated NV concentrations are same for both samples. Therefore values for sample 1 and 3 are given only.

$$R_s = \left| \frac{n_1 \cos\theta_i - n_2 \sqrt{1 - \left(\frac{n_1}{n_2}\sin\theta_i\right)^2}}{n_1 \cos\theta_i + n_2 \sqrt{1 - \left(\frac{n_1}{n_2}\sin\theta_i\right)^2}} \right|^2 \tag{5.10}$$

$$R_p = \left| \frac{n_1 \sqrt{1 - \left(\frac{n_1}{n_2}\sin\theta_i\right)^2} - n_2 \cos\theta_i}{n_1 \sqrt{1 - \left(\frac{n_1}{n_2}\sin\theta_i\right)^2} + n_2 \cos\theta_i} \right|^2 \tag{5.11}$$

In the equations 5.10 and 5.11, R_s and R_p are the reflectances for s and p polarized light, n_1 and $n_2$are the refractive indices for air ($n_1 = 1$) and diamond ($n_1 = 2.4$) and θ_i is the angle of incidence. The angle of incidence was 10° in all the measurements. For sample 1 and 3, the path length l were 2.4 mm 2.5 mm respectively.

Out of these samples shown in figure 5.8 all the magnetometry experiments were done with sample 1,2, and 3. With sample 4 it was not possible to perform the experiments even with single pass (SP) configuration due to high absorption of the pump laser.The grown diamond samples used in the experiments had to cut and polish to realize the different experimental configurations shown in figure 5.1. For LTDW configuration it was necessary that the sidewalls of the diamond samples are parallel to each other. Otherwise, the maintaining overlap of the laser beams inside the diamond sample was not possible. Apart from the parallelism of the sidewalls, it was necessary to have a cut corner for the diamond samples for all the configurations. Primary polishing and cutting of

the sample 1 and 2 were done by Element6 while for sample number 3 there were no prior polishing or cut corner. These samples were again investigated by laser scanning microscope to check the parallelism of the sidewalls. Images taken with laser scanning microscope are shown in figure 5.9. In the figure 5.9, solid red lines are drawn to show the 90° angle and the dotted purple line emphasize on the inclined sidewalls. From these images it was evident that the sidewalls of the samples were not parallel and measurement showed angle deviation of more than 1° in some cases and further polishing was required.

Therefore to prepare the samples to perform magnetometry experiments with above configurations (figure 5.1) samples were sent for further polishing (Sample 1 and 2) and cutting (Sample 3) to a diamond polishing company Almax easy-Lab. After re-polishing of the samples, the parallelism of the sample sidewalls were verified again with laser scanning microscope which showed the deviation was $\sim 0.01°$.

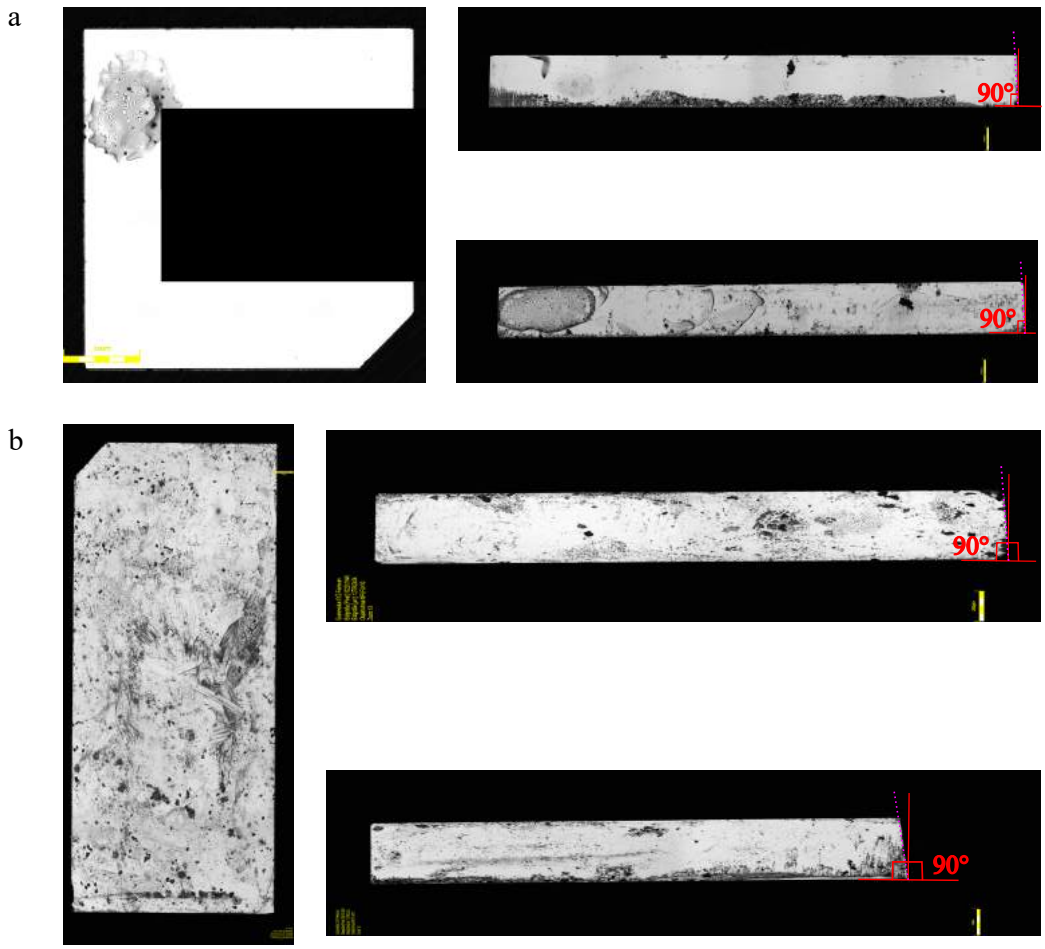

Figure 5.9: **Laser Scanning Microscope images** of the sample number 1 and 2 are shown here. From these images it is evident that all the sidewalls were not perfectly parallel with each other. To show the inclination of some of such sidewalls sold red lines and dotted purple lines are drawn in the images. Refer to text for more details.

6 Fluorescence magnetometry

Though in this presented work our main focus was to investigate the infrared absorption magnetometry we also performed fluorescence magnetometry along with it. Magnetic field sensitivity in the fluorescence magnetometry was measured for the same configurations (see section 5.2) of infrared absorption magnetometry. The results from fluorescence magnetometry give the scope to compare both the magnetometry methods. Before we performed IR absorption magnetometry, we investigated the dephasing time (T_2^*) and fluorescence ODMR contrast to characterize our magnetometers. In this chapter the results for sample characterization for magnetometry is first discussed in section 6.1. In section 6.2 we present the results obtained from high NV concentration sample for Fluorescence magnetometry and in section 6.3 the results for low NV concentration sample is presented. Finally in section 6.4 we discuss the results regarding hyperfine coupling.

In the figure 5.8 all the available samples are shown with label. Out of these four samples only sample 1, 2, and 3 were used for magnetometry experiments (figure 5.8). With sample 1, we performed magnetometry in LTDW configuration (see section 5.2 for all the mentioned configurations), whereas with sample 2 we used only DP configuration. In figure 6.1, an attempt to realize LTDW configuration (see section 5.2) with sample 3 is shown. Due to high absorption of the green laser by the sample, more than 95 % of the input optical power was absorbed within an interaction path length of ~ 5 mm (calculated with equation 5.9). Also in the figure 6.1 it can be seen that after two total internal reflections the pump laser is completely absorbed. Therefore we performed SP and DP configuration with this sample. In section 6.1 we discuss the characterizations of our magnetometers.

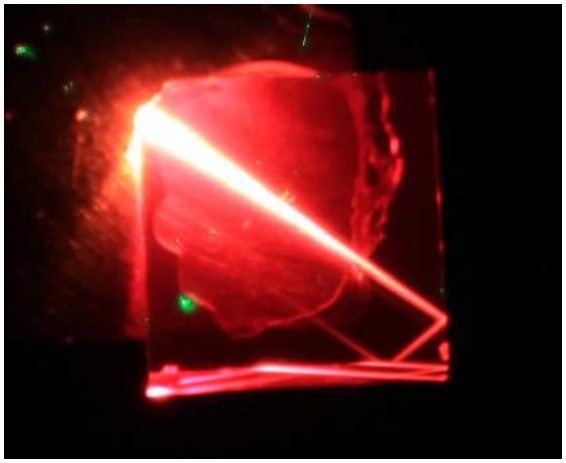

Figure 6.1: **LTDW trial with high NV concentration sample.** In this figure an attempt for LTDW configuration with sample 3 (see figure 5.8) is shown . For more details refer to the text.

6.1 Magnetometer characterization

To characterize the diamond samples we performed some series of experiments. From the theoretical simulation results (see figure 4.6), it is evident that the highest contrast for fluorescence ODMR is reach with a certain green laser power. In order to experimentally verify that, we performed set of ODMR experiments by varying green laser power when the MW power was fixed at highest level we could apply. For results of IR absorption ODMR contrast please refer to the chapter 7. Here the main discussion is related to the results obtained from fluorescence ODMR experiments. In figure 6.2 a) and b) the results for pump power saturation for fluorescence ODMR contrast is shown. Figure 6.2 a) shows the results obtained from low NV concentration sample (sample number 2 figure 6.1 a)) for DP configuration with path length of approximately 9.5 mm. For this series of experiments the green pump laser power was increased from 1 mW to 440 mW (maximum power achievable) while the MW power was fixed at 7 dBm at MW source with 45 dB amplification thereafter. It can be seen that the contrast increased with high pump power and reached the highest value at 10 mW. Increasing the pump power further resulted in decreasing the contrast. In LTDW configuration with sample 1 (figure 5.8), a similar trend with ODMR contrast was observed except that the highest contrast was at 50 mW (see figure 6.2 b)). For LTDW configuration the path length was approximately 28 mm. The results obtained with high NV concentration sample (sample 3 in

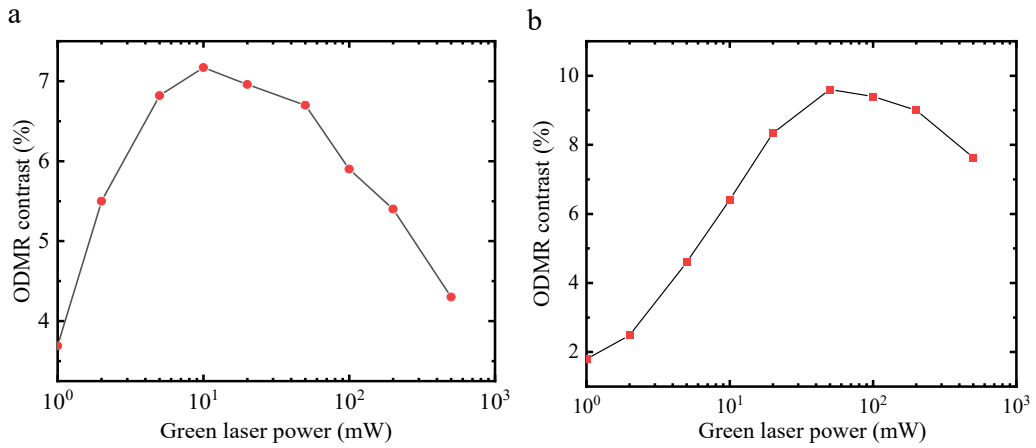

Figure 6.2: **Contrast with pump power variation for low NV concentration sample.** In figure a) it can be seen, that the fluorescence contrast was highest at 10 mW of pump power with low NV concentration sample (sample 2 in figure 5.8) in DP configuration. Figure b) shows the results obtained with low NV concentration sample (sample 1 in figure 5.8) in LTDW configuration, in this case the highest contrast is at 50 mW pump power. For both set of experiments the MW power was fixed at 7 dBm at MW source. Please refer to the text for more details.

figure 5.8) in figure 6.3 shows that the contrast was increasing with increased laser power (20 mW to 440 mW). All these experiments were done without any applied bias magnetic field.

The experimental results with low NV concentration samples (see figure 6.2) have the same trend of saturation and roll off of the ODMR contrast as seen with simulation (figure 4.6). Although the experimental results have same trend as simulation results, the ODMR contrast values at saturation points are not exactly same. It might have happened due to non-ideal photon collection efficiency. The explanation of the saturation behavior as well as the roll off of contrast value is already explained in chapter 4.1.

From the results of ODMR contrast with low and high NV concentration sample (sample 1 and 3 in figure 5.8) it can be concluded that the contrast is primarily dependent on the NV concentration in the diamond sample. In case of high NV concentration sample (sample 3 in figure 5.8, [NV] = 1.47 ppm), the ODMR contrast is $\sim$ 18 % compared to $\sim$ 10 % contrast in case of low NV concentration sample (sample 1 in figure 5.8, [NV] = 36 ppb). Another observation from the low NV concentration sample contrast values (see figure 6.2 a) and b)) is that, with increasing sensing volume, contrast can be effectively enhanced.

In DP and LTDW configurations the contrast values are approximately 7 % and 10 %. This increment happens due to the fact that, in LTDW configuration higher number of pump photon is converted to fluorescence photon as well as the required pump power to saturate the ensemble of NV in the sensing volume is increased. Compared to DP configuration in LTDW configuration the sensing volume is increased more than 100 %.

The saturation of ODMR contrast with increasing MW power was also investigated with both samples. In this series of experiments, the pump laser power was kept constant and the MW power was decreased gradually from the MW source. In figure 6.4 a) and b), the results for these experiments with high and low NV concentration samples are shown respectively. It can be seen that with increasing MW power the contrast increased and reached a saturation level at the MW power of 5 dBm (from source). All the experiments were performed without any applied bias magnetic field. With applied MW signal the NV spin population is transferred from $m_s = 0$ state to $m_s = \pm 1$ states. At one point $m_s = 0$ state becomes depopulated, or in another word this transition rate becomes higher than the relaxation rate from singlet metastable state to this state (see section 4.1). This is the point saturation of ODMR contrast with increasing MW power is observed [126].

For our magnetometry experiments we drove the MW transitions at high rates for better contrasts. At these set points, the resonance features were strongly power broadened, concealing the intrinsic linewidth as given by the transition's pure dephasing time. To access the dephasing time we additionally evaluated the resonance linewidth as function of MW power. On that account a magnetic bias field was applied and only a small sensing volume was address by choosing a short beam path. To realize that, the sample's top facet was placed perpendicular to the beam (shown in figure 8.3). For high NV concentration sample the interaction path length was 0.5 mm whereas for low NV concentration sample the path length was 2 mm (sample 3 and 1 respectively in figure 5.8). In this way we gained access to the hyperfine transitions as described in section 6.4. Series of ODMR spectrum with hyperfine coupling were obtained by varying MW power. These hyperfine coupling mainly arose from the coupling of NV electron spins with ^{14}N nuclear spins (see figure 6.5). In the limit of very small MW powers (-20 dBm to -40 dBm) the linewidth converges to a constant when reaching the dephasing time limit, which can be seen in figure 6.5 c) and d). These data points were fitted with an exponential decay func-

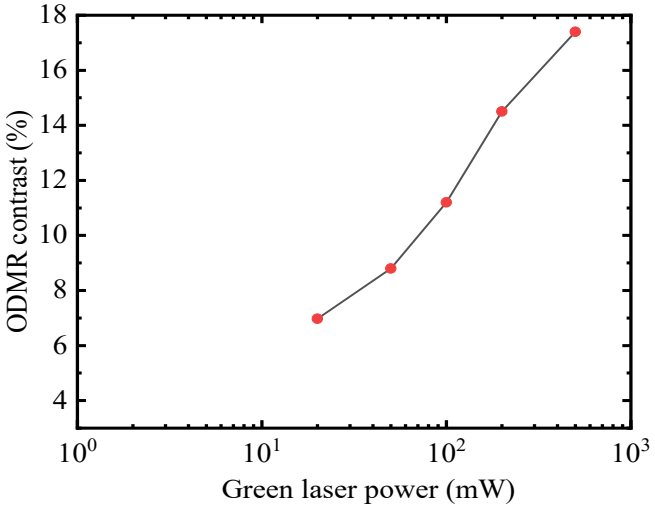

Figure 6.3: **Contrast with pump power variation for high NV concentration sample.** This figure shows the contrast variation with pump power for the high NV concentration sample (sample 3 in figure 5.8) the fluorescence contrast was highest at 500 mW. MW power was fixed at 7 dBm at MW source for each ODMR experiment.

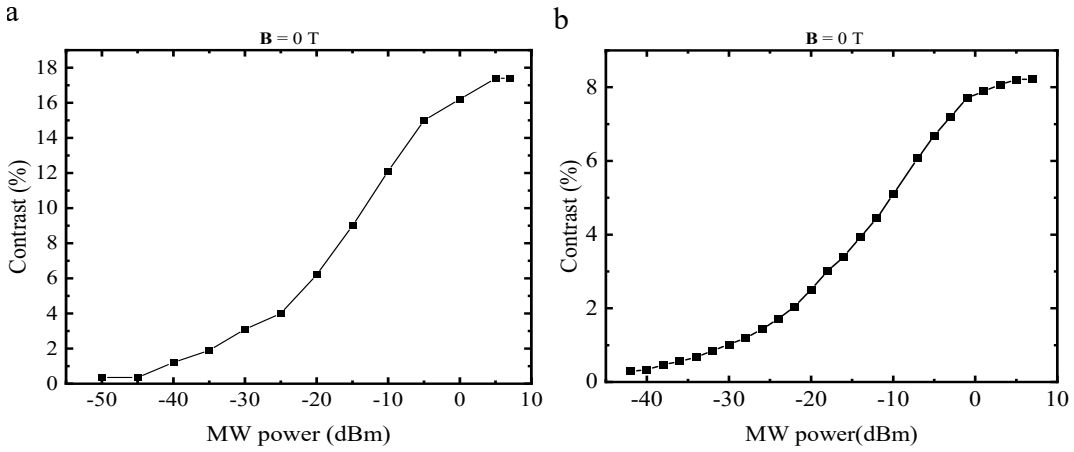

Figure 6.4: **Saturation of contrast with increasing MW power.** In figure a) the ODMR saturation with MW power for high NV concentration sample is depicted. Figure b) shows the results obtained with high low concentration sample. All the measurements were done without applied magnetic field. For more details please refer to the text.

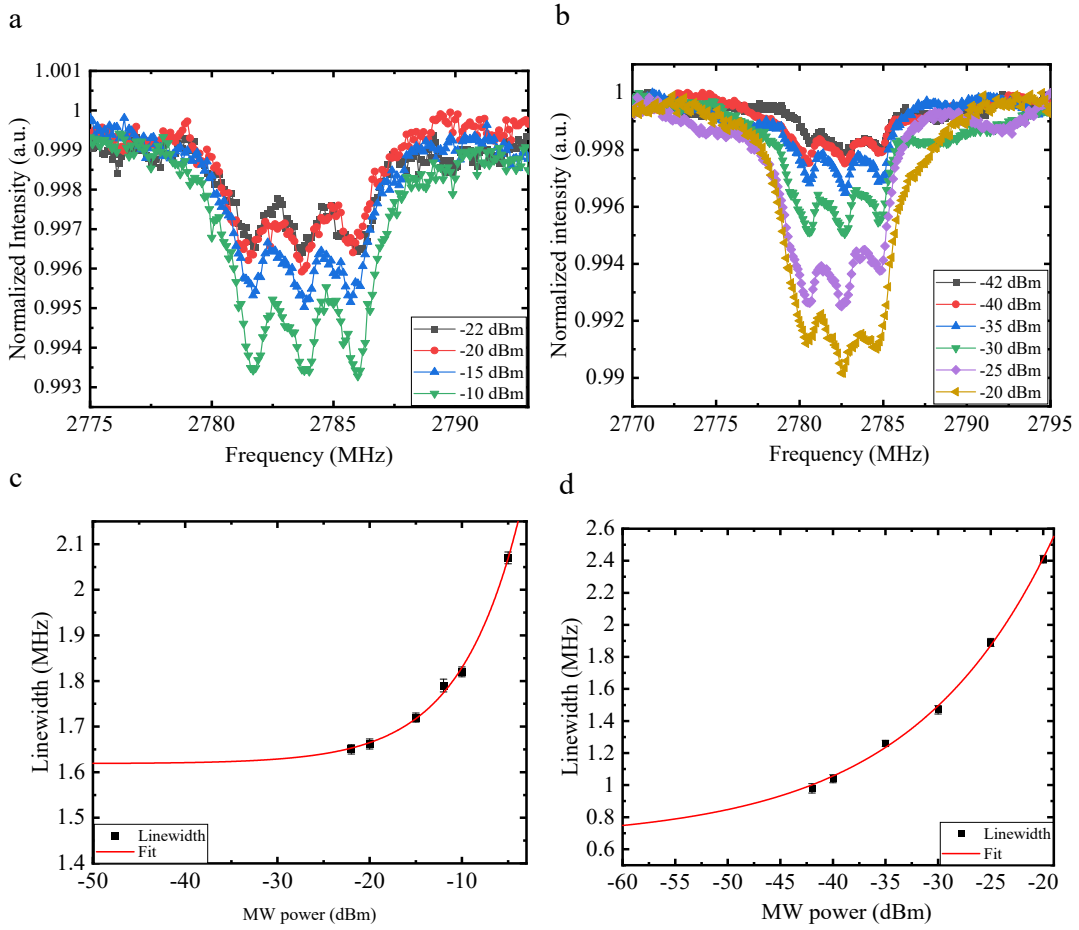

Figure 6.5: **Dephasing time measurements.** Figure a) and b) shows the ODMR spectrum with visible hyperfine coupling resonance features for high and low NV concentration samples respectively (sample 3 and 1 in figure 5.8). In figure c) and d) linewidth (FWHM) measurements at very low MW power is shown for the high and low NV concentration samples respectively. See text for details on dephasing time.

tion and the linewidth was extrapolated at almost zero MW power (see figure 6.5). The FWHM linewidth (γ) in the zero power-broadening limit is related to the pure dephasing time via the following equation $T_2^* = \frac{1}{\pi\gamma}$ [59, 126]. From the obtained linewidth at these very small MW powers the dephasing time is approximately 200 ns and 460 ns for the high NV concentration sample and for the low NV concentration samples respectively.

Taken into account the measured NV concentration ([NV]) for the samples (1.47 ppm and 36 ppb respectively) and the initial nitrogen concentrations for each sample (15 ppm and 0.15 ppm) the dephasing time can be explained. For the high NV concentration sample (sample 3 in figure 5.8) approximately 10 % substitutional nitrogen is converted to NV centers whereas for low NV concentration sample (sample 1 in figure 5.8) it is 24 %. Therefore there is a very high number of substitutional nitrogen (^{14}N atoms, experimentally verified see figure 6.5 a) and b)) present in the samples compared to NV centers. Also the samples contain 1.1 % natural ^{13}C isotopes (not verified experimentally). As discussed in section 3.1, all these spin species present in a diamond sample lead to lower dephasing time. Taken into all these factors which can diminish dephasing time. With these number probability of hyperfine coupling between the present substitutional atoms and NV centers in the diamond samples the dephasing times for each sample are in agreement with previous observations [59, 127, 164, 165, 166].

In table 6.1, a brief literature survey on the dephasing time (T_2^*) for ensemble of NV centers is presented. In the table along with the dephasing time, initial nitrogen concentration [N], NV concentration [NV], abundance of isotope ^{13}C isotope in the diamond crystal, conversion efficiency of initial nitrogen concentration to NV concentration (E_{conv}), and the T_2^* time is given. Samples with with higher E_{conv} tend to have longer dephasing time. Also the samples which are enriched with ^{12}C isotope, have longer T_2^* time. From the reported values of the dephasing times and the sample parameters, it can be concluded that all the above mentioned factors influence the dephasing time (see also equation 3.7).

Ref	[N] (ppm)	[NV] (ppm)	C isotope	$E_{conv}(\%)$	$T_2^*(\mu s)$
This work	20	1.47	nat. ab. ^{13}C	~ 7.35	~ 0.200
This work	0.15	0.036	nat. ab. ^{13}C	~ 24	~ 0.460
[59]	$\lesssim$100	10	nat. ab. ^{13}C	$\gtrsim 10$	~ 0.066
[59]	$\lesssim 1$	0.012	nat. ab. ^{13}C	$\gtrsim 1$	~ 0.291
[59]	$\lesssim 200$	0.02	nat. ab. ^{13}C	~ 0.01	~ 0.128
[127]	1	—	99.95% + ^{12}C	—	~ 10
[127]	40	—	nat. ab. ^{13}C	—	~ 0.20
[121]	16	3.8	99.97% + ^{12}C	~ 24	~ 1.12
[164]	0.75	—	99.95% + ^{12}C	$\lesssim 1$	1 - 10
[164]	10	—	nat. ab. ^{13}C	$\lesssim 1$	0.3 - 1.2
[165]	—	—	—	—	~ 0.36

Table 6.1: **Dephasing time in ensemble of NV centers in diamond.** This table summarizes dephasing time (T_2^*), initial nitrogen concentration [N], NV concentration [NV], abundance of isotope ^{13}C isotope in the diamond crystal, conversion efficiency (E_{conv}) for different samples from literature. The symbol (—) in the table means that those values were not reported in respective articles.

6.2 High NV concentration sample results

In this section the magnetometry results obtained with high NV concentration sample (sample 3 in figure 5.8) is presented. With this sample we could achieve only SP and DP configuration (see figure 5.1). LTDW configuration could not be performed due to high absorption of the green pump laser as already stated previously. The path length for DP and SP configurations were 4.8 mm and 2.5 mm approximately. Green pump laser power was set to 440 mW. The MW power was at 7 dBm at source with an 45 dB amplification from an amplifier.

6.2.1 Magnetometry with double pass configuration

In this section the results from the DP configuration are discussed. With an applied bias magnetic field to the NV ensemble fluorescence ODMR spectrum was recorded. The magnetic field was aligned to the NV axis of one (class A) out of four classes (class B, C, and D) of NV center present in the ensemble (see section 5.4). Presence of four classes of NV was confirmed with another ODMR spectrum with eight resonance feature (as shown in figure 2.6). With this alignment of the magnetic field in the ODMR spectrum the outer resonance features arising from class A sub-ensemble of NVs had a symmetric splitting

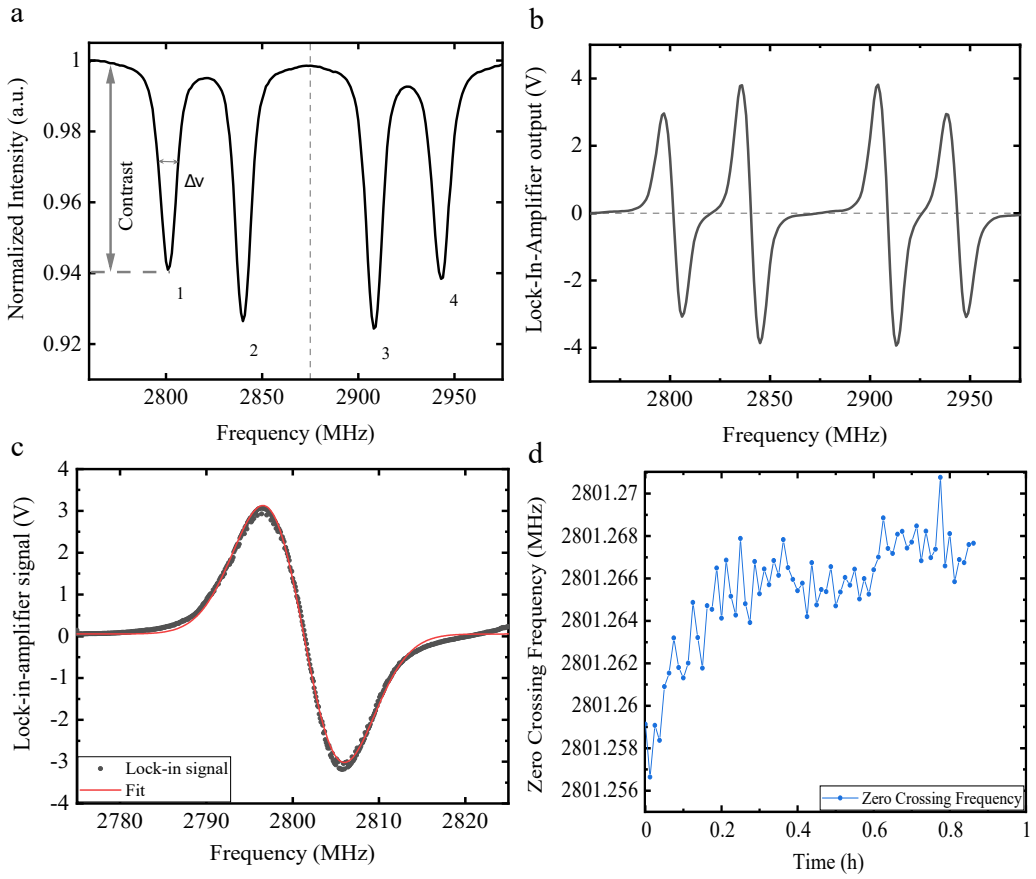

Figure 6.6: **Fluorescence magnetometry with DP configuration on high NV concentration sample.** In figure a) and b) the ODMR spectrum and the LIA response of the ODMR spectrum for DP configuration is shown respectively. Figure c) depicts the measured LIA response (black dots) of dip 1 in a) with fit (red line) to extract the slope for magnetometry, for the resonance feature with zero crossing frequency of 2801.2 MHz. Figure d) shows the drift of the zero crossing frequency due to magnetic field fluctuation over time.

with respect to the zero field splitting (ZFS) transition at 2.87 GHz, with similar contrast if not the same. The two inner dips are the cumulative resonance feature of the other three NV classes. In the figure 6.6 a), the fluorescence ODMR spectrum is shown after the magnetic field was aligned while figure b) shows the same spectrum recorded with LIA. The linewidths for the outer resonance features were 9.87 MHz (dip 1) and 9.98 MHz(dip 4), and the inner resonance features had linewidths of 10.1 MHz and 10.2 MHz for dip 3 and 4 respectively. Contrasts for the outer dips were approximately 6 % , where as the contrasts for the inner dips were approximately 7.7 % . The outer dips were the results of the Zeeman splitting of $m_s = \pm 1$ spin state of one class of NV rather than three class of NVs in case of the inner dips. Therefore the outer ODMR dips had lower contrast and linewidth compared to the inner dips.

For magnetometry measurements we used a lock-in-amplifier after the photodiode, and the microwave (MW) source was frequency modulated as described in the magnetometry with LIA scheme in section 5.1.2. As we used frequency modulation (FM) of the MW source to perform magnetometry, one crucial parameter was the frequency deviation f_{dev}, of the FM modulated microwave signal. With independent fluorescence ODMR spectrum (figure 6.6 a)), the linewidth of the resonance feature was measured on which we performed the magnetometry experiment. Our choice for this value was $f_{dev} \geq \Delta\nu$, where, $\Delta\nu$ is the linewidth of the resonance feature of interest to perform magnetometry. We chose dip 1 of figure 6.6 a) for magnetometry which had linewidth of 9.87 MHz. For this reason we chose the frequency deviation, $f_{dev} = 10$ MHz whereas modulation frequency, f_{mod} was set to 3.5 kHz.

For calibration of this resonance feature we performed ODMR around this ODMR dip for around 40 min with the LIA scheme as shown in figure 6.6 c). This data was fitted with first order derivative of a Gaussian function (equation 6.2). The Gaissian function and the derivate of the function is given in equations 6.1 and 6.2 respectively.

$$I(\nu) = I_0 + C(\nu - \nu_0)e^{-\left(\frac{\nu-\nu_0}{\Delta\nu}\right)^2}. \tag{6.1}$$

$$I'(\nu) = Ce^{-\left(\frac{\nu-\nu_0}{\Delta\nu}\right)^2} - \frac{2C}{(\Delta\nu)^2}e^{-\left(\frac{\nu-\nu_0}{\Delta\nu}\right)^2}. \tag{6.2}$$

Where $I(\nu)$ is the intensity of the ODMR spectrum, I_0 is the baseline in-

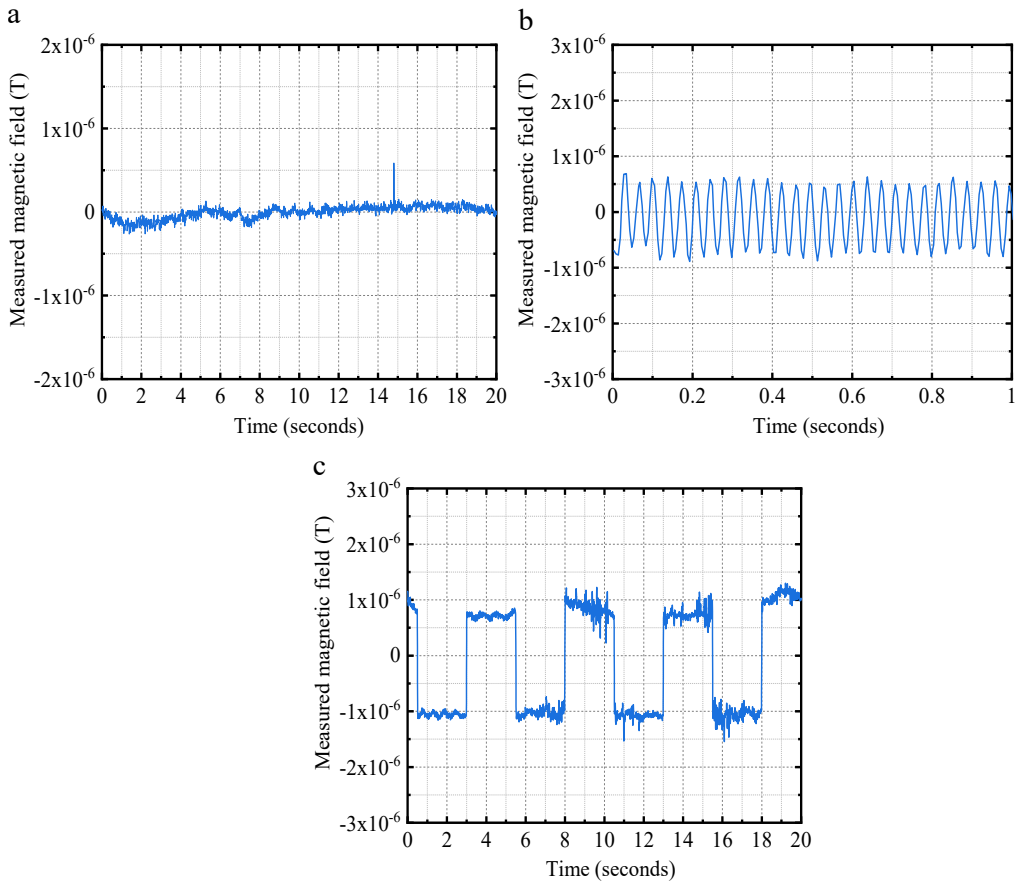

Figure 6.7: **Measured magnetic field with test coil for DP configuration with high NV concentration sample in fluorescence magnetometry.** Figure a) shows the time trace for magnetically sensitive spectrum without any applied test field. Figure b), and c) shows the time trace of the sinusoidal test fields of 28 Hz and square test field of 28 Hz respectively. For more details refer to text please.

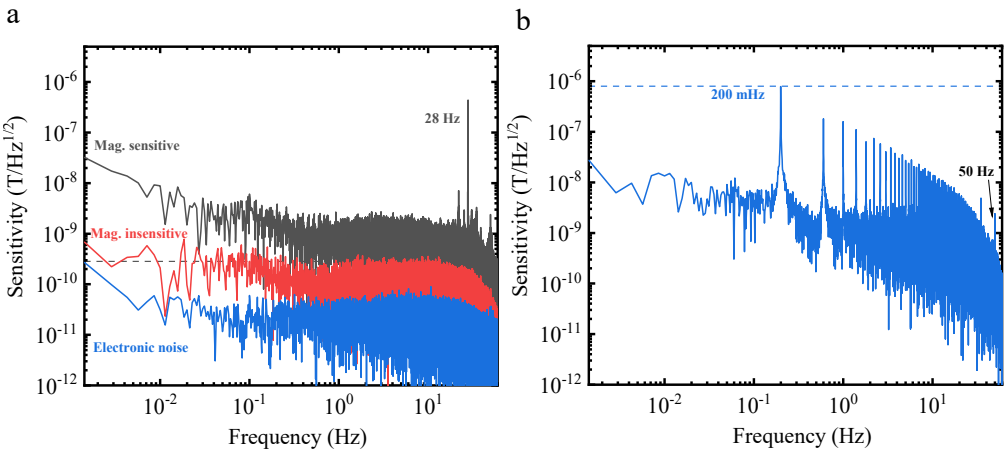

Figure 6.8: **Fluorescence sensitivity measurements for DP configuration with high NV concentration sample.** In figure a) the magnetic field noise spectrum for sensitivity measurement is shown. Here the black spectrum is the magnetically sensitive spectrum with an environment limited noise floor of 1.97 nT/$\sqrt{\text{Hz}}$ between 0.10 Hz and 40 Hz . The red spectrum is the magnetically insensitive noise spectrum with a sensitivity of 200 pT/$\sqrt{\text{Hz}}$ in between 0.001 and 40 Hz. The blue spectrum is the electronic noise which is below 30 pT/$\sqrt{\text{Hz}}$ in between 0.001 Hz to 40 Hz. Figure b) shows the magnetically sensitive spectrum for test magnetic field of 200 mHz (red spectrum) and 22 Hz (blue spectrum) . The line frequency of 50 Hz is pointed with black text and arrow.

tensity or the intensity when the MW is off resonance, C is the contrast of the resonance, ν_0 is the resonance frequency and $\Delta\nu$ is the linewidth of the resonance. Note here, the resonance frequency ν_0 in equation 6.2, is the zero crossing frequency for the LIA signal (see figure 6.6 c)).

From this calibration we determined the zero crossing frequency of signal obtained from the LIA and the slope b (see equation 6.4 and 6.5) of the resonance feature at zero crossing frequency. This slope is an important parameter for the magnetometry scheme as mentioned before, which was 1.07 V/MHz. In figure 7.5 d), a small drift of the ZCF over time can be seen. The LIA parameters were as follows; time constant 5 ms, sensitivity of the LIA was 5 mV, and output filter was set to 24 db/Octave.

Once the calibration was performed on the chosen resonance feature for magnetometry, we performed magnetometry measurements on that resonance feature. For magnetometry measurement, we used FM modulated microwave whose carrier frequency f_c was set to the zero crossing frequency of the LIA sig-

nal, which was 2801.2 MHz. The modulation frequency, f_{mod} and the frequency deviation, f_{dev} were kept same as it was used to record the ODMR spectrum, 3.5 kHz and 10 MHz respectively. In most of our experiments (fluorescence and infrared absorption magnetometry) from now onward we have used the f_{mod} and f_{dev} same as here unless otherwise stated.

With this FM modulated MW, the LIA output signal signal was recorded for a time trace of 10 min. The LIA parameters were kept same as the calibration measurement for the magnetometry resonance feature.From this recorded voltage signal the magnetic field sensitivity was calculated by the following equations [40] (also discussed in section 5.1.2):

$$B_{measured}\left(t\right) = C_{LIA} V_{LIA}\left(t\right). \tag{6.3}$$

Where $B_{measured}\left(t\right)$ is the measured magnetic field, $V\left(t\right)$ is the recorded voltage in the timetrace from the LIA output and C_{LIA} is the voltage-to-magnetic field conversion factor given by:

$$C_{LIA} = \frac{\hbar}{g_e \mu_B b}. \tag{6.4}$$

Where $\hbar$ is Planck constant, g_e is the electron g-factor, and b is the slope of dispersion lineshape at the zero-crossing. Slope is calculated in the following way:

$$b = \frac{dV_{LIA}}{df} \mid_{V_{LIA}=0}. \tag{6.5}$$

In figure 6.6 b), the calibration measurement is shown, where the black dots are the data points collected from the LIA response and the red line is the fit to extract the zero crossing frequency and the slope for magnetometry measurement.

To measure the sensitivity for this magnetometer, time trace was recorded with the LIA for 10 min and with equation 6.3 and 6.4 the voltage signal from the LIA was converted to measured magnetic field as shown in figure 6.7. By performing Fourier transform of those recorded time traces we obtained the magnetic field noise spectrum which in principle shows the sensitivity of our magnetometers. The equation for Fourier transform is given as:

$$B_{measured}(f) = \frac{1}{\sqrt{2\pi T_m}} \int_{-\infty}^{\infty} B_{measured}(t)\, e^{-i2\pi f t} dt. \tag{6.6}$$

In the above equation 6.6, T_m is the total measurement time. For Fast Fourier transform algorithm to compute the Fourier transform in Matlab, the sampling time T_s was set to 5 ms.

For testing the magnetometer, different test fields were applied with a coil magnet as described in section 5.4. In figure 6.8 a) the magnetically sensitive and insensitive spectrum is shown along with electronic shot noise of the system. In this figure the black spectrum is the magnetically sensitive spectrum recorded with a test magnetic field of 28 Hz with an environment limited noise floor of 1.97 nT/$\sqrt{\text{Hz}}$ between 0.10 Hz and 40 Hz . The red spectrum is the magnetically insensitive spectrum obtained with off resonant MW excitation or without any MW excitation. Both the cases are fundamentally same as in both cases the magnetometer is insensitive to magnetic field fluctuations. This red spectrum has a noise floor of 200 pT/$\sqrt{\text{Hz}}$ in between 0.001 and 40 Hz. The blue spectrum is the electronic noise which is below 30 pT/$\sqrt{\text{Hz}}$ in between 0.001 Hz to 40 Hz. Figure 6.8 b) shows the the magnetically sensitive spectrum with square test magnetic field of 200 mHz.

Figure 6.7 a) shows the time trace for magnetically sensitive spectrum without any applied test field. In this trace it can be seen, that there are some magnetic field fluctuations though there was no test field applied to the magnetometer. We concluded that this fluctuations might have came from some nearby laboratory instruments. In the time trace shown in figure c) for 200 mHz test field this noise is also visible sometime. From the time traces shown in the figure 6.7 b), and c) the magnetic field strength of the test fields of 28 Hz and 200 mHz can be measured which are approximately 0.8 μT and 1.0 μT respectively. The applied magnetic field strength was calculated using the following equation (see section 5.4) [40]:

$$B_{test} = \frac{\mu_0 N_{turns} I_{coil} r_{coil}^2}{2\left[z_{coil}^2 + r_{coil}^2\right]^{3/2}}. \tag{6.7}$$

The values for calculating the applied field strength were as follows; the number of turns, N = 10, radius of the coil r_{coil} = 1.0 cm, the distance from the magnetometer z_{coil} was approximately 20 cm, the coil current I_{coil} was 0.200

mA, the applied magnetic field strength was 1.12 μT. It shows that there is an error of 9 % from the applied test field strength and the measured field strength. This might have been caused by the orientation imperfection of the coil magnet. When the applied test magnetic field is not aligned with the NV axis of the sub-ensemble of NVs on which magnetometry measurements are performed there will be an error. In our experiment the test magnetic field and the applied bias magnetic field were in orthogonal planes to space constraint in the experimental setup (refer to section 5.4). Another source of error might be the distance of the test coil from the magnetometer z_{coil} .

The value for photon-shot-noise limited sensitivity is calculated by the following equation [126] (see section 3.1):

$$\eta_{CW} = P_F \frac{h}{g_e \mu_B} \frac{\Delta\nu}{C_{CW}\sqrt{R}}. \tag{6.8}$$

In the above equation C_{CW} is the contrast of the resonance, R is the photon detection rate, $\Delta\nu$ is the linewidth of the resonance, h is the Planck's constant, $g_e$is the Lande´ g-factor, $\mu_B$is the Bohr magneton, and P_F is the prefactor, which depends on the resonance lineshape. In our analysis we used Gaussian fit for fitting the resonance lineshape, therefore $P_F = \sqrt{e/8\ln 2} \approx 0.70$ (see section 3.1). In DP configuration C_{CW} is 6 %, $\Delta\nu$ is 9.87 MHz, and $R \sim 7.20\times10^{10}$ s^{-1} therefore the calculated photon-shot-noise limited sensitivity η_{CW} is 170 $pT/\sqrt{Hz}$. Note here that the experimentally obtained value for this is 200 $pT/\sqrt{Hz}$ as already mentioned.

For spin based magnetometers the fundamental sensitivity is limited by the noise intrinsic to quantum projection. For a magnetometer with N number of spins with characteristics dephasing time T_2^* the spin-projection-noise limited sensitivity η_{SPN} is given by the following equation [5, 34]:

$$\eta_{SPN} = \frac{\hbar}{g_e \mu_B} \frac{1}{\sqrt{NT_2^*}}. \tag{6.9}$$

The sample used in the above experiments has a NV concentration ([NV]) of 1.47 ppm or 2.572×10^{23} m^{-3} (in diamond 1 ppm corresponds to 1.75×10^{23} m^{-3}) without any preferential orientation. Illumination volume (V) was 0.0603×10^{-10} m^3. Magnetometry measurement was performed on one class of NV in the ensemble, therefore from the relation; ([NV] $\times$ V)$\div$4 ,the number of effective NV spins in the magnetometer was calculated. In this case this was 4.075 $\times$

10^{11}. The electron gyromagnetic ratio for NV spin is $\gamma = g_e\mu_B/\hbar = 1.76 \times 10^{11}\mathrm{s}^{-1}\mathrm{T}^{-1}$, and the measured T_2^* is 200 ns, which gives the spin-projection-noise-limited sensitivity $\eta_{SPN} \sim$ 20 fT/$\sqrt{\mathrm{Hz}}$. For the magnetometer this is the ultimate limit for sensitivity. From the experimental values for environment limited noise and photon-shot-noise limited sensitivity (1.97 pT/$\sqrt{\mathrm{Hz}}$ and 200 pT/$\sqrt{\mathrm{Hz}}$ respectively), we can see that there is still room for improvements of the achievable sensitivity for the magnetometer.

6.2.2 Magnetometry with single pass configuration

To compare the sensitivity results obtained for DP configuration with SP configuration, magnetometry experiments were performed in SP configuration as well. In SP configuration with path length of 2.5 mm the sensing volume decreased approximately two times. All the parameters for LIA and MW power were same as DP configuration. In figure 6.9 a) and b) the calibration measurements are shown. From the calibration measurements we extracted the zero crossing frequency and the slope to perform magnetometry which were 2759.8 MHz and 2 V/MHz respectively. Here we obtained an environment limited sensitivity of 2.04 nT/$\sqrt{\mathrm{Hz}}$ between 0.001 Hz and 40 Hz (see figure 6.9). For SP configuration the theoretical value of photon-shot-noise limited sensitivity (η_{CW}) is approximately 400pT/$\sqrt{\mathrm{Hz}}$ obtained with equation 6.8; with C_{CW} is 2.7 %, $\Delta\nu$ is 9.97 MHz, and $R \sim 6.60\times10^{10}$ s^{-1}. In this configuration spin-projection-noise limited sensitivity η_{SPN} is approximately 28 fT/$\sqrt{\mathrm{Hz}}$ obtained with equation 6.9. All the relevant parameters are given in table 6.2. The environment limited sensitivity in this configuration is almost same as DP configuration (1.97 nT/$\sqrt{\mathrm{Hz}}$), although some parameters are different.

From these sensitivity values it can be inferred that the measured sensitivity for DP (1.97 nT/$\sqrt{\mathrm{Hz}}$) and SP (2.04 nT/$\sqrt{\mathrm{Hz}}$) configurations can be enhanced even more as the theoretical photon-shot-noise limited sensitivity in case of DP configuration is 170 pT/$\sqrt{\mathrm{Hz}}$. Some improvement can be expected when an identical reference photodiode is used to eliminate shot noise arising from the instability of pump laser. But the main reason for the limited sensitivity is inhomogeneous magnetic field distribution over the magnetometers. We found that due to this inhomogeneous magnetic field, in our experiments hyperfine coupling was not resolved. By resolving hyperfine coupling smaller linewidth can be achieved, which in turn leads to higher LIA slope b (see result and dis-

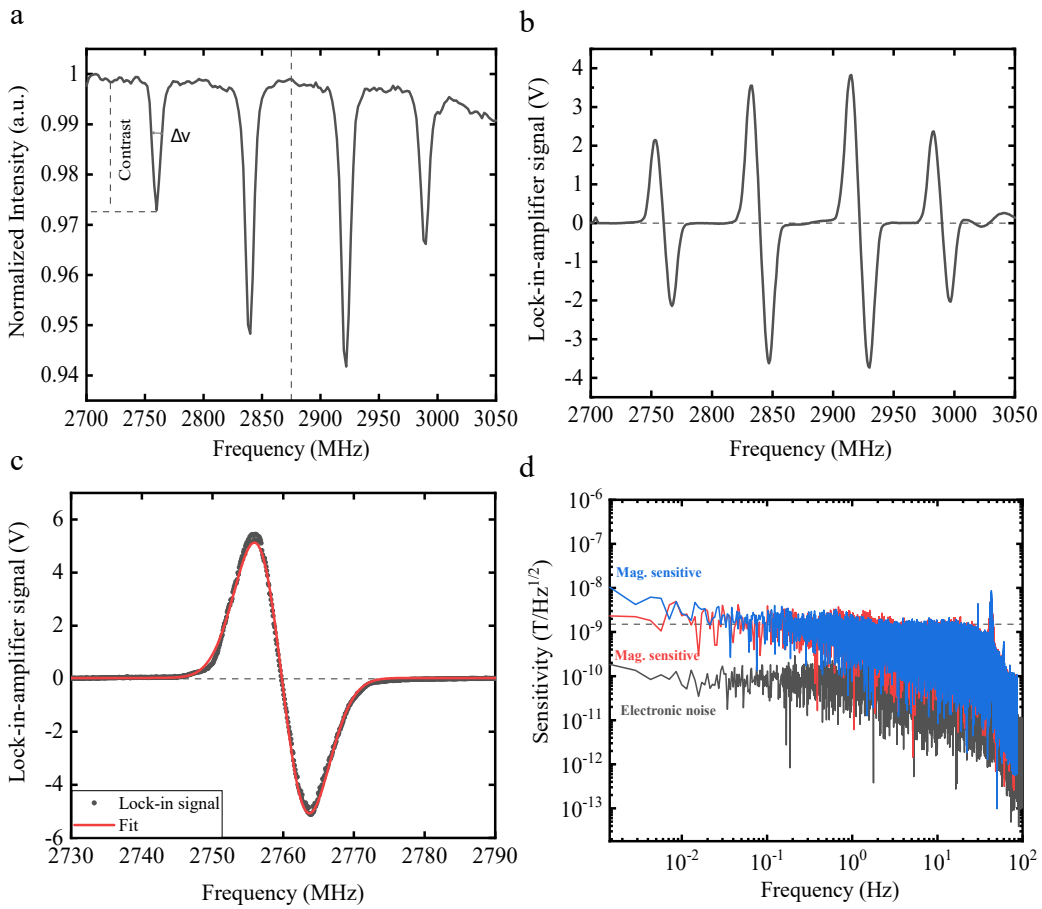

Figure 6.9: **Fluorescence sensitivity measurements for SP configuration with high NV concentration sample.** In figure a) and b) shows the ODMR spectrum and the LIA signal for the same. The calibration measurements is shown in figure c). Figure d) shows the magnetic field noise spectrum for sensitivity measurement. Here the blue spectrum is the magnetically sensitive spectrum with an environment limited noise floor of 2.04 nT/$\sqrt{\text{Hz}}$ between 0.001 Hz and 40 Hz . The magnetically insensitive spectrum is shown by red line and the electronic noise is shown with black line.

cussion in section 6.4). Apart from inhomogeneous magnetic field distribution over the diamond sample, other reasons for linewidth broadening are high laser power and MW power. All these affects the previously mentioned slope b of the resonance feature for magnetometry measurements.

6.3 Low NV concentration sample results

In this section we present the results obtained from low NV concentration samples (sample 1 and 2 in figure 5.8). As mentioned in section 6.1 for low NV concentration samples (sample 1 and 2 in figure 5.8) we performed series of ODMR measurements to identify the laser power at which the fluorescence ODMR contrast was the highest. In our experimental results we noticed that while for DP configuration with sample 2 the maximum contrast was when the laser power was ∼10 mW for LTDW configuration with sample 1 the highest contrast was at 50 mW (figure 6.2). In the DP configuration the path length of the pump laser was 9.5 mm where as in the LTDW configuration the path length was approximately 28 mm (see figure 7.10). Therefore the sensing volume increased effectively twice in the LTDW configuration.

6.3.1 Magnetometry with DP configuration

It was not possible to achieve higher interaction path length due to lack of parallelism of the side walls of the diamond sample in volume with sample 2 (see figure 6.1). On the other hand with sample 1 we achieved a path length of ∼ 28 mm (see Appendix D: Path length calculation for LTDW). From the previously mentioned fact that sensitivity increases with increasing sensing volume for a given NV concentration it was clear that higher sensitivity is achievable in LTDW configuration with sample 1. Nonetheless we performed sensitivity measurements with DP configuration to measure the sensitivity level but did not perform any experiments with test magnetic fields. Therefore unlike other results here we present only representative calibration measurement spectrum and the magnetic field noise spectrum.

In figure 6.10 a) such a calibration measurement is shown, from this measurement we extracted the zero crossing frequency to be 2752.2 MHz and the slope was 0.47 V/MHz. For magnetometry experiment the f_c was set to 2752.2 MHz along with the previously mentioned values for modulation frequency, f_{mod}

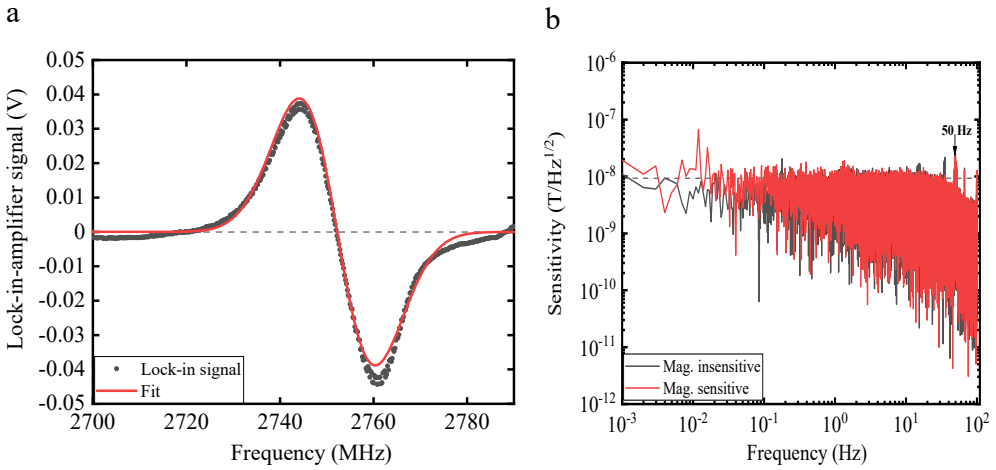

Figure 6.10: **Sensitivity measurement for DP configuration with low NV concentration sample.** In figure a), the LIA response (black dots) with fit (red line) to extract the slope for magnetometry, for the resonance feature with zero crossing frequency of 2752.2 MHz is shown. Figure b) shows the the magnetic field noise spectrum for the magnetically sensitive spectrum (red line) and magnetically insensitive spectrum (black line) of the magnetometer with an environment limited noise floor of 9.97 nT/$\sqrt{\text{Hz}}$ between 0.001 Hz and 40 Hz.

and frequency deviation, f_{dev}. As already mentioned for DP configuration we performed the sensitivity measurement with magnetically sensitive scheme and the photon shot noise limited magnetically insensitive scheme. LIA parameters were as follows; time constant 5 ms, sensitivity of the LIA was 50 μV, and output filter was set to 24 db/Octave. The sensitivity measurement revealed that the environment noise limited sensitivity for the magnetometer with DP configuration was 10 nT/$\sqrt{\text{Hz}}$. The calculated photon shot noise limited sensitivity in this case is 3 nT/$\sqrt{\text{Hz}}$(refer to table 6.3). This result is compared and discussed along with other results at the end of this chapter (see tables 6.2 and 6.3) .

6.3.2 Magnetometry with LTDW configuration

In this section the magnetometry results with LTDW configuration with low NV concentration sample (sample 1 in figure 5.8) is presented. In figure 6.11 a) the ODMR spectrum with all the resonant feature is shown while figure b) shows the same spectrum recorded with LIA. Here all the eight resonance

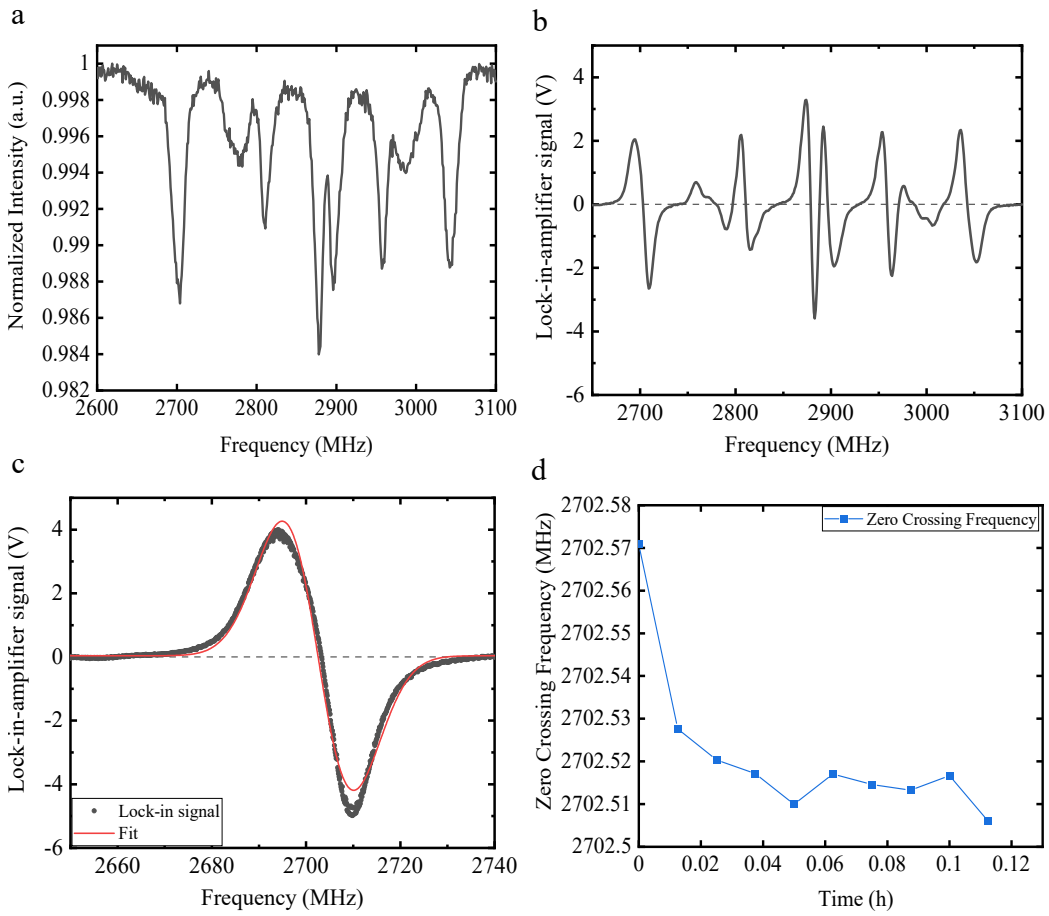

Figure 6.11: **Fluorescence magnetometry with LTDW configuration for low NV concentration sample.** In figure a) and b) the ODMR spectrum and the LIA response of the ODMR spectrum for LTDW configuration is shown respectively. Figure c) depicts the LIA response (black dots) with fit (red line) to extract the slope for magnetometry, for the resonance feature with zero crossing frequency of 2702.5 MHz. Figure d) depicts shows the deviation of the zero crossing frequency due to magnetic field fluctuation over time. Data obtained with calibration measurement over measurement time of 6 min.

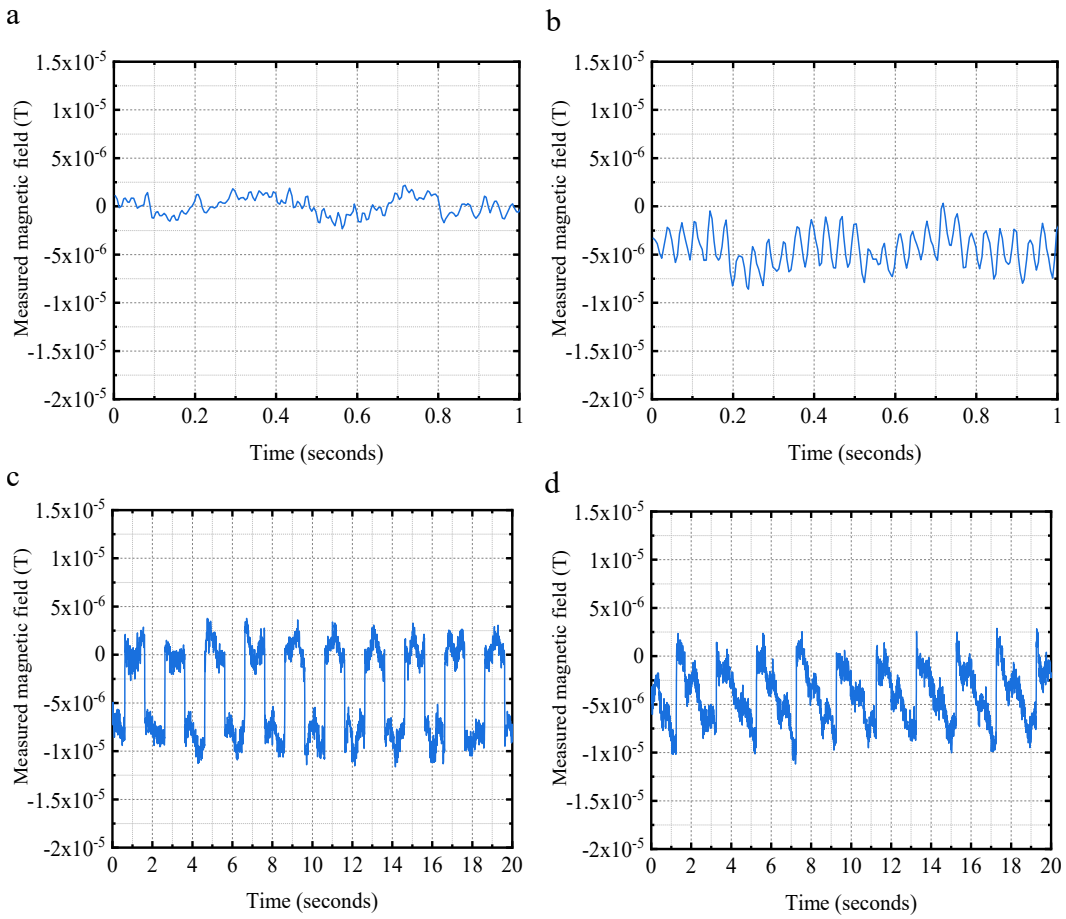

Figure 6.12: **Measured magnetic field for LTDW configuration with low NV concentration sample.** Figure a) shows the time trace for magnetically sensitive spectrum without any applied test field. In figure b) time trace for 28 Hz test field is shown. Figure shows c) and d) the time trace for 500 mHz test field for square wave and ramp wave.

features arising from the all four classes of NV can be seen. In this configuration the field alignment was not perfect due to the fact that the magnetic field was not homogeneous all over the sample. The problem of inhomogeneous magnetic field is discussed in details in section 6.4. For magnetometry purpose we chose the outermost resonance feature at 2702.5 MHz. This resonance feature has the contrast and line width of 1.4 % and 10.1 MHz respectively. After the calibration measurement with LIA scheme on this resonance feature the slope, which was 0.98 V/MHz. In figure 6.11 c) and d) the calibration measurements are shown. Modulation frequency, frequency deviation and the LIA parameters were same as DP configuration.

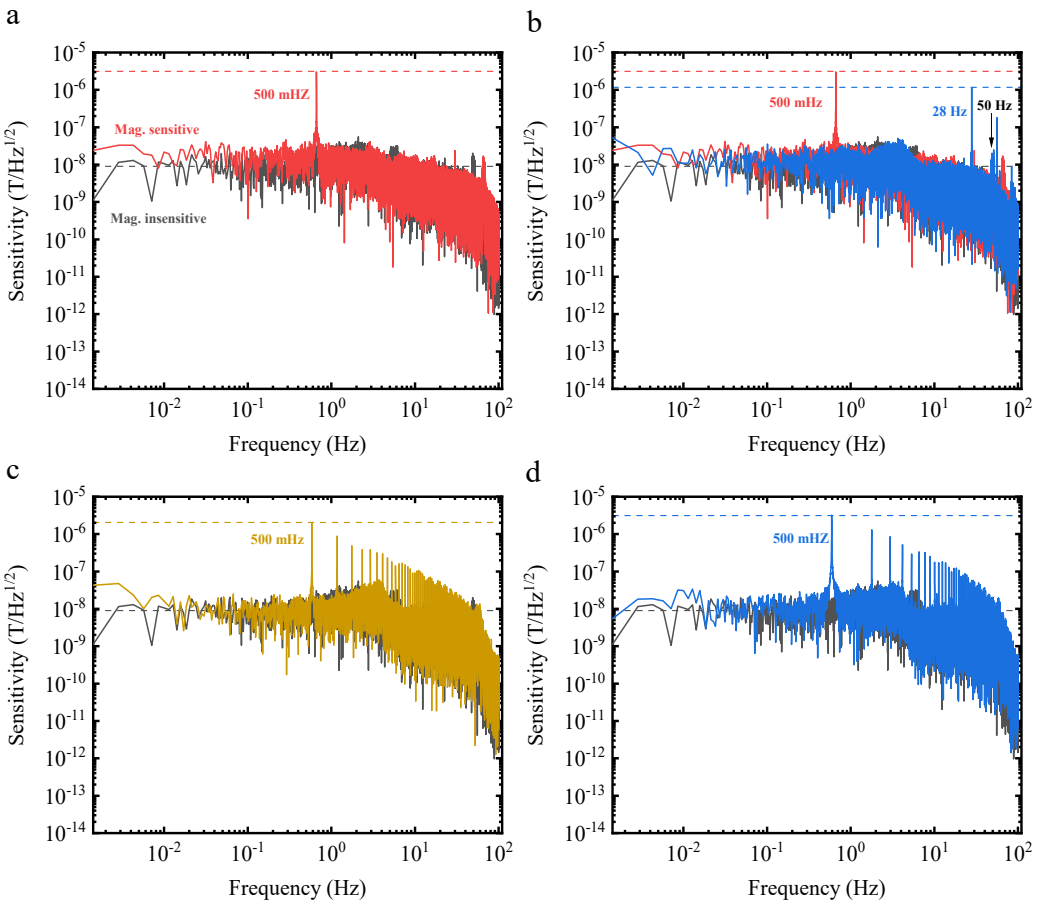

Figure 6.13: **Sensitivity measurements for LTDW configuration with low NV concentration sample in fluorescence magnetometry.** Figure a) shows the magnetically sensitive spectrum (red line) with a test magnetic field of 500 mHz and magnetically insensitive spectrum (black line) . The environment limited sensitivity was 9.97 nT/$\sqrt{\text{Hz}}$ between 0.001 Hz and 40 Hz (black dashed line). Figure b) shows magnetically sensitive spectrum for applied test field of 500 mHz and 28 Hz along with line frequency of 50 Hz. Figure c) and d) respectively shows the magnetically sensitive spectrum for applied test field of 500 mHz square wave and 500 mHz ramp wave.

Time trace was recorded with the LIA for 10 min and with equation 6.3 and 6.4 the voltage signal from the LIA was converted to measured magnetic field. In figure 6.12 a) to d) all the recorded time traces for calculating the magnetic field is shown which is then converted to magnetic field noise spectrum as described in 6.2.1. In figure 6.13 a) the magnetically sensitive (red line) and insensitive spectrum (black line) are shown. The magnetically sensitive spectrum was recorded with a test magnetic field of 500 mHz. The environment limited sensitivity was 9.97 nT/$\sqrt{\text{Hz}}$ between 0.001 Hz and 40 Hz. Figure 6.13 b) shows magnetically sensitive spectrum with applied test field of 500 mHz and 28 Hz. Figure 6.13 c) and d) respectively shows the magnetically sensitive spectrum for applied test field of 500 mHz square wave and 500 mHz ramp wave. In the corresponding noise spectrum for square and ramp wave, the higher harmonics of 500 mHz frequency can be seen.

Figure 6.12 a) shows the time trace for magnetically sensitive spectrum without any applied test field. In this trace, the same magnetic field fluctuations which is mentioned before in section 6.2.1 can be seen. In figure 6.12 c) and d) the time trace for 500 mHz test field for square wave and ramp wave have been shown. These noise is also visible in all the time traces recorded for test magnetic fields. The magnetic field strength for 28 Hz, and 500 mHz test fields are approximately 0.55 μT. The applied magnetic field strength was calculated using the before mentioned equation 6.7. With the following parameters of number of turns, N = 10, radius of the coil r_{coil} = 1.0 cm, the distance from the magnetometer was approximately 30 cm, the coil current I_{coil} was 0.200 mA, the applied magnetic field strength was 0.39 μT. It shows that there is an error of $\sim$ 9 % from the applied test field strength and the measured field strength. regarding the factors which might have contributed to this error is discussed in section 6.2.1.

For LTDW configuration the calculated value of photon-shot-noise limited sensitivity (η_{CW}) with equation 6.8 is approximately 680 pT/$\sqrt{\text{Hz}}$ compared to measured value of 9.97 nT/$\sqrt{\text{Hz}}$. The spin-projection-noise-limited sensitivity (η_{SPN}) is approximately 55 fT/$\sqrt{\text{Hz}}$ and 26 fT/$\sqrt{\text{Hz}}$ for DP and LTDW configurations respectively (obtained with equation 6.9). All the relevant parameters are given in table 6.2. As the sensing volume increased approximately two times in LTDW configuration compared to the DP configuration the spin-projection-noise-limited sensitivity is also increased approximately two times. The spin-projection-noise-limited sensitivity is the ultimate achievable sensitiv-

ity. By comparing the environment limited sensitivity and the spin-projection-noise-limited sensitivity, it can be concluded that there is still room to improve the achievable sensitivity. Different ways to improve the sensitivity of these magnetometers is discussed in chapter 8.

6.4 Magnetometry with hyperfine coupling

In this section we address the observation of hyperfine coupling of the NV spins with ^{14}N nuclear spins in the ensemble magnetometer. This has not observed in any of the configurations (i.e. SP, DP, and LTDW) for IR absorption magnetometry (see chapter 7) and the fluorescence magnetometry. Most common reasons for that is power broadening of the resonance linewidth due to high pump power and MW power and magnetic field inhomogeneity over NV ensemble magnetometer based on bulk diamonds. In our magnetometers also we initially did not observe any hyperfine coupling most probably due to high green pump laser power, which was 440 mW for all the IR absorption magnetometry measurements and fluorescence magnetometry with high NV concentration sample. Also we did not observe the hyperfine coupling for fluorescence magnetometry with low NV concentration sample, where the pump laser power was 10 mW and 55 mW for DP and LTDW configurations. In all the above mentioned experiments the MW power was set to 7 dBm from the MW source with an 45 dB amplification to realize high contrast.

To characterize the magnetometers we needed to know the dephasing time T_2^*, therefore we investigated with low green laser power and MW power. In both samples the linewidth was limited to 5.65 MHz (see figure 6.14), even at low green laser power as well as low MW power. At higher laser and MW powers the linewidth of a single resonance feature on which we have performed magnetometry measurements is in between 9 MHz to 10 MHz (for details see section 6.2 and chapter 7). This led us to conclude that there must have been hyperfine coupling arising from ^{14}N nuclear spins (three lines, each split by 2.2 MHz, see figure 2.6 c)) which were not resolved due to broadening of the resonance feature due to magnetic field inhomogeneities across the sample further broadening and masking the resonance features. As field inhomogeneities increase with the sensing volume, we here show measurements with reduced interaction length, revealing the hyperfine splitting. We reduced the sensing

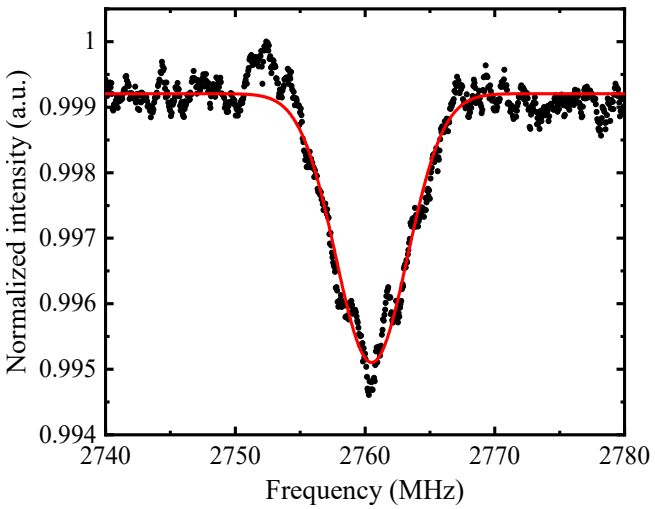

Figure 6.14: **ODMR spectrum without hyperfine features.** The ODMR spectrum is shown in this figure was obtained with sample 3 in SP configuration. MW power was set to -35 dBm from MW source and the green laser power was 20 mW. Note one thing here, for highest contrast (18 %) the MW power and laser power was set 7 dBm and 440 mW respectively.

volume by making interaction path length of green laser 0.50 mm and 2.0 mm for sample 3 and 2 respectively (see figure 8.3 in Appendix B: Sample orientation for hyperfine coupling). Figure 6.15 a) shows an ODMR spectrum at a path length of merely 0.50 mm sample 3 in figure 5.8. In the outer peaks we now observe three individual resonances stemming from hyperfine splitting, however, not fully resolved. For approximately the same bias magnetic field we were unable to detect hyperfine splitting at a path length of 2.5 mm with the same sample (see figure 6.15 b)). Due to comparative high laser power and MW power there was some linewidth broadening for the the ODMR spectrum with hyperfine coupling in figure 6.15 a), therefore except the outer resonance feature other resonance feature did not show the resonance features coming from hyperfine coupling very clearly. Once we observed the hyperfine coupling we also performed magnetometry experiments with one of the resonance feature. For proper comparison of the suspected inhomogeneous magnetic field distribution over the extension of the magnetometer, except the path length all other experimental parameters were kept the same.

Figure 6.16 a) and b) shows the ODMR spectrum with all the resonance features and the chosen resonance feature for magnetometry purpose while figure 6.16 c) and d) shows the LIA signal for figure 6.16 a) and b) respectively. For

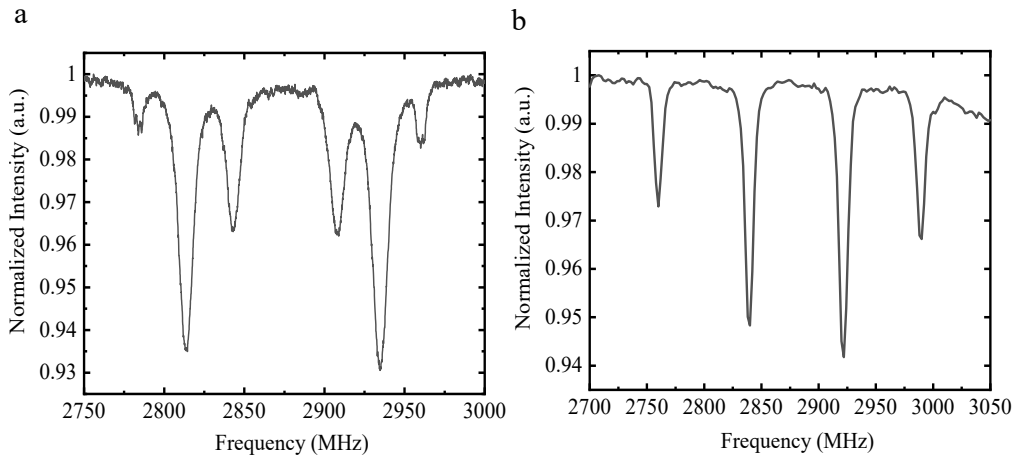

Figure 6.15: **Comparison of ODMR spectrum for Hyperfine coupling.** Figure a) shows the ODMR spectrum with hyperfine coupling of the NV spins with ^{14}N nuclear spins obtained with 0.5 mm path length. Figure b) shows the ODMR spectrum without hyperfine coupling for sample 3 (figure 5.8) in SP configuration (see figure 5.1).

magnetometry we chose the resonance feature centered around 2783.7 MHz. Note in figure 6.16 b), that here we have three resonant frequencies (2781.5 MHz, 2783.7 Mhz, and 2786 MHz), and five zero crossing frequencies from the LIA response. For magnetometry we chose the zero crossing frequency of 2783.7 MHz. The modulation frequency, f_{mod} and the frequency deviation, f_{dev} were 3.5 kHz and 1.54 MHz respectively. The LIA parameters were as follows; time constant 5 ms, sensitivity of the LIA was 20 μV, and output filter was set to 24 db/Octave.

We obtained the slope (b) from the red fit in figure 6.16 d) which is 6.4 V/MHz. In comparison to this the slope we obtained for fluorescence magnetometry in SP configuration with same sample was 2 V/MHz (without hyperfine coupling). Therefore we can see that the slope is increased 3 times when we were able to resolve the hyperfine coupling. In figure 6.17 a) the magnetic field noise spectrum for sensitivity measurement is shown, where the blue spectrum is the magnetically sensitive spectrum with an environment limited noise floor of 20 nT/$\sqrt{\text{Hz}}$ between 0.10 Hz and 40 Hz . The red spectrum is the spectrum for magnetically insensitive noise floor with a sensitivity of 10 nT/$\sqrt{\text{Hz}}$ in between 0.01 and 40 Hz. The black spectrum is the electronic noise. Figure b) shows the magnetically sensitive spectrum for test magnetic field of 100 mHz. For comparison with SP configuration results (see figure 6.9) presented before,

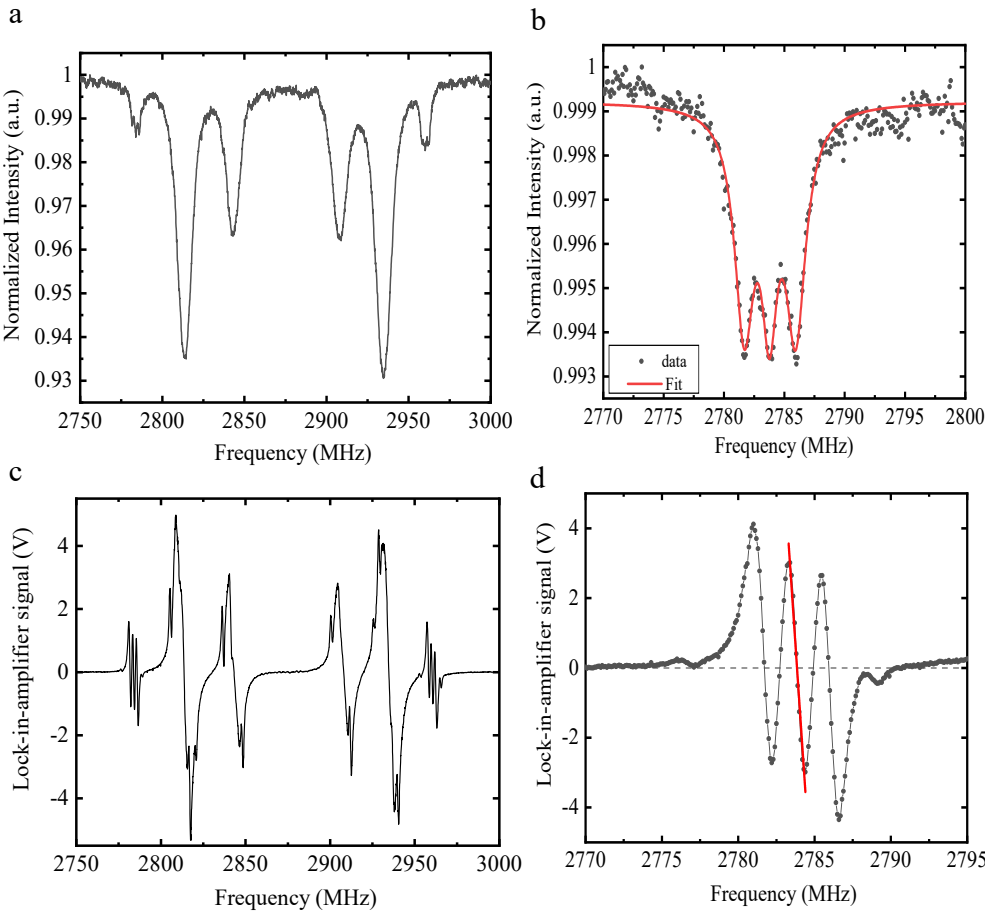

Figure 6.16: **Hyperfine coupling for high NV concentration sample.** Figure a) shows the ODMR spectrum with all the resonance features with hyperfine coupling. Figure b) shows the chosen resonance feature for magnetometry purpose centered around 2783.7 MHz with three Lorentzian fit. In figure c) LIA response of the ODMR spectrum is shown, and in figure d) LIA response of the resonance feature for magnetometry purpose centered around 2783.7 MHz is depicted. The red line in figure d) is the linear fit to extract the slope for magnetometry purpose.

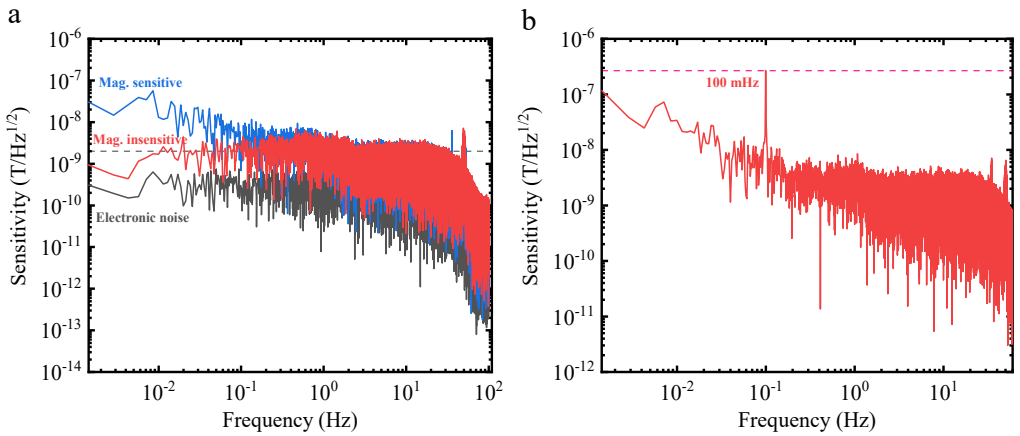

Figure 6.17: **Sensitivity measurements for Hyperfine coupling.** In figure a) the magnetic field noise spectrum for sensitivity measurement is shown. Here the blue spectrum is the magnetically sensitive spectrum with an environment limited noise floor of 20 nT/$\sqrt{\text{Hz}}$ between 0.10 Hz and 40 Hz . The red spectrum is the magnetically insensitive with a noise floor of 10 nT/$\sqrt{\text{Hz}}$ in between 0.01 and 40 Hz. The black spectrum is the electronic noise.The black dashed line depicts the photon shot noise limited sensitivity for the whole frequency range. Figure b) shows the magnetically sensitive spectrum for test magnetic field of 100 mHz (red spectrum).

we obtained an environment limited sensitivity of 2.04 nT/$\sqrt{\text{Hz}}$ between 0.10 Hz and 40 Hz for .

Figure 6.18 b), shows the time trace of the sinusoidal test fields of 100 mHz. The field strength for test field of 100 mHz can be verified with the timetrace which was 0.5 μT. The applied magnetic field strength was calculated using the before mentioned equation 6.7. It can be seen in figure 6.18 a) and b) that the time traces are very noisy. If we compare the results presented with the same sample in previous sections we see that the time trace signals do not have this much noise. Also here we increased the slope almost three times compared to SP with the same sample but the sensitivity is not enhanced three times. It can be understood from the point of statistical averaging advantage in ensemble measurements. The reason for that is, in this situation we also have reduced the sensing volume by reducing the path length almost five times (2.5 mm to 0.5 mm). Compared to the previous measurements in this case the the number of NV spin sensors is quite low (see table 6.2). Therefore the signal-to-noise ratio is worse in this case. Note in this case the spin-projection-noise-limited sensitivity (η_{SPN}) is approximately 63 fT/$\sqrt{\text{Hz}}$ compared to 28 fT/$\sqrt{\text{Hz}}$ in case

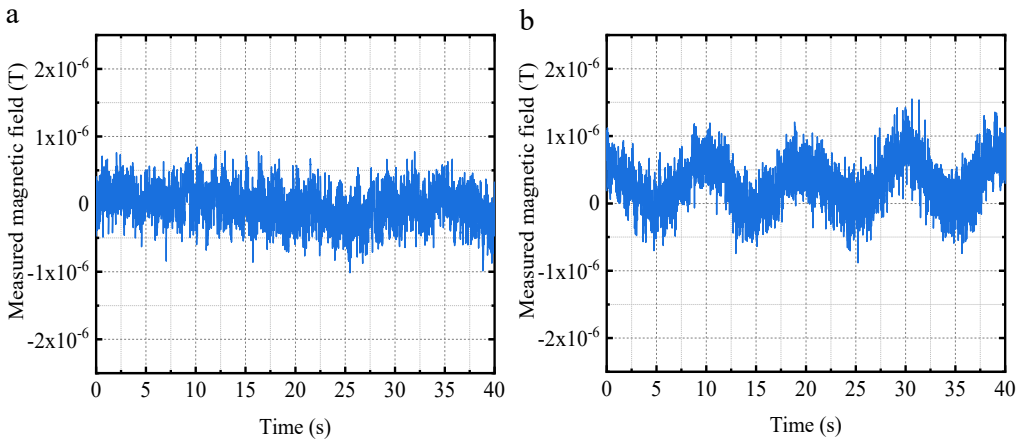

Figure 6.18: **Time traces and measured magnetic field for sensitivity measurements for hyperfine coupling.** Figure a) shows the time trace for magnetically sensitive spectrum without any applied test field. Figure b) shows the time trace of the sinusoidal test fields of 100 mHz.

of SP configuration. In an ensemble of NV by the virtue of statistical averaging over a huge number of NV spins the SNR is improved (see section 3.1). This improvement was not achieved here. The best way would be to have SP or DP configuration along with hyperfine coupling resolved ODMR spectrum. To do that a homogeneous magnetic field over the extension of the magnetometer is needed which is discussed in the section 8

Summary:

In the tables 6.2, 6.3, and 6.4 the spin-projection-noise limited sensitivity (η_{SPN}), the photon-shot-noise limited sensitivity (η_{CW}), and the environment limited sensitivity ($\eta_{environment}$) is listed along with the relevant parameters for all the magnetometers. For high NV concentration sample (sample 3 in figure 5.8) we tried to improve the sensitivity by increasing sensing volume via increasing path length. It can be seen in table 6.4 that the achieved sensitivities are almost same,whereas from table 6.3 values, it cab be inferred that the sensitivity can be improved by almost a factor of two. For low NV concentration samples (sample 1 and 2 in figure 5.8) the same trend can be seen. The achieved sensitivities therefore are limited by experimental conditions. Most important factor here was the inhomogeneous magnetic field distribution all over the magnetometer, which is discussed in details section 6.4. Apart from that another very important parameter for LIA assisted magnetometry scheme (see section 5.1.2)

Configurations	[NV] (m^{-3})	T_2^* (ns)	N_{NV}	η_{SPN} $\left(T/\sqrt{Hz}\right)$
HC DP	2.5725×10^{23}	$\sim$200	$\sim4.07\times10^{11}$	$\sim20\times10^{-15}$
HC SP	2.5725×10^{23}	$\sim$200	$\sim2.02\times10^{11}$	$\sim28\times10^{-15}$
HC Hyperfine	2.5725×10^{23}	$\sim$200	$\sim4.04\times10^{10}$	$\sim63\times10^{-15}$
LC DP	6.30×10^{21}	$\sim$460	$\sim2.38\times10^{10}$	$\sim55\times10^{-15}$
LC LTDW	6.30×10^{21}	$\sim$460	$\sim9.82\times10^{10}$	$\sim26\times10^{-15}$

Table 6.2: **Parameters and spin-projection-noise limited sensitivity.** In this table all the parameters to calculate spin-projection-noise limited sensitivity along with the spin-projection-noise limited sensitivity is given. [NV] is the NV concentration, T_2^* is the characteristics dephasing time, N_{NV} is the number of spin used in the magnetometer, and η_{SPN} is the spin-projection-noise limited sensitivity calculated via equation 6.9. HC denotes high NV concentration sample while LC stands for low NV concentration sample. DP, SP, LTDW stands for double pass, single pass and light trapping diamond waveguide configurations.

Configuration	C (%)	R (s^{-1})	$\Delta\nu$ (MHz)	η_{CW} $\left(T/\sqrt{Hz}\right)$
HC DP	6.0	$\sim7.20\times10^{10}$	9.87	$\sim 170\times10^{-12}$
HC SP	2.7	$\sim 6.60\times10^{10}$	9.97	$\sim 400\times10^{-12}$
HC Hyperfine	1.0	$\sim3.00\times10^{10}$	1.50	$\sim 220\times10^{-12}$
LC DP	1.2	$\sim3.00\times10^{10}$	10.20	$\sim 3.0\times10^{-9}$
LC LTDW	1.4	$\sim8.40\times10^{10}$	10.80	$\sim 680\times10^{-12}$

Table 6.3: **Parameters and calculated photon-shot-noise limited sensitivity for fluorescence magnetometry.** This table contains the parameters to calculate photon-shot-noise limited sensitivity for fluorescence magnetometry and the sensitivity for different sample and configurations. HC denotes high NV concentration sample while LC stands for low NV concentration sample. C, R, and $\Delta\nu$ are contrast, photon rate, and linewidth of the resonance feature respectively. DP, SP, LTDW stands for double pass, single pass and light trapping diamond waveguide configurations. Photon-shot-noise limited sensitivity $\eta_{CW}$is calculated by equation 6.8.

Configuration	C (%)	b (V/MHz)	$\Delta\nu$ (MHz)	$\eta_{environment}$ $\left(\mathrm{T}/\sqrt{\mathrm{Hz}}\right)$
HC DP	6.0	1.07	9.87	$\sim 1.97 \times 10^{-9}$
HC SP	2.7	2	9.97	$\sim 2.04 \times 10^{-9}$
HC Hyperfine	1.0	6.4	1.50	$\sim 20.0 \times 10^{-9}$
LC DP	1.2	0.47	10.20	$\sim 10.0 \times 10^{-9}$
LC LTDW	1.4	0.98	10.80	$\sim 9.97 \times 10^{-9}$

Table 6.4: **Parameters and environment limited sensitivity for fluorescence magnetometry.** In this table environment limited sensitivity for fluorescence magnetometry and experimentally verified parameters are summarized for different sample and configurations. HC denotes high NV concentration sample while LC stands for low NV concentration sample. C, b, $\Delta\nu$, and $\eta_{environment}$ are contrast, slope, linewidth of the resonance feature and environment limited sensitivity respectively. DP, SP, LTDW stands for double pass, single pass and light trapping diamond waveguide configurations.

is the slope b . The higher the slope for a given sensing volume the higher the sensitivity. This is seen with hyperfine coupling magnetometry. Due to imhomogeneous broadening of the resonance linewidth in all the cases (except HC Hyperfine, mentioned in tables 6.2, 6.3, 6.4) we were not able to increase the slope. From the values of contrast (C), slope (b), linewidth of the resonance ($\Delta\nu$), empirically it can be said that the relation of these three factor is following $b \propto \frac{C}{\Delta\nu}$. By comparing tables 6.2, and 6.4 we can conclude that the achievable sensitivity level fundamentally depends on number of NV spins in the sensing volume. Therefore to achieve higher sensitivity level it is better to use high NV concentration sample and higher interaction path length as seen with HC DP configuration ($\sim 1.97\mathrm{nT}/\sqrt{\mathrm{Hz}}$) mentioned in the tables. In LC LTDW configuration the above mentioned limiting factors limited the environment limited sensitivity ($\sim 9.97\ \mathrm{nT}/\sqrt{\mathrm{Hz}}$) to a great extent compared to photon-shot-noise limited sensitivity ($\sim 680\ \mathrm{pT}/\sqrt{\mathrm{Hz}}$). Another factor affecting the LIA slope is the contrast (C). In the high NV concentration sample (sample 3 in figure 5.8), the ODMR contrast was more than 17 % without applied magnetic field. On the other hand in the low NV concentration samples (sample 1 and 2 in figure 5.8), the ODMR contrast was around 10 % without applied magnetic field. With applied magnetic field in the HC DP and HC SP (as mentioned in the tables) configurations higher contrast was achieved compared to LC DP and LC LTDW configurations with sample 1 and 2 (in

figure 5.8). These results indicate that higher the NV concentration higher the ODMR contrast is achievable. All these parameters and results listed in the tables (tables 6.2, 6.3, and 6.4) indicate that for to achieve a magnetic field sensitivity of nT/$\sqrt{\text{Hz}}$ or sub-nT/$\sqrt{\text{Hz}}$ high NV concentration is needed along with homogeneous magnetic field all over the diamond sample.

In a previous work done by Clevenson *et al.* [69], in waveguide configuration, magnetic field sensitivity of 290 pT/$\sqrt{\text{Hz}}$ was achieved, where the number of sensing spins (N_{NV}) were in order of 10^{13}. Also in another work by Barry *et al.* [40], a magnetic field sensitivity of 15±1 pT/$\sqrt{\text{Hz}}$ was achieved with a number of sensing spins (N_{NV}) in order of 10^{17}. In a very recent work by Zhang *et al.* [167] a sensitivity of 2.86 pT/$\sqrt{\text{Hz}}$ is achieved with CW-ODMR magnetometry, where the number of sensing spin were in order of 10^{13}. In comparison to these results, number of sensing spin in our work was in the order of 10^{11} or 10^{10}. All these previous results along with our presented result point to the most important factor to achieve high sensitivity level, which is enhancing the number of sensing spins. Which is possible when we have high NV concentration ($\geq$ 1 ppm) and longer interaction path length.

7 Infrared absorption magnetometry

In this chapter the results for infrared (IR) absorption ODMR and magnetometry is discussed. To investigate the enhancement of sensitivity for ensemble NV based magnetometer with IR absorption magnetometry we primarily increased the sensing volume by increasing the interaction path length inside the diamond samples. Magnetometry experiments were performed with the same samples as mentioned in chapter 6. In section 7.1 we first discuss the IR absorption ODMR results for high NV concentration sample (sample 3 in figure 5.8) and compare them with the theoretical values obtained with our Gaussian beam optimized NV rate equation model (see chapter 4). After that we discuss the magnetometry results for the same sample for different configurations. In section 7.2 we discuss the result obtained from low NV concentration samples (sample 1 and 2 in figure 5.8) in same manner.

7.1 High NV concentration sample results

7.1.1 Infrared absorption ODMR

In the following sections we discuss the results from a high NV concentration sample (sample number 3 in figure 5.8). Here the NV concentration is measured to be 1.47 ppm, and the dimension of the sample is 2.5 mm $\times$ 2.5 mm. For further details of the sample see the sample preparation section in section 5.5. To increase the sensor number the most feasible way is to increase the path length of the laser beams inside the diamond samples and to do so we first tried to achieve LTDW configuration (see section 5.1) for our sample . Due to high absorption of the green pump laser (λ @ 532 nm) it was not possible to achieve the LTDW configuration, where a fraction of the diamond sample volume could be covered by the lasers due to multiple total internal reflections of the laser

beams on the diamond sidewalls as shown in figure in section 5.1. In the figure 6.1, the trial for LTDW configuration with sample 3 is shown. Here it can be noted that the pump laser with an optical power of approximately 440 mW was used to test the LTDW configuration for infrared absorption magnetometry. Only two total internal reflections on the diamond sidewalls happened and the pump laser got completely absorbed within an effective path length of approximately 5 mm. This path length is not significantly longer than the path length achieved in DP configuration (4.8 mm).

For this reason, the configuration used for infrared absorption magnetometry for this sample was single pass (SP) and double pass (DP) as shown in figure 5.1. The respective antenna shapes and positions are also shown in figure 5.5. As discussed in section 5.1, first the sample was characterized with fluorescence ODMR measurements (see section 6.1) and after that all the measurements with infrared absorption magnetometry were performed. In a set of preliminary measurements for the infrared absorption magnetometry, we performed IR absorption ODMR without bias magnetic field or LIA scheme (see section 5.1.2) to compare the contrast with the theoretical value obtained from the rate equation model for NV as discussed in chapter 4. In figure 7.1, the experimental results for SP and DP configuration, corresponding to 2.5 mm and 4.8 mm path length respectively are shown. Figure 7.1 a) and c) show the respective theoretical estimations. In black and red the residual optical IR power along the interaction path without and with MW signal are plotted. The contrast is taken at the end of the interaction path. For the simulation we used experimentally available parameters, i.e. green pump power and IR laser power is taken as 440 mW and 10 mW respectively. Beam waist for the lasers are approximately 20 μm (see also 8), and NV concentration is 1.47 ppm (refer to section 5.5 for more details). For microwave drive, the power from microwave source is set to 7 dBm with a 45 dB amplification with an amplifier.

In the figure 7.1 b) and d) the experimental result for DP and SP configurations are shown respectively. In SP configuration all the parameters for theoretical calculation and experiment are same as DP configuration except the path length. In the theoretical estimation a contrast value of $\sim 0.158\%$ is seen, whereas the experimental value is $\sim 0.160\%$, being in excellent agreement with the predicted contrast value. The theoretical and experimental values for the IR absorption ODMR contrast in case of SP configuration are 0.143% and 0.100% respectively. In this case also the values are of same order, though not

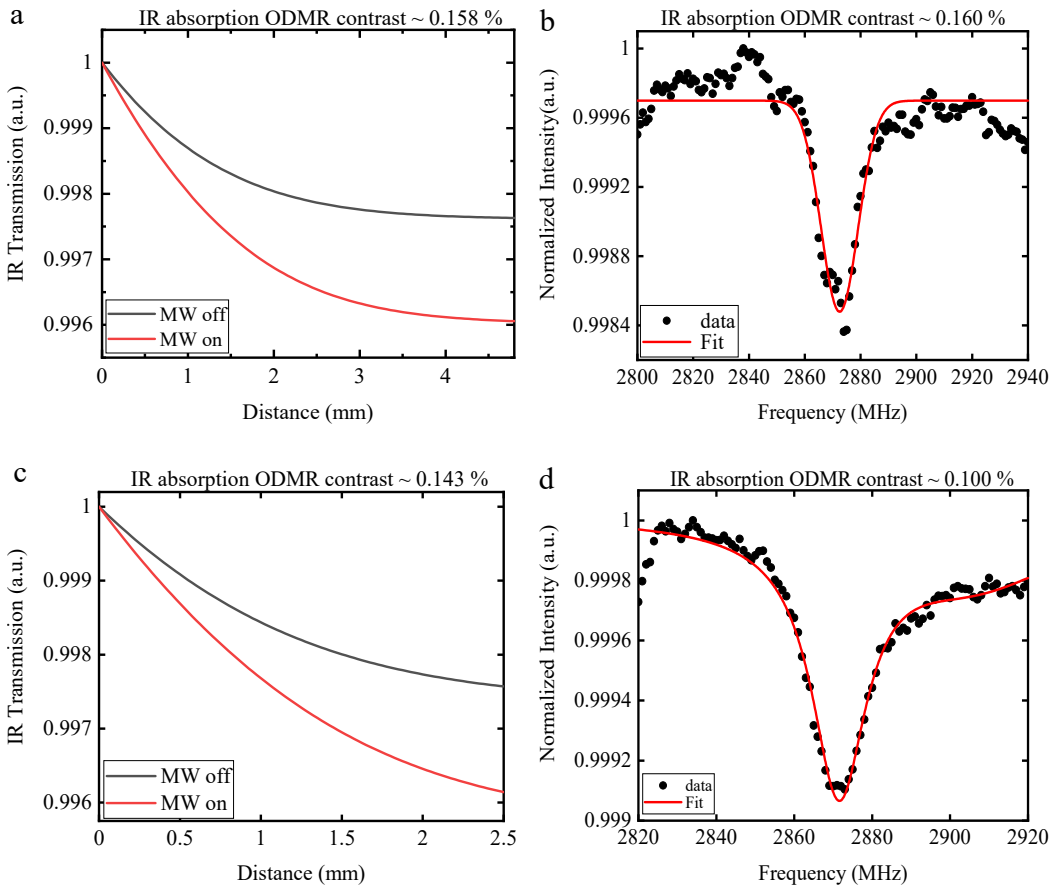

Figure 7.1: **IR ODMR for high NV concentration sample.** a) This graph shows the theoretical value for contrast of IR absorption ODMR in DP configuration. Figure b) shows the measured IR absorption ODMR for DP configuration along with a fit (red line). In figure c) the graph shows the theoretical value for contrast of IR absorption ODMR in SP configuration. d) This is the measured IR absorption ODMR for SP configuration. All the experiments were done without any bias magnetic field applied to the NV ensemble therefore ODMR dips are centered around 2870 MHz. For more details refer to text in this section as well as in chapter 4.

matching extremely precisely. As the predicted theoretical contrast value is already quite low, we performed the experiments over a long time ($\sim$ 30 min) to achieve a good signal-to-noise ratio for the ODMR spectrum. In the ODMR spectrum of 7.1 b) and d) the ODMR resonance features are around 2870 MHz, which is the value for zero field splitting (ZFS) without any bias magnetic field. The difference in the SP theoretical and experimental values is not completely understood. This mismatch might be due to inclined baseline in figure 7.1 d) which was taken into account while the ODMR spectrum was fitted. Both the obtained ODMR spectrum in figure 7.1 c) and d) is fitted with Gaussian fit function as described in section 6.2.

7.1.2 Magnetometry with single pass configuration

In the previous section in figure 7.1 c) and d) it is shown that the theoretical and experimental values of IR absorption ODMR contrast in SP and DP configurations are in the same order of magnitude. Although the experimental values of contrast are very similar we first performed magnetometry with SP configuration and then with DP configuration to see the effect of increasing sensing volume on sensitivity measurements. Here we present the results for the SP configuration. For magnetometry with IR absorption scheme, we used the already explained lock-in-amplifier scheme (see section 5.1.2). After the primary investigation of the IR absorption contrast a bias magnetic field was applied to the NV ensemble and a lock-in-amplifier was used after the photodiode. Also the microwave (MW) source was frequency modulated. As a lock-in-amplifier was used after the photodiode, the obtained ODMR spectrum was first order derivative of the resonance features as shown in figure 7.2. As we used frequency modulation (FM) of the MW source to perform magnetometry with lock-in-amplifier, one crucial parameter was the frequency deviation f_{dev}, of the FM modulated microwave signal. With independent fluorescence ODMR spectrum, we determined the linewidth of the resonance feature on which we performed the magnetometry experiments (see section 6.2). Our choice for this value was $f_{dev} \geq \Delta\nu$, where, $\Delta\nu$ is the linewidth of the resonance feature. For the ODMR spectrum shown in figure 7.2, the modulation frequency, f_{mod} used was 3.5 kHz; frequency deviation, f_{dev} was 10 MHz. The green and infrared laser powers and the MW power used in these experiments are same as mentioned in section 7.1.1.

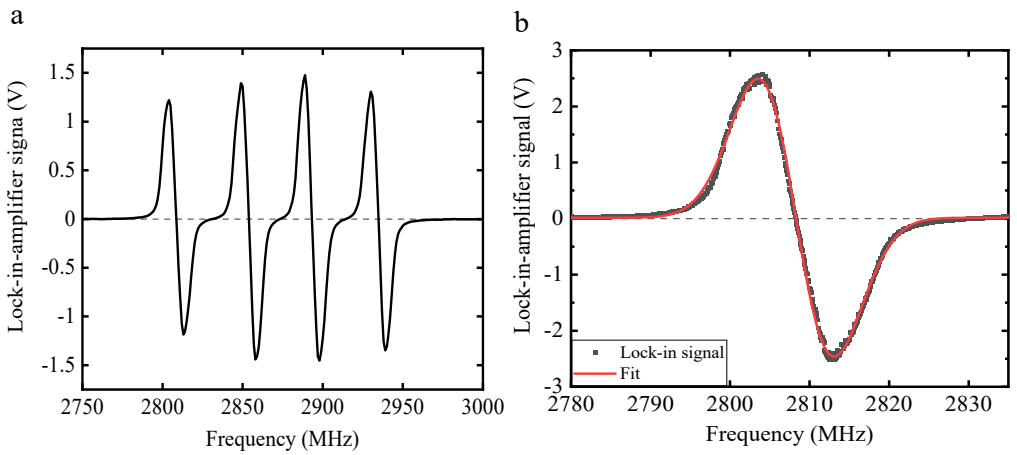

Figure 7.2: **Magnetic field alignment and calibration for SP configuration with high NV concentration sample in IR absorption magnetometry.** In figure a) all the resonance features are shown from the obtained ODMR spectrum after magnetic field alignment. Figure b) depicts the calibration measurement from which we extracted the zero crossing frequency and the slope for magnetometry measurements. Details regarding the slope and zero crossing frequency is given in the text.

The chosen resonance feature for magnetometry measurement was the resonance feature with zero crossing frequency of 2808.3 MHz as shown in the figure 7.2 b). From the calibration of the resonance feature on which we performed magnetometry experiment for the SP configuration we determined the zero crossing frequency as 2808.3 MHz. The slope for the lock-in signal was 0.85 V/MHz. The LIA parameters used were as follows; time constant 5 ms, sensitivity of the LIA was 5 mV, and output filter was set to 24 db/Octave. After calibration we performed magnetometry measurements on that resonance feature. For magnetometry measurement, we used FM modulated microwave whose carrier frequency f_c was 2808.3 MHz with the same modulation frequency and frequency deviation parameters used to calibrate the resonance feature. To extract the sensitivity, time trace was recorded with the LIA for 10 min and with equations 6.3 and 6.4 LIA voltage was converted to measured magnetic field. The time traces for the measured magnetic fields are shown in figure 7.3 a) to d).

In the figure 7.4 a), the magnetic field noise spectrum for sensitivity measurement is shown, where the black spectrum is the magnetically sensitive spectrum with an environment limited noise floor of 1.2 nT/$\sqrt{\text{Hz}}$ between 0.1 Hz and 40

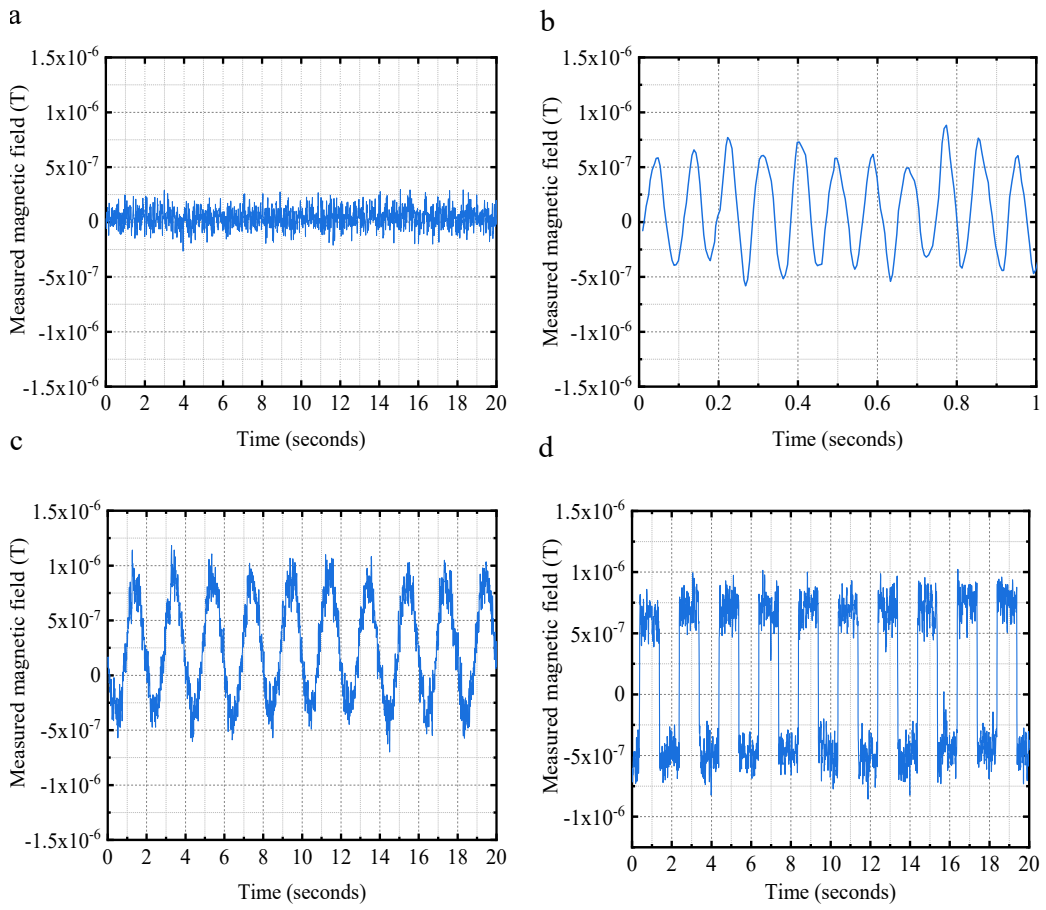

Figure 7.3: **Measured magnetic field with test coil for SP configuration for high NV concentration sample in IR absorption magnetometry.** Figure a) shows the time trace for magnetically sensitive spectrum without any applied test field. Figure b), c), and d) shows the time traces for sinusoidal test fields of 11 Hz and 500 mHz and a square test field of 500 mHz respectively. Discussion regarding the magnetic field strength measurement is given in the text in details.

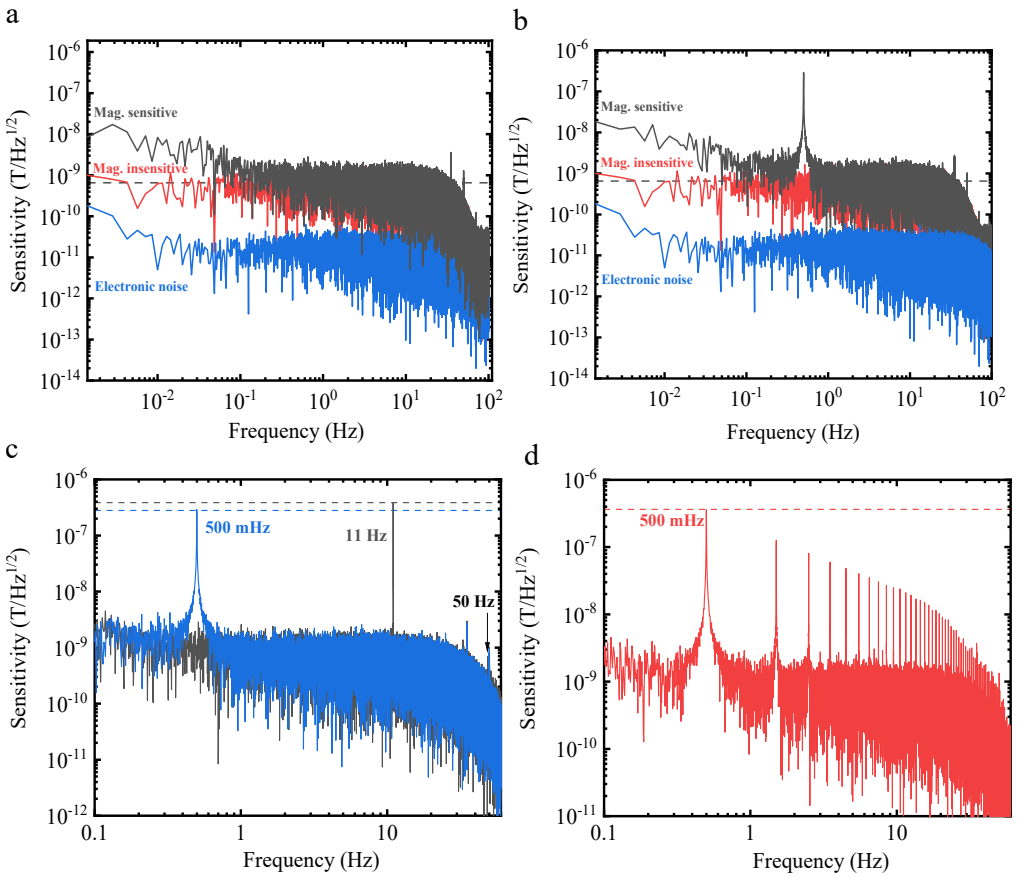

Figure 7.4: **Sensitivity Measurement spectrum for SP configuration with high NV concentration sample in IR absorption magnetometry.** Figure a) shows the magnetically sensitive spectrum (black) with an environment limited noise floor of 1.2 nT/$\sqrt{\text{Hz}}$ between 0.1 Hz and 40 Hz along with magnetically insensitive spectrum with noise floor of 700 pT/$\sqrt{\text{Hz}}$ in between 0.001 and 40 Hz and electronic noise spectrum (blue), with noise floor mostly below 100 pT/$\sqrt{\text{Hz}}$ over the frequency range. Figure b), and c) shows all the magnetically sensitive spectrum for with applied sinusoidal test fields of 500 mHz and 11 Hz respectively. In figure d) the spectrum for a square test field of 500 mHz is shown.

Hz . The red spectrum in that figure is the magnetically insensitive spectrum or photon shot noise limited sensitivity, obtained with off resonant MW excitation. Which is 700 pT/$\sqrt{\text{Hz}}$ in between 0.001 and 40 Hz. The blue spectrum is the electronic noise, which was obtained by blocking the lasers from photodiode and the noise level is mostly below 100 pT/$\sqrt{\text{Hz}}$ over the frequency range of 0.001 and 40 Hz.

The magnetometer with SP configuration was tested by applying test magnetic fields with the same coil magnet which was used to test the magnetometer in DP configuration. Figure 7.4 b), c), shows all the magnetically sensitive spectrum for with applied sinusoidal test fields of 500 mHz and 11 Hz respectively along with the line frequency of 50 Hz. In figure 7.4 d) shows the spectrum for a square test field of 500 mHz, here the higher harmonics of the 500 mHz frequency can be seen in the spectrum.

From the time traces shown in the figure 7.3 b), c), and d) the magnetic field strength of the test magnetic fields can be measured. Figure 7.3 a) shows the time trace for magnetically sensitive spectrum without any applied test field. Figure b), c), and d) shows the time traces for sinusoidal test fields of 11 Hz and 500 mHz and a square test field of 500 mHz respectively. The magnetic field strength detected for 11 Hz and 500 mHz test fields are approximately 0.57 μT and 1.0 μT respectively. For the 500 mHz square test field the measured field strength is approximately 0.7 μT. The applied magnetic field strength was calculated using the before mentioned equation 6.7 taken into account the number of turns, N = 10, radius of the coil r_{coil} = 1.0 cm, the distance from the magnetometer was approximately 30 cm, the coil current I_{coil} was 0.200 mA, the applied magnetic field strength was 0.39 μT. It shows that there is an error of 30 % from the applied test field strength and the measured field strength. The reasons for this error in the measurements is discussed already in the previous sections.

7.1.3 Magnetometry with double pass configuration

In this section the results from the DP configuration are discussed. The green and infrared laser powers and the MW power used in these experiments are same as mentioned in section 7.1.1. For the LIA scheme to obtain the ODMR spectrum shown in figure 7.5 a), the modulation frequency, f_{mod} and the frequency deviation, f_{dev} were used same as mentioned in SP configuration.

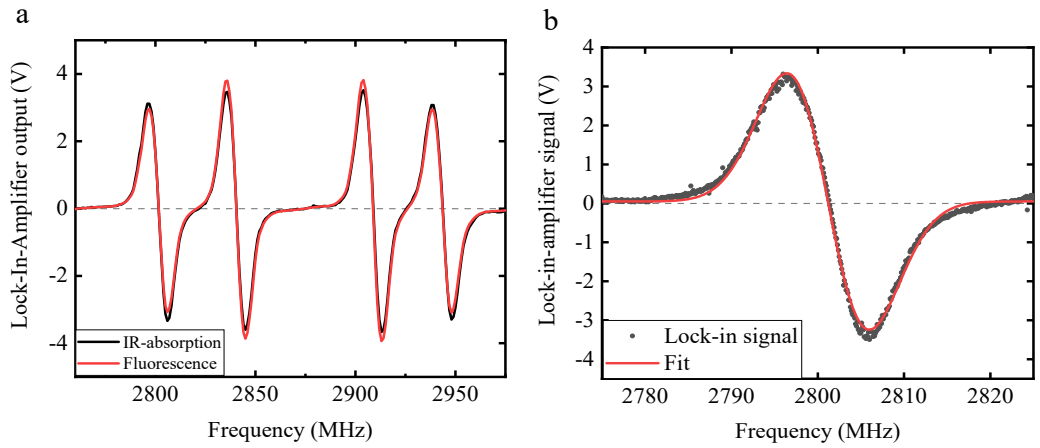

Figure 7.5: **Magnetic field alignment and calibration for high NV concentration sample in DP configuration in IR absorption magnetometry.** In figure a) the fluorescence and IR absorption ODMR spectrum shows four resonance features after the magnetic field was aligned. In figure b) the calibration measurement for the magnetometry with the chosen resonance feature is shown. The zero crossing frequency in this spectrum is 2801.2 MHz.

In the figure 7.5 a), the ODMR spectrum of infrared absorption and fluorescence are shown after the magnetic field was aligned. We chose the left most resonance feature in the figure 7.5 a) for magnetometry measurements. For calibration of this resonance feature we performed ODMR around this ODMR dip for around 40 min with the LIA scheme as shown in figure 7.5 b). From this calibration we determined the zero crossing frequency of signal obtained from the lock-in-amplifier (LIA) and the slope of the resonance feature at zero crossing frequency which was 2801.2 MHz. The slope of the magnetometry resonance feature was 1.2 V/MHz. For magnetometry measurement, carrier frequency f_c was the zero crossing frequency of the LIA signal. As mentioned before the modulation frequency, f_{mod} and the frequency deviation, f_{dev} were same as calibration measurement. For the LIA scheme the LIA parameters were as follows; time constant 5 ms, sensitivity of the LIA was 5 mV, and output filter was set to 24 db/Octave. At this point, note that the LIA parameters for SP configuration was kept same as DP configuration. It was done on purpose to compare the real difference in sensitivity for SP and DP configuration. As a matter of fact all the electrical parameters were kept same for these experiments along with the LIA parameters, such as gain of the photodiode and termination. If we compare the sensitivity spectrum for electronic noise for DP

(figure 7.7) and SP configuration 7.4 it can be noted that those are having the same noise floor.

As the magnetometry method is described in section 6.2, we took time traces while the magnetometer is magnetically sensitive without any test magnetic field and with different test magnetic fields. The LIA voltage signal is converted to measured magnetic field with equation 6.3 and 6.4. The time traces for all the test magnetic fields and the time trace for magnetically sensitive spectrum without any applied test magnetic field are shown in figure 7.6. Figure 7.6 a) shows the time trace for magnetically sensitive spectrum without any applied test field. Figure b), c), and d) shows the time traces for sinusoidal test fields of 11 Hz and 200 mHz and a square test field of 500 mHz respectively.

In the figure 7.7 a), the magnetic field noise spectrum for sensitivity measurement is shown, where the black spectrum is the magnetically sensitive spectrum with an environment limited noise floor of 700 pT/$\sqrt{\text{Hz}}$ between 10 and 40 Hz. The red spectrum is the magnetically insensitive spectrum obtained with off resonant MW excitation or without any MW excitation. This red spectrum is the magnetically insensitive spectrum of the magnetometer with a noise floor of 350 pT/$\sqrt{\text{Hz}}$ in between 0.001 and 40 Hz. The blue spectrum is the electronic noise, which was obtained by blocking the lasers from photodiode. In the frequency regime lower than 10 Hz, it can be noted that the magnetically sensitivity spectrum is showing higher magnetic field, which is not present in the magnetically insensitive spectrum. Therefore it might have caused due to environment induced slowly varying magnetic field, though the source could not be detected. Figure 7.7 b) and c) shows all the magnetic field noise spectrum for magnetically sensitive with applied sinusoidal test fields of 11 Hz and 200 mHz along with the magnetically insensitive and electronic noise spectrum. In figure c) the line frequency of 50 Hz can be seen distinctively along with the test frequencies. In figure d) spectrum for a square test field of 500 mHz is shown, here the higher harmonics of the 500 mHz frequency can be observed.

The measured test field strength by the magnetometer can be seen from figure 7.6 a) to d). For 200 mHz and 500 mHz test fields the measured field strength is approximately 1 μT and for the 11 Hz test field it is 0.8 μT . Taken into account the number of turns, N = 10, radius of the coil r_{coil} = 1.0 cm, the distance from the magnetometer was approximately 20 cm, the coil current I_{coil} was 0.200 mA, the applied magnetic field strength was 1.12 μT. Test field strength is calculated by using equation 6.7. The measured and calculated test

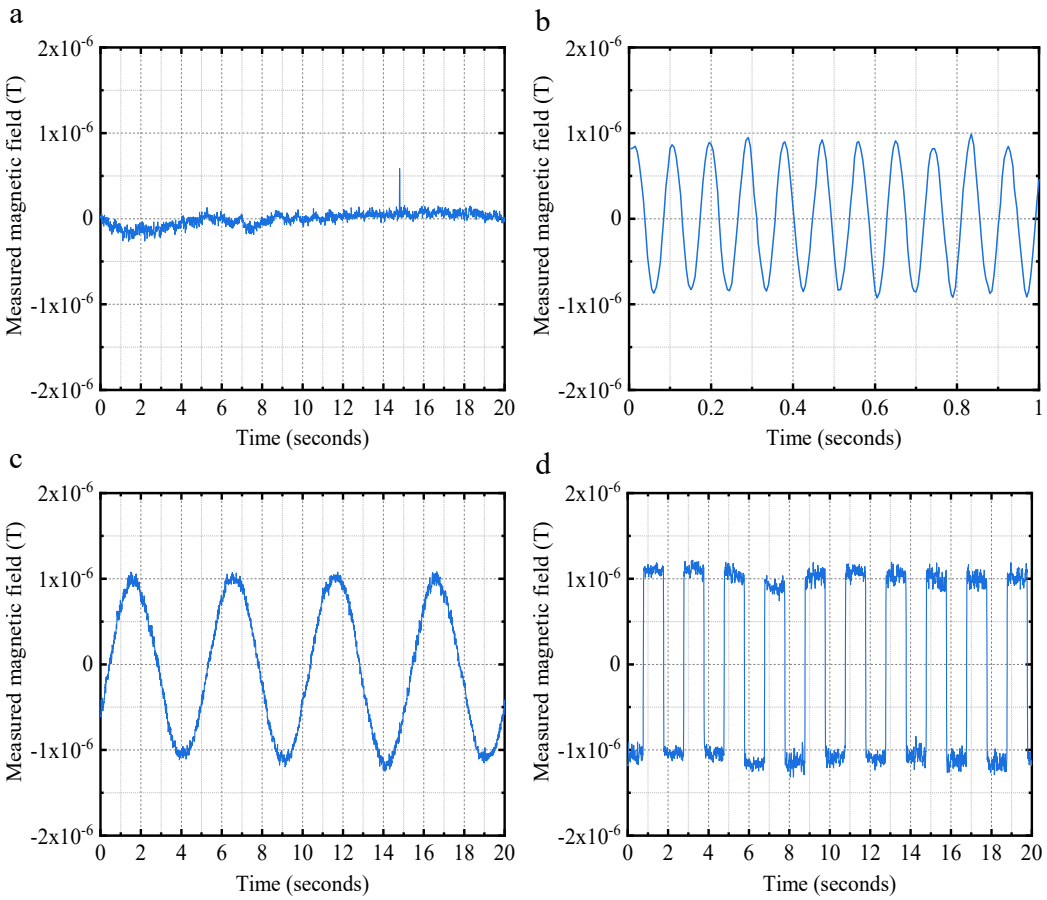

Figure 7.6: **Measured magnetic field in DP configuration with IR absorption magnetometry with high NV concentration sample.** Figure a) shows the time trace for magnetically sensitive spectrum without any applied test magnetic field. Figure b), c), and d) shows the time traces for sinusoidal test fields of 11 Hz and 200 mHz and a square test field of 500 mHz respectively. Discussion regarding magnetic field strength measured with the magnetometer is given in the text.

field strength values shows that there is an error of 9 %. This might have been caused by the orientation and placement imperfection of the test coil from the magnetometer as described in section 6.2.

For comparison of the sensitivity we performed magnetometry with the high NV concentration sample in SP and DP configuration. The above results shows that, there was indeed an improvement of the sensitivity measurement in case of DP configuration (700 pT/$\sqrt{\text{Hz}}$) compared to SP configuration (1.2 nT/$\sqrt{\text{Hz}}$). The path length increased approximately 2 times in DP configuration in comparison with SP configuration, taken that into account the sensitivity should have improved 2 times, which is more or less the value we have observed in the magnetometry experiments. In principle it is showed in this work that the sensitivity gets enhanced with increased path length. More precisely it occurs because of the fact that the increased path length increases the sensing volume hence the sensitivity increases. From table 6.2, it can be seen that the number of spins are 2.02×10^{11} m^{-3} and 4.07×10^{11} m^{-3} for SP and DP magnetometers. The spin-projection-noise limited sensitivity η_{SPN} are 20 fT/$\sqrt{\text{Hz}}$ and 28 fT/$\sqrt{\text{Hz}}$ for DP and SP configuration respectively. Note that unlike fluorescence magnetometry in IR absorption magnetometry we have not provided the photon-shot-noise limited sensitivity obtained via equation 6.8. In IR absorption magnetometry the contrast was already quite low (below 0.20 %) without bias magnetic field compared to fluorescence contrast with applied bias magnetic field (in between 1 to 6 %). It was one of the reasons to use LIA scheme in case of IR absorption magnetometry (see section5.1.2). In such situation, the exact contrast of resonance feature used in magnetometry experiments is not known. The contrast value is needed to calculate the photon-shot-noise limited sensitivity of a certain magnetometer (equation 3.3). That is why in this chapter, only the measured value for environment limited sensitivity (see table 7.1) is given.

7.2 Low NV concentration results

In this sections we discuss the results from low NV concentration samples (sample number 1 and 2 in figure 5.8). For both the samples NV concentration is measured to be 36 ppb and the dimension of the samples are 4.8 mm×2.4 mm×0.5 mm and 4.8 mm × 4.8 mm×0.5 mm respectively. For sample number

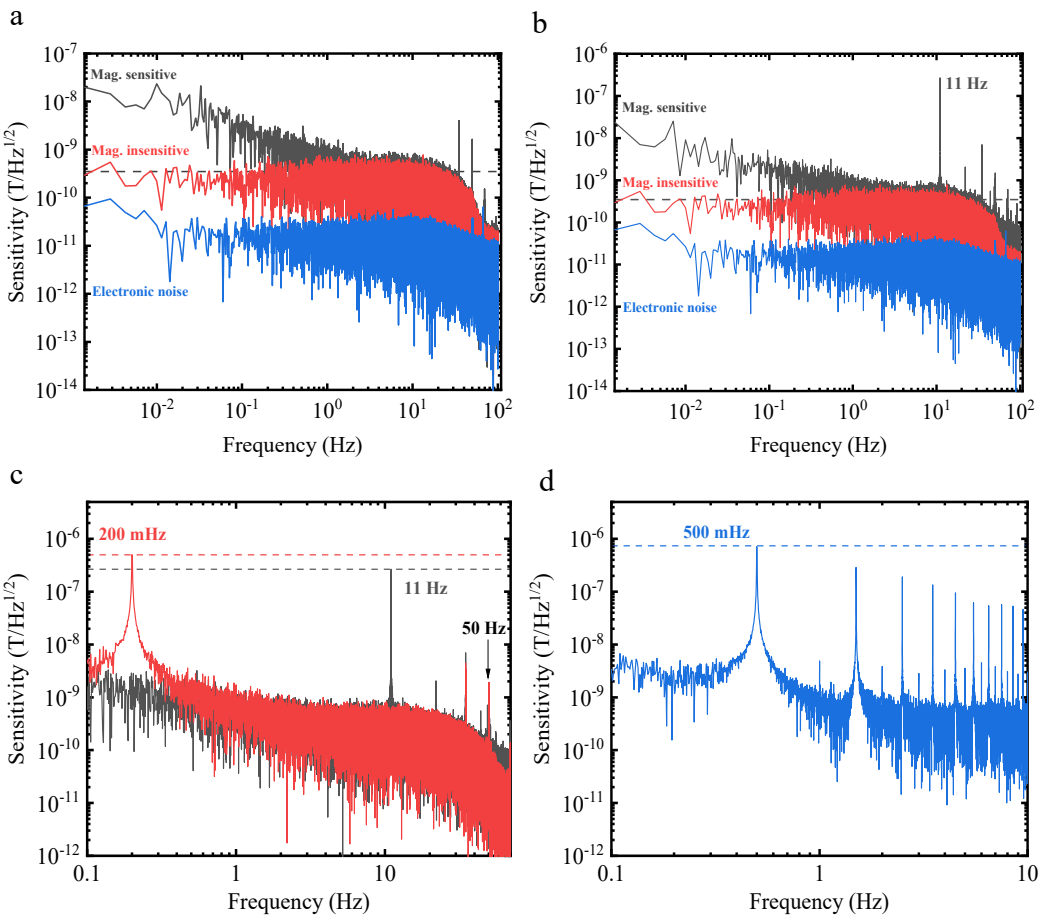

Figure 7.7: **IR absorption magnetometry sensitivity noise spectrum for DP configuration with high NV concentration sample.** Figure a) shows the magnetic field noise spectrum for sensitivity measurement with magnetically sensitive spectrum (black) with an environment limited noise floor of 700 pT/$\sqrt{\text{Hz}}$ between 10 and 40 Hz . This red spectrum for magnetically insensitive measurement. The blue spectrum is the electronic noise. In figure b), c) and d) the magnetically sensitive spectrum for applied test field of 11 Hz, 200 mHz and a square test of 500 mHz is shown respectively.

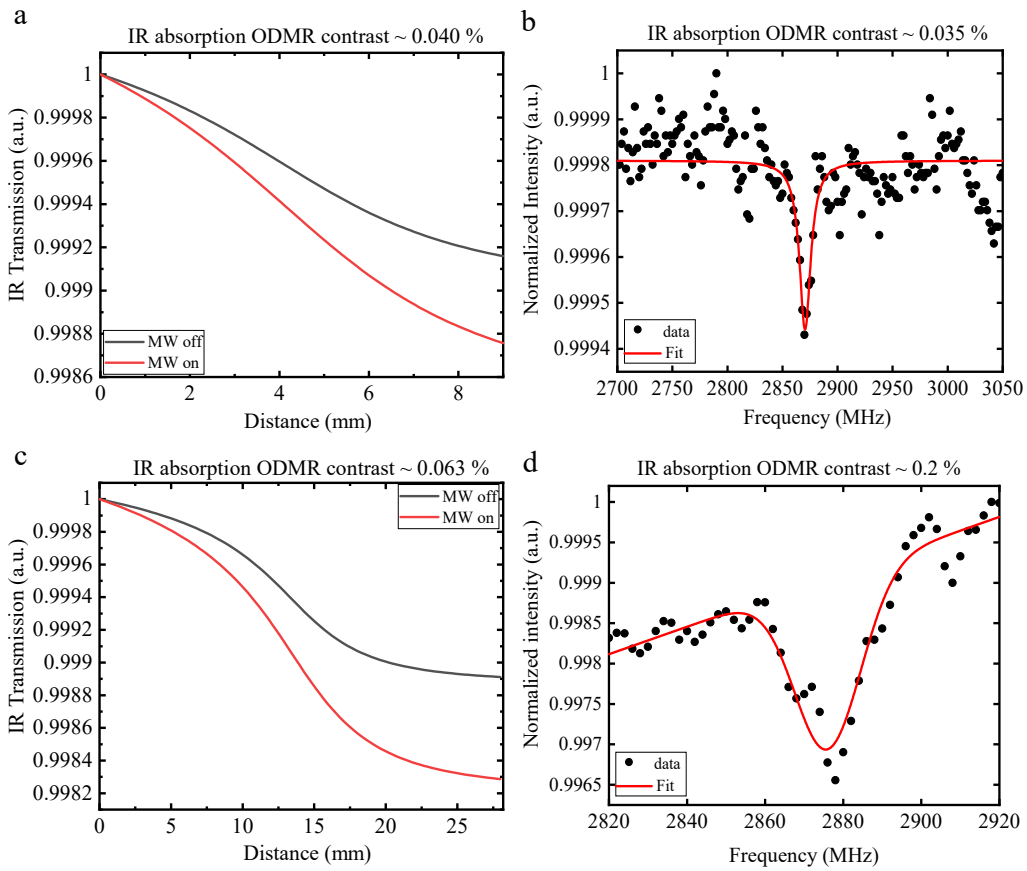

Figure 7.8: **IR absorption ODMR for low NV concentration sample.** In figure a), the theoretical value of contrast for IR absorption ODMR in DP configuration is shown and figure b) shows the measured IR absorption ODMR for DP configuration with sample 3 in figure 5.8. In figure c) and d) the graphs shows the theoretical value and the measured contrast of IR absorption ODMR in LTDW configuration with sample 1 in figure 6.1 a). For more details please refer to text.

1, we were able to perform magnetometry experiment in waveguide or LTDW configuration whereas for sample number 2 we were able to achieve only DP configuration which was due to a insufficient side wall parallelism, prohibiting the a proper transmission of the pump and probe laser beams. This made difficult to maintain the overlapping of the pump and probe beams inside the diamond samples for path length greater than 9.5 mm. As both samples have equal NV concentrations, their results are comparable and is used to discuss the sensitivity enhance for increased path lengths.

7.2.1 Magnetometry with DP configuration

In the figure 7.8 a) and b) the contrast for IR absorption ODMR without applied bias magnetic field is shown for theoretical simulation and for experimental realization respectively. For theoretical calculation, the path length of the combined laser beams was taken as 9.5 mm, Green pump power and IR laser power, and beam waist was same as for high NV concentration sample. The NV concentration was 36 ppb. These parameters were kept same in the experiments. While the theoretical value for ODMR contrast was predicted to be 0.04 % , in the experiment we observed the contrast to be 0.035 % which is in the same order. The ODMR spectrum of figure 7.8 b) was obtained without LIA and measurement time was around 30 min. Due to the fact that the ODMR contrast is very low for IR absorption ODMR compared to the obtained fluorescence ODMR spectrum (section 6.3), here the ODMR spectrum has low signal-to-noise ratio.

As the contrast without applied magnetic field was already very low, with applied magnetic field the contrast for each resonance feature would have been even lower. Therefore to have a good signal to noise ratio and for the purpose to investigate the sensitivity in this sample and in DP configuration we used LIA after the primary ODMR experiment. In the following figure 7.9 a) the ODMR spectrum is shown after the magnetic field was aligned with the NV axis of one of the four classes of NV present in the NV ensemble. The outer resonance features are from one class of NV whereas the inner resonance feature are coming from all the other three classes of NV. For magnetometry purpose we chose the left most resonance feature with zero crossing frequency of 2736.2 MHz. In figure 7.9 b) a representative sweep across this feature during a 10 minutes calibration measurement is depicted. The slope for this resonance feature was extracted from the calibration measurement, which was 0.0024 V/MHz. To measure the sensitivity for this magnetometer, time trace was recorded with the LIA for 10 min and with equation 6.3 and 6.4 measured magnetic field was calculated. The measured magnetic field was then converted to magnetic field noise spectrum as discussed in section 6.2. The LIA parameters are same as mentioned in section 6.3. In figure 7.9 c), the magnetically sensitive and insensitive spectrum for the magnetic field noise spectrum is shown. The environment limited sensitivity is approximately 100 $\mathrm{nT}/\sqrt{\mathrm{Hz}}$ in between 0.001 Hz and 40 Hz.

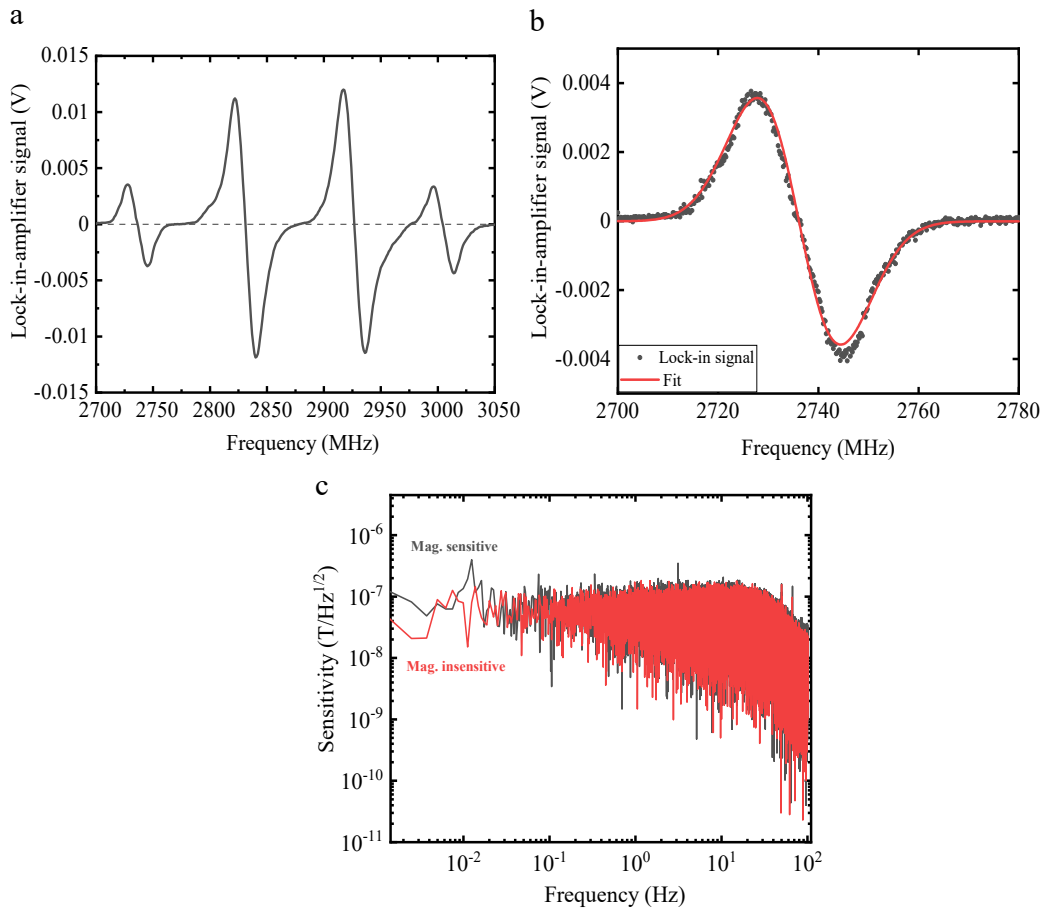

Figure 7.9: **Sensitivity measurement for low NV concentration sample in DP configuration.** The magnetometry results for DP configuration is shown here. In figure a) ODMR spectrum with all the resonance features is shown, whereas the calibration of the magnetometry resonance feature is shown in figure b). Figure c) shows the environment limited sensitivity 100 nT/$\sqrt{\text{Hz}}$. For details please refer to text.

7.2.2 Magnetometry with LTDW configuration

From the results obtained with DP configuration with the low NV concentration sample magnetometer, it was evident that to improve the sensitivity we needed to increase the path length of the combined laser beam. As mentioned before for the polishing imperfection with sample 2 (figure 5.8) we were not able to increase the path length and therefore opted for sample 1 to realize waveguide configuration (see figure 7.10). In this configuration we were able to achieve a path length of $\sim$ 28 mm (see also Appendix D: Path length calculation for LTDW) where the lasers were overlapped inside the diamond. The theoretical simulation and the experimental result for IR absorption ODMR without bias magnetic field in LTDW configuration is shown in figure 7.8 c) and d). For theoretical calculation, the path length of the combined laser beams was taken as 28 mm which was achieved in the experiment and the NV concentration was taken as 36 ppb. The green laser and the IR laser power along with the beam waist was taken same as mentioned previously in section 7.1.1. All the parameters were kept same in the experiments. The transmitted IR beam had an optical power of 0.260 mW where the incident beam had a power of 10 mW. We suspect imperfect facet polishing to be the origin of the heavy losses, as we observed significant scattering whenever the beam hits a side wall. Here the theoretical value for ODMR contrast was 0.063 % (figure 7.8 c)), while in the experiment we observed the contrast to be 0.2 % (figure 7.8 d)). The mismatch between the predicted and the obtained ODMR contrast is also not fully understood either with our theoretical model or experiments. Also with repeated measurement we obtained several ODMR spectrum where the baselines had some slope. The reason for this slope in the baseline is not known to us till date. In our Gaussian fit of the ODMR spectrum to extract the contrast this slope was incorporated. This inclined baseline might have caused error in extracting the real experimental ODMR contrast.

In the following figure 7.11 a) the fluorescence ODMR spectrum is shown after magnetic field alignment procedure. Figure 7.11 b) shows the ODMR spectrum obtained with LIA for fluorescence signal (red line) and the IR signal (black line). As the applied bias magnetic field could not be aligned similar as other experiments, here all the eight resonance features arising from four sub classes of NV centers present in the ensemble can be seen. In this configuration the field alignment was not perfect due to the fact that the applied magnetic

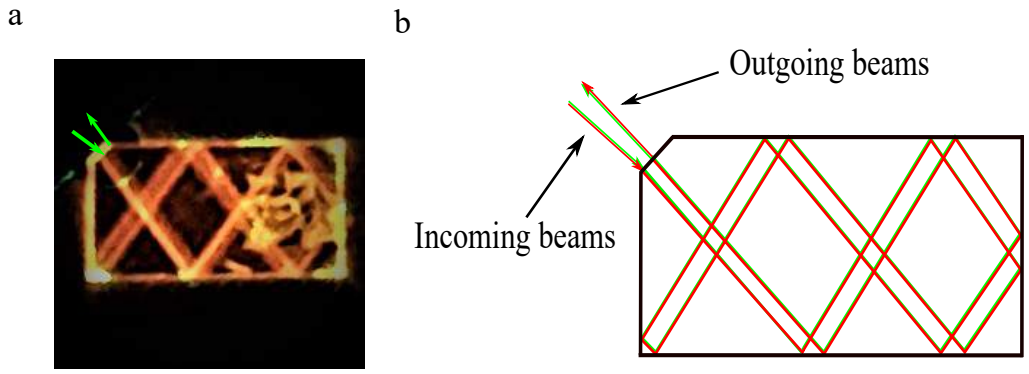

Figure 7.10: **LTDW image and schematic.** In figure a) image of the LTDW configuration is shown where green arrows shows the incoming and outgoing laser beam paths. Figure b) depicts the schematic diagram of the same configuration.

field was not homogeneous all over the sample. The problem of inhomogeneous magnetic field is already discussed in details in in section 6.4.

For magnetometry measurements we chose the left most resonance feature with zero crossing frequency of 2700.78 MHz as shown in the figure 7.11 c) and performed calibration measurement for about 40 min. The slope for this resonance feature extracted from the calibration measurement was 0.65 V/MHz. From the same calibration measurement we observed the same drift of the ZCF over time in figure 7.11 d). For LIA scheme all the parameters were kept same as mentioned before.

To measure the sensitivity for this magnetometer, time trace was recorded with the LIA for 10 min and with equation 6.3 and 6.4 magnetic field was calculated as shown in figure 7.12. In figure 7.13 a) the magnetically sensitive and insensitive spectrum is shown without any test magnetic field applied with the coil magnet as described in the previous sections. Figure 7.13 b), c), and d) shows the the magnetically sensitive spectrum with sinusoidal test magnetic field of 100 mHz, 500 mHz and a square test field of 200 mHz respectively. In this spectrum the environment limited sensitivity is approximately 65 $\mathrm{nT}\sqrt{\mathrm{Hz}}$ in between 0.001 Hz and 40 Hz.

From the time traces shown in the figure 7.12 b), c), and d) the magnetic field strength of the sinusoidal test fields of 100 mHz, 500 mHz and a square test field of 200 mHz can be measured respectively whereas figure 7.12 a) shows the time trace for magnetically sensitive spectrum without any applied test field. The magnetic field strength for 100 mHz and 200 mHz test fields are approximately

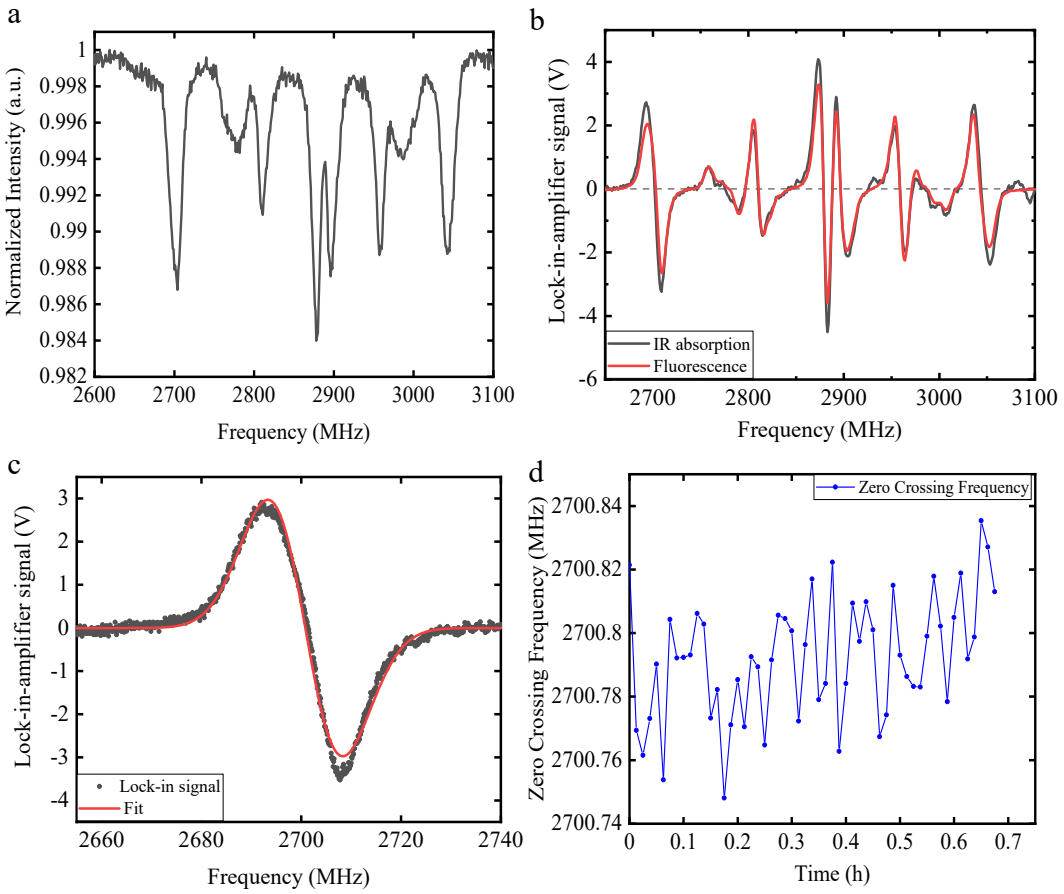

Figure 7.11: **Magnetic field alignment and calibration for low NV concentration sample in waveguide configuration.** In figure a) shows the fluorescence ODMR spectrum with all eight resonance feature and in b) ODMR spectrum for fluorescence and IR absorption with same magnetic field alignment is shown with red and black solid lines respectively. Figure c) depicts the LIA response (black dots) for the left most resonance feature in figure a) with fit (red line) to extract the slope for magnetometry, for the resonance feature with zero crossing frequency of 2700.78 MHz. Figure d) depicts shows the drift of the zero crossing frequency over time (40 min).

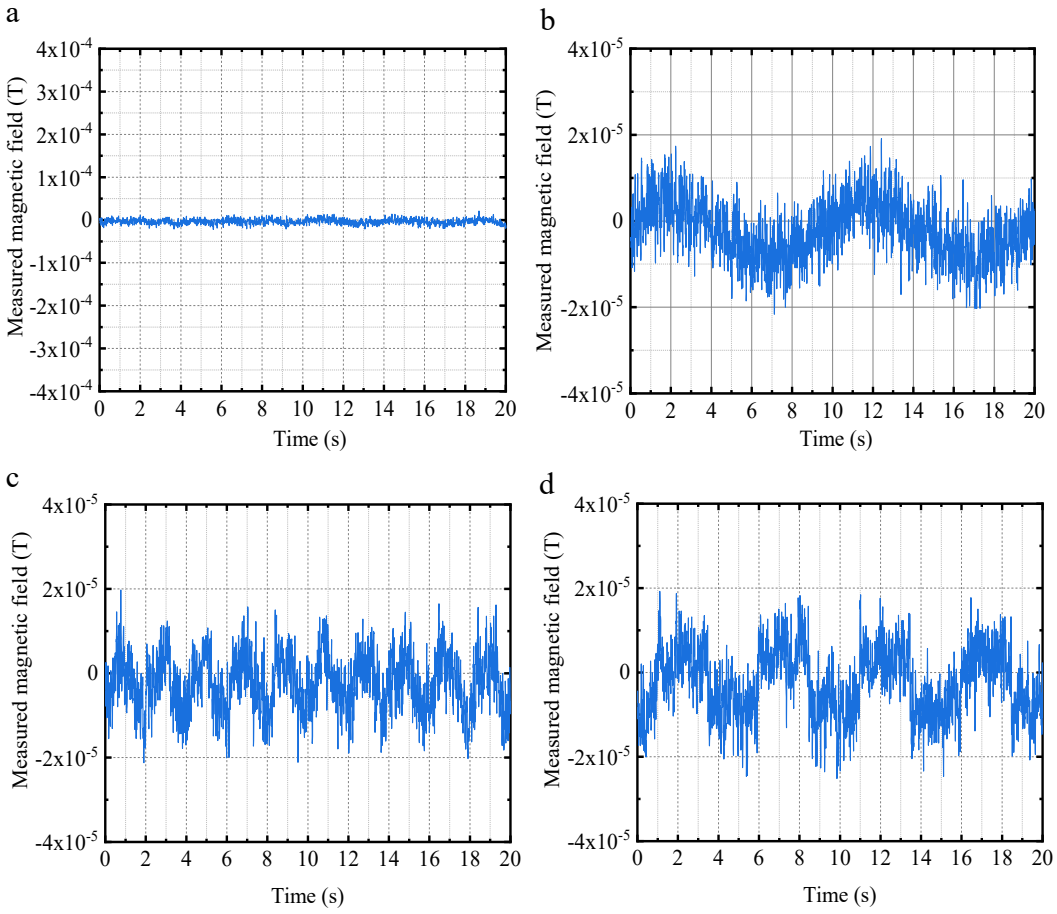

Figure 7.12: **Measured magnetic field with test coil for LTDW configuration.** In figure a) the time trace for magnetically sensitive spectrum without any applied test field is depicted. Figure b), c), and d) shows the time trace for the applied sinusoidal test magnetic fields of 100 mHz and 500 mHz and a square test field of 200 mHz respectively. For details please refer to text.

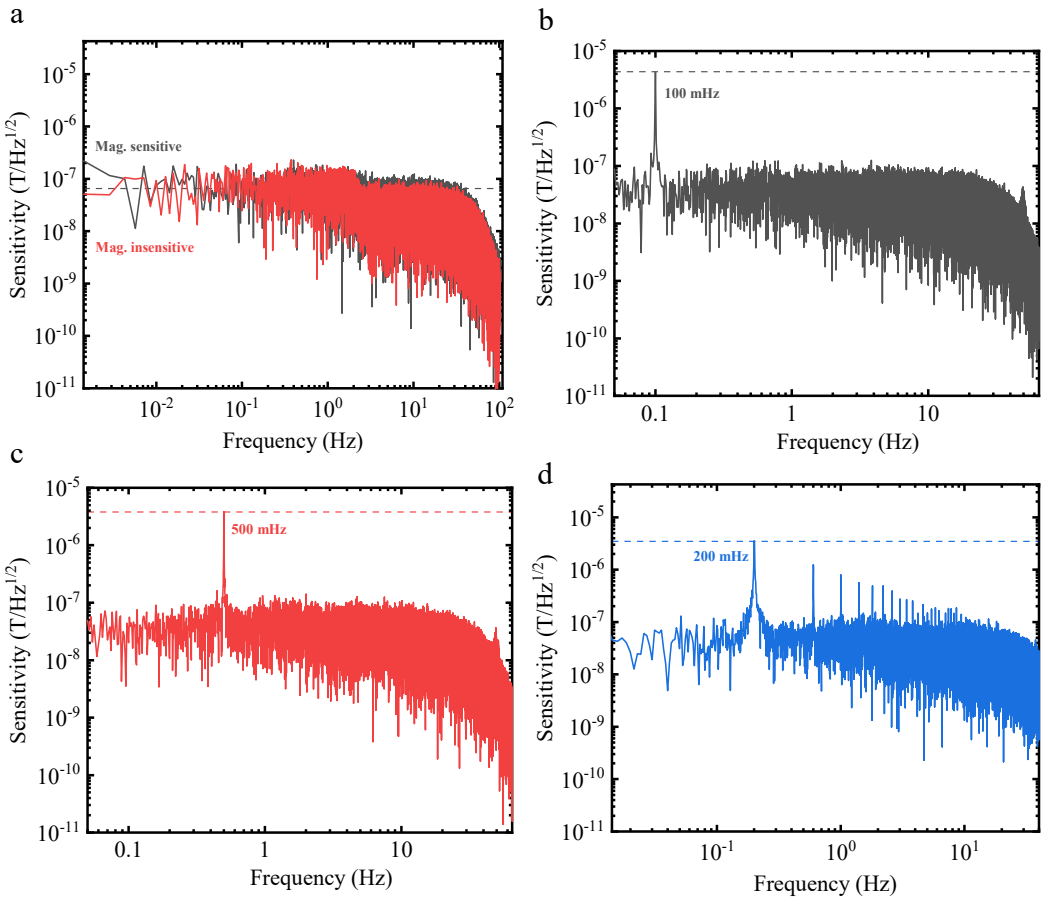

Figure 7.13: **Sensitivity measurement spectrum for LTDW configuration.** Figure a) shows the magnetically sensitive spectrum (black line) and magnetically insensitive spectrum (red line) . The environment limited sensitivity was 65 nT/$\sqrt{\text{Hz}}$ in between 0.001 Hz and 40 Hz (black dashed line). Figure b) shows magnetically sensitive spectrum for applied test field of 100 mHz. Figure c) shows the magnetically sensitive spectrum for applied test magnetic field with 500 mHz . In figure d) magnetically sensitive spectrum for applied test field of 200 mHz square wave is shown.

4.24 μT respectively. The applied magnetic field strength was calculated using the before mentioned equation 6.7. With the following parameters of number of turns, N = 10, radius of the coil r_{coil} = 1.0 cm, the distance from the magnetometer was approximately 10 cm, the coil current I_{coil} was 0.200 mA, the applied magnetic field strength was 4.42 μT . It shows that there is an error of 4 % from the applied test field strength and the measured field strength. It can be noted in figure 7.12 that, the time traces are very noisy. It might be due to the comparatively low sensitivity of the magnetometer.

The above results shows that, there was an improvement of the sensitivity in case of LTDW configuration (65 nT$\sqrt{\text{Hz}}$) compared to DP configuration (100 nT$\sqrt{\text{Hz}}$) with low NV concentration magnetometer. In this context the previously reported sensitivity with a path length in between 15 mm to 28 mm is betwenn 100 nT$\sqrt{\text{Hz}}$ to 600 nT$\sqrt{\text{Hz}}$ by Bougas *et al.* [68]. For our magnetometers the path length increased more than 2 times in LTDW configuration ($\sim$ 28 mm) in comparison with DP configuration (9.5 mm). Accordingly the number of spins for DP and LTDW magnetometers are 2.38×10^{10} m^{-3} and 9.82×10^{10} m^{-3} respectively. The spin-projection-noise limited sensitivity (η_{SPN}) is obtained for DP and LTDW magnetometers via equation 6.9, which are 55 fT$\sqrt{\text{Hz}}$ and 26 fT$\sqrt{\text{Hz}}$. It is evident that the spin-projection-noise limited sensitivity is improved with enhanced interaction path length. Also in our experiments we observed that the environment noise limited sensitivity increased in a similar manner and more or less of the same order. As discussed before that, for LTDW configuration we observed scattering of the lasers due to imperfect polishing which might have restricted us to reach better sensitivity value with this magnetometer. The spin-projection-noise-limited sensitivity (η_{SPN}) for the magnetometers in IR absorption magnetometry are same as fluorescence magnetometry as given in table 6.2. Comparing the values from table 6.2 with the sensitivity results obtained from IR absorption magnetometry in different configurations it can be inferred that sensitivity can be improved even further.

Summary

In the table 7.1, all the experimental results along with ODMR contrast values (without magnetic field), the extracted slopes (b) from LIA scheme (see section 5.1.2) for each configuration is summarized. From the results we see that the

Configuration	C (%)	b (V/MHz)	$\eta_{environment}\left(\mathrm{T}\sqrt{\mathrm{Hz}}\right)$
HC DP	0.16	1.2	$\sim 0.70 \times 10^{-9}$
HC SP	0.10	0.85	$\sim 1.2 \times 10^{-9}$
LC DP	0.035	0.0024	$\sim 100.0 \times 10^{-9}$
LC LTDW	0.20	0.65	$\sim 65 \times 10^{-9}$

Table 7.1: **Parameters and environment limited sensitivity for IR absorption magnetometry.** In this table the environment limited sensitivity for IR absorption magnetometry and the slope measured with LIA scheme is listed for different sample and configurations. HC denotes high NV concentration sample while LC stands for low NV concentration sample. C, b, and $\eta_{environment}$ are the contrast, slope and environment limited sensitivity respectively in the table. DP, SP, LTDW stands for double pass, single pass and light trapping diamond waveguide configurations.

environment limited sensitivity achieved with high NV concentration sample (sample in figure 5.8) is more than 60 times better than the results obtained with low NV concentration sample. By comparing the contrast, slope and environment limited sensitivity for each configuration it can be inferred that the sensitivity level is high when slope is high. Note here, that with higher contrast the slope is also higher similar as discussed in the summary section of chapter 6. In previous discussions in this chapter, it was observed that with higher NV concentration along with higher interaction path length, we were able to achieve higher contrast value. This again indicate that to achieve high sensitivity it is necessary to increase the number of spins by enhancing sensing volume of the magnetometers.

In IR absorption magnetometry also environment limited sensitivity were limited by the inhomogeneous magnetic field distribution all over the magnetometers. Along with this, use of high MW power to achieve higher ODMR contrast broadened the resonance features on which we performed magnetometry experiments. Due to these factors hyperfine coupling was not resolved in IR absorption magnetometry. As already seen in section 6.4, linewidth is indeed smaller (see table 6.3) while the resonance features are hyperfine coupling resolved. That also leads to higher slope and in turn higher sensitivity level.

The environment limited sensitivity level achieved in IR absorption magnetometry with HC DP and HC SP configurations are in the same order or slightly better compared fluorescence magnetometry (see tables 6.4 and 7.1). On the

other hand results obtained from LC DP and LC LTDW configurations are showing opposite trends. Most importantly it can be noted in table 7.1, that in both of these situation contrast is smaller compared to HC DP and HC SP. Due to low NV concentration in these magnetometers, absorption of IR laser was smaller than the other magnetometers. Which effectively led to comparatively smaller sensitivity and therefore no advantage is gained compared to fluorescence magnetometry.

A higher magnetic field sensitivity (28 $\mathrm{pT}\sqrt{\mathrm{Hz}}$) than we report in this work is achieved by Chatzidrosos *et al.* [67] by employing an optical cavity was used to enhance interaction path length. The work presented by Jensen *et al.* [66] also have used an optical cavity and achieved sensitivity of 2.5 $\mathrm{nT}\sqrt{\mathrm{Hz}}$. From the results presented in this dissertation and the mentioned previous results [66, 67], we can conclude few things. First of all to achieve higher sensitivity in IR absorption magnetometry high NV concentration is required. As the absorption cross section of NV centers for IR laser is very low (see chapter 4) interaction path length should be enhanced either by means of employing an optical cavity around the diamond sample or by multiple total internal reflection inside the diamond waveguide (see section 7.2). Another conclusion can be drawn from the presented results, that there is a possibility to achieve similar if not better sensitivity than cavity enhanced magnetometry [66, 67], with waveguide structures in IR absorption magnetometry.

8 Outlook and conclusion

In the last two chapters (6 and 7) we have presented the results of our magnetometry experiments. Although the main focus was to investigate and enhance the magnetic field sensitivity with IR absorption magnetometry (chapter 7), we also investigated the sensitivity in fluorescence magnetometry (chapter 6) in same manner along with magnetometer characterizations. Our results from the Gaussian beam optimized NV rate equation model as described in chapter 4 agreed well with experimental observations. As already stated in the previous chapters that there are scopes to further enhance the sensitivity. In this chapter we discuss how that can be achieved. To this end we first discuss a short outlook on a number of further improvements which can be employed to improve the magnetic field sensitivity via IR absorption magnetometry with ensembles of NV centers in diamond. Later we discuss some important results from chapter 7 to conclude this thesis.

Outlook

Infrared absorption magnetometry.

To increase the sensitivity of the magnetometer for infrared absorption magnetometry we need to increase the infrared absorption. From the results presented in chapter 7 and from the theoretical simulations in chapter 4, it can be noted that the infrared absorption is increased by increased interaction path length of the overlapped lasers (pump and probe) inside the diamond sample. Another way to increase infrared absorption is to increase the pump power while the interaction path length inside the diamond sample remains the same. For these reasons in future experiments the following modification can be employed to achieve better sensitivity.

i) **Pump power increment:** In the experiments presented here, the green pump power was limited to 440 mW. The contrast of infrared absorption ODMR

for high NV concentration sample (sample 3 in figure 5.8) in DP configuration was 0.160 % (theoretical value 0.158 %, see section 7.1). Given the fact that in this configuration we observed the highest sensitivity, we increased the pump power from 500 mW to 5 W in our theoretical model (red solid line in figure 4.5 b)). The theoretical value for contrast of infrared absorption ODMR with these pump powers increased to 0.4 % at around 2 W of green laser power. As observed in our experiments (chapter 7) that the sensitivity increases with increased contrast, it can be inferred that high pump power will certainly lead to improved sensitivity the magnetometers. Similar calculation for low NV concentration sample (sample 1 in figure 5.8) based magnetometer was also performed for the LTDW configuration (red solid line in figure 4.5 a)). In this case increasing pump power did not show significant improvement, but increasing interaction path length increased the contrast.

ii) **Interaction path length increment:** As mentioned earlier, another way to increase the infrared absorption ODMR contrast is to increase the interaction path length inside the diamond samples. For the high NV concentration sample we observed that due to high absorption of the green pump laser we were not able to achieve the LTDW configuration as shown in figure 6.1. With increased pump power it will definitely be possible to achieve longer path length as well as higher ODMR contrast. But the relation of increasing ODMR contrast with increased path length is not straight forward. With increased path length the sensing volume also increases and for a constant pump power with increased path length the contrast decreases after an optimum path length. This happens because a higher sensing volume needs higher pump power to reach saturation for the ensemble NV system (figure 4.5). From figure 4.5 a) and b) it is evident that there is a trade off between increasing the interaction path length and the pump power. It is necessary to use an optimum pump power to achieve higher ODMR contrast for a certain sensing volume of the NV ensemble. For example with high NV concentration sample (sample 3 in figure 5.8) a interaction path length of 10 mm increases the contrast around 0.6 %, which will definitely enhance the sensitivity of the magnetometer. In future experiments these effects can be investigated to reach higher sensitivity.

With low NV concentration samples we did not ran into the problem of pump power depletion. However due to polishing imperfection we were able to perform LTDW experiment only with sample 1 but sample 2 (figure 5.8). With sample 2 (figure 5.8) only DP configuration was possible. Better polishing of

sample 2 can give the opportunity to increase the path length more than 28 mm. In one of our preliminary experiments a path length of approximately 40 mm was observed, but due to imperfect geometry the lasers were not overlapped all through the interaction path inside the diamond. Also it was experimentally challenging to detect the transmitted IR beam clearly. In figure 4.5 a), the increment in contrast for a path length of 40 mm is shown. It is reaching a saturation value of 0.05 % at around 2.5 W of green power.

One important point to consider for higher path length is the walkoff (see figure 5.6) of the laser beams due to slightly different refractive index of diamond for green and infrared lasers. To circumvent this problem the following approach can be employed. The whole diamond sample can be illuminated with green pump laser from the side, which have the same dimension as the diamond sidewall (e.g. 2.4 mm x 0.5 mm for sample 1). The beam shaping of the pump laser can be achieved by anamorphic prism pairs. The infrared laser enters the diamond sample from the cut corner and after multiple total internal reflections inside the diamond exist from the same cut corner (as shown in figure 5.1). By employing this method path length can be increased while at the same time the problem of beam walk off is circumvented as already performed by Bougas *et al.* [68], where a pump power of approximately 2 W was used.

For side pumping effectively the NV sensing volume remains same, as it depends on the IR laser path length. For a given path length, the IR absorption ODMR contrast depends on the pump power and the beam waist 4. In our simulation of LTDW configuration we have seen that the IR absorption is significantly higher near the beam waist inside the diamond because of high intensity of the pump laser (figure 4.4). Taken into account the incident pump power as 440 mW and a NV concentration of 36 ppb; at around 14 mm inside the diamond sample, the pump power becomes 350 mW. The beam waist was 20 μm, therefore the pump laser intensity at beam waist was approximately 3 GW/m^2. For side pumping we assume that the beam area at beam waist will be; $2.4\text{mm} \times 0.5\text{mm} = 1.2\text{mm}^2$. To reach the same intensity, that was achieved with a beam waist of 20 μm,a pump power of 4 W is required.

Monolithic ring cavity: For enhancing the interaction path length another approach was taken in our experiments. In that approach we tried to achieve a monolithic ring cavity with sample 1 and 2. In a cavity effectively the interaction path length increases and in our approach we wanted to use this basic principle to enhance the sensitivity. Previously an optical cavity is used

to enhance sensitivity for infrared absorption magnetometry [67]. In those experiments the diamond samples have been placed inside an optical cavity. Our approach was to make a monolithic ring cavity from the diamond sample itself. Here were coupled the pump and probe lasers to the monolithic cavity by evanescent coupling by a prism.

Though with green laser it appeared to be a ring at first (see Appendix A: Monolithic ring cavity setup), detailed examination with infrared laser scanning showed no cavity mode. Later on sample examination showed geometrical imperfections with the samples. We concluded that due to these imperfection there were no cavity operation. Most likely the ring was not forming properly, although from the images taken with camera it appeared to form a ring. Sample number 1 and 3 (see figure 5.8) have been re-polished and re-examined with laser scanning microscope. Results from laser scanning microscope shows that the sidewalls are now parallel to each other within tolerance bound (see section 5.5). Therefore this approach can also be taken to enhance the sensitivity with infrared absorption magnetometry. More details regarding the experimental setup and the observations are given in Appendix A: Monolithic ring cavity setup.

iii) **Homogeneous magnetic field**: As discussed before in the section 6.4 in chapter 6, one of the major problem with ensemble based NV magnetometers is applying a homogeneous bias magnetic field all over the magnetometer. We used one permanent magnet (refer to section 5.4) for all our experiments. To apply homogeneous bias magnetic field either Helmholtz coil [69] or Halbach array [168] with 4 or more permanent magnets can be used in future experiments. In our experiments we observed hyperfine coupling of the NV spin with ^{14}N nuclear spin with all the samples only when a very small sensing volume was used and with the collected fluorescence signal only (see section 6.4). It can be concluded that the hyperfine coupling was not resolved in case of infrared absorption ODMR experiments due to broadening of resonance linewidth due to inhomogeneous bias magnetic field over the large sample volume. Although there are other factors which can lead to broadening of resonance linewidth such as green laser power and microwave power. Which were high in our experiments, but absence of a homogeneous bias magnetic field is also another primary factor (also discussed in section 6.4). From our experimental observations, it can be concluded that to enhance the sensitivity for ensemble NV based magnetometers a homogeneous magnetic field is needed.

In the equations 6.3 and 6.4, it can be noted that the magnetic field sensitivity is dependent on the slope of the first order derivative of the resonance feature, which is recorded by lock-in-amplifier. The higher the slope, the higher the sensitivity that can be reached by a particular magnetometer. In section 6.4 of chapter 6 we have seen that the slope acquired for hyperfine resonance is higher compared to the slope when hyperfine coupling is not resolved. For example, the slope for recorded hyperfine coupled resonance feature was 6 V/MHz compared to 2 V/MHz when hyperfine coupling was not resolved for the resonance feature. Simultaneous excitation of the all three resonance of a hyperfine coupled resonance feature will increase the slope even more as shown in previous experiments [169, 170].

In future experiments to enhance the sensitivity with infrared absorption magnetometry the methods discussed above can be used. We can imagine a situation where all the experimental parameters are identical to the experiment where we achieved a sensitivity level of 700 pT/$\sqrt{\text{Hz}}$. Employing a homogeneous magnetic field and resolving the hyperfine coupling resonance feature itself will lead to a sensitivity of approximately 200 pT/$\sqrt{\text{Hz}}$. Now in addition to this if the pump power is increased above 2 W, that will enhance the sensitivity two fold reaching approximately 100 pT/$\sqrt{\text{Hz}}$. With simple DP configuration in waveguide structure, reaching this sensitivity level would be outstanding. So far for IR absorption magnetometry with waveguide structures a sensitivity level of 100 to 600 nT/$\sqrt{\text{Hz}}$ was possible [68].

Conclusion

In chapter 7 we have shown with two different samples with different NV concentrations how we can enhance the sensitivity via enhancing the sensing volume. From the results it can be seen that it is indeed possible to achieve a sub nano Tesla (700 pT/$\sqrt{\text{Hz}}$) sensitivity with infrared absorption magnetometry using a comparatively simple configuration without employing an optical cavity. For a low NV concentration sample, increasing the sensing volume by the means of multiple total internal reflections inside the diamond is also shown. Compared to a previous similar attempt (sensitivity level of 100 - 600 nT/$\sqrt{\text{Hz}}$) [68] here we show that the achieved sensitivity in our experiment is better with a sensitivity level of 65 nT/$\sqrt{\text{Hz}}$. In our experiment the sensitivity improved mostly

due to the use of two overlapped optimized Gaussian beams instead of side illumination of diamond sample with pump laser. It is shown in chapter 4, that with optimized Gaussian beams IR absorption ODMR contrast is increased. Another factor is dephasing time T_2^*, which we measured to be around 460 ns compared to 100 ns and 320 ns [68]. The ultimate sensitivity of magnetometers are limited by this dephasing time T_2^*. So far for IR absorption magnetometry the best sensitivity reached was about 28 $\mathrm{pT}/\sqrt{\mathrm{Hz}}$ by cavity enhanced diamond magnetometer [67]. From our results we can conclude that by optimizing the NV concentration and interaction path length it is possible to realize IR absorption magnetometers with even higher sensitivity level. The advantage of such magnetometers would be the simpler experimental realization.

We have seen that with fluorescence magnetometry based NV magnetometers are finding their places in day to day life applications [81, 82]. It is being possible mostly due to the possibility to miniaturize such magnetometers. It intrigues us, as an alternative method, whether IR absorption based NV magnetometers can find their places in our life in similar way. From our experimental results and previous experiments [64, 65, 66, 67, 68], we see that there is a possibility to reach an even higher magnetic field sensitivity level with IR absorption magnetometry. Still there remain some constraints for the IR absorption based magnetometers to be used in day to day life for practical purposes. First, in this method compared to fluorescence magnetometry instead of only green laser we need both green and IR lasers. Second, to reach a sensitivity level of $\mathrm{nT}/\sqrt{\mathrm{Hz}}$ or sub-$\mathrm{nT}/\sqrt{\mathrm{Hz}}$, high green laser power ($\gtrsim$ 500 mW) is needed. Third, to increase the interaction path length either an optical cavity has to be employed, or waveguide structures [68] should be used, where via multiple total internal reflection path length is increased. Potentially a monolithic ring cavity can also be used for the same purpose as discussed in 8. In all these methods both the lasers should be carefully overlapped to reach optimum magnetic field sensitivity level. All these factors add up to the complexity to realize compact NV magnetometers based on IR absorption magnetometry method, to be used in daily life [80, 81, 82].

Although miniaturization seems to be challenging at this point; due to the potential for higher sensitivity with IR absorption magnetometry, these magnetometers can still be investigated and used in laboratory setups. At this point it can be said, that further studies are required to optimize the sensitivity of such magnetometer via different approaches as already discussed.

Appendices

Appendix A: Monolithic ring cavity setup

To achieve the monolithic ring cavity [171], with available diamond samples, our approach was following. In our first attempt to achieve a monolithic ring cavity we chose the sample 2 (refer to figure 6.1). Here our goal was to achieve a square ring for both the lasers which were overlapped to perform infrared absorption magnetometry. For a square ring all the angles of incident θ_1 inside the cavity are the same, i.e. 45°. The optical cavity is surrounded by air with refractive index of 1 and our monolithic cavity is made of diamond, which has a refractive index (n_d) of 2.41 and 2.39 for green (532 nm) and infrared (1042.5 nm) wavelength respectively. Therefore it is possible to confine an optical wave inside the monolithic cavity as the condition of $n_{surrounding}/n_{cavity} > 1.41$ is satisfied.

Coupling in and out the photons from the monolithic cavity is only possible by frustrated total internal reflection. To achieve frustrated total internal reflection we needed a prism of refractive index n_p which satisfy the condition of $n_p > n_d \sin\theta_1$. We took into accountn_d as 2.41 and θ_1 as 45° and found that the prism material should have a refractive index more than 1.70. We chose a Rutile prism (ADT-6, Thorlabs) which has a refractive index of more than 2.5 for both the wavelengths (532 nm and 1042.5 nm). With the following equation 8.1 [155], we calculated the angles θ_{2g} and θ_{2ir} which were 40.95° and 43.18° respectively as shown in figure 8.1. In equation 8.1, θ_p and θ_d are the generalized angles in side the prism and the diamond sample respectively. In the schematics (in figure 8.1) these angles are referred as θ_{2g} , θ_{2ir} and θ_1.

$$n_p \sin\theta_p = n_d \sin\theta_d \tag{8.1}$$

Using these angles we calculated angles θ_{3g} and $\theta_{3ir}$for the air and prism interface (see figure 8.1) with the following equation 8.2, which were 10.58° and

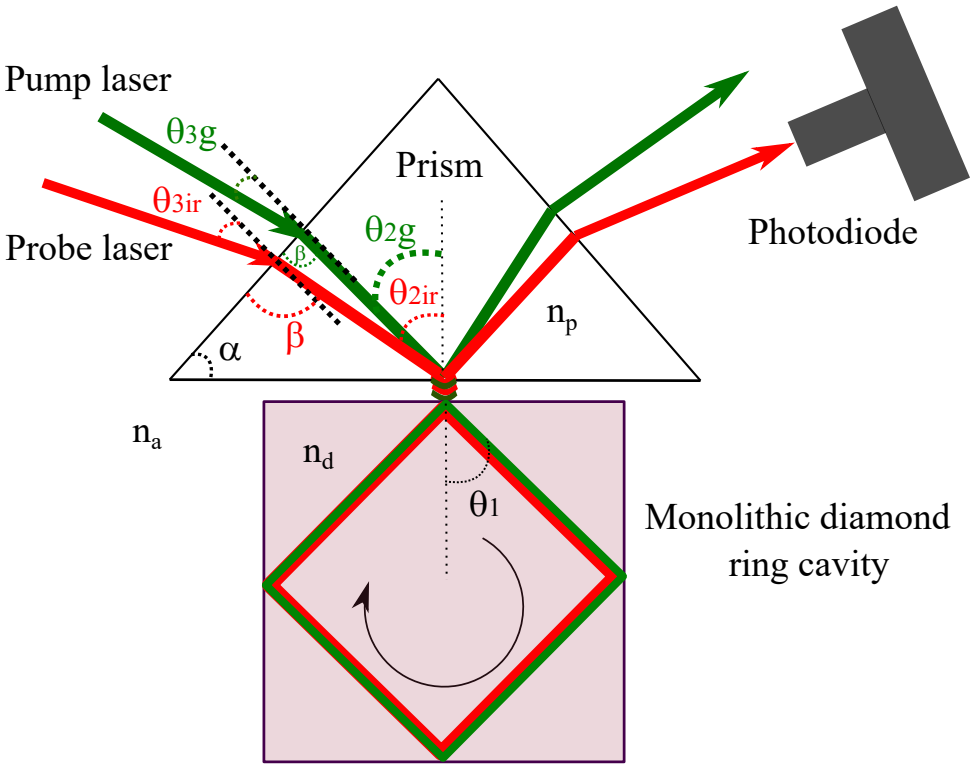

Figure 8.1: **Schematic diagram for monolithic ring cavity.** In this schematic diagram the approach for the monolithic ring cavity with evanescent coupling of the pump and probe lasers by Rutile prism is shown. Refer to text for the details regarding the labeled angles to achieve monolithic ring cavity and the overall set up.

4.51°. In equation 8.2 $\theta_a = \theta_{3g}/\ \theta_{3ir}$ for green and infrared lasers. From angles θ_{2g} and θ_{2ir} and angle α (45°) and β as shown in figure 8.1 the angle θ_p was calculated. For green and infrared lasers θ_p are 4.05° and 1.81° respectively.

$$n_a \sin\theta_a = n_p \sin\theta_p \tag{8.2}$$

The sample for monolithic cavity was mounted on a system of two translational stages and a mirror holder. The translational stages were used to move the sample horizontally in x and y direction to achieve the evanescent coupling. The mirror holder was used to correct any tilt angle in between the prism surface and the diamond surface. For efficient evanescent coupling it is necessary that those surfaces are parallel to each other. The whole system was fixed on a rotational stage to maintain the precise angles as described before. The transmitted infrared laser beam was collected by a photodiode (same photodiode as

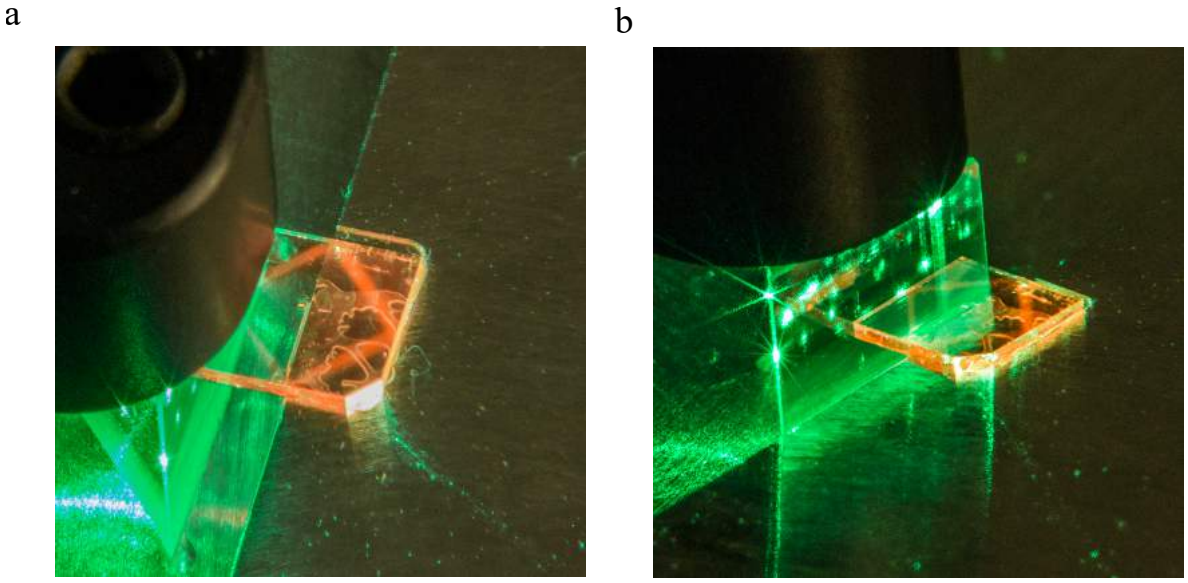

Figure 8.2: **Observation of ring with green laser.** In this figure the images of the attempted monolithic ring cavity are shown. Images were taken with a canon camera without any optical filter. Figure a) is the top view and figure b) is the side view of the monolithic ring cavity. The fluorescence ring pattern can be seen in the images.

mentioned in section 5.2). With green laser we first observed a ring as shown in figure 8.2.

To confirm and further perform infrared absorption magnetometry we scanned the monolithic cavity with a infrared laser (same laser as described in section 5.2). We were unable to find any cavity mode by this method. Later investigation of the sample confirmed that the sidewalls of the diamond sample was not parallel to each other (average deviation measured to be approximately 1.50°). Therefore we concluded that due to this design imperfection of the sample we were unable to achieve a proper ring cavity.

Appendix B: Sample orientation for hyperfine coupling

As already described in section 6.4, we had to use different configuration other than SP, DP, and LTDW to achieve hyperfine coupling resolved ODMR spectrum. In the figure 8.3 the difference between SP and orientation to achieve hyperfine coupling is shown. In this configuration the green laser is passing perpendicular to the top facet of the diamond samples (sample 2 and 3 in figure 5.8). In SP, DP, LTDW we wanted to achieve higher interaction path length. In this orientation our goal was to have minimum path length. The path length in this case is 0.50 mm, which is the thickness of the diamond samples.

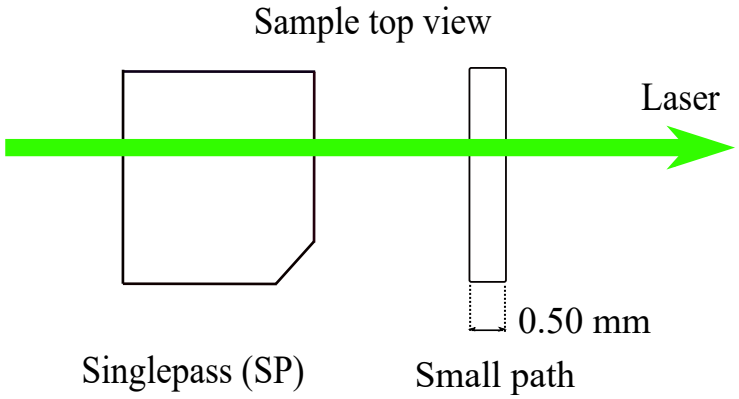

Figure 8.3: **Sample orientation for hyperfine coupling measurements.** This figures shows the difference between SP configuration and the configuration used to achieve hyperfine coupling resolved ODMR. For both configuration top view is shown here for comparison.

Appendix C: Beam waist determination

The beam waist was calculated by knife edge method. In different positions of the green laser beam a sharp edge knife was placed. By blocking the beam slowly in μm steps by the knife placed on a translational stage, optical power was recorded by a power-meter. Along the beam path at six positions this method was performed determine beam radius at those positions. These power reading at each position of the knife is then fitted with the following equation [172, 173]:

$$P = P_0 + \frac{P_{max}}{2}\left(1 - erf\left(\frac{\sqrt{2}\,(x - x_0)}{w}\right)\right). \tag{8.3}$$

Where P_0 is the background power or the dark count recorded by the power-meter after blocking the optical beam, P_{max} is the maximum power recorded, erf is the error function, x is the distance traveled by the knife edge from initial position, x_0 is the knife edge position where the optical power is reduced to half of the maximum power, and w is the beam radius.

These beam radius is then fitted with Gaussian beam radius equation 8.4 [172, 173]. In this equation w is the beam radius, w_0 is the beam waist. In z direction; z_1 is the position of the beam waist, z_0 is the Rayleigh's range.

$$w = w_0\sqrt{1 + \left(\frac{z - z_1}{z_0}\right)^2}. \tag{8.4}$$

In figure 8.4 a) and b), one example of beam radius determination at a position and the extracted beam waist is shown. The fit shows that the beam waist from 100 mm lens is around 15 μm. Where as our calculation (section 5.2.1) shows the beam waist should be around 20 μm. To conclude whether determination of beam radius with the sharp edge knife method was precise, we compared experimental values for ODMR contrast with simulation values with different beam waists. The experimental results are more comparable while we took the beam waist around 20 μm. Therefore in all our theoretical assumptions we considered this value. Also we conclude that there was some error performing this method to precisely determine the beam waist.

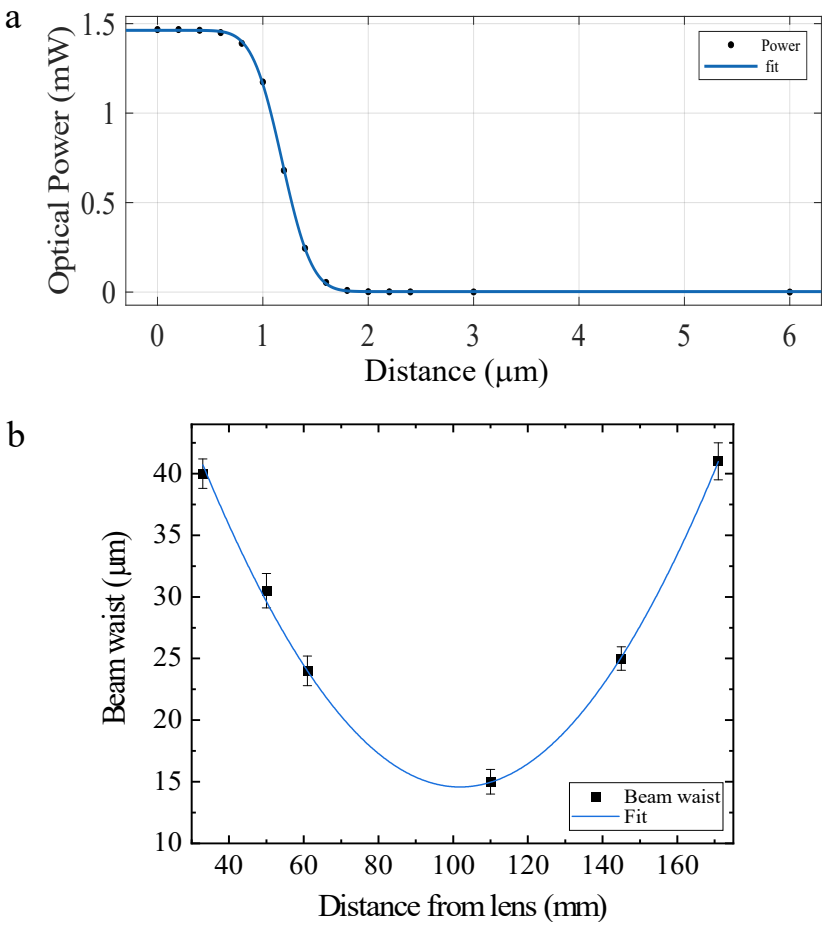

Figure 8.4: **Beam waist determination by sharp knife edge method.** Figure a) shows here one of the analysis with recorded power values to calculate beam radius. Figure b) shows the Gaussian radius fit with all the calculated beam radius in six positions.

Appendix D: Path length calculation for LTDW

The path length achieved in the LTDW configuration was calculated in the following ways:

1. From the image analysis: In this process visible path was traced in a image analysis software (Inkscape). As we know the dimension of the diamond sample (4.8 mm $\times$ 2.4 mm), first a certain length (2.4 mm) from the visible sample image was calibrated with pixel size. The scale (labeled as S) is shown in green solid lines and text in figure 8.5, path tracing lines are not shown in the figure, to maintain the clarity of the image. Then we traced the visible path with line tracing tool in the software. By comparing these numbers we calculated the approximate path length, which is $\sim$ 29 mm.

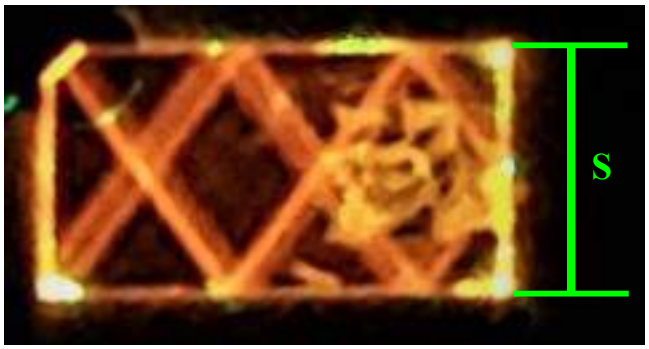

Figure 8.5: **LTDW image analysis.** In this figure scale for image analysis of LTDW configuration is shown.

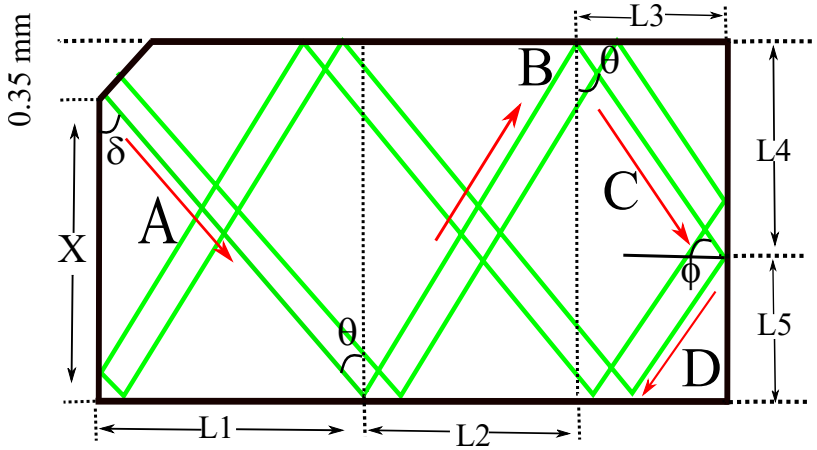

Figure 8.6: **LTDW path length calculation.** In this figure the path length calculation with trigonometric analysis is shown. Path marked with red arrows (A, B,C, and D) were calculated. Angles which were taken into consideration is labeled as δ, θ, and ϕ respectively. The diamond sidewall segments; L1, L2, L3, L4, L5 and x were also calculated. Further details are given in text.

2. The second method was geometric calculation of the path: For that we calculated the angles δ, θ, and ϕ and the segments of the path labeled A, B, C, and D in the figure 8.6. To calculate δ,we take in account the incidence angle (20°), and with Snell's law (equation 8.1) calculated the angle of refraction (∼8°). Along with that we considered the fact, that the angles between the input facet and the diamond sidewalls are 45°. The input beams entered the diamond sample near one corner (see also figure 7.10). To simplify calculation with trigonometric relations, here we considered that the beams entered from the corner edge of the input facet. By considering all of these, angles δ , and θ were calculated, which are approximately 37°.

X = 2.40 − 0.35 = 2.05 mm; path segment A = $2.05/cos(\delta) = 2.05/cos(37°)$ ≈2.55 mm, and L1 = $2.05 \cdot tan(\delta) = 2.05 \cdot tan(37°)$ ≈1.54 mm.

Path segment B = $2.40/cos(\theta) = 2.40/cos(37°)$ ≈3.00 mm, L2 = $2.40 \cdot tan(\theta) = 2.40 \cdot tan(37°)$ ≈1.80 mm, L3 = (4.80 − (1.54 + 1.80))=1.46 mm.

Path segment C = $L3/cos(90° - \theta) = 1.46/cos(53°)$ ≈2.42 mm, L4 = 1.10 mm, L5 = 1.30 mm, and angle $\phi = 53°$.

Path segment D = $L5/cos(90° - \phi) = 1.30/cos(37°)$ ≈1.62 mm.

Therefore; Path segment A + Path segment B + Path segment C + Path segment D: $L \approx 9.60$ mm. From the figure 8.6 and 7.10 it can be seen, that the laser beam travel the path (A+B), 4 times and the path (C+D), 2 times

inside the diamond sample. Therefore, total path length is $(4 \times (2.55 + 3.00) \times 2(1.62 + 1.42))$ mm ≈ 28.28 mm.

Results obtained from both analysis is similar. From our simulation results, we did not observe significant change of IR absorption contrast value while plugged these values. Therefore, taken into account the approximations and probable errors in image analysis, we considered the total path length we calculated via trigonometric analysis.

Bibliography

[1] J. P. Dowling and G. J. Milburn, "Quantum technology: the second quantum revolution," Phil. Trans. R. Soc. Lond. A, **361**, 1655 - 1674, (2003).

[2] D. Deutsch, "Quantum theory, the Church–Turing principle and the universal quantum computer," Proc. R. Soc. Lond. A, **400** ,97–117, (1985).

[3] N. Gisin, G. Ribordy, W. Tittel, and H. Zbinden, "Quantum cryptography," Rev. Mod. Phys., **74**, 145, (2002).

[4] C. L. Degen, F. Reinhard, and P. Cappellaro, "Quantum sensing," Rev. Mod. Phys., **89**, 035002, (2017).

[5] D. Budker and M. Romalis, "Optical magnetometry," Nat. Phys., **3**, 227–234, (2007).

[6] F. Dolde, H. Fedder, M. W. Doherty, T. Nöbauer, F. Rempp, G. Balasubramanian, T. Wolf, F. Reinhard, L. C. L. Hollenberg, F. Jelezko, and J. Wrachtrup, "Electric-field sensing using single diamond spins," Nat. Phys., **7**, 459-463, (2011).

[7] M. W. Doherty, V. V. Struzhkin, D. A. Simpson, L. P. McGuinness, Y. Meng, A. Stacey, T. J. Karle, R. J. Hemley, N. B. Manson, L. C. L. Hollenberg, and S. Prawer, "Electronic properties and metrology of the diamond NV^- center under pressure," Phys. Rev. Lett., **112**, 047601, (2014).

[8] L. Rondin, J.-P. Tetienne, T. Hingant, J.-F. Roch, P. Maletinsky, and V. Jacques, "Magnetometry with nitrogen-vacancy defects in diamond," Rep. Prog. Phys., **77**, 056503, (2014).

[9] M. W. Doherty, N. B. Manson, P. Delaney, F. Jelezko, J. Wrachtrup, and L. C. Hollenberg, "The nitrogen-vacancy colour centre in diamond," Phys. Rep., **528**, 1–45, (2013).

[10] D. P. DiVincenzo, "The Physical Implementation of Quantum Computation," Fortschr. Phys., **48**, 771-783, (2000).

[11] I. Kominis, T. Kornack, and J. Allred, "A subfemtotesla multichannel atomic magnetometer," Nature, **422**, 596–599, (2003).

[12] H. J. Mamin, T. H. Oosterkamp, M. Poggio;| C. L. Degen; C. T. Rettner, and D. Rugar, "Isotope-Selective Detection and Imaging of Organic Nanolayers," Nano Lett.; , 9, 3020–3024, (2009).

[13] R. Maiwald, D. Leibfried, and J. Britton, "Stylus ion trap for enhanced access and sensing," Nature Phys, **5**, 551–554, (2009).

[14] P. P. Herrmann, J. Hoffnagle, N. Schlumpf, V. L. Telegdi, and A. Weis, "Stark spectroscopy of forbidden two-photon transitions: a sensitive probe for the quantitative measurement of small electric fields", J. Phys. B: Atom. Mol. Phys., **19**, 1271, (1986).

[15] N. Huntemann, C. Sanner, B. Lipphardt, Chr. Tamm, and E. Peik, "Single-Ion Atomic Clock with 3×10^{-18} Systematic Uncertainty," Phys. Rev. Lett., **116**, 063001, (2016).

[16] G. S. Waters and P. D. Francis, "A nuclear magnetometer," J. Sci. Instrum., **35**, 88, (1958).

[17] D. Drung, C. Abmann, J. Beyer, A. Kirste, M. Peters, F. Ruede, and T. Schurig, "Highly Sensitive and Easy-to-Use SQUID Sensors," IEEE Trans. Appl. Supercond., 17, 699-704, (2007).

[18] Y. Nakamura, Y. Pashkin, and J. Tsai, "Coherent control of macroscopic quantum states in a single-Cooper-pair box," Nature; **398**, 786–788, (1999).

[19] E. Abe, and K. Sasaki, "Tutorial: Magnetic resonance with nitrogen-vacancy centers in diamond - microwave engineering, materials science, and magnetometry," J. Appl. Phys, **123**, 161101 (2018).

[20] T. van der Sar, Z. H. Wang, M. S. Blok, H. Bernien, T. H. Taminiau, D. M. Toyli, D. A. Lidar, D. D. Awschalom, R. Hanson, and V. V. Dobrovitski, "Decoherence-protected quantum gates for a hybrid solid-state spin register," Nature, **484**, 82-86, (2012).

[21] J. Cai, A. Retzker, F. Jelezko, and M. B. Plenio, "A large-scale quantum simulator on a diamond surface at room temperature," Nat. Phys., **9**, 168-173, (2013).

[22] L. Childress, and R. Hanson, "Diamond NV centers for quantum computing and quantum networks," MRS Bulletin, **38**, 134–138, (2013).

[23] G. Balasubramanian, P. Neumann, D. Twitchen, M. Markham, R. Kolesov, N. Mizuochi, J. Isoya, J. Achard, J. Beck, J. Tissler, V. Jacques, P. Hemmer, F. Jelezko, and J. Wrachtrup, "Ultralong spin coherence time in isotopically engineered diamond," Nat. Mater., **8**, 383-387, (2009).

[24] G. Balasubramanian, I. Chan, R. Kolesov, M. Al-Hmoud, J. Tisler, C. Shin, C. Kim, A. Wojcik, P. R. Hemmer, A. Krueger, T. Hanke, A. Leitenstorfer, R. Bratschitsch, F. Jelezko, and J. Wrachtrup, "Nanoscale imaging magnetometry with diamond spins under ambient conditions," Nature, **455**, 648-651, (2008).

[25] M. S. Grinolds, M. Warner, K. De Greve, Y. Dovzhenko, L. Thiel, R. L. Walsworth, S. Hong, P. Maletinsky, and A. Yacoby, "Subnanometre resolution in three-dimensional magnetic resonance imaging of individual dark spins," Nat. Nanotech., **9**, 279 –284, (2014).

[26] E. Bourgeois, A. Jarmola, P. Siyushev, M. Gulka, J. Hruby, F. Jelezko, D. Budker, and M. Nesladek "Photoelectric detection of electron spin resonance of nitrogen-vacancy centres in diamond," Nat Commun., **6**, 8577, (2015).

[27] D. A. Hopper, H. J. Shulevitz, and L. C. Bassett, "Spin Readout Techniques of the Nitrogen-Vacancy Center in Diamond," Micromachines, **9**, 437, (2018).

[28] L. du. Preez, "Electron Paramagnetic Rsonance and Optical Investigations of Defect Centers in Diamond," PhD Thesis, (1965).

[29] C. D. Clark and C. A. Norris, "Photoluminescence associated with the 1.673, 1.944 and 2.498 eV centres in diamond," J. Phys. C Solid State Phys., **4**, 2223–2229, (1971).

[30] A. Gruber, A. Dräbenstedt, C. Tietz, L. Fleury, J. Wrachtrup, and C. von Borczyskowski, "Scanning Confocal Optical Microscopy and Magnetic Resonance on Single Defect Centers," Science, **276**, 2012-2014, (1997).

[31] C. Kurtsiefer, S. Mayer, P. Zarda, and H.Weinfurter, "Stable Solid-State Source of Single Photons," Phys. Rev. Lett., **85**, 290, (2000).

[32] F. Jelezko, T. Gaebel, I. Popa, A. Gruber, and J. Wrachtrup, "Observation of Coherent Oscillations in a Single Electron Spin," Phys. Rev. Lett., **92**, 076401, (2004).

[33] F. Jelezko, T. Gaebel, I. Popa, M. Domhan, A. Gruber, and J. Wrachtrup, "Observation of Coherent Oscillation of a Single Nuclear Spin and Realization of a Two-Qubit Conditional Quantum Gate," Phys. Rev. Lett., **93**, 130501, (2004).

[34] J. M. Taylor, P. Cappellaro, L. Childress, L. Jiang, D. Budker, P. R. Hemmer, A. Yacoby, R. Walsworth, and M. D. Lukin, "High-sensitivity diamond magnetometer with nanoscale resolution," Nat. Phys., **4**, 810–816, (2008).

[35] C. L. Degen, "Scanning magnetic field microscope with a diamond single-spin sensor," Appl. Phys. Lett., **92**, 243111, (2008).

[36] J. R. Maze, P. L. Stanwix, J. S. Hodges, S. Hong, J. M. Taylor, P. Cappellaro, L. Jiang, M. V. G. Dutt, E. Togan, A. S. Zibrov, A. Yacoby, R. L. Walsworth, and M. D. Lukin, "Nanoscale magnetic sensing with an individual electronic spin in diamond," Nature, **455**, 644–647, (2008).

[37] D. Le Sage, L. M. Pham, N. Bar-Gill, C. Belthangady, M. D. Lukin, A. Yacoby, and R. L. Walsworth, "Efficient photon detection from color centers in a diamond optical waveguide," Phys. Rev. B, **85**, 121202, (2012).

[38] L. M. Pham, D. L. Sage, P. L. Stanwix, T. K. Yeung, D. Glenn, A. Trifonov, P. Cappellaro, P. R. Hemmer, M. D. Lukin, H. Park, A. Yacoby, and R. L. Walsworth, "Magnetic field imaging with nitrogen-vacancy ensembles," New J. Phys., **13**, 045021, (2011).

[39] V. M. Acosta, A. Jarmola, E. Bauch, and D. Budker, "Optical properties of the nitrogen-vacancy singlet levels in diamond," Phys. Rev. B, **82**, 201202, (2010).

[40] J. F. Barry, M. J. Turner, J. M. Schloss, D. R. Glenn, Y. Song, M. D. Lukin, H. Park, and R. L. Walsworth, "Optical magnetic detection of single-neuron action potentials using quantum defects in diamond," Proc. Natl. Acad. Sci., **113**, 14133–14138, (2016).

[41] J. M. Schloss, J. F. Barry, M. J. Turner, and R. L. Walsworth, "Simultaneous broadband vector magnetometry using solid-state spins," Phys. Rev. Appl., **10**, 034044, (2018).

[42] C. S. Shin, C. E. Avalos, M. C. Butler, D. R. Trease, S. J. Seltzer, J. Peter Mustonen, D. J. Kennedy, V. M. Acosta, D. Budker, A. Pines, and V. S. Bajaj, "Room-temperature operation of a radiofrequency diamond magnetometer near the shot-noise limit," J. Appl. Phys., **12**, 124519, (2012).

[43] M. Loretz, T. Rosskopf, and C. L. Degen, "Radio-frequency magnetometry using a single electron spin," Phys. Rev. Lett., **110**, 017602, (2013).

[44] J. M. Boss, K. Chang, J. Armijo, K. Cujia, T. Rosskopf, J. R. Maze, and C. L. Degen, "One- and two-dimensional nuclear magnetic resonance spectroscopy with a diamond quantum sensor," Phys. Rev. Lett., **116**, 197601, (2016).

[45] J. D. A. Wood, D. A. Broadway, L. T. Hall, A. Stacey, D. A. Simpson, J.-P. Tetienne, and L. C. L. Hollenberg, "Wide-band nanoscale magnetic resonance spectroscopy using quantum relaxation of a single spin in diamond," Phys. Rev. B, **94**, 155402, (2016).

[46] J. Cai, F. Jelezko, M. B. Plenio, and A. Retzker, "Diamond-based single molecule magnetic resonance spectroscopy," New J. Phys., **15**, 013020, (2013).

[47] S. Steinert, F. Ziem, L. T. Hall, A. Zappe, M. Schweikert, N. Götz, A. Aird, G. Balasubramanian, L. Hollenberg, and J. Wrachtrup, "Magnetic spin imaging under ambient conditions with sub-cellular resolution," Nat. Commun., **4**, 1607, (2013).

[48] I. Lovchinsky, A. O. Sushkov, E. Urbach, N. P. de Leon, S. Choi, K. De Greve, R. Evans, R. Gertner, E. Bersin, C. Müller, L. McGuinness, F.

Jelezko, R. L. Walsworth, H. Park, and M. D. Lukin, "Nuclear magnetic resonance detection and spectroscopy of single proteins using quantum logic," Science, **351**, 836–841, (2016).

[49] L. M. Pham, S. J. DeVience, F. Casola, I. Lovchinsky, A. O. Sushkov, E. Bersin, J. Lee, E. Urbach, P. Cappellaro, H. Park, A. Yacoby, M. Lukin, and R. L. Walsworth, "NMR technique for determining the depth of shallow nitrogenvacancy centers in diamond," Phys. Rev. B, **93**, 045425, (2016).

[50] L. Shao, M. Zhang, M. Markham, A. M. Edmonds, and M. Loncar, "Diamond radio receiver: Nitrogen-vacancy centers as fluorescent transducers of microwave signals," Phys. Rev. Appl., **6**, 064008, (2016).

[51] J. M. Boss, K. S. Cujia, J. Zopes, and C. L. Degen, "Quantum sensing with arbitrary frequency resolution," Science, **356**, 837–840, (2017).

[52] S. Schmitt, T. Gefen, F. M. Stürner, T. Unden, G. Wolff, C. Müller, J. Scheuer, B. Naydenov, M. Markham, S. Pezzagna, J. Meijer, I. Schwarz, M. Plenio, A. Retzker, L. P. McGuinness, and F. Jelezko, "Submillihertz magnetic spectroscopy performed with a nanoscale quantum sensor," Science, **356**, 832–837, (2017).

[53] N. Aslam, M. Pfender, P. Neumann, R. Reuter, A. Zappe, F. Fávaro de Oliveira, A. Denisenko, H. Sumiya, S. Onoda, J. Isoya, and J. Wrachtrup, "Nanoscale nuclear magnetic resonance with chemical resolution," Science, **357**, 67–71, (2017).

[54] J.-P. Tetienne, T. Hingant, L. Rondin, A. Cavaillès, L. Mayer, G. Dantelle, T. Gacoin, J. Wrachtrup, J.-F. Roch, and V. Jacques, "Spin relaxometry of single nitrogen-vacancy defects in diamond nanocrystals for magnetic noise sensing," Phys. Rev. B, **87**, 235436, (2013).

[55] M. Pelliccione, B. A. Myers, L. M. A. Pascal, A. Das, and A. C. Bleszynski Jayich, "Two-dimensional nanoscale imaging of gadolinium spins via scanning probe relaxometry with a single spin in diamond," Phys. Rev. Appl., **2**, 054014, (2014).

[56] L. T. Hall, P. Kehayias, D. A. Simpson, A. Jarmola, A. Stacey, D. Budker, and L. C. L. Hollenberg, "Detection of nanoscale electron spin resonance

spectra demonstrated using nitrogen-vacancy centre probes in diamond," Nat. Commun., **7**, 10211, (2016).

[57] K. Arai, C. Belthangady, H. Zhang, N. Bar-Gill, S. J. DeVience, P. Cappellaro, A. Yacoby, and R. L. Walsworth, "Fourier magnetic imaging with nanoscale resolution and compressed sensing speed-up using electronic spins in diamond," Nat. Nanotech., **10**, 859–864, (2015).

[58] J.-C. Jaskula, E. Bauch, S. Arroyo-Camejo, M. D. Lukin, S. W. Hell, A. S. Trifonov, and R. L. Walsworth, "Superresolution optical magnetic imaging and spectroscopy using individual electronic spins in diamond," Optics Express, **25**, 11048–11064, (2017).

[59] V. M. Acosta, E. Bauch, M. P. Ledbetter, C. Santori, K.-M. C. Fu, P. E. Barclay, R. G. Beausoleil, H. Linget, J. F. Roch, F. Treussart, S. Chemerisov, W. Gawlik, and D. Budker, "Diamonds with a high density of nitrogen-vacancy centers for magnetometry applications," Phys. Rev. B, **80**, 115202, (2009).

[60] H. C. Davis, P. Ramesh, A. Bhatnagar, A. Lee-Gosselin, J. F. Barry, D. R. Glenn, R. L. Walsworth, and M. G. Shapiro, "Mapping the microscale origins of magnetic resonance image contrast with subcellular diamond magnetometry," Nat. Commun., **9**, 131, (2018).

[61] S. Steinert, F. Dolde, P. Neumann, A. Aird, B. Naydenov, G. Balasubramanian, F. Jelezko, and J. Wrachtrup, "High sensitivity magnetic imaging using an array of spins in diamond," Rev. Sci. Instrum., **81**, 043705, (2010).

[62] B. J. Maertz, A. P. Wijnheijmer, G. D. Fuchs, M. E. Nowakowski, and D. D. Awschalom, "Vector magnetic field microscopy using nitrogen vacancy centers in diamond," Appl. Phys. Lett., **96**, 092504, (2010).

[63] D. Le Sage, K. Arai, D. R. Glenn, S. J. DeVience, L. M. Pham, L. Rahn-Lee, M. D. Lukin, A. Yacoby, A. Komeili, and R. L. Walsworth, "Optical magnetic imaging of living cells," Nature, **496**, 486–489, (2013).

[64] V. M. Acosta, E. Bauch, A. Jarmol, L. J. Zipp, M. P. Ledbetter, and D. Budker, "Broadband magnetometry by infrared-absorption detection of

nitrogen-vacancy ensembles in diamond," Appl. Phys. Lett., **97**, 174104, (2010).

[65] Y. Dumeige, M. Chipaux, V. Jacques, F. Treussart, J.-F. Roch, T. Debuisschert, V. M. Acosta, A. Jarmola, K. Jensen, P. Kehayias, and D. Budker, "Magnetometry with nitrogen-vacancy ensembles in diamond based on infrared absorption in a doubly resonant optical cavity," Phys. Rev. B, **87**,155202, (2013).

[66] K. Jensen, N. Leefer, A. Jarmola, Y. Dumeige, V. M. Acosta, P. Kehayias, B. Patton, and D. Budker, "Cavity-Enhanced Room-Temperature Magnetometry Using Absorption by Nitrogen-Vacancy Centers in Diamond," Phys. Rev. Lett., **112**, 160802, (2014).

[67] G. Chatzidrosos, A. Wickenbrock, L. Bougas, N. Leefer, T. Wu, K. Jensen, Y. Dumeige, and D. Budker, "Miniature cavity-enhanced diamond magnetometer," Phys. Rev. Applied, **8**, 044019, (2017).

[68] L. Bougas, A. Wilzewski, Y. Dumeige, D. Antypas, T. Wu, A. Wickenbrock, E. Bourgeois, M. Nesladek, H. Clevenson, D. Braje, D. Englund, and D.Budker, "On the Possibility of Miniature Diamond-Based Magnetometers Using Waveguide Geometries," Micromachines, **9**, 276, (2018).

[69] H. Clevenson, M. E. Trusheim, C. Teale, T. Schroder, D. Braje, and D. Englund, "Broadband magnetometry and temperature sensing with a light-trapping diamond waveguide," Nat. Phys., **11**, 393–397, (2015).

[70] D. M. Toyli, C. F. de las Casas, D. J. Christle, V. V. Dobrovitski, and D. D. Awschalom, "Fluorescence thermometry enhanced by the quantum coherence of single spins in diamond," Proc. Natl. Acad. Sci., **110**, 8417-8421, (2013).

[71] G. Kucsko, P. C. Maurer, N. Y. Yao, M. Kubo, H. J. Noh, P. K. Lo, H. Park, and M. D. Lukin, "Nanometre-scale thermometry in a living cell," Nature, **500**, 54–58, (2013).

[72] M. S. J. Barson, P. Peddibhotla, P. Ovartchaiyapong, K. Ganesan, R. L. Taylor, M. Gebert, Z. Mielens, B. Koslowski, D. A. Simpson, L. P. McGuinness, J. McCallum, S. Prawer, S. Onoda, T. Ohshima,

A. C. Bleszynski Jayich, F. Jelezko, N. B. Manson, and M. W. Doherty, "Nanomechanical sensing using spins in diamond," Nano Lett., **17**, 1496–1503, (2017).

[73] D. R. Glenn, R. R. Fu, P. Kehayias, D. Le Sage, E. A. Lima, B. P. Weiss, and R. L. Walsworth, "Micrometer-scale magnetic imaging of geological samples using a quantum diamond microscope," Geochem. Geophys. Geosyst., **18**, 3254–3267, (2017).

[74] R. R. Fu, B. P. Weiss, E. A. Lima, R. J. Harrison, X.-N. Bai, S. J. Desch, D. S. Ebel, C. Suavet, H. Wang, D. Glenn, D. Le Sage, T. Kasama, R. L. Walsworth, and A. T. Kuan, "Solar nebula magnetic fields recorded in the semarkona meteorite," Science, **346**, 1089–1092, (2014).

[75] E. Farchi, Y. Ebert, D. Farfurnik, G. Haim, R. Shaar, and N. Bar-Gill, "Quantitative vectorial magnetic imaging of multi-domain rock forming minerals using nitrogen-vacancy centers in diamond," SPIN, **07**, 1740015, (2017).

[76] F. Casola, T. van der Sar, and A. Yacoby, "Probing condensed matter physics with magnetometry based on nitrogen-vacancy centres in diamond," Nat. Rev. Mater., **3**, 17088, (2018).

[77] R. Schirhagl, K. Chang, M. Loretz, and C. L. Degen, "Nitrogen-vacancy centers in diamond: Nanoscale sensors for physics and biology," Annu. Rev. Phys. Chem., **65**, 1, 83–105, (2014).

[78] Y. Wu, F. Jelezko, M. B. Plenio, and T. Weil, "Diamond quantum devices in biology," Angew. Chem. Int. Ed.,**55**, 6586–6598, (2016).

[79] F. Shi, Q. Zhang, P. Wang, H. Sun, J. Wang, X. Rong, M. Chen, C. Ju, F. Reinhard, H. Chen, J. Wrachtrup, J. Wang, and J. Du, "Single-protein spin resonance spectroscopy under ambient conditions," Science, **347**, 1135–1138, (2015).

[80] G. Chatzidrosos, J. S. Rebeirro, H. Zheng, M. Omar, A. Brenneis, F. M. Stürner, T. Fuchs, T. Buck, R. Rölver, T. Schneemann, P. Blümler, D. Budker, A. Wickenbrock, "Fiberized diamond-based vector magnetometers," arXiv:2102.11902v2, (2021).

[81] F. M. Stürner, A. Brenneis, T. Buck, J. Kassel, R. Rölver, T. Fuchs, A. Savitsky, D. Suter, J. Grimmel, S. Hengesbach, M. Förtsch, K. Nakamura, H. Sumiya, S. Onoda, J. Isoya, and F. Jelezko, "Integrated and Portable Magnetometer Based on Nitrogen-Vacancy Ensembles in Diamond," Adv. Quantum Technol., **4**, 2000111, (2021).

[82] F. M. Stürner, A. Brenneis, J. Kassel, U. Wostradowski, R. Rölver, T. Fuchs, K. Nakamura, H. Sumiya, S. Onoda, J. Isoya, and F. Jelezko, "Compact integrated magnetometer based on nitrogen-vacancy centres in diamond," Diam. Relat. Mater., **93**, 59-65, (2019).

[83] J. Teissier, A. Barfuss, P. Appel, E. Neu, and P. Maletinsky, "Strain coupling of a nitrogen-vacancy center spin to a diamond mechanical oscillator," Phys. Rev. Lett., **113**, 020503, (2014).

[84] V. Ivády, T. Simon, J. R. Maze, I. A. Abrikosov, and A. Gali, "Pressure and temperature dependence of the zero-field splitting in the ground state of NV centers in diamond: A first-principles study," Phys. Rev. B, **90**, 235205, (2014).

[85] R. S. Balmer, J. R. Brandon, S. L. Clewes, H. K. Dhillon, J. M. Dodson, I. Friel, P. N. Inglis, M. T. D., M. L. Markham, T. P. Mollart, N. Perkins, G. A. Scarsbrook, D. J. Twitchen, A. J. Whitehead, J. J. Wilman, and S. M. Woollard, "Chemical vapour deposition synthetic diamond: materials, technology and applications," J. Phys.: Condens. Matter, **21**, 364221, (2009)

[86] C. J. H. Wort, R. S. Balmer, "Diamond as an electronic material," Materials Today, **21**, 364221, (2008),

[87] S. Jin and H. Mavoori, "Processing and Properties of CVD Diamond for Thermal Management," J. Electron. Mater., **27**, 1148, (1998).

[88] A. M. Zaitsev, "Optical Properties of Diamond", A Data Handbook, Springer-Verlag, Berlin Heidelberg, (2001).

[89] B. Dischler, "Handbook of Spectral Lines in Diamond, Volume 1: Tables and Interpretations," Springer-Verlag Berlin Heidelberg, (2012).

[90] H. B. Dyer, F. A. Raal, L. Du Preez, and J. H. N. Loubser, "Optical absorption features associated with paramagnetic nitrogen in diamond," Phoilosophical Magazine, **11**, 763-744, (1965).

[91] F. P. Bundy, H. T. Hall, H. M. Strong, and R. H. Wentorf, "Man-Made Diamonds," Nature, **176**, 51, (1955),

[92] R. P. Mildren and J. R. Rabeau, "Optical Engineering of Diamond," Wiley- VCH, (2013).

[93] J. E. Butler, Y. A. Mankelevich, A. Cheesman, J. Ma, and M. N. R. Ashfold, "Understanding the chemical vapor deposition of diamond: recent progress," J. Phys. Condens. Matter, **21**, 364201, (2009).

[94] N. Mizuochi, J. Isoya, N. J., T. Sekiguchi, H. Watanabe, H. Kato, T. Makino, H. Okushi, and S. Yamasaki, "Isotope effects between hydrogen and deuterium microwave plasmas on chemical vapor deposition homoepitaxial diamond growth," J. Appl. Phys, **101**, 103501, (2007).

[95] T. Teraji, T. Taniguchi, S. Koizumi, K. Watanabe, M. Liao, Y. Koide, and J. Isoya, "Chemical Vapor Deposition of ^{12}C Isotopically Enriched Polycrystalline Diamond," Jpn. J. Appl. Phys., **51**, 090104, (2012).

[96] C. Müller, X. Kong, J.-M. Cai, K. Melentijevic, A. Stacey, M. Markham, D. Twitchen, J. Isoya, S. Pezzagna, J. Meijer, J. F. Du, M. B. Plenio, B. Naydenov, L. P. McGuinness, and F. Jelezko, "Nuclear magnetic resonance spectroscopy with single spin sensitivity," Nature Commun., **5**, 4703, (2014).

[97] N. Aslam, G. Waldherr, P. Neumann, F. Jelezko, and J. Wrachtrup, "Photo-induced ionization dynamics of the nitrogen vacancy defect in diamond investigated by single-shot charge state detection," New J. Phys., **15**, 013064, (2013).

[98] J. Meijer, B. Burchard, M. Domhan, C. Wittmann, T. Gaebel, I. Popa, F. Jelezko, and J. Wrachtrup, "Generation of single color centers by focused nitrogen implantation," Appl. Phys. Lett., **87**, 261909, (2005).

[99] B. Naydenov, V. Richter, J. Beck, M. Steiner, P. Neumann, G. Balasubramanian, J. Achard, F. Jelezko, J. Wrachtrup, and R. Kalish, "Enhanced

generation of single optically active spins in diamond by ion implantation," Appl. Phys. Lett., **96**, 163108, (2010).

[100] S. Pezzagna, B. Naydenov, F. Jelezko, J.Wrachtrup, and J. Meijer, "Creation efficiency of nitrogen-vacancy centres in diamond," New J. Phys., **12**, 065017, (2010).

[101] S. Pezzagna, D. Rogalla, H.-W. Becker, I. Jakobi, F. Dolde, B. Naydenov, J. Wrachtrup, F. Jelezko, C. Trautmann, and J. Meijer, "Creation of colour centres in diamond by collimated ion-implantation through nanochannels in mica," Phys. Status Solidi A., **208**, 2017-2022, (2011).

[102] C. Santori, P. E. Barclay, K.-M. C. Fu, and R. G. Beausoleil, "Vertical distribution of nitrogen-vacancy centers in diamond formed by ion implantation and annealing," Phys. Rev. B, **79**, 125313, (2003).

[103] K.-M. C. Fu, C. Santori, P. E. Barclay, and R. G. Beausoleil, "Conversion of neutral nitrogen-vacancy centers to negatively charged nitrogen-vacancy centers through selective oxidation," Appl. Phys. Lett., **96**, 121907, (2010).

[104] E. Kim, V. M. Acosta, E. Bauch, D. Budker, and P. R. Hemmer, "Electron spin resonance shift and linewidth broadening of nitrogen-vacancy centers in diamond as a function of electron irradiation dose," Appl. Phys. Lett., **101**, 082410, (2012).

[105] B. K. Ofori-Okai, S. Pezzagna, K. Chang, M. Loretz, R. Schirhagl, Y. Tao, B. A. Moores, K. Groot-Berning, J. Meijer, and C. L. Degen, "Spin properties of very shallow nitrogen vacancy defects in diamond," Phys. Rev. B, **86**, 081406(R), (2012).

[106] P. Neumann, R. Kolesov, B. Naydenov, J. Beck, F. Rempp, M. Steiner, V. Jacques, G. Balasubramanian, M. L. Markham, D. J. Twitchen, S. Pezzagna, J. Meijer, J. Twamley, F. Jelezko, and J. Wrachtrup, "Quantum register based on coupled electron spins in a room-temperature solid," Nature Physics, **6**, 249, (2010).

[107] A. M. Edmonds, U. F. S. D'Haenens-Johansson, M. E. Newton, K. M. C. Fu, C. Santori, R. G. Beausoleil, D. J. Twitchen, and M. L. Markham,

"Production of oriented nitrogen-vacancy color centers in synthetic diamond," Phys. Rev. B., **86**, 035201, (2012).

[108] A. M. Edmonds, M. Hart, C. A. Hart, M. J. Turner, P. -O. Colard, J. M. Schloss, K. Olsson, R. Trubko, M. L. Markham, A. Rathmill, B. Horne-Smith, W. Lew, A. Manickam, S. Bruce, P. G. Kaup, J. C. Russo, M. J. DiMario, J. T. South, J. T. Hansen, D. J. Twitchen, and R. L. Walsworth, "Generation of nitrogen-vacancy ensembles in diamond for quantum sensors: Optimization and scalability of CVD processes," arXiv:2004.01746, (2020).

[109] K. Ohno, F. J. Heremans, L. C. Bassett, B. A. Myers, D. M. Toyli, A. C. B. Jayich, C. J. Palmstrøm, and D. D. Awschalom, "Engineering shallow spins in diamond with nitrogen delta-doping," Appl. Phys. Lett., **101**, 082413, (2012).

[110] J. Achard, A. Tallaire, R. Sussmann, and A. Gicquel, "The control of growth parameters in the synthesis of high-quality single crystalline diamond by CVD," Journal of Crystal Growth, **284**, 396, (2005).

[111] J. R. Maze, A. Gali, E. Togan, Y. Chu, A. Trifonov, E. Kaxiras, and M. D. Lukin, "Properties of nitrogen-vacancy centers in diamond: the group theoretic approach," New J. Phys., **13**, 025025, (2011).

[112] N. R. S. Reddy, N. B. Manson, and E. R. Krausz, "Two-laser spectral hole burning in a colour centre in diamond," Journal of Luminescence, **38**, 46, (1987).

[113] G. D. Fuchs, V. V. Dobrovitski, R. Hanson, A. Batra, C. D. Weis, T. Schenkel, and D. D. Awschalom, "Excited-State Spectroscopy Using Single Spin Manipulation in Diamond," Phys. Rev. Lett., **101**, 117601, (2008).

[114] P. Neumann, R. Kolesov, V. Jacques, J. Beck, J. Tisler, A. Batalov, L. Rogers, N. B. Manson, G. Balasubramanian, F. Jelezko, and J. Wrachtrup, "Excited-state spectroscopy of single NV defects in diamond using optically detected magnetic resonance," New J. Phys., **11**, 013017, (2009).

[115] G. Davies and M. F. Hamer, "Optical Studies of the 1.945 eV Vibronic Band in Diamond," Proc. Math. Phys. Eng., **348**, 285, (1976).

[116] G. Davies, S. C. Lawson, A. T. Collins, A. Mainwood, and S. J. Sharp, "Vacancy-related centers in diamond," Phys. Rev. B, **46**, 13157, (1992).

[117] M. L. Goldman, M. W. Doherty, A. Sipahigil, N. Y. Yao, S. D. Bennett, N. B. Manson, A. Kubanek, and M. D. Lukin, "State-selective intersystem crossing in nitrogen-vacancy centers," Phys. Rev. B, **91**, 165201, (2015).

[118] M. L. Goldman, A. Sipahigil, M. W. Doherty, N. Y. Yao, S. D. Bennett, M. Markham, D. J. Twitchen, N. B. Manson, A. Kubanek, and M. D. Lukin, "Phonon-Induced Population Dynamics and Intersystem Crossing in Nitrogen- Vacancy Centers," Phys. Rev. Lett., **114**, 145502, (2015).

[119] A. Batalov, C. Zierl, T. Gaebel, P. Neumann, I.-Y. Chan, G. Balasubramanian, P. R. Hemmer, F. Jelezko, and J. Wrachtrup, "Temporal Coherence of Photons Emitted by Single Nitrogen-Vacancy Defect Centers in Diamond Using Optical Rabi-Oscillations," Phys. Rev. Lett., **100**, 077401, (2008).

[120] H. A. R. El-Ella, S. Ahmadi, A. M. Wojciechowski, A. Huck, and U. L. Andersen, "Optimised frequency modulation for continuous-wave optical magnetic resonance sensing using nitrogen-vacancy ensembles," Optics Express, **25**, 14809-14821, (2017).

[121] A. M. Edmonds, C. A. Hart, M. J. Turner, P.-O. Colard, J. M. Schloss, K. S. Olsson, R. Trubko, M. L. Markham, A. Rathmill, and B. Horne-Smith, "Characterisation of CVD diamond with high concentrations of nitrogen for magnetic-field sensing applications," Mater. Quantum. Technol., **1**, 025001, (2021).

[122] M. W. Doherty, F. Dolde, H. Fedder, F. Jelezko, J. Wrachtrup, N. B. Manson, and L. C. L. Hollenberg, "Theory of the ground-state spin of the NV^- center in diamond," Phys. Rev. B, **85**, 205203, (2012).

[123] S. Felton, A. M. Edmonds, M. E. Newton, P. M. Martineau, D. Fisher, D. J. Twitchen, and J. M. Baker, "Hyperfine interaction in the ground state of the negatively charged nitrogen vacancy center in diamond," Physical Review B, **79**, 075203 (2009).

[124] J. Rabeau, P. Reichart, G. Tamanyan, D. N. Jamieson, S. Prawer, F. Jelezko, T. Gaebel, I. Popa, M. Domhan, and J. Wrachtrup, "Implantation of labelled single nitrogen vacancy centers in diamond using ^{15}N," Appl. Phys. Lett., **88**, 023113, (2006).

[125] V. M. Acosta, E. Bauch, M. P. Lebetter, A. Waxman, L.-S. Bouchard, and D. Budker, "Temperature Dependence of the Nitrogen-Vacancy Magnetic Resonance in Diamond," Phys. Rev. Lett., **104**, 070801, (2010).

[126] A. Dréau, M. Lesik, L. Rondin, P. Spinicelli, O. Arcizet, J.-F. Roch, and V. Jacques, "Avoiding power broadening in optically detected magnetic resonance of single NV defects for enhanced dc magnetic field sensitivity," Phys. Rev. B, **4**, 195–204, (2011).

[127] J. F. Barry, J. M. Schloss, E. Bauch, M. J. Turner, C. A. Hart, L. M. Pham, and R. L. Walsworth, "Sensitivity optimization for NV diamond magnetometry," Rev. Mod. Phys., **92**, 015004, (2020).

[128] C. Müller, "Sensing single spins with colour centres in diamond," PhD thesis, Universität Ulm, (2016).

[129] P. Neumann, "Towards a room temperature solid state quantum processor – The nitrogen-vacancy center in diamond, PhD thesis," Universität Stuttgart, (2011).

[130] K. Ohashi, T. Rosskopf, H. Watanabe, M. Loretz, Y. Tao, R. Hauert, S. Tomizawa, T. Ishikawa, J. Ishi-Hayase, S. Shikata, C. L. Degen, and K. M. Itoh, "Negatively Charged Nitrogen-Vacancy Centers in a 5 nm Thin ^{12}C Diamond Film," Nano Letters , **13**, 4733, (2013).

[131] N. Bar-Gill, L. M. Pham, A. Jarmola, D. Budker, and R. Walsworth, "Solidstate electronic spin coherence time approaching one second," Nat. Commun., **4**, 1743, (2013).

[132] E. L. Hahn, "Spin Echoes," Phys. Rev., **80**, 580, (1950).

[133] C. P. Slichter, "Principles of Magnetic Resonance," Springer-Verlag, New York, (1990).

[134] L. Childress, M. V. G. Dutt, J. M. Taylor, A. S. Zibrov, F. Jelezko, J.Wrachtrup, P. R. Hemmer, and M. D. Lukin, "Coherent Dynamics of Coupled Electron and Nuclear Spin Qubits in Diamond," Science, **318**, 281, (2006).

[135] R. Hanson, V. V. Dobrovitski, A. E. Feiguin, O. Gywat, and D. D. Awschalom, "Coherent Dynamics of a Single Spin Interacting with an Adjustable Spin Bath," Science, **320**, 352, (2008).

[136] J. R. Maze, J. M. Taylor, and M. D. Lukin, "Electron spin decoherence of single nitrogen-vacancy defects in diamond," Phys. Rev. B, **78**, 094303, (2008).

[137] M. V. G. Dutt, L. Childress, L. Jiang, E. Togan, J. Maze, F. Jelezko, A. S. Zibrov, P. R. Hemmer, and M. D. Lukin, "Quantum register based on individual electronic and nuclear spin qubits in diamond," Science, **316**, 1312 (2007).

[138] P. Appel, Doctoral Thesis, "Scanning nanomagnetometry : probing magnetism with single spins in diamond," University of Basel, (2017).

[139] S. K. Sekatskii, and V. S. Letokhov, "Nanometer-resolution scanning optical microscope with resonance excitation of the fluorescence of the samples from a single-atom excited center," Jetp Lett., **63**, 319–323, (1996).

[140] B. M. Chernobrod, and G. P. Berman , "Spin microscope based on optically detected magnetic resonance," J. Appl. Phys., **97**, 014903 (2005).

[141] G. de Lange, Z. H. Wang, D. Ristè, V. V. Dobrovitski, and R. Hanson, "Universal dynamical decoupling of a single solid-state spin from a spin bath," Science, **330**, 60–63, (2010).

[142] M. S. Grinolds, S. Hong, P. Maletinsky, L. Luan, M. D. Lukin, R. L. Walsworth, and A. Yacoby, "Nanoscale magnetic imaging of a single electron spin under ambient conditions," Nat. Phys., **9**, 215, (2013).

[143] H. J. Mamin, M. Kim, M. H. Sherwood, C. T. Rettner, K. Ohno, D. D. Awschalom, and D. Rugar, "Nanoscale Nuclear Magnetic Resonance with a Nitrogen-Vacancy Spin Sensor," Science, **339**, 557, (2013).

[144] T. Staudacher, F. Shi, S. Pezzagna, J. Meijer, J. Du, C. A. Meriles, F. Reinhard, and J. Wrachtrup, "Nuclear Magnetic Resonance Spectroscopy on a (5-Nanometer)^3 Sample Volume," Science, **339**, 561, (2013).

[145] G. de Lange, D. Ristè, V. V. Dobrovitski, and R. Hanson, "Single-Spin Magnetometry with Multipulse Sensing Sequences," Phys. Rev. Lett., **106**, 080802, (2011).

[146] J. P. Haddena, J. P. Harrison, A. C. Stanley-Clarke, L. Marseglia, Y.-L. D. Ho, B. R. Patton, J. L. O'Brien, and J. G. Rarity, "Strongly enhanced photon collection from diamond defect centers under microfabricated integrated solid immersion lenses," Appl. Phys. Lett., **97**, 241901, (2010).

[147] Y. Dumeige, J.-F. Roch, F. Bretenaker, T. Debuisschert, V. Acosta, C. Becher, G. Chatzidrosos, A. Wickenbrock, L. Bougas, A. Wilzewski, and D. Budker, "Infrared laser threshold magnetometry with a NV doped diamond intracavity etalon," Opt. Express, **27**, 1706-1717, (2019).

[148] B. A. Myers, A. Ariyaratne, and A. C. B. Jayich, "Double-quantum spin-relaxation limits to coherence of near-surface nitrogen-vacancy centers," Phys. Rev. Lett., **118**, 197201, (2017).

[149] I. Friel, S.L. Clewes, H.K. Dhillon, N. Perkins, D.J. Twitchen, and G.A. Scarsbrook, "Control of surface and bulk crystalline quality in single crystal diamond grown by chemical vapour deposition," Diamond and Related Materials, **18**, 808-815, (2009).

[150] M. Fox, "Quantum Optics: An Introduction," Oxford University Press, Oxford, (2006).

[151] Y. Dumeige, F. Treussart, R. Alléaume, T. Gacoin, J.-F. Roch, and P. Grangier, "Photo-induced creation of nitrogen-related color centers in diamond nanocrystals under femtosecond illumination," J. Lumin., **109**, 61–67, (2004).

[152] N. B. Manson, J. P. Harrison, and M. J. Sellars, "Nitrogen-vacancy center in diamond: Model of the electronic structure and associated dynamics," Phys. Rev. B, **74**, 104303 (2006).

[153] I. Meirzada, Y. Hovav, S. A. Wolf, and N. Bar-Gill, "Negative charge enhancement of near-surface nitrogen vacancy centers by multicolor excitation," Phys. Rev. B, **98**, 245411, (2018).

[154] M. Mrózek, D. Rudnicki, P. Kehayias, A. Jarmola, D. Budker, and W. Gawlik, "Longitudinal spin relaxation in nitrogen-vacancy ensembles in diamond," EPJ Quantum Technol., **2**, 22, (2015).

[155] A. Yariv, and P. Yeh, "Photonics: Optical Electronics in Modern Communications," Oxford University Press, Oxford, (2007).

[156] J.-P. Tetienne, L. Rondin, P. Spinicelli, M. Chipaux, T. Debuisschert, J.-F. Roch, and V. Jacques, "Magnetic-field dependent photodynamics of single NV defects in diamond: an application to qualitative all-optical magnetic imaging," New J. Phys., **14**, 103033, (2012).

[157] T.-L. Wee, Y.-K. Tzeng, C.-C. Han, H.-C. Chang, W. Fann, J.-H. Hsu, K.-M. Chen, and Y.-C. Yu, "Two-photon excited fluorescence of nitrogen-vacancy centers in proton-irradiated type Ib diamond," J. Phys. Chem. A ,**111**, 9379–9386, (2007).

[158] P. Siyushev, H. Pinto, M. Vörös, A. Gali, F. Jelezko, and J. Wrachtrup, "Optically Controlled Switching of the Charge State of a Single Nitrogen-Vacancy Center in Diamond at Cryogenic Temperatures," Phys. Rev. Lett., **110**, 167402, (2013).

[159] R. H. Dicke "The measurement of thermal radiation at microwave frequencies," Rev. Sci. Instrum., **17**, 268-275 (1946).

[160] H. Clevenson, Ph.D. dissertation, "Sensing and timekeeping using a light-trapping diamond waveguide," Massachusetts Institute of Technology, (2017).

[161] A. Wickenbrock, H. Zheng, L. Bougas, N. Leefer, S. Afach, A. Jarmola, V. M. Acosta, and D. Budker, "Microwave-free magnetometry with nitrogen-vacancy centers in diamond," Appl. Phys. Lett., **109**, 053505, (2016).

[162] H. Taub, and D. L. Schilling, "Principles of Communication Systems," McGraw-Hill, New York, (1986).

[163] T. G. Mayerhöfer, S. Pahlow, and J. Popp, "The Bouguer-Beer-Lambert Law: Shining Light on the Obscure," ChemPhysChem, **21**, 2029, (2020).

[164] E. Bauch, C. A. Hart, J. M. Schloss, M. J. Turner, J. F. Barry, P. Kehayias, S. Singh, and R. L. Walsworth, "Ultralong Dephasing Times in Solid-State Spin Ensembles via Quantum Control," Phys. Rev. X, **8**, 031025, (2018).

[165] E. R. MacQuarrie, T. A. Gosavi, A. M. Moehle, N. R. Jungwirth, S. A. Bhave, and G. D. Fuchs, "Coherent control of a nitrogen-vacancy center spin ensemble with a diamond mechanical resonator," Optica, **2**, 233-238, (2015).

[166] E. Bauch, S. Singh, J. Lee, C. A. Hart, J. M. Schloss, M. J. Turner, J. F. Barry, L. M. Pham, N. Bar-Gill, S. F. Yelin, and R. L. Walsworth, "Decoherence of ensembles of nitrogen-vacancy centers in diamond," Phys. Rev. B, **102**, 134210, (2020).

[167] C. Zhang, F. Shagieva, M. Widmann, M. Kübler, V. Vorobyov, P. Kapitanova, E. Nenasheva, R. Corkill, O. Rhrle, K. Nakamura, H. Sumiya, S. Onoda, J. Isoya, and J. Wrachtrup, "Diamond Magnetometry and Gradiometry Towards Subpicotesla dc Field Measurement," Phys. Rev. Appl., **15**, 064075, (2021).

[168] A. Wickenbrock, H. Zheng, G. Chatzidrosos, J. S. Rebeirro, T. Schneemann, and P. Blümler, "High homogeneity permanent magnet for diamond magnetometry," Journal of Magnetic Resonance, **322**, (2021).

[169] S. Ahmadi, H. A. R. El-Ella, A. M. Wojciechowski, T. Gehring, J. O. B. Hansen, A. Huck, and U. L. Andersen, "Nitrogen-vacancy ensemble magnetometry based on pump absorption," Phys. Rev. B, **97**, 024105, (2018).

[170] E. Bernardi, E. Moreva, P. Traina, G. Petrini, S. D. Tchernij, J. Forneris, Ž. Pastuovic, I. P. Degiovanni, P. Olivero, and M. Genovese, "A biocompatible technique for magnetic field sensing at (sub)cellular scale using Nitrogen-Vacancy centers," EPJ Quantum Technol., 7, 13, (2020).

[171] S. Schiller, I. I. Yu, M. M. Fejer, and R. L. Byer, "Fused-silica monolithic total-internal-reflection resonator," Opt. Lett., **17**, 378-380, (1992).

[172] M. A.C. de Araújo, R. Silva, E. de Lima, D. P. Pereira, and P. C. de Oliveira, "Measurement of Gaussian laser beam radius using the knife-edge technique: improvement on data analysis," Applied Optics, **48**, 393-396, (2009).

[173] M. Bonnett Del Alamo, C. Soncco, R. Helaconde, J. L. Bazo Alba, and A. M. Gago , "Laser spot measurement using simple devices", AIP Advances, **11**, 075016 (2021).

Publications

- "Magnetic field sensing based on IR absorption in NV centers using diamond waveguide geometries," Himadri Chatterjee, Benjamin Kambs, Georgios Chatzidrosos, Arne Wickenbrock, Andrew Edmonds, Matthew Markham, Dmitry Budker, Christoph Becher, (in preparation), 2021.

Acknowledgments

After all these years, having reached at the point of completion of the thesis, I would like to take the opportunity to convey my heartiest thanks to all the people, without whose help and support I would not have reached this point. I would like to begin by thanking my research adviser Prof. Dr. Christoph Becher, for giving me the opportunity to join Quantum Optics group as a PhD student. I am sincerely grateful for his constant support and encouragement over the past years. His guidance related to scientific works and professional matters taught me a lot and has enhanced my capabilities as an experimental physicist.

I would also like to thank Prof. Dr. Rainer Birringer, for taking his time out to be the second referee of this thesis.

Many thanks go to Dr. Benjamin Kambs for helping me on many matters of this work. His knowledge and expertise enriched me during the time period he worked with me. I came to know about many useful experimental and simulation skills during our discussions, which was of great help. He was never tired of helping me in lab or discussing physics with me. Special thanks for taking out time from his busy schedule to proofread the thesis. Also in many occasions outside work, he helped me to a great extent.

I would like to thank Prof. Dr. Dimitry Budker, Dr. Arne Wickenbrock, and Georgios Chatzidrosos for their help with experimental apparatus at a very crucial time of our work. Special thanks to Georgios for discussing many technical know how of the magnetometry experiments, which enriched my knowledge. At one point, during our experiments Dr. Mina Mohammadi-Kambs also provided us with experimental apparatus. I would like to take this opportunity to thank her as well.

The results presented in this dissertation, would not have been achieved without the well prepared diamond samples. Therefore, I would like to extend my thanks to the people from Element 6, along with Matthew Markham and Andrew Edmonds for the high quality diamonds they have provided us. High

quality polishing of our diamond samples was very crucial for all the works I have presented in this dissertation. Therefore I would like to thank the people from Almax easylabs, for their outstanding work.

I feel fortunate to join a dynamic, talented, creative and motivated research group. I would like to thank all present and past members of our group. I also learned many things while I was working in the lab with Alexender Bommer, Matthias Bock, Philipp Fuchs, and Sarah Linder. Special thanks to Philipp Fuchs, for helping me out in some occasions with his brilliant skills of photography to take some high quality photographs of our tiny diamond samples.

Much help came from our electronic workshop. I wish to thank Mr. Stefan Leow and Mr. Günther Marchand, for their help with electronics. I would also thank all the people from the mechanical workshop, who for many instances made mechanical components for our set up.

When it comes to non-scientific assistance, there are some more people who helped me a lot and made things easier. Therefore, I want to thank Mrs. Elke Huschens and Mrs. Nina Apfelbaum for helping on everything regarding administration and paper works.

I would also like to thank some persons outside from our group at this occasion. My time in Saarbrücken became more enjoyable and endurable because of their friendship. I thank Nimba Pandey and Sukhvinder Singh for their friendship, support and motivation.

All I've accomplished up to this point traces back to my parents and grandparents.I would take this opportunity to remember my grandfathers Mr.Bankim Chatterjee and Mr. Swadhin Banerjee who are no longer with us but without their encouragement and blessings, I would not have come to this point. My interest in science was instilled by my parents in my childhood as I recall now. Stargazing at night or making science models with my father Mr. Debidas Chattopadhyay or attending science quizzes with my mother Mrs. Radha Chatterjee in my early years has a great deal to shape my inquisitiveness. I am so grateful to my *Boromama* Dr. Manojit Mookherjee, for helping me gain the courage to change course toward the new and unknown. I am also fortunate to have very supportive in-laws. Mr. Tapas Mukherjee and Mrs. Jhuma Mukherjee have shown me more love and support than I ever could have imagined. Their continuous love and support have made this journey a lot more smoother. Last but not the least I thank all my relatives who at any point pushed me for excellence.

I would like to take this opportunity to thank my teachers and professors. I have had the good fortune to learn many things from Mr. Parimal Thakur, Mr. Pratap SinhaRoy, Mr. Arup Roy, Prof. Uttam Ghosh and Mr. Milan Das. I started my journey in experimental physics under the guidance of Prof. Dr. Fedor Jelezko and PD Dr. Boris Naydenov at Institute of Quantum Optics in Ulm University. The knowledge and skills I gained there under their supervision helped me to pursue my PhD studies. At this occasion, I would like to than them as well.

Finally, I owe everything to my wife and best friend, Mayuri Mukherjee. Her contributions to my PhD are mostly invisible, but they are considerable. Throughout my Ph.D., she was a sounding board. Her support and constant belief in me sustained me through the most difficult parts of my Ph.D. Her joy in my achievements made those successes sweeter. She made the last five years more wonderful than I could ever have imagined and hoped for. I am so happy and grateful to have you in my life.